

Mechanical modelling of sand considering simple shear condition and its application to pile foundation

Zexiang Wu

► **To cite this version:**

Zexiang Wu. Mechanical modelling of sand considering simple shear condition and its application to pile foundation. Civil Engineering. École centrale de Nantes, 2017. English. NNT : 2017ECDN0045 . tel-02124190

HAL Id: tel-02124190

<https://tel.archives-ouvertes.fr/tel-02124190>

Submitted on 9 May 2019

HAL is a multi-disciplinary open access archive for the deposit and dissemination of scientific research documents, whether they are published or not. The documents may come from teaching and research institutions in France or abroad, or from public or private research centers.

L'archive ouverte pluridisciplinaire **HAL**, est destinée au dépôt et à la diffusion de documents scientifiques de niveau recherche, publiés ou non, émanant des établissements d'enseignement et de recherche français ou étrangers, des laboratoires publics ou privés.

Thèse de Doctorat

Zexiang WU

*Mémoire présenté en vue de l'obtention
du grade de Docteur de l'Ecole Centrale de Nantes
Sous le label de l'UNIVERSITÉ BRETAGNE LOIRE*

École doctorale : Sciences pour l'ingénieur

Discipline : Génie Civil

Unité de recherche : Institut de recherche en génie civil et mécanique

Soutenue le 13/12/2017

Modélisation du comportement des sables sous la condition de cisaillement simple et applications au calcul des pieux

JURY

Président :	Madhia HATTAB , Professeure des universités, Université de Lorraine
Rapporteurs :	Jean-Claude DUPLA , Professeur, Ecole des Ponts ParisTech France Xian-feng LIU , Professeur, Université Jiaotong du Sud- Ouest, Chengdu, Chine
Examineurs:	Madhia HATTAB , Professeure des universités, Université de Lorraine Zhen-Yu YIN , Maître de conférences HDR, Ecole Centrale de Nantes
Directeur de thèse :	Pierre-Yves HICHER , Professeur émérite, Ecole Centrale de Nantes
Co-directeur de thèse :	Christophe DANO , Maître de conférences, Université Grenoble Alpes

Thèse de Doctorat

Zexiang WU

Modélisation du comportement des sables sous la condition de cisaillement simple et applications au calcul des pieux

Mechanical modelling of sand considering simple shear condition and its application to pile foundation

Résumé

La thèse vise à étudier le comportement mécanique des sables sous la condition de cisaillement simple et à son application au calcul des pieux. Tout d'abord, un modèle de sable récemment développé (SIMSAND) prenant en compte l'état critique est introduit avec une procédure directe de détermination des paramètres. Le modèle est implanté dans un code de calcul aux éléments finis qui a fait l'objet de différentes validations. Ensuite, le modèle est amélioré en considérant l'anisotropie inhérente lors de la rotation des contraintes principales sous la condition de cisaillement simple et a été validé en utilisant les résultats des essais triaxiaux et de cisaillement simple sur le sable de Fontainebleau. Les essais de cisaillement simple sont analysés en imposant les conditions de sollicitations réelles tridimensionnelles appliquées par l'appareillage utilisé. L'inhomogénéité de l'échantillon avec l'effet de la taille de l'échantillon est également étudiée. Puis, des essais de cisaillement simple cycliques drainés et non-drainés sur le sable de Fontainebleau sont effectués pour étudier les caractéristiques sous charges cycliques, telles que la dégradation de la contrainte normale effective et l'accumulation de la déformation volumique, compte tenu de certains facteurs comme l'indice des vides initial, la contrainte normale appliquée, le rapport de contrainte de cisaillement cyclique et le rapport de contrainte de cisaillement moyenne. Sur la base de ces résultats, deux modèles analytiques sont proposés pour prédire la dégradation à long terme de la contrainte normale effective et l'accumulation des déformations volumiques en fonction du nombre de cycles. En outre, les essais cycliques de cisaillement simple sont simulés par le modèle SIMSAND amélioré en utilisant une technique d'inversion de contrainte. Enfin, on simule une série de pieux modèles sous charges monotone et cyclique pour laquelle la résistance en pointe du pieu est évaluée ainsi que la réponse du sol entourant le pieu.

Mots clés

Cisaillement simple; rotation des contraintes principales; comportement cyclique; loi de comportement, fondation sur pieux

Abstract

The thesis aims to study the mechanical behaviour of sand under simple shear condition and to apply the results to the numerical simulation of pile foundation. First, a recently developed critical state sand model (SIMSAND) is introduced with a straightforward procedure of parameters determination, implemented into a finite element code and then subjected to a series of validations. Then, the model is enhanced by considering the inherent anisotropy during the principal stress rotation under the simple shear condition and validated by using results of both triaxial tests and simple shear tests on Fontainebleau sand. Simple shear tests are analysed by simulating in three-dimensions the real conditions imposed by the simple shear apparatus. The inhomogeneity of the samples with the effect of sample size is also investigated. Furthermore, undrained and drained cyclic simple shear tests on Fontainebleau sand are conducted to investigate the cyclic responses, such as the effective normal stress degradation and the volumetric strain accumulation, respectively, considering some impact factors such as the initial void ratio, the normal stress, the cyclic shear stress ratio and the average shear stress ratio. Based on these results, two analytical models are proposed to predict the long-term degradation of the effective normal stress and the accumulation of the volumetric strain with the number of cycles. Moreover, the cyclic simple shear tests are simulated by the enhanced SIMSAND model by incorporating the stress reversal technique. Finally, a series of model pile tests under monotonic and cyclic loadings are simulated based on which the cone resistance of the piles is evaluated as well as the response of the soil surrounding the pile.

Key Words

Simple shear; principal stress rotation; cyclic loading; constitutive model, sand, pile foundation

Acknowledgments

The author would like to express his sincere thanks to all the people who he worked with during this PhD period, without them the research could not be accomplished.

Prof. Pierre-Yves HICHER, as the supervisor of my PhD study over past three years, did a lot of efforts in improving my knowledge and academic ability in the field of geotechnical engineering. He showed me his patience and strictness, his knowledge and modesty in directing my research. His excellent academic attitude and kind personality are greatly appreciated.

Dr. Christophe DANO, is also my supervisor of the PhD study. During my PhD study he provided the consultant support to arrange our high-standard laboratory for simple shear tests in Ecole Centrale de Nantes. I am greatly indebted to him for his continuous help and strong support. His wealth of ideas has enriched this dissertation and is highly appreciated.

The two supervisors of mine provided me with great freedom which allowed me to dive into the sea of research and to think freely. Words are not enough to express my appreciations.

I am extremely grateful to Dr. Zhenyu YIN with whom I worked closely together during my PhD study. Due to his large experience and knowledge on fields of constitutive modelling and numerical method, he contributed many good ideas for my thesis. With his efforts and encouragements, this work could be successfully proceeded. Moreover, I also wish to extend my gratitude to Prof. Shuilong SHEN and Prof. Chuang YU for their continuous help and concern throughout this research.

I would like to thank Mrs. HICHER (Shimu) for her effort to help me learn the language and French culture. She is like a mentor and a family member. With her charming personalities, she made my life here very enjoyable.

I have my indebtedness to Dr. Zheng LI and Dr. Yinfu JIN, who have taught me Finite Element simulation and optimization method which I benefited most in my research.

My thanks are also dedicated to my exceptional colleagues I met in ECN: Dr. Qian ZHAO, Dr. Menghuan GUO, Chaofa ZHAO, Jiangxin Liu, Jie YANG, Zhuang JIN, Ran

ZHU and Huan WANG. Without their friendship, the three-year journey could be a little boring and frustrating.

My special appreciation goes to Dongmei TU and Zuoxi WU, my wife and son who always stand beside me. Their love, strength, and wisdom have inspired me to be the best.

Finally, Kisses to my parents and brother for their love and supports to my study abroad of CHINA, which is the greatest power in the world and drives me to success.

Table of constants

TABLE OF CONSTANTS	I
LIST OF FIGURES	V
LIST OF TABLES	XIII
NOTATION.....	XIV
ABSTRACT.....	XVII
GENERAL INTRODUCTION.....	XIX
CHAPTER 1 LITERATURE REVIEW	
1.1 Engineering background	1
1.2 Cyclic soil-elementary tests applied to pile-foundation.....	1
1.2.1 Triaxial shearing condition	1
1.2.2 Soil-structure interface shearing condition	3
1.2.3 Simple shearing condition.....	4
1.3 Experimental investigation of simple shear tests	6
1.3.1 Monotonic behaviour of simple shear test	7
1.3.2 Fabric anisotropy during principal stress rotation	9
1.3.3 Cyclic behaviour of simple shear test	10
1.3.4 Analytical models for cyclic response	12
1.4 Constitutive modelling of granular materials	15
1.4.1 Phenomenological models	15
1.4.2 Multi-scale models.....	15
1.4.3 Discrete element models	16
1.5 Thesis organization	17
CHAPTER 2 A STRAIGHTFORWARD PROCEDURE OF DETERMINING PARAMETERS OF SIMSAND MODEL	
2.1 Introduction.....	19
2.2 Simple critical-state based sand model	20
2.2.1 Elastic behaviour.....	20
2.2.2 Plastic behaviour.....	20
2.2.3 Critical state and interlocking effect	22
2.2.4 Summary of model parameters	23

2.3	Procedure for determining parameters	24
2.3.1	Determination of the elasticity related parameters	25
2.3.2	Determination of critical state related parameters	27
2.3.3	Determination of plasticity interlocking related parameters.....	28
2.4	Validation by real laboratory tests.....	31
2.5	Implementation into a finite element code.....	36
2.5.1	Explicit finite element method.....	36
2.5.2	Evaluation by modelling of footings.....	40
2.6	Conclusion	42

CHAPTER 3 FINITE ELEMENT ANALYSIS OF SIMPLE SHEAR TEST

3.1	Introduction.....	43
3.2	Enhanced constitutive model	44
3.2.1	Basic framework of SIMSAND model.....	44
3.2.2	Consideration of soil anisotropy	44
3.2.3	Calibration of the model from triaxial tests on Fontainebleau sand	46
3.2.4	Sensitivity of anisotropic parameters at simple shear condition.....	49
3.3	Finite element analysis of simple shear tests	49
3.3.1	Laboratory simple shear tests.....	49
3.3.2	Finite element modelling	51
3.3.3	Test validation.....	53
3.3.4	Distribution of normal stress.....	53
3.3.5	Distribution of shear stress, deviatoric plastic strain and anisotropic variable.....	56
3.4	Evaluation of aspect ratio of sample	59
3.4.1	Finite element modelling	59
3.4.2	Simulation results for different aspect ratios	60
3.4.3	Inhomogeneity analysis	60
3.5	Conclusion	63

CHAPTER 4 NORMAL EFFECTIVE STRESS DEGRADATION IN SAND UNDER UNDRAINED SIMPLE SHEAR CONDITION

4.1	Introduction.....	65
4.2	Material and testing program.....	67
4.3	Test results and interpretation	70
4.3.1	Monotonic stress-strain behavior.....	70
4.3.2	Symmetrical cyclic loading.....	72
4.3.3	Non-symmetrical cyclic loading	74

4.4	Evaluation of the degradation of the effective normal stress.....	78
4.4.1	Number of cycles to liquefaction.....	78
4.4.2	Degradation of effective normal stress	79
4.4.3	Calibration procedure.....	80
4.4.4	Validation of the suggested relationship.....	82
4.5	Conclusions.....	84

CHAPTER 5 CYCLIC VOLUMETRIC STRAIN ACCUMULATION OF SAND UNDER DRAINED SIMPLE SHEAR CONDITION

5.1	Introduction.....	85
5.2	Experimental investigation	86
5.2.1	Testing program.....	86
5.2.2	Cyclic densification	87
5.2.3	Influence of strain accumulation to post-cyclic behaviour	89
5.3	Interpretation of experimental results	91
5.3.1	Effect of relative density.....	91
5.3.2	Effect of normal stress level	92
5.3.3	Effect of cyclic shear stress ratio	93
5.3.4	Effect of average shear stress ratio	94
5.4	Analytical model of volumetric strain accumulation.....	95
5.5	Validation.....	97
5.6	Conclusion	98

CHAPTER 6 MODELLING OF CYCLIC BEHAVIOUR OF SAND-PILE FOUNDATION

6.1	Introduction.....	101
6.2	Incorporation of the shear stress reversal technique.....	101
6.3	Model validation on Toyoura sand.....	103
6.3.1	Constant mean effective pressure cyclic triaxial tests	103
6.3.2	Drained cyclic triaxial tests.....	104
6.3.3	Undrained cyclic triaxial tests.....	105
6.4	Model validation on Fontainebleau sand.....	107
6.4.1	Drained cyclic triaxial tests at constant- p'	107
6.4.2	Undrained cyclic triaxial tests.....	107
6.4.3	Undrained cyclic simple shear tests.....	109
6.4.4	Drained cyclic simple shear tests.....	111
6.5	Simulation of a mini-scale model pile penetration test.....	113

6.5.1	3SR mini-scale model pile and FE modelling	113
6.5.2	Simulation results.....	114
6.5.3	Parametrical study.....	116
6.6	Simulation of ICP model pile penetration test	116
6.6.1	ICP model pile and FE modelling.....	116
6.6.2	Simulation results.....	118
6.6.3	Monotonic response of sand surrounding the pile	119
6.7	Simulation of cyclic model pile test	120
6.7.1	Modelling of cyclic pile test`	120
6.7.2	Simulation results.....	121
6.7.3	Cyclic response of sand around pile	122
6.8	Conclusion	122
 CHAPTER 7 GENERAL CONCLUSIONS AND PERSPECTIVES		
7.1	General conclusions	125
7.2	Perspectives	127
REFERENCES.....		128
APPENDIX A MATLAB CODE FOR PARAMETERS OF SIMSAND		140
LIST OF PUBLICATIONS		146

List of figures

Figure 1.1 Schematic diagram (a) soil element around pile, (b) specimen loading path after (Sim et al. 2013b; Aghakouchak et al. 2015)	2
Figure 1.2 Stress-strain state under cyclic loading on Fontainebleau sand (a) degradation of mean effective stress, (b) accumulation of axial stress (Aghakouchak et al. 2015).....	3
Figure 1.3 Schematic diagram of soil-pile interface direct shear tests (Pra-ai and Boulon 2017)	3
Figure 1.4 Experimental results (a) degradation of normal stress; (b) evaluation of stress ratio (Pra-ai and Boulon 2017)	4
Figure 1.5 Schematic diagram of soil-pile interface (Randolph and Wroth 1981).....	4
Figure 1.6 Offshore wind foundation and its schematic diagram of loads (Nikitas et al. 2017)	5
Figure 1.7 Cyclic drained simple shear tests with 100kPa normal stress: (a) vertical strain with cyclic number, (b) shear modulus with cyclic number (Nikitas et al. 2017)	6
Figure 1.8 Simple shear apparatus: (a) Cambridge type (Budhu and Britto 1987), (b) NGI type (Budhu and Britto 1987) and (c) GDS type.....	7
Figure 1.9 Monotonic undrained behaviour at various densities on Fraser River sand: (a) shear stress γ versus shear stress τ , (b) effective normal stress σ'_n versus shear stress τ ..	7
Figure 1.10 Monotonic drained simple shear tests on Ottawa sand various densities: (a) shear stress γ versus shear stress ratio τ/σ'_n , (b) shear stress γ versus volume strain ε_v	8
Figure 1.11 Dependence of dilation angle on relative density and stress level (Cole 1969).....	8
Figure 1.12 Variation of undrained strength at stress with void ratio and initial effect normal stress in simple shear (a) τ_{pt} versus e ; (a) τ_{pt}/σ'_{n0} versus e (Vaid and Sivathayalan 1996)	9
Figure 1.13 Tests of simple shear tests: (a) comparing to triaxial tests by Vaid and Sivathayalan (1996) and (b) principal stress rotation of simple shear tests by Wood et al. (1979)	9
Figure 1.14 Cyclic drained simple shear test on Fraser River sand by Sriskandakumar (2004)	10
Figure 1.15 Undrained cyclic simple shear tests with different CSRs (a) σ'_{n0} versus τ on CSR=0.08; (b) γ versus τ on CSR=0.08; (c) σ'_{n0} versus τ on CSR=0.1; (b) γ versus τ on CSR=0.1	11
Figure 1.16 Undrained non-symmetrical cyclic simple shear tests with different average shear stress, (a-b) with stress reversal cyclic loading; (c-d) non-stress reversal cyclic loading	12
Figure 1.17 Rate of pore pressure generation: (a) Curves from Lee and Albaisa, 1974, and (b) Curves from Booker et al. (1976).....	13
Figure 1.18 Parameters calibration of Ishibashi et al model: (a) calibration parameter χ , (b) calibration parameter C_{1-3} (after Ishibashi et al. 1977)	14

Figure 2.1 Principle of SIMSAND model	21
Figure 2.2 Synthetic data using a set of given model parameters for isotropic compression test and conventional drained triaxial tests: (a) void ratio versus mean effective stress, (b) stress ratio versus axial strain, (c) mean effective stress and deviatoric stress and (d) void ratio versus mean effective stress	24
Figure 2.3 Procedure of proposed straightforward method from (a) elasticity related parameters, (b) critical state related parameters to (c) plasticity interlocking related parameters	25
Figure 2.4 New interpreted curves from isotropic compression curve in (a) Elastic bulk moduli versus mean effective stress and (b) Elastic bulk moduli versus void ratio	26
Figure 2.5 Increments of plastic strain of drained triaxial tests: (a) stress ratio versus deviatoric plastic strain; (b)) stress ratio versus ratio of plastic strain increment	29
Figure 2.6 Comparison between original given and calibrated parameters.....	30
Figure 2.7 Comparison between synthetic results and simulated results by calibrated parameters: (a) stress ratio versus axial strain; (b) volumetric strain versus axial strain.	31
Figure 2.8 Experimental results of isotropic compression and conventional drained triaxial tests on Toyoura sand for calibrating parameters: (a) void ratio versus mean effective stress, (b) stress ratio versus axial strain, (c) mean effective stress and deviatoric stress and (d) void ratio versus mean effective stress	32
Figure 2.9 Interpreted results from isotropic compression curves of Toyoura sand for calibrating parameters: (a) void ratio versus mean effective stress and (b) Elastic bulk moduli versus mean effective stress	32
Figure 2.10 Increments of plastic strain of drained triaxial tests on Toyoura sand: (a) stress ratio versus deviatoric plastic strain; (b)) stress ratio versus ratio of plastic strain increment	33
Figure 2.11 Comparison between experiments and simulations for six drained triaxial tests on Toyoura sand under confining stresses of 100 kPa and 500 kPa plotted in void ratio versus mean effective stress space	34
Figure 2.12 Comparison between experiments and simulations for six drained triaxial tests on Toyoura sand under confining stresses of 100 kPa and 500 kPa plotted in (a) and (c) deviatoric stress versus axial strain, (b) and (d) void ratio versus axial strain.....	35
Figure 2.13 Comparison between experiments and simulations of undrained triaxial tests on Toyoura sand under confining stresses of 100 kPa and 1000 kPa plotted in (a) and (c) deviatoric stress versus axial strain, (b) and (d) stress path in mean effective stress and deviatoric stress	36
Figure 2.14 Flow chart of explicit finite element analysis based on ABAQUS/Explicit	36
Figure 2.15 Schematic diagram of a general cutting plane algorithm	38
Figure 2.16 Flow chart of the cutting plane algorithm	39

Figure 2.17 Finite element model for footing tests by ABAQUS	41
Figure 2.18 Comparison between measurements and predictions of bearing load versus settlement for three footing tests in sand with three different initial void ratios.....	41
Figure 2.19 Simulated mean effective stress field of three footings at the settlement of 2.8 mm for the initial void ratio of: (a) $e_0=0.67$; (b) $e_0=0.71$; (c) $e_0=0.81$	42
Figure 3.1 Parameters determination from isotropic compression and triaxial drained tests on Fontainebleau NE34 sand: (a) isotropic compression line, (b) deviatoric stress versus axial strain, and (c) void ratio versus mean effective stress.....	47
Figure 3.2 Simulation results of triaxial drained tests on medium dense and very dense Fontainebleau sand: (a, c) deviatoric stress versus axial strain; (b, d) deviatoric stress versus void ratio	48
Figure 3.3 Simulation results of triaxial undrained tests on very loose Fontainebleau sand: (a) deviatoric stress versus axial strain; (b) deviatoric stress versus mean effective stress for undrained tests; (c) pore pressure versus axial strain for undrained	48
Figure 3.4 Model simulation for stress strain relation based on incorporation parameters, (a, b, c) constant a with different \tilde{c}_1 ; (c, d, e) constant \tilde{c}_1 with different a	49
Figure 3.5 Particle shape of Fontainebleau sand	50
Figure 3.6 Details of cylindrical boundary for simple shear specimen	51
Figure 3.7 Three-dimensional FEM model for simple shear tests: (a) initial state, (b) shearing state, (c) mesh in viewpoint of x-y space, (d) mesh in viewpoint of x-y space.	52
Figure 3.8 Calibration of anisotropic parameters: (a) shear strain versus shear stress (b) shear strain versus void ratio	53
Figure 3.9 Simulation results by ideal and full three-dimensional simple shear tests (a) constant normal stress simple shear in γ - τ space; (b) constant normal simple shear in γ - e space; (c) constant volume simple shear in γ - τ space; (d) constant volume simple shear in σ'_n - τ space.	54
Figure 3.10 The distribution of vertical effective stress for constant normal stress test S-3 (a) along with path-1, (b) along with path-2 and (c) along with path-3	54
Figure 3.11 The distribution of vertical effective stress for constant volume test S-5 (a) along with path-1, (b) along with path-2 and (c) along with path-3	55
Figure 3.12 Normal distribution of vertical stress σ'_z with constant normal stress condition (a) $\gamma=1\%$, (b) $\gamma=5\%$, (c) $\gamma=10\%$ and (d) $\gamma=20\%$; and with constant volume condition (e) $\gamma=1\%$, (f) $\gamma=5\%$, (g) $\gamma=10\%$ and (h) $\gamma=20\%$	56
Figure 3.13 Profiles of successive simple shearing process for constant normal stress condition at $\sigma'_n = 416\text{kPa}$: (a) contours of shear stress τ , (b) contours of deviatoric plastic strain ε_d^p ; (c) contours of anisotropic variable A	57

Figure 3.14 Profiles of successive simple shearing process for constant volume condition at $\sigma'_n = 416\text{kPa}$: (a) contours of shear stress τ , (b) contours of deviatoric plastic strain ε_d^p ; (c) contours of anisotropic variable A	58
Figure 3.15 Probability distribution analysis with increasing of shear strain based on constant normal stress (a) shear stress, (b) plastic strain and (c) anisotropic variable, and constant volume (d) shear stress, (e) plastic strain and (f) anisotropic variable.....	59
Figure 3.16 Finite element meshes for different aspect ratio of cylinder specimen: (a) $H_0 = 15\text{mm}$; (a) $H_0 = 25\text{mm}$; (c) $H_0 = 35\text{mm}$	59
Figure 3.17 Comparison results between different aspect ratios of specimens: (a) constant normal stress simple shear in γ - τ space; (b) constant normal simple shear in γ - e space; (c) constant volume simple shear in γ - τ space; (d) constant volume simple shear in σ'_n - τ space.	60
Figure 3.18 Results for different aspect ratios of specimens about distribution of normal stress and shear stress on the Path-1: (a) constant normal stress condition ($\sigma'_{n0} = 208\text{kPa}$); (b) constant normal stress condition ($\sigma'_{n0} = 416\text{kPa}$); (c) constant volume condition ($\sigma'_{n0} = 208\text{kPa}$); (d) constant volume condition ($\sigma'_{n0} = 416\text{kPa}$).....	61
Figure 3.19 Comparisons of different aspect ratios of specimens for the constant normal stress condition (test S-2): (a) contour of shear stress at $\gamma = 10\%$, (b) contour of deviatoric plastic strain at $\gamma = 10\%$, (c) contour of Anisotropic variable A at $\gamma = 10\%$...	62
Figure 3.20 Comparisons of different aspect ratios of specimens for the constant volume condition (test S-4): (a) contour of shear stress at $\gamma = 10\%$, (b) contour of deviatoric plastic strain ε_d^p at $\gamma = 10\%$, (c) contour of Anisotropic variable A at $\gamma = 10\%$	62
Figure 3.21 Probability distribution analysis with different aspect ratios at 10% shear strain: (a-b) for vertical stress σ'_z , (c-d) for shear stress τ and (e-f) for deviatoric plastic strain ε_d^p	63
Figure 4.1 Analysis of soil element adjacent to pile based on simple shear apparatus	66
Figure 4.2 Undrained monotonic test results on Fontainebleau sand: (a-b) comparison results with different initial void ratios; (c-d) comparison results with different initial effective normal stresses; (e-f) normalized monotonic behaviour with different initial void ratios and effective normal stresses.....	71
Figure 4.3 Shear stress at phase transformation as a function of experimental variables initial effective normal stress and relative density: (a) shear stress at phase transformation versus initial relative density; (b) normalized shear stress at phase transformation versus initial relative density	72

Figure 4.4 Symmetrical cyclic response of Fontainebleau sand: (a) shear stress versus effective normal stress; (b) shear stress versus shear strain, (c) shear strain versus number of cycles; (d) effective normal stress versus number of cycles.....	73
Figure 4.5 Degradation of effective normal stress under different initial effective normal stresses (a) 104 kPa, (b) 208 kPa, (c) 314 kPa and (d) 416 kPa.....	73
Figure 4.6 Normalized cyclic shear stress versus number of cycles to liquefaction	74
Figure 4.7 Non-symmetrical cyclic response of Fontainebleau sand with stress reversal loading: (a) shear stress versus effective normal stress; (b) shear stress versus shear strain, (c) shear strain versus number of cycles; (d) effective normal stress versus number of cycles.....	75
Figure 4.8 Non-symmetrical cyclic response of Fontainebleau sand with no-stress reversal loading: (a) shear stress versus effective normal stress; (b) shear stress versus shear strain, (c) shear strain versus number of cycles; (d) effective normal stress versus number of cycles.....	76
Figure 4.9 Degradation of effective normal stress under different average shear stresses: (a) 5.2 kPa; (b) 10.4 kPa; (c)20.8 kPa; (d) 41.6 kPa.....	77
Figure 4.10 Evaluation of effective residual normal stress in no-stress reversal cyclic loading	78
Figure 4.11 Cyclic resistance surface for cyclic simple shear tests on Fontainebleau sand....	78
Figure 4.12 Cyclic resistance diagram for cyclic simple shear tests on Fontainebleau sand: (a) relationship between normalized cyclic shear stress and normalized average shear stress; (b) empirical curves for number of cyclic to liquefaction.....	79
Figure 4.13 Normalized effective normal stress against normalized number of cycles to liquefaction.....	80
Figure 4.14 Calibration procedure for the degradation of the effective normal stress	81
Figure 4.15 Calibration results of normalized shear stress at phase transformation state: (a) Fraser River sand; (2) Quiou sand; (3) Karlsruhe sand.....	82
Figure 4.16 Calibration results of numbers of cycles to instability: (a) Fraser River sand; (2) Quiou sand; (3) Karlsruhe sand.....	82
Figure 4.17 Comparisons between simulations and experiments on Fontainebleau sand: (a) training tests; (b) additional tests.....	83
Figure 5.1 Summary of drained cyclic simple shear results: (a)-(b) comparisons by different initial relative densities; (c)-(d) comparisons by different effective normal stresses; (e)-(f) comparisons by different cyclic shear stress ratios and (g)-(h) comparisons by different average shear stress ratios.	89
Figure 5.2 Summary of drained monotonic simple shear after 5000 cycles: (a)-(c) comparisons by different initial relative densities; (d)-(f) comparisons by different	

effective normal stresses; (h)-(j) comparisons by different cyclic shear stress ratios; (k)-(m) comparisons by different average shear stress ratios.....	90
Figure 5.3 volumetric strain accumulation with different relative densities: (a) volumetric strain versus number of cycles; (b) volumetric strain versus relative density; (c) reference volumetric strain versus number of cycles	91
Figure 5.4 volumetric strain accumulation with different normal stress level: (a) volumetric strain versus number of cycles; (b) volumetric strain versus normal stress level; (c) reference volumetric strain versus number of cycles	92
Figure 5.5 volumetric strain accumulation with different cyclic stress ratio: (a) volumetric strain versus number of cycles; (b) normalized volumetric strain versus cyclic shear stress ratio; (c) reference volumetric strain versus number of cycles	94
Figure 5.6 Volumetric strain accumulation with different average shear stress ratio: (a) volumetric strain versus number of cycles; (b) normalized volumetric strain versus average shear stress ratio; (c) reference volumetric strain versus number of cycles	95
Figure 5.7 Performance of analytical model: (a) calibration with different relative densities; (b) calibration with different effective normal stresses; (c) calibration with different cyclic shear stress; (d) calibration with different average shear stress.....	96
Figure 5.8 Validation of the analytical model by five additional tests No.16-20.....	97
Figure 5.9 Volumetric strain accumulation evolution with 10, 100 and 4000 cycles for different effects of (a) α and CSR , (b) D_r and CSR , (c) σ'_n/p_{at} and CSR , (d) D_r and α , (e) σ'_n/p_{at} and α and (f) σ'_n/p_{at} and D_r	98
Figure 6.1 Principle of stress reversal in loading and unloading after (Yin et al. 2013).....	103
Figure 6.2 Comparison between experimental and numerical results of constant- p' drained cyclic tests on Toyoura sand: (a)-(c) loose specimen and (d)-(f) dense specimen.....	104
Figure 6.3 Comparison between experimental and numerical results for drained cyclic triaxial tests on Toyoura sand: in (a) stress ratio versus deviatoric strain, (b) void ratio versus deviatoric strain and (c) void ratio versus stress ratio	104
Figure 6.4 Comparison between the experimental and numerical results of undrained triaxial tests under cyclic loading on Toyoura sand with different initial void ratios: in (a) and (c) stress path in mean effective stress versus deviatoric stress; (b) and (d) deviatoric stress versus deviatoric strain.....	105
Figure 6.5 Comparison between the experimental and numerical results of undrained triaxial tests under cyclic loading on Toyoura sand with different initial void ratios: in (a), (c) and (e) stress path in mean effective stress versus deviatoric stress; (b), (d) and (f) deviatoric stress versus deviatoric strain	106
Figure 6.6 Comparison between experimental and numerical results of constant- p' drained cyclic tests on Fontainebleau sand: (a)-(b) experiment, and (c)-(d) simulation.....	107

Figure 6.7 Comparison between experimental and numerical results of undrained cyclic tests on loose Fontainebleau sand: (a)-(b) experiment with $q_{cyc}=100kPa$, (c)-(d) simulation with $q_{cyc}=100kPa$ (e)-(f) experiment with $q_{cyc}=55kPa$ and (g)-(h) simulation with $q_{cyc}=55kPa$	108
Figure 6.8 Comparison between experimental and numerical results of undrained cyclic tests on loose Fontainebleau sand: (a)-(b) experiment with $q_{cyc}=80kPa$, (c)-(d) simulation with $q_{cyc}=80kPa$ (e)-(f) experiment with $q_{cyc}=48kPa$ and (g)-(h) simulation with $q_{cyc}=48kPa$	109
Figure 6.9 Experimental and numerical results of undrained cyclic tests on medium dense Fontainebleau sand on 416kPa initial normal stress: (a)-(d) comparison on condition ($\tau_{ave} = 0kPa$, $\tau_{cyc} = 20.8kPa$), (e)-(h) comparison on condition ($\tau_{ave} = 10.4kPa$, $\tau_{cyc} = 20.8kPa$) and (e)-(h) comparison on condition ($\tau_{ave} = 41.6kPa$, $\tau_{cyc} = 20.8kPa$).....	111
Figure 6.10 Comparison of experimental and numerical results of strain-controlled drained cyclic simple shear tests on loose Fontainebleau sand: (a-c) experiment and (e-g) simulation	112
Figure 6.11 Comparison of experimental and numerical results of stress-controlled drained cyclic simple shear tests on medium dense Fontainebleau sand: (a-b) experiment and (c-d) simulation.....	112
Figure 6.12 Details of 3SR mini-scale model pile tests (Silva 2014), (a) model pile with micro-CT scan apparatus and (b) geometry of model-pile penetration tests	114
Figure 6.13 Finite element analysis of 3SR mini model pile.....	114
Figure 6.14 Comparison between experiment and simulation of 3SR mini model pile test with confining pressure of (a) 100kPa and (b) 200kPa	115
Figure 6.15 Comparison of strain profiles between experiment and simulation (a) vertical strain and (b) horizontal strain.....	115
Figure 6.16 Influence of inherent anisotropy related parameters on pile resistance to investigate: (a) the effect of parameter \tilde{c}_1 , and (b) the effect of sensitivity of parameter \tilde{c}_2	116
Figure 6.17 General arrangement for pile test (Rimoy 2013).....	117
Figure 6.18 Modelling of ICP07 penetration tests.....	117
Figure 6.19 Comparison between experiment and simulation of model pile test in Fontainebleau sand for the pile resistance against the penetration depth.....	118
Figure 6.20 Comparison of radial stress between test and simulation considering (a) different penetration depth, (b) different radial distance, and (c) combined 3D plot	119
Figure 6.21 Simulation results of mean effective stress field around the cone of pile at the penetration depth of (a) 0.285m; (b) 0.46m and (c) 0.76m in Fontainebleau sand NE34	119

Figure 6.22 Displacement distribution surrounding the pile for penetration 0.46m (a) directions and (b) contours	120
Figure 6.23 Simulated void ratio field of three penetration depths: (a) 0.285m, (b) 0.46m and (c) 0.76m	120
Figure 6.24 Geometry of cyclic model-pile penetration tests: (a) model-pile apparatus, (b) Geometry of centrifuge (Bekki et al. 2016) and (c) FEM modelling.....	121
Figure 6.25 Cone resistance of cyclic model pile test (a) experiment and (b) simulation.....	122
Figure 6.26 Cyclic densification behaviour surrounding the pile with different number of cycles (a) N=1 cycle, (b) N=10 cycles, (c) N=50 cycles and (c) N=100 cycles	122

List of tables

Table 2.1 Values of model parameters for generating test data.....	24
Table 2.2 Calibration of elasticity related parameters K_0 and ζ based on synthetic data	27
Table 2.3 Calibration of plasticity interlocking related parameters based on synthetic data ..	30
Table 2.4 Calibration of model parameters K_0 and ζ for Toyoura sand	32
Table 2.5 Calibration of model parameter A_d , n_d , k_p and n_p for Toyoura sand.....	34
Table 2.6 Summary of model parameters by back calculation procedure for Toyoura sand ..	34
Table 3.1 Basic constitutive equations of SIMSAND	44
Table 3.2 Drained triaxial tests on Fontainebleau sand with different void ratios	47
Table 3.3 Summary of model parameters for Fontainebleau sand	48
Table 3.4 Physical properties of standard Fontainebleau sand	50
Table 3.5 Summary of monotonic simple shear tests on Fontainebleau sand	51
Table 4.1 Summary of experiments on tested Fontainebleau sand.....	69
Table 4.2 Physical properties of three studied sands	81
Table 4.3 Parameters of empirical model for number of cyclic to liquefaction	82
Table 5.1 Experimental program of cyclic simple shear tests	87
Table 5.2 Summary of the empirical function with parameters of Fontainebleau sand	95

Notation

$C_{1\sim 7}$	Volumetric strain related parameters
CSR	Cyclic Stress Ratio
C_u	Coefficient of uniformity
\tilde{c}_1, \tilde{c}_2	Incorporated parameters for simple shear condition
D	Elastic matrix
D_0	Diameter of simple shear specimen
D_{50}	Mean grain size of granular material
d_{ij}	Deviatoric part of the fabric tensor
D_r	Relative density
$d\lambda$	Plastic multiplier
e	Void ratio
e_0	Void ratio after consolidation
e_c	Void ratio at critical state line
e_i	Void ratio before consolidation
e_{\max}	The maximum void ratio
e_{\min}	The minimum void ratio
e_{ref}	Reference void ratio
F_{ij}	Fabric tensor
G	Elastic shear moduli
G_0	Reference elastic shear moduli
G_s	Specific gravity
H_0	Height of simple shear specimen
H_c	Specimen height after consolidation
K	Elastic bulk moduli
k	The slope corresponding to number of cycles to liquefaction in cyclic resistance digram
K_0	Reference bulk moduli
k_p	Parameter related to the plastic shear modulus
M_1, M_2	Parameters for calculating shear stress at phase transformation state
M_p	Stress ratio corresponding to the peak strength
M_{pt}	Stress ratio corresponding to the phase transformation line
N	Cyclic number
N_L	Number of cycles to liquefaction

n_p, n_d	model interlocking parameters
n_1, n_2	Volumetric accumulation related parameters
p'	The mean effective stress
p_{at}	Atmospheric pressure (101.4 kPa)
PTL	Phase transformation line
q	Deviatoric stress
s_{ij}	Deviatoric stress tensor
U_N^*	The residual pore pressure ratios at the N th cycles
A	Joint invariant
Δ	Cross anisotropy parameters
ΔH	Change of specimen height
α	Average shear stress ratio
x	Sample for probability analysis
χ	Parameters related non-stress reversal cyclic tests
δ_{ij}	Kronecker delta
ε_a	Axial strain
ε_v	Volumetric strain
$\varepsilon_{ij}, \dot{\varepsilon}_{ij}$	Total strain tensor, and total strain rate tensor
$\varepsilon_{ij}^e, \dot{\varepsilon}_{ij}^e$	Total elastic strain tensor, and total elastic strain rate tensor
$\varepsilon_{ij}^p, \dot{\varepsilon}_{ij}^p$	Total plastic strain tensor, and total plastic strain rate tensor
$\varepsilon_v^e, \varepsilon_d^e$	Volumetric and deviatoric elastic strain
$\varepsilon_v^p, \varepsilon_d^p$	Volumetric and deviatoric plastic strain
ϕ_f	Friction angle at failure
ϕ_p	Peak strength friction angle
ϕ_{pt}	Phase transformation friction angle
ϕ_μ	Critical state friction angle
γ	Shear strain
κ^*	Hardening variable
λ	Parameter control the nonlinear slope of the CSL
μ	Mean of the distribution of probability density function
θ	Lode's angle
$\bar{\theta}$	Material parameters for effective normal stress degradation
σ	Standard deviation of probability density function
σ_n	Effective normal stress
σ_{n0}	Initial effective normal stress

σ'_{n-pt}	Effective normal stress at phase transformation state
$\sigma'_{n-residual}$	Effective normal stress at phase transformation state
$\sigma'_{ij}, \sigma'^{R}_{ij}$	Stress state and reversal stress state
τ_{ave}	Average shear stress
τ_{cyc}	Cyclic shear stress
τ_{pt}	Shear stress at the phase transformation state
ν	Poisson's ratio
ξ	Parameter control the nonlinear slope of the CSL
ψ_1, ψ_2	Parameters related cyclic resistance
ζ	Parameter controls the nonlinearity of confining stress effect
$\bar{\zeta}$	Parameters related number of cycles to liquefaction

Abstract

The thesis aims to study the mechanical behaviour of sand under simple shear condition and to apply the results to the numerical simulation of pile foundation. First, a recently developed critical state sand model (SIMSAND) is introduced with a straightforward procedure of parameters determination, implemented into a finite element code and then subjected to a series of validations. Then, the model is enhanced by considering the inherent anisotropy during the principal stress rotation under the simple shear condition and validated by using results of both triaxial tests and simple shear tests on Fontainebleau sand. Simple shear tests are analysed by simulating in three-dimensions the real conditions imposed by the simple shear apparatus. The inhomogeneity of the samples with the effect of sample size is also investigated. Furthermore, undrained and drained cyclic simple shear tests on Fontainebleau sand are conducted to investigate the cyclic responses, such as the effective normal stress degradation and the volumetric strain accumulation, respectively, considering some impact factors such as the initial void ratio, the normal stress, the cyclic shear stress ratio and the average shear stress ratio. Based on these results, two analytical models are proposed to predict the long-term degradation of the effective normal stress and the accumulation of the volumetric strain with the number of cycles. Moreover, the cyclic simple shear tests are simulated by the enhanced SIMSAND model by incorporating the stress reversal technique. Finally, a series of model pile tests under monotonic and cyclic loadings are simulated based on which the cone resistance of the piles is evaluated as well as the response of the soil surrounding the pile.

Keywords: Simple shear; principal stress rotation; cyclic loading; constitutive model, sand, pile foundation

Résumé

La thèse vise à étudier le comportement mécanique des sables sous la condition de cisaillement simple et à son application au calcul des pieux. Tout d'abord, un modèle de comportement pour le sable récemment développé (SIMSAND), prenant en compte l'état critique, est introduit avec une procédure directe de détermination des paramètres. Le modèle est implanté dans un code de calcul aux éléments finis qui a fait l'objet de différentes validations. Ensuite, le modèle est amélioré en considérant l'anisotropie inhérente lors de la rotation des contraintes principales sous la condition de cisaillement simple et a été validé en utilisant les résultats des essais triaxiaux et de cisaillement simple sur le sable de Fontainebleau. Les essais de cisaillement simple sont analysés en imposant les conditions de sollicitations réelles tridimensionnelles appliquées par l'appareillage utilisé. L'inhomogénéité de l'échantillon en lien avec la taille de l'échantillon est également étudiée. Puis, des essais de cisaillement simple cycliques drainés et non-drainés sur le sable de Fontainebleau sont effectués pour étudier les caractéristiques sous charges cycliques, telles que la dégradation de la contrainte normale effective et l'accumulation de la déformation volumique, compte tenu de certains facteurs comme l'indice des vides initial, la contrainte normale appliquée, le rapport de contrainte de cisaillement cyclique et le rapport de contrainte de cisaillement moyenne. Sur la base de ces résultats, deux modèles analytiques sont proposés pour prédire la dégradation à long terme de la contrainte normale effective et l'accumulation des déformations volumiques en fonction du nombre de cycles. En outre, les essais cycliques de cisaillement simple sont simulés par le modèle SIMSAND amélioré en utilisant une technique d'inversion de contrainte. Enfin, on simule une série de pieux modèles sous charges monotone et cyclique pour laquelle la résistance en pointe du pieu est évaluée ainsi que la réponse du sol entourant le pieu.

Mots-clés: Cisaillement simple; rotation des contraintes principales; comportement cyclique; loi de comportement, fondation sur pieux

General introduction

In offshore engineering, pile foundations are generally subjected to a series of combined cyclic loading, lateral and axial, monotonic and cyclic. The degradation of the shaft capacity of pile foundation can occur when the structure is subjected to a very long-term cyclic loading or to other extreme natural conditions. This effect can be explained by the degradation of the radial effective stress and also by the accumulation of volumetric strains in the soil element surrounding the piles under cyclic shearing condition. In laboratory, the simple shear test is considered as an effective and reliable tool to reproduce the shearing condition within the soil. Therefore, the aim of this thesis is to study the mechanical response of sand and also its engineering application to pile foundation. It is divided into seven chapters presenting the experimental and numerical studies of simple shear tests, and is outlined as follows:

In chapter 1, the available test results on soils are first summarized and applied to investigate the soil mechanical behaviour surrounding the pile. These results demonstrate that the simple shear tests can well reproduce the in-situ shearing condition around the pile. Then, current monotonic and cyclic simple shear tests are presented to review the basic mechanical responses. Then, constitutive models for granular materials, ranging from phenomenological, multi-scale to discrete element models, are also summarized.

In chapter 2, the framework of a recently developed critical-state based sand model (SIMSAND) is introduced. Then, a straightforward method for calibrating the model parameters is proposed. Moreover, the SIMSAND model is implemented into a finite element code and verified by simulating several footing tests with the straightforwardly determined parameters.

In chapter 3, the SIMSAND model is enhanced by considering the inherent anisotropy accounting for the effect of principal stress rotation. Then, three-dimensional finite element analyses of the real GDS-type simple shear apparatus are performed to illustrate the inhomogeneity of the loading conditions caused by the absence of complementary shear stress on the lateral boundary. Furthermore, complementary simulations with different aspect ratios of the cylindrical specimens are conducted and discussed.

In chapter 4, undrained monotonic and cyclic simple shear tests on Fontainebleau sand are presented to study the degradation of the effective normal stress in order to represent the behaviour of a soil element surrounding the pile. Then, an analytical model to evaluate the normal stress degradation is formulated and the procedure of parameter identification is also presented. The performance of the suggested analytical model is analyzed, based on elementary test results on Fraser River sand, Quiou sand, and Karlsruhe sand, and it is also validated by a series of additional tests on Fontainebleau sand.

In chapter 5, stress-controlled drained simple shear tests with 5000 cycles on Fontainebleau sand are presented to investigate four influential parameters on the cyclic strain accumulation, i.e. the initial void ratio, the normal stress, the cyclic shear stress ratio and the average shear stress ratio. Then, the influence of each parameter on the volumetric strain accumulation is summarized and a simple analytical model is proposed to estimate the cyclic accumulation of the volumetric strain accounting for these four effects. The applicability of the model is finally examined by simulating another series of tests with the parameters calibrated from the training tests.

In chapter 6, the SIMSAND model is enhanced by the shear stress reversal technique to describe both monotonic and cyclic behaviours of granular materials. The predictive ability of the model for reproducing the basic cyclic features of granular materials is first examined, based on undrained cyclic triaxial tests, drained cyclic tests and also constant mean effective pressure (p') triaxial tests on Toyoura sand. Then, the performance of the model in simulating both triaxial and simple shear cyclic tests on Fontainebleau sand is also analysed. Finally, a series of model pile tests under monotonic and cyclic loadings are simulated based on which the cone resistance of the piles is evaluated as well as the mechanical response of the soil surrounding the pile.

Chapter 7 presents the general conclusions and perspectives.

Introduction générale

En ingénierie offshore, les fondations sur pieux sont généralement soumises à une série de charges cycliques combinées, latérales et axiales, monotones et cycliques. La dégradation de la capacité portante de la fondation peut se produire lorsque la structure sera soumise à un chargement cyclique à très long terme ou à d'autres conditions naturelles extrêmes. Cela peut s'expliquer par la dégradation de la contrainte radiale effective ainsi que par l'accumulation de la déformation volumique de l'élément de sol soumis à des conditions de cisaillement cyclique autour du pieu. Au laboratoire, l'essai de cisaillement simple est considéré comme un moyen efficace et fiable de reproduire l'état de cisaillement du sol autour des pieux. Par conséquent, visant à étudier la réponse mécanique du sable et aussi son application à l'ingénierie, la thèse est divisée en huit chapitres comprenant études expérimentales et numériques de l'essai de cisaillement simple, comme suit:

Dans le chapitre 1, les essais élémentaires réalisés sur différents types de sol sont d'abord résumés et sont utilisés pour étudier le comportement mécanique du sol entourant le pieu, ce qui démontre que les essais de cisaillement simple peuvent reproduire l'état de cisaillement in situ autour du pieu. Ensuite, les essais de cisaillement simple monotones et cycliques, disponibles dans la littérature, sont présentés, pour passer en revue les réponses mécaniques de base. Puis, les modèles de comportement des matériaux granulaires sont également résumés, comprenant des modèles phénoménologiques, multi-échelles et aux éléments discrets.

Dans le chapitre 2, un modèle de sable basé sur l'état critique récemment développé (SIMSAND) est introduit. Une méthode directe d'identification des paramètres du modèle est proposée. Le modèle SIMSAND est ensuite implémenté dans un code aux éléments finis et vérifié en simulant plusieurs essais de fondation superficielle avec les paramètres directement déterminés.

Dans le chapitre 3, le modèle SIMSAND est amélioré en considérant la prise en compte de l'anisotropie inhérente lors de la rotation des contraintes principales. L'analyse par éléments finis tridimensionnels de l'appareil de cisaillement simple de type GDS est réalisée pour illustrer les caractéristiques de non homogénéité du chargement au sein de l'échantillon, causées par l'absence de contrainte de cisaillement complémentaire sur la paroi latérale. De plus, des simulations complémentaires avec différents rapports d'aspect d'échantillons cylindriques sont conduites et discutées.

Au chapitre 4, les essais de cisaillement simple monotone et cyclique non drainés réalisés sur le sable de Fontainebleau sont présentés pour étudier la dégradation de la contrainte normale effective afin de représenter le comportement de l'élément de sol

entourant le pieu. Ensuite, un modèle analytique pour évaluer la dégradation de la contrainte normale est formulé et la procédure d'identification des paramètres est également présentée. La performance du modèle analytique proposé est analysée à partir de résultats d'essais sur le sable du fleuve Fraser, le sable de Quiou et le sable de Karlsruhe. Elle est également validée par une série d'essais complémentaires sur le sable de Fontainebleau.

Dans le chapitre 5, les essais de cisaillement simple drainés à contrainte contrôlée comprenant 5000 cycles sont effectués sur le sable de Fontainebleau pour étudier quatre effets sur l'accumulation des déformations cycliques : l'indice des vides initial, la contrainte normale, l'amplitude de la contrainte cyclique et la valeur de la contrainte moyenne. Ensuite, l'accumulation de la déformation volumique en régime cyclique pour chaque effet est analysée et un modèle analytique simple est également proposé pour estimer le comportement cyclique en tenant compte de ces quatre effets. L'applicabilité du modèle est finalement examinée en simulant une série d'essais différents de ceux utilisés pour caler les paramètres du modèle.

Dans le chapitre 6, le modèle SIMSAND est amélioré par la technique d'inversion de la contrainte de cisaillement pour décrire les comportements monotones et cycliques des matériaux granulaires. La capacité prédictive du modèle à reproduire les caractéristiques des matériaux granulaires est d'abord examinée pour les essais triaxiaux cycliques non drainés, les essais triaxiaux cycliques sous contrainte moyenne effective (p') constante sur le sable de Toyoura. Ensuite, la performance du modèle sur la simulation des essais triaxiaux et de cisaillement simple sur sable de Fontainebleau est également analysée. Finalement, une série d'essais de pieux sous des charges monotones et cycliques est simulée, au cours de laquelle la résistance en pointe des pieux ainsi que la réponse mécanique du sol entourant le pieu sont calculées.

Le chapitre 7 présente les conclusions et perspectives générales.

Chapter 1 Literature review

1.1 Engineering background

As a result of instabilities induced by long-term cyclic loadings in offshore engineering, the radial stress of soil surrounding the pile gradually decreases, causing the pile foundation to lose shaft capacity. Many field and laboratory pile load tests have been performed over the decades in hopes of explaining the basic mechanisms of a pile under cyclic loading. In laboratory conditions, tests using the mini-ICP (Imperial College Pile) model pile installed in a pressurized calibration chamber (Yang et al. 2010; Tsuha et al. 2012a) have also provided key information for improving the modelling of pile–soil interaction and design rules. Based on recent work treating the degradation of shaft capacity in model pile tests, scholars (Lehane et al. 1993; Dupla and Canou 1994, 2003; Anderson 2009; Rimoy 2013; Bekki et al. 2016) have shown that the local shear stress τ acting on the pile shaft can be expressed by the simple Coulomb criterion $\tau = \sigma'_r \tan \delta$, where δ is the friction angle between soil and pile and σ'_r is the radial effective stress acting on the shaft at failure, in which the degradation of radial effective stress σ'_r will greatly decrease the local shaft shear stress τ and eventually cause the pile to lose shaft capacity (Jardine et al. 2005). Accordingly, the investigation of the mechanical response of the soil element adjacent to the pile plays an important role in understanding the behaviour of shaft capacity.

1.2 Cyclic soil-elementary tests applied to pile-foundation

Comparing to the model pile tests, conducting a soil elementary test in the laboratory provides an easy and effective way of investigating the basic mechanical behaviour of soil. For this kind of laboratory test, the in-situ conditions should be replicated as closely as possible, thus to ensure high-quality, reliable data that can be applied to the engineering field. Various laboratory elementary tests have also been conducted to study the cyclic behaviour of a soil element surrounding the pile, including the three general categories of triaxial testing, direct interface shear testing and simple shear testing (Boulon and Foray 1986; Anderson 2009).

1.2.1 Triaxial shearing condition

Extensive cyclic triaxial tests have been conducted to investigate the mechanical behaviour of soil (Ishibashi et al. 1977; Hyodo et al. 1991; Vaid and Sivathayalan 1996; Uchida and Stedman 2001; Vaid et al. 2001). Regrettably, however, they have done so

without replicating the in-situ conditions surrounding the pile and thus have reached nothing more than general conclusions concerning pile shaft capacity.

As shown in Figure 1.1(a), the shaft capacity of a pile depends on the radial stress surrounding the pile. Sim et al. (2013a) suggested that the deviatoric stress $q (= \sigma_1 - \sigma_3)$ of triaxial tests is analogous to the pile shaft shear stress τ_{rz} and the degradation of mean effective stress p' under cyclic undrained triaxial tests can be taken as an indicator of how local shaft radial stress σ'_r may change close to the pile under cyclic loading.

Sim et al. (2013a) and Aghakouchak et al. (2015) investigated the cyclic behaviour of the soil element through cyclic triaxial tests while conducting complementary analysis of shaft capacity degradation behaviour for the pile, studied through the in-situ field Dunkerque pile tests (Jardine and Standing 2000, 2012) as well as through mini-ICP model pile tests (Yang et al. 2010; Tsucha et al. 2012a; Rimoy 2013). To replicate in-situ conditions, the soil specimen was first K_0 consolidated to point B, and then stress levels were unloaded to preloading point C. Drained and undrained cyclic tests were both carried out to measure strain accumulation and stress degradation, respectively.

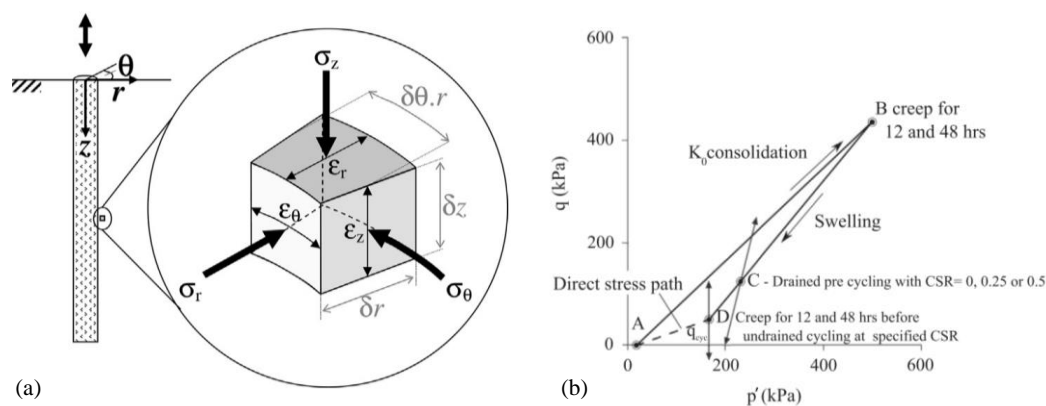


Figure 1.1 Schematic diagram (a) soil element around pile, (b) specimen loading path after (Sim et al. 2013a; Aghakouchak et al. 2015)

Figure 1.2 presents the mean effective stress and axial strain versus the number of cycles under different cyclic stress ratios ($CSR = q_{cyc}/p'_0$ for triaxial), showing that an increase of CSR will increase both mean effective stress degradation rate and axial strain accumulation rate. When $CSR > 0.5$, noticeable drift can be found along the curves of both mean effective pressure and axial strain, indicating that the loading condition $CSR > 0.5$ corresponds to an unstable zone. Moreover, the range of $0.3 < CSR < 0.5$ corresponds to a metastable zone, and $CSR < 0.3$ corresponds to a stable zone. These cyclic triaxial results match the cyclic loading responses of the pile shafts, sharing similar behaviours about the stable, metastable and unstable zones as outlined by Jardine et al. (2005; 2012).

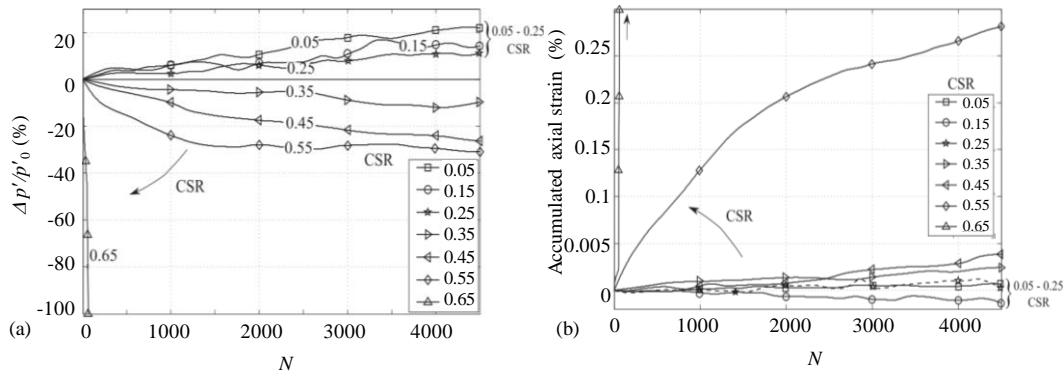


Figure 1.2 Stress-strain state under cyclic loading on Fontainebleau sand (a) degradation of mean effective stress, (b) accumulation of axial stress (Aghakouchak et al. 2015)

1.2.2 Soil-structure interface shearing condition

Boulon and Foray (1986) suggested that a direct interface shear test having a condition of constant normal stiffness (CNS) can be used to explain the progressive degradation of radial stress at the pile shaft, as shown in Figure 1.3, using a spring of appropriate stiffness (an infinite stiffness is similar to a constant volume condition). Constant normal stiffness was imposed by a constant ratio $\Delta\sigma_n/\Delta u$ between the variation of normal stress acting on the interface $\Delta\sigma_n$ divided by the variation of normal displacement Δu . However, in past decades, numbers of soil–structure cyclic interface tests had been performed with only few cycles (typically 10^2 cycles) as in (Al-Douri and Poulos 1992; Fakharian and Evgin 1997; Oumarou and Evgin 2005; Mortara et al. 2007) and tests with large number of cycles still have hardly been studied, except by Pra-ai and Boulon (2017).

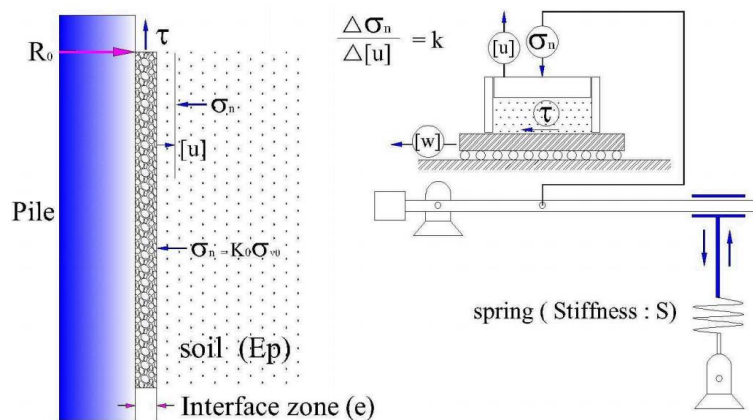


Figure 1.3 Schematic diagram of soil-pile interface direct shear tests (Pra-ai and Boulon 2017)

Most recently, long-term cycles ($>10^4$) of soil–structure interface shear tests were performed on Fontainebleau sand having a condition of constant normal stiffness, first by Pra-Ai (2013) and then by Pra-ai and Boulon (2017). Experimental results show that a higher normal stiffness corresponds to a greater-than-normal stress degradation, as seen in Figure 1.4(a). What’s more, the average stress ratio (τ_{ave}/σ'_n) under the highest stiffness

(5000kPa/mm) rapidly moved toward the critical stress ratio (as η_{cr}), as seen in Figure 1.4(b), where η_{cr} is the critical stress ratio, τ_{ave} the level of the mean cyclic shear stress, τ_{cyc} the cyclic component of the shear stress (half amplitude) and σ'_n the mean cyclic normal stress.

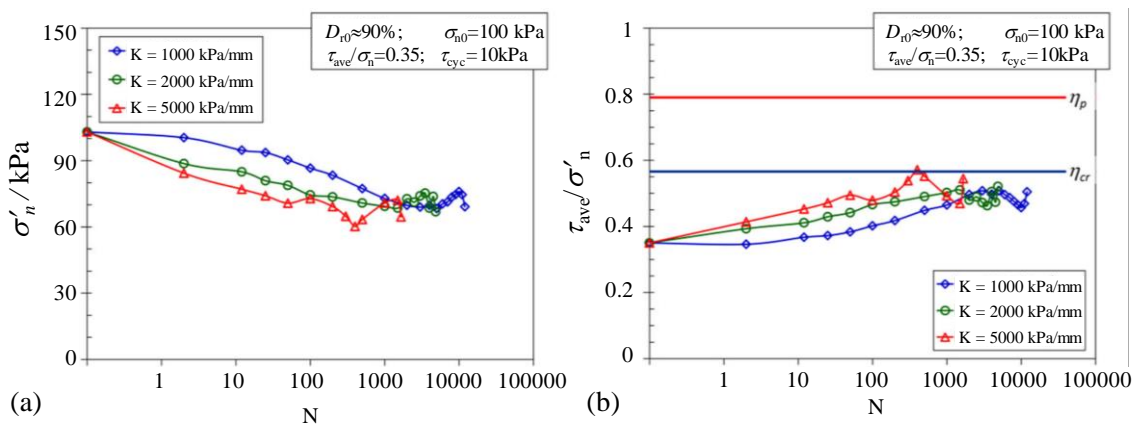


Figure 1.4 Experimental results (a) degradation of normal stress; (b) evaluation of stress ratio (Pra-ai and Boulon 2017)

1.2.3 Simple shearing condition

Because of its operability and simplicity, the simple shear test has been widely used to assess the shearing behaviour of soil under field loading conditions (e.g., slope, pile driving, landslides, earthquakes). Randolph and Wroth (1981) suggested that the shaft capacity of the driven pile can be well replicated by means of the simple shear tests as shown in Figure 1.5. More, Anderson (2009) noted that the simple shear test is acknowledged as providing more representative in-situ shearing conditions (e.g., symmetrically cyclic shear strain when considering principal stress rotation) than those offered by triaxial tests and direct shear tests.

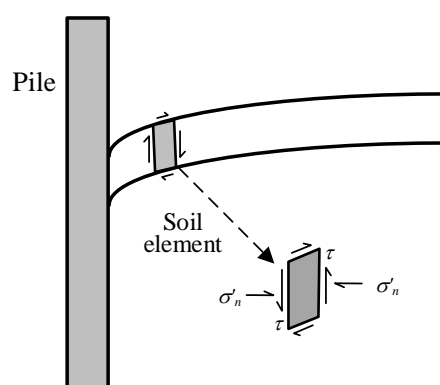


Figure 1.5 Schematic diagram of soil-pile interface (Randolph and Wroth 1981)

In recent decades, numerous cyclic simple shear tests have been conducted on sand with low cyclic numbers (Peacock 1968; Martin et al. 1975; Ishihara and Yamazaki 1980; Vaid and Sivathayalan 1996; Mao and Fahey 2003; Wood and Budhu 2014). The cyclic simple shear responses of soils (e.g., liquefaction, strain accumulation, shear stiffness, damping ratio degradation) have been investigated (Vaid et al. 2001; Matsuda et al. 2011; Da Fonseca et al.

2015; Porcino et al. 2015), and without an eye to explaining the links between the simple shear response and the shaft capacity degradation of a pile, especially for long-term cyclic loading.

Most recently, Nikitas et al. (2017) suggested that the pile foundation of an offshore wind turbine (OWT) suffered a series of combined cyclic loadings (Anderson 2009), including cyclic overturning moment (caused by both wind thrust loading and wave loading), as depicted in Figure 1.6. Two types of soil-pile interaction boundaries were pointed out by Nikitas et al. (2017): (1) cyclic soil compression (caused by lateral pile deflection) and (2) cyclic shaft shearing (caused by pile bending).

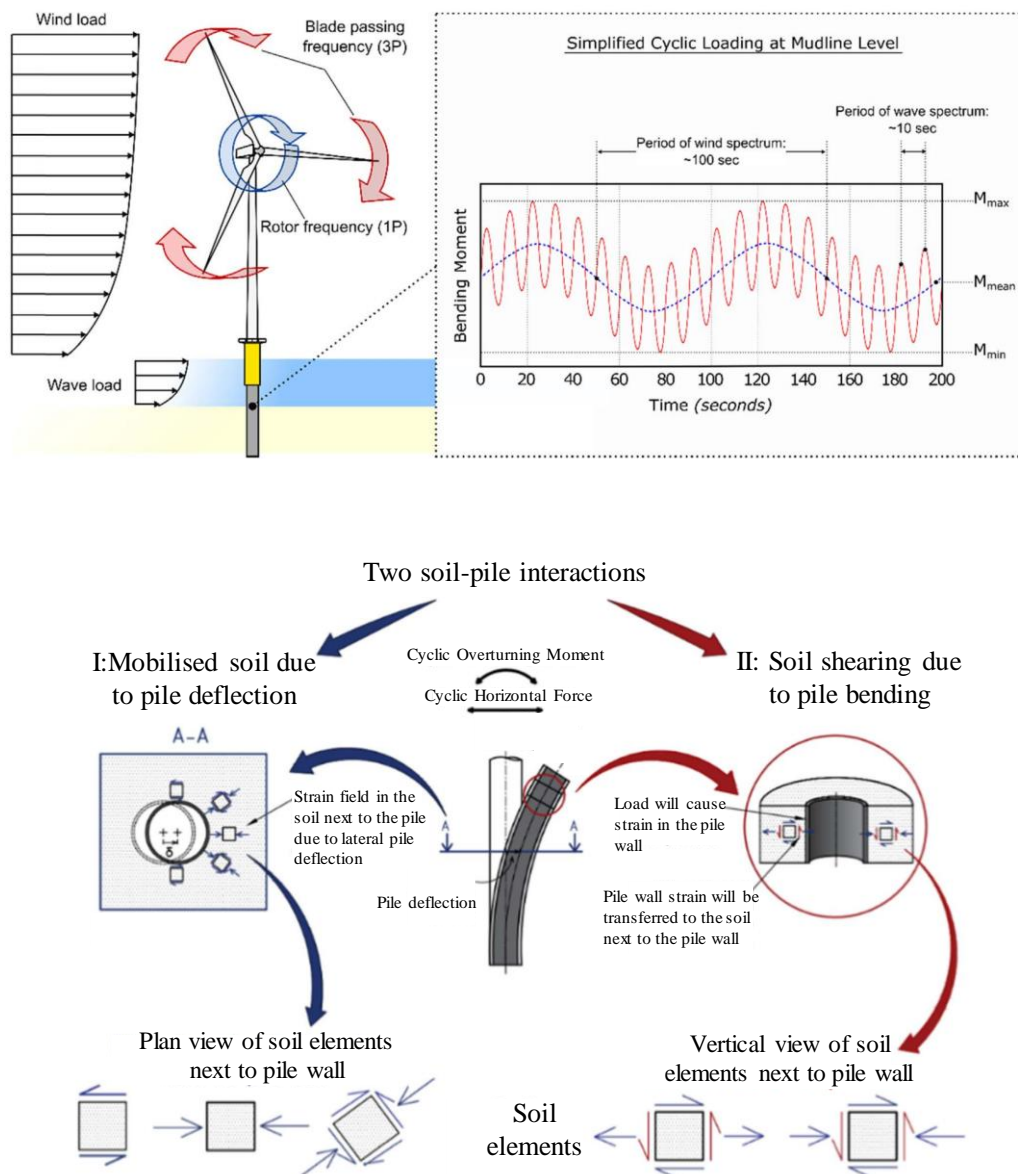


Figure 1.6 Offshore wind foundation and its schematic diagram of loads (Nikitas et al. 2017)

Nikitas et al. (2017) presented the results of cyclic drained simple shear tests (strain-controlled by cyclic shear strain γ_{cyc}) with 50,000 cycles considering various shear strain

amplitudes, cyclic stress ratios and normal stresses, examining the change in shear modulus and the accumulation of strain during long-term cyclic loading. Figure 1.7 shows that enlarging the shear strain amplitude will increase the accumulation rate of vertical strain (Figure 1.7a) and reduce the shear modulus (Figure 1.7b). Accordingly, the experimental results showed that the shear modulus generally increases with loading cycles, consistent with the observations made during model tests of offshore wind foundation as well as during field tests (Bhattacharya et al. 2011; Cuéllar et al. 2012; Cui and Bhattacharya 2016).

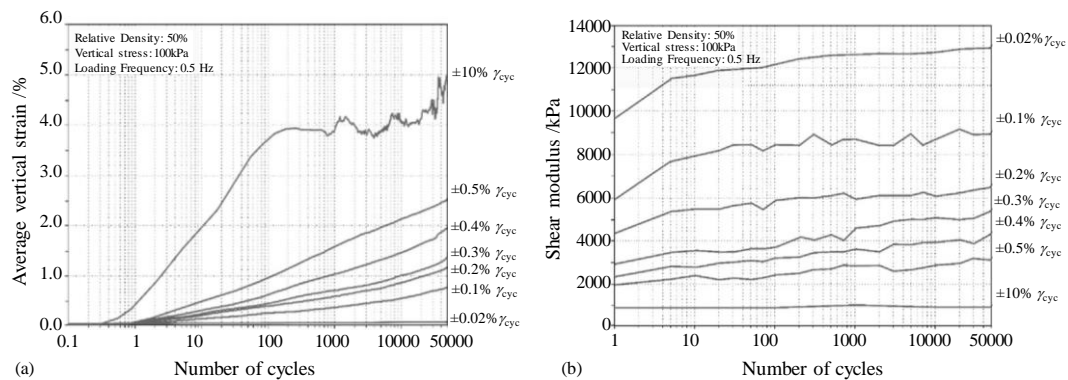


Figure 1.7 Cyclic drained simple shear tests with 100kPa normal stress: (a) vertical strain with cyclic number, (b) shear modulus with cyclic number (Nikitas et al. 2017)

1.3 Experimental investigation of simple shear tests

Over the past decades, several types of the simple shear apparatus have been developed, such as the Cambridge-type apparatus with cubical specimen and rigid boundaries (Roscoe 1953), the NGI-type apparatus with cylindrical specimen and wire-reinforced membrane (Bjerrum and Landva 1966) and the GDS-type apparatus with cylindrical specimen and stacked steel rings (Kjellman 1951; Hooker 2002), seen in Figure 1.8.

The Cambridge-type simple shear apparatus, shown in Figure 1.8(a), can host a cubical specimen 100 mm long, 100 mm wide and 20 mm high and has straight lateral boundaries (Roscoe 1953). These lateral boundaries are frictionless, in contrast to the top and bottom boundaries, which are rough. The simple shear strain is applied by displacing the bottom boundary while simultaneously rotating the two rigid lateral boundaries.

For the NGI-type simple shear apparatus originally developed by Kjellman (1951) and modified by Bjerrum and Landva (1966), as shown Figure 1.8(b), a cylindrical soil specimen 80 mm high and 20 mm in diameter is laterally confined by a wire-reinforced membrane between the rigid top and bottom platens. Simple shear strain can be imposed by displacement of the top boundary. The reinforced membrane is stiff enough to ensure one-dimensional consolidation and also conserves a constant volume during shearing.

For the GDS-type simple shear apparatus depicted in Figure 1.8(c), whose design is close to that of the NGI-type simple shear apparatus, cylindrical specimens 70 mm high and

25 mm in diameter are confined in a soft butyl membrane 0.2 mm thick, itself placed against stacks of rigid circular Teflon-coated thin rings (1 mm each) having a 70 mm inner diameter that maintains a constant cross-sectional area but allows simple shear deformation. On both top and bottom faces of the specimen, the sand is in contact with rough sintered stainless steel plates to prevent any sliding between the pedestals and the specimen.

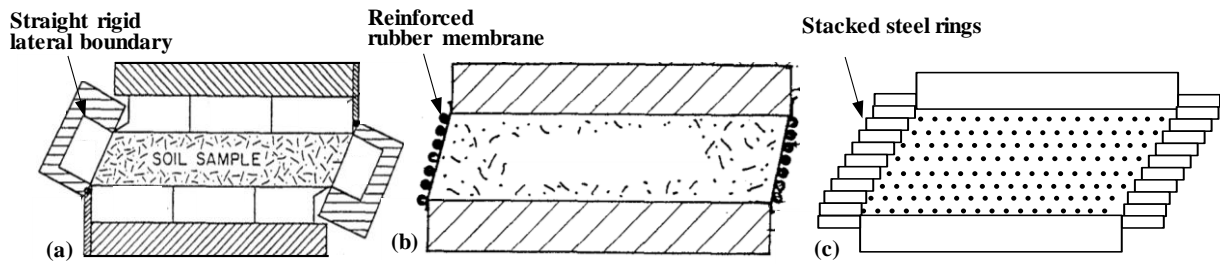


Figure 1.8 Simple shear apparatus: (a) Cambridge type (Budhu and Britto 1987), (b) NGI type (Budhu and Britto 1987) and (c) GDS type

1.3.1 Monotonic behaviour of simple shear test

The monotonic behaviour observed in simple shear tests has been widely studied over the decades. It basically shows contractive/dilative behaviour, shear strength, fabric anisotropy and principal stress rotation. Figure 1.9 relates the results of undrained simple shear tests conducted by Sivathayalan (1994) on Fraser River sand at 200kPa normal stress with void ratio after consolidation varying from 0.836 to 0.902. Experimental results show that the decreasing void ratio promotes less contractive and more dilative behaviour.

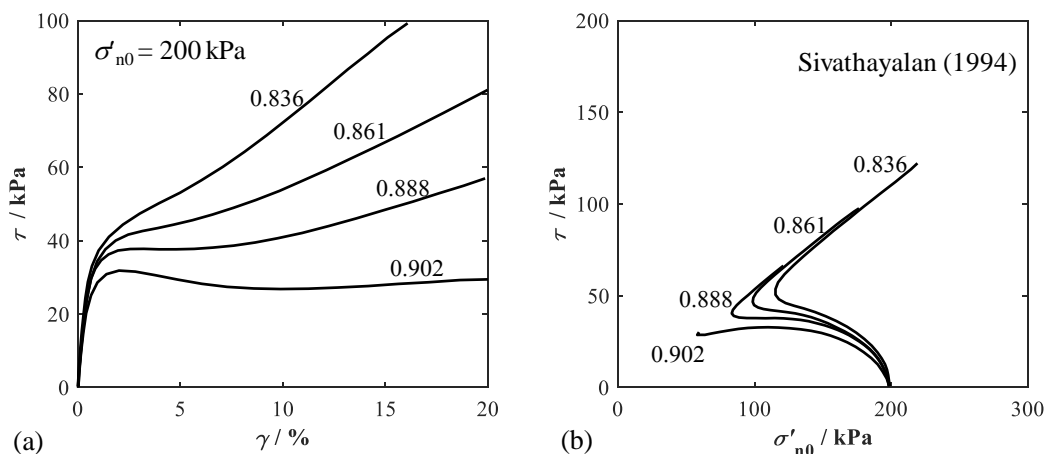


Figure 1.9 Monotonic undrained behaviour at various densities on Fraser River sand: (a) shear stress γ versus shear stress τ , (b) effective normal stress σ'_n versus shear stress τ

Figure 1.10 shows drained simple shear tests conducted on Ottawa sand at 200kPa by Vaid et al. (1981), in which the relative density varied from 27% to 93%. Based on the

experimental results, the dilative behaviour is magnified with the relative densities from loose to dense sand; only very dense sand for which $D_r=93\%$ showed a drop in peak stress ratio at large strain.

Cole (1969) discussed the influences of relative density and normal stress level on dilation angle under the simple shear condition, as shown in Figure 1.11. Considering the example of Leighton Buzzard sand, the sand exhibits more dilation when the initial effective normal stress decreases and the relative density increases.

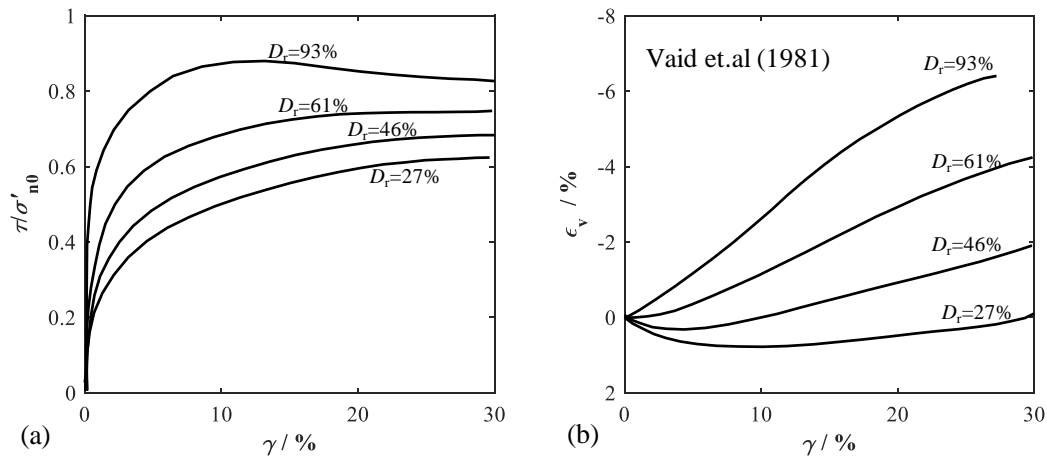


Figure 1.10 Monotonic drained simple shear tests on Ottawa sand various densities: (a) shear stress γ versus shear stress ratio τ/σ'_n , (b) shear stress γ versus volume strain ϵ_v

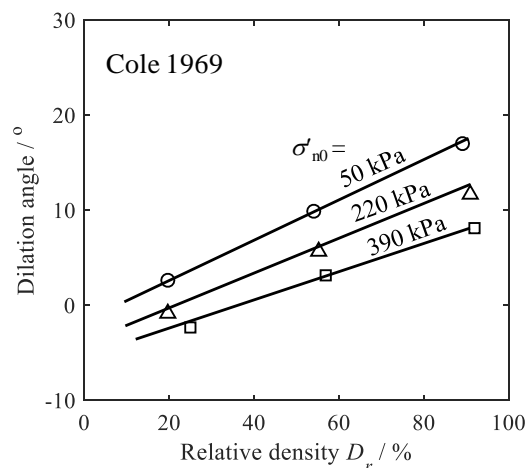


Figure 1.11 Dependence of dilation angle on relative density and stress level (Cole 1969)

In addition, for the undrained simple shear condition, the increase of the effective normal stress occurs after the stress path reaches the phase transformation state. Based on the behaviour observed in Fraser Delta sand, Vaid and Sivathayalan (1996) summarized uniformed phase transformation strength during undrained simple shear dilative behaviour. Figure 1.12(a) shows that for a given void ratio, the shear stress at phase transformation state decreases with an increase of the void ratio and increases with the initial normal stress level.

A unique relationship between void ratio e , shear stress at phase transformation state τ_{pt} and initial normal stress σ'_{n0} can be found when shear strength in the phase transformation state is normalized by the initial normal stress τ_{pt}/σ'_{n0} versus void ratio e , as shown in Figure 1.12(b).

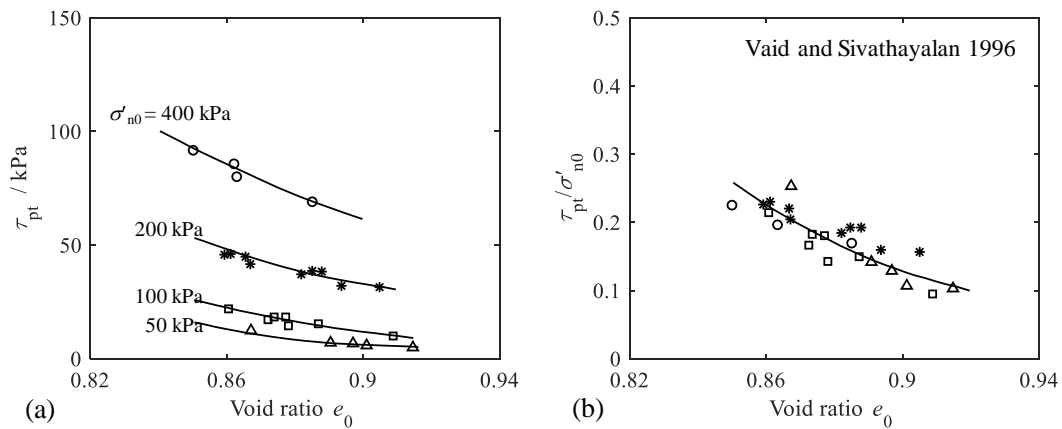


Figure 1.12 Variation of undrained strength at stress with void ratio and initial effect normal stress in simple shear (a) τ_{pt} versus e ; (a) τ_{pt}/σ'_{n0} versus e (Vaid and Sivathayalan 1996)

1.3.2 Fabric anisotropy during principal stress rotation

Vaid and Sivathayalan (1996) showed that the shear stiffness during simple shear tests is much smaller than that of triaxial tests, using comparisons between triaxial and simple shear tests as shown in Figure 1.13(a). Unlike for triaxial tests, principal stress during the simple shear state rotates during the shear process, varying by ± 45 degrees, as seen in Figure 1.13(b) (Roscoe 1970; Wood et al. 1979). In addition, fabric anisotropy has been widely recognized as affecting the strength of granular material (Oda 1972; Miura et al. 1986; Oda and Nakayama 1989; Yao and Kong 2011; Gao and Zhao 2012, 2017). Accordingly, such a degradation of shear stiffness can be explained primarily by anisotropy of stress during the principal stress rotation process, such as in the simple shearing stage.

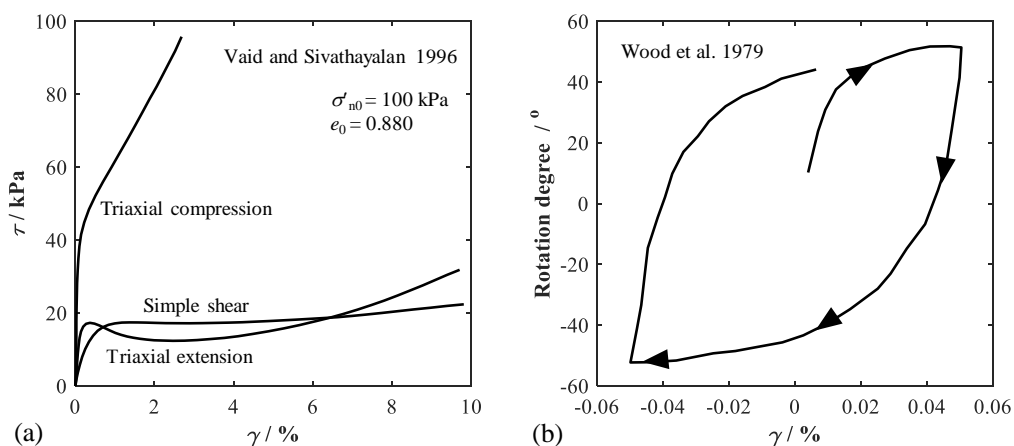


Figure 1.13 Tests of simple shear tests: (a) comparing to triaxial tests by Vaid and Sivathayalan (1996) and (b) principal stress rotation of simple shear tests by Wood et al. (1979)

1.3.3 Cyclic behaviour of simple shear test

The cyclic behaviour of sand from simple shear tests has been widely studied for decades in the form of strain accumulation, degradation of shear stiffness, damping ratio and cyclic liquefaction behaviours. From drained cyclic simple shear tests, Sriskandakumar (2004) presented cyclic strain accumulation behaviours in low cycles tests when considering the effect of relative density on Fraser River sand, as seen in Figure 1.14. This showed that for both loose and dense sand, contractive strain gradually accumulates with number of cycles, with loose sand corresponding to greater volumetric strain accumulation. Moreover, Nikitas et al. (2017) also carried out drained cyclic simple shear tests, considering the effect of cyclic shear stress ratio (CSR) while studying the degradation of shear stiffness with large numbers of cycles: greater CSR corresponds to greater strain accumulation and also greater degradation of shear stiffness.

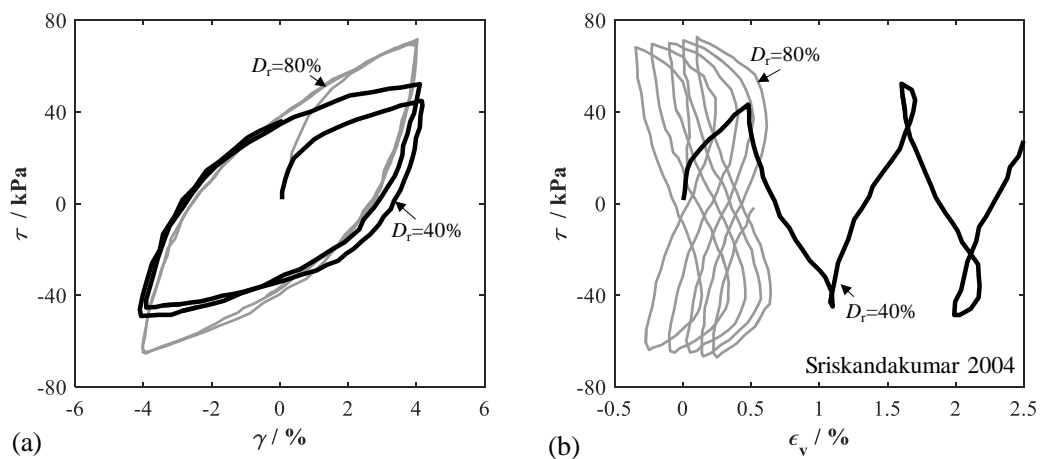


Figure 1.14 Cyclic drained simple shear test on Fraser River sand by Sriskandakumar (2004)

The undrained cyclic simple shear test has been used primarily to study the liquefaction potential of a soil, including how the normal effective stress gradually degrades under cyclic loading. Large numbers of undrained simple shear tests have been conducted to reveal the effects of cyclic shear stress ratios ($CSR = \tau_{cyc} / \sigma'_{n0}$), relative densities and initial normal stress levels (σ'_{n0}) on normal stress degradation behaviour. Figure 1.15 presents a comparison of cyclic responses between different cyclic shear stress ratios during cyclic simple shear testing conducted on Fraser River sand by Sriskandakumar (2004) with initial conditions of 200kPa initial effective normal stress, zero average shear stress and 44% relative density. The results show that the number of cycles to liquefaction decrease with increases in cyclic stress ratio CSR level.

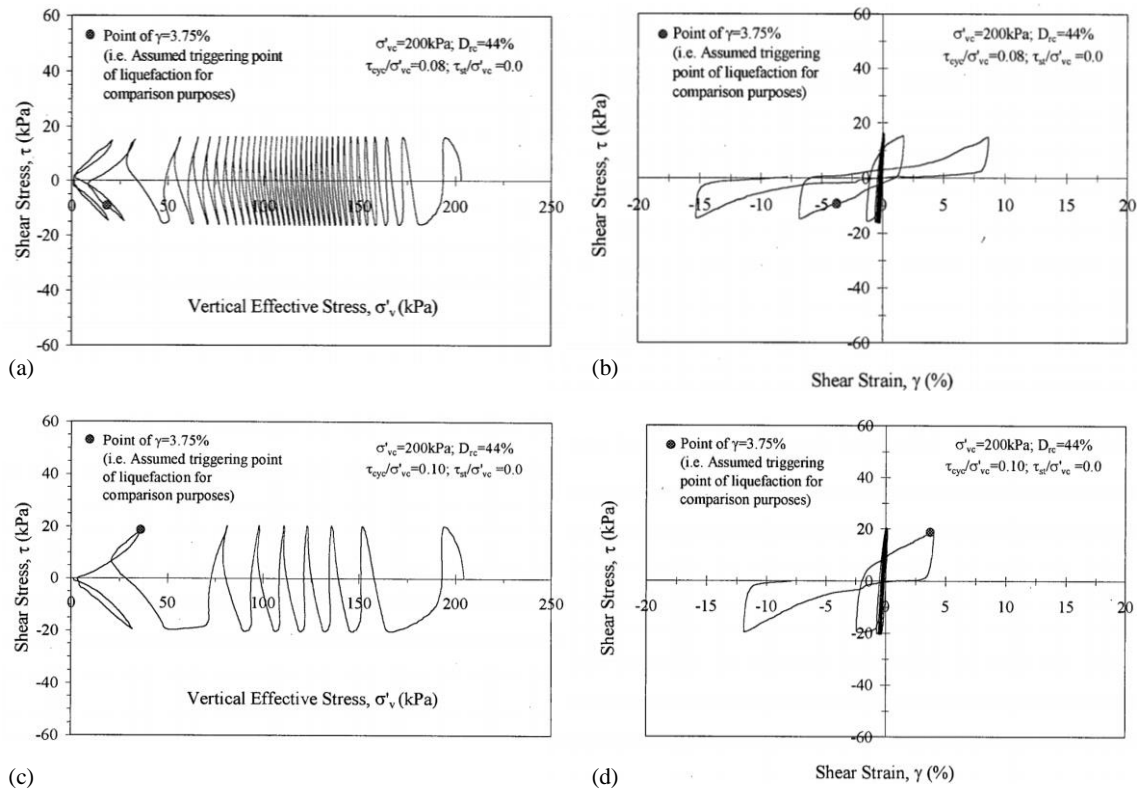


Figure 1.15 Undrained cyclic simple shear tests with different CSRs (a) σ'_{n0} versus τ on CSR=0.08; (b) γ versus τ on CSR=0.08; (c) σ'_{n0} versus τ on CSR=0.1; (d) γ versus τ on CSR=0.1

Unlike the cyclic liquefaction feature in a symmetrical cyclic simple shear (e.g. average shear stress $\tau_{ave}=0$), a residual effective normal stress can be found under non-symmetrical cyclic simple shear (average shear stress $\tau_{ave}\neq 0$). Hence the average shear stress also plays an important role in determining cyclic response during simple shear test. Through stress-controlled non-symmetrical cyclic simple shear tests, Wijewickreme et al. (2005) have presented cyclic normal stress degradation behaviour between different average shear stress ratios, comparing conditions of stress reversal and no stress reversal, with initial conditions of 200kPa effective normal stress and 44% relative density. The results corresponded to the stress reversal condition seen in Figure 1.16(a-b), for which the effective normal stresses decreased to zero that is, a liquefied state. For the non-stress reversal condition, seen in Figure 1.16(c-d), effective normal stress decreased to residual stress.

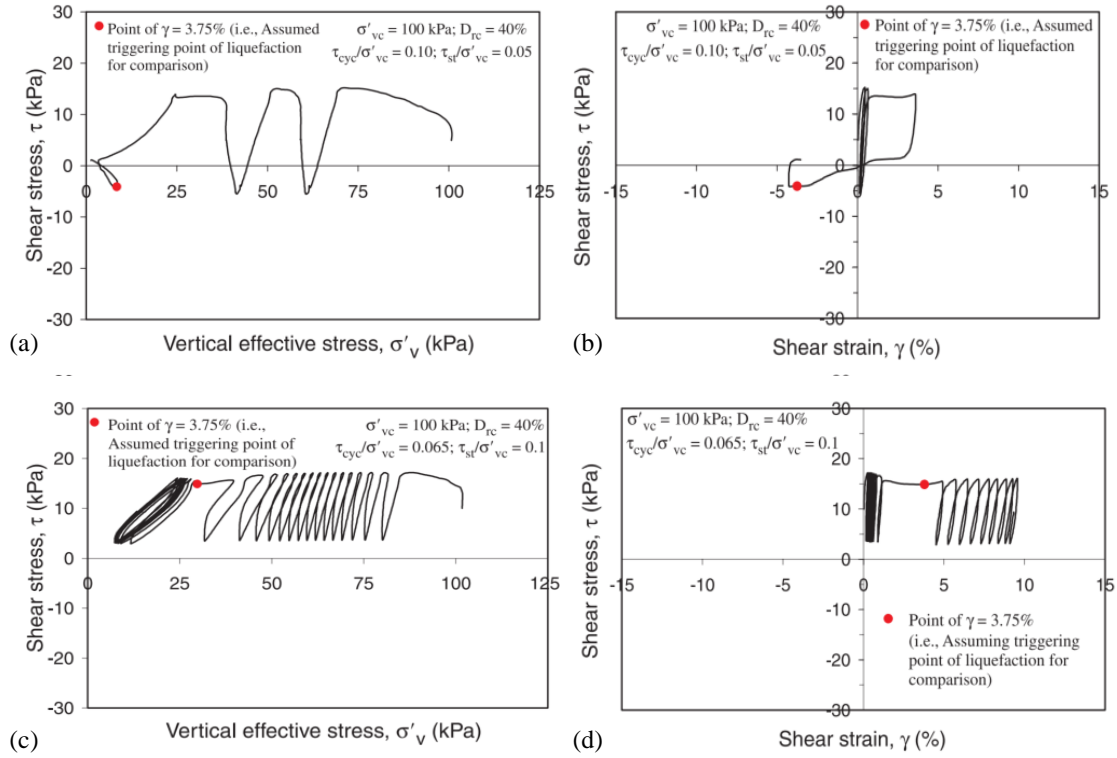


Figure 1.16 Undrained non-symmetrical cyclic simple shear tests with different average shear stress, (a-b) with stress reversal cyclic loading; (c-d) non-stress reversal cyclic loading

1.3.4 Analytical models for cyclic response

One problem remains open: that of developing an analytical or empirical model able to describe the basic cyclic response under various loading conditions. Lee and Albaisa (1974) have indicated that pore pressure generation (or mean effective pressure degradation) during dynamic tests falls within a band, as shown in Figure 1.17(a). Subsequently, Seed et al. (1975) developed an empirical model with reference to cyclic undrained triaxial results obtained on sands for purposes of predicting excess pore pressure ratio r_u ($=\Delta u/\sigma'_0$), where Δu is the excess pore pressure and σ'_0 the confining pressure. In the model proposed by Seed et al. (1975), the function of excess pore pressure ratio r_u is composed of an empirically determined parameter $\bar{\theta}$ and the cyclic number ratio of the currently applied number of cycles (N) and the number of cycles to cause liquefaction (N_L).

$$r_u = \frac{1}{2} + \frac{1}{\pi} \arcsin \left(2 \cdot \left(\frac{N}{N_L} \right)^{1/\bar{\theta}} - 1 \right) \quad (1-1)$$

Later, Booker (1976) proposed a simplified alternative expression:

$$r_u = \frac{2}{\pi} \arcsin \left(\frac{N}{N_L} \right)^{1/(2\bar{\theta})} \quad (1-2)$$

Hence Seed et al.'s model defined a uniformed ‘‘S’’ shape for the generation of excess pore pressure, as shown in Figure 1.17(b), in which two empirical parameters (i.e., N_L and θ') can be determined from stress-controlled cyclic laboratory elementary tests. Because of the simplicity of the conceptual model used to analyse the generation of excess pore pressure, it has been widely used over the past decades (Mitchell and Dubin 1986; Polito et al. 2008; Chang et al. 2014; Mohtar et al. 2014; Porcino et al. 2015). However, for a given soil, the value of N_L depends on void ratio e , cyclic shear stress ratio (CSR) and average shear stress ratio α , which can lead to difficulty for calibrating its value.

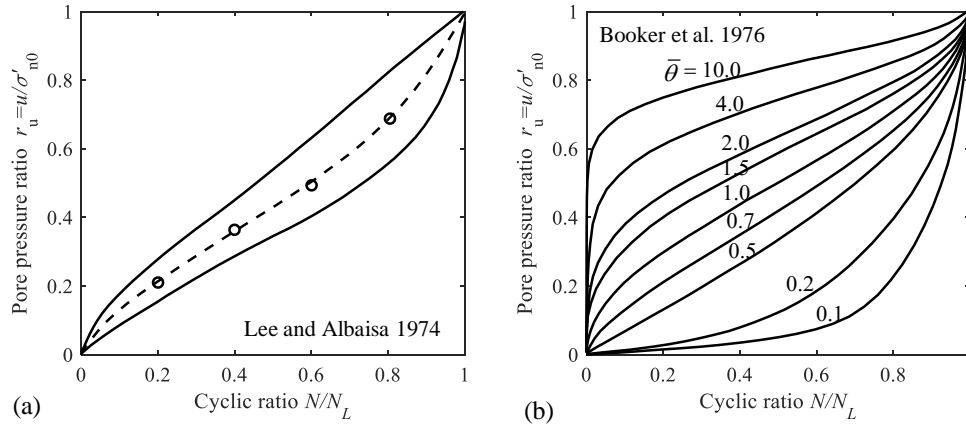


Figure 1.17 Rate of pore pressure generation: (a) Curves from Lee and Albaisa, 1974, and (b) Curves from Booker et al. (1976)

Ishibashi et al. (1977) proposed that the generation of excess pore pressure was a product of three functions: stress history \bar{H} , cyclic number \bar{N} and stress intensity \bar{I} , as shown in Eq. (3),

$$\Delta U_N^* = \overbrace{(1 - U_{N-1}^*)}^{\bar{H}} \cdot \overbrace{\left(\frac{\bar{C}_1 \cdot N}{N \bar{C}_2 - \bar{C}_3} \right)}^{\bar{N}} \cdot \overbrace{\left(\frac{\tau_N}{\sigma'_{N-1}} \right)^{\bar{\chi}}}_{\bar{I}} \quad (1-3)$$

where U_N^* and U_{N-1}^* are the residual pore pressure ratios of excess pore water pressure normalized by the initial effective confining pressure σ'_0 at the N th and $(N-1)$ th cycles, respectively, where N is the number of cycles, τ_N the shear stress at the N th cycle and \bar{C}_{1-3} and $\bar{\chi}$ material parameters.

Figure 1.18 presents the calibration procedure used in the model proposed by Ishibashi et al., based on undrained triaxial tests on loose Ottawa sand under cyclic loading. The stress intensity function \bar{I} related to parameter χ can be obtained by fitting the slope between the increment of normalized pore pressure $\Delta U_N^*/\bar{H}$ and the shear stress ratio τ_N/σ'_0 , which remains constant for each cycle as shown in Figure 1.17(a). The cyclic number function \bar{N} -

related parameter \bar{C}_{1-3} can be obtained by fitting the results of $\Delta U_N^*/(\bar{H} \cdot \bar{I})$ versus number of cycles (N), as shown in Figure 1.17(b). Four model parameters in the equation are material-dependent.

Noting that density and stress level are not considered as variables. Sherif et al. (1978) and Ishibashi et al. (1982) re-evaluated the values for the four constants in hopes of accounting for variations in density, mean grain size, sand uniformity coefficient and angularity. Such an excess pore pressure prediction method has been widely used by a number of experimental studies (Sherif et al. 1978; Krishnaswamy and Thomas Isaac 1995; Georgiannou and Tsomokos 2008; Konstadinou and Georgiannou 2014).

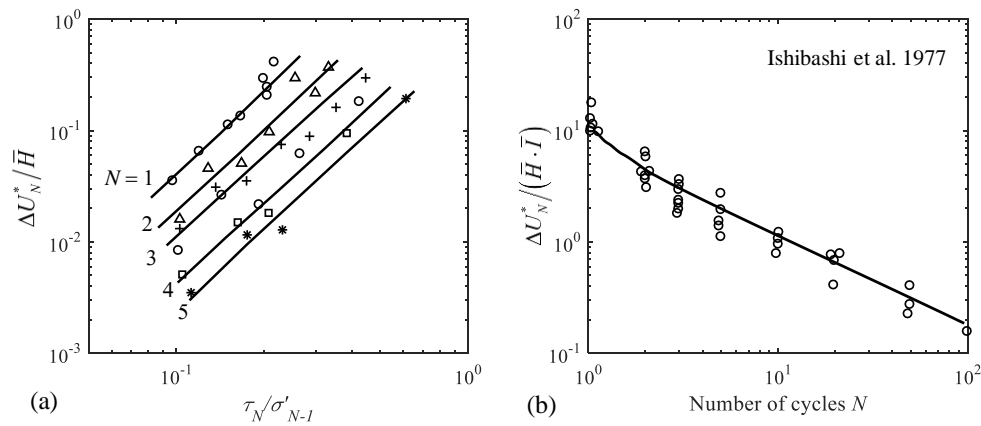


Figure 1.18 Parameters calibration of Ishibashi et al model: (a) calibration parameter χ , (b) calibration parameter C_{1-3} (after Ishibashi et al. 1977)

Field and laboratory model pile tests have been performed to understand the evolution of shaft capacity during pile installation and during service conditions such as induce by cyclic axial loading (Jardine et al. 2000; Jardine et al. 2005; Yang et al. 2010; Jardine and Standing 2012; Aghakouchak et al. 2015). Full-scale pile tests subjected to axial cyclic loading, performed by Jardine and Standing (2000), demonstrated that high-level cyclic loading can be highly detrimental to shaft capacity. In laboratory conditions, tests using the mini-ICP model pile installed in a pressurized calibration chamber (Tsuha et al. 2012a) have also provided key information to improve modelling of pile–soil interaction and the design rules of pile foundation. Based on their recent works on the degradation of shaft capacity in model pile tests, Jardine et al. (2005) have suggested an empirical “ABC” formulation, associated with the ICP design method, involving the shaft cyclic shear stress (τ_{cyc}) normalized by the maximum static shear stress $\tau_{max,static}$ and the number of cycles (N),

$$\frac{\Delta \sigma'_n}{\sigma'_{n0}} = A \cdot \left[B + \frac{\tau_{cyc}}{\tau_{max,static}} \right]^C \cdot \log_{10}(N) \quad (1-4)$$

where σ'_{n0} is the initial effective normal stress to the shaft and $\Delta\sigma'_n$ the variation (degradation) of the normal effective stress. A, B and C are three constant empirical values that can be identified through back-analysis of pile tests or through calibration during laboratory experiments. However, the influence of the mean shear stress τ_{ave} has not been introduced in the ABC model, the calibration is not robust and the degradation not limited.

Overall, the initial average shear stress is a key factor for the cyclic resistance of sand (Vaid and Chern 1983; Vaid et al. 2001; Yang and Sze 2011; Yang and Pan 2017), which is usually missing in current studies. Hence, a more efficient approach should consider this factor.

1.4 Constitutive modelling of granular materials

Owing to their complex behaviour, numerous constitutive models have been developed for sand. Three categories of models can be classified as follows: phenomenological models, multiscale models and discrete element models.

1.4.1 Phenomenological models

According to the mechanical behaviour of granular materials, phenomenological models have been featured to describe the frictional behaviour (asymptotic relationship between the stress ratio and the shear strain), the contractive or dilative behaviour (shear-induced volume change) and the critical state behaviour (the unique ultimate state of a given material attainable in the $p'-q$ and the $e-p'$ planes for any initial state). Numerous constitutive models have been developed: (1) nonlinear hypoelastic models (Duncan and Chang, 1970), (2) incrementally nonlinear models (Darve and Labanieh 1982; Darve 1990), (3) hypoplastic models (Wu et al. 1996; Niemunis and Herle 1997; Mašin and Khalili 2012) and (4) elastoplastic models based on the critical state concept (Jefferies 1993; Yu 1998; Gajo and Wood 1999; Taiebat and Dafalias 2008; Yao et al. 2008; Yin et al. 2013).

These phenomenological models are commonly adopted in engineering practice for their efficiency in finite element analysis. However, successfully capturing all mechanical features usually requires more than 10 parameters of more or less complicated formulation. Accordingly, developing a simple model having a small number of parameters for application to engineering remains a challenge.

1.4.2 Multi-scale models

In past decades, by comparison with the traditional continuum model, microscopic models have been increasingly used to explain soil mechanical behaviour from a multiscale approach. Such multiscale approaches build a constitutive relation on the specimen (material point) scale by taking microstructural information into account and linking the macro scale to the micro scale, which is still a challenge when studying micromechanical behaviour granular

materials. Chang et al. (1992) and Chang and Misra (1989) related incremental stress and strain to the contact forces and the contacts based on the contact fabric distribution. Building on this pioneering work, Chang and Hicher (2005) developed a micromechanics-based model considering interparticle forces and displacements that was itself enhanced by Yin et al. (2009; 2010b; 2014) with a view to accounting for stress reversal on a contact plane and for density state dependent dilatancy.

1.4.3 Discrete element models

The discrete element method (DEM) introduced by Cundall and Strack (1979) has been widely used to investigate the behaviour of granular media. In the DEM model, rigid spheres are used to represent soil particles and rigid walls to represent the boundary condition. The basic calculation principle of the DEM model includes Newton's second law and the force displacement law, using the former to determine the motion of each particle arising from the contact and body forces and using the latter to update the contact forces arising from the relative motion at each contact.

Many investigations have indicated that the DEM method is able to capture the basic features of granular materials: dilative/contractive stress, grain size distribution effect, fabric effect, cyclic stress stiffness degradation and strain accumulation (Iwashita and Oda 1998; Zhao and Evans 2009; Yimsiri and Soga 2010; Fu and Dafalias 2011; Li et al. 2014; Liu et al. 2014). Moreover, because of the highly replicable behaviour of the elementary test in a laboratory by DEM method, stress inhomogeneity caused by specimen preparation and consolidation stages, can also be well studied something otherwise difficult to investigate in the laboratory (Dabeet 2014; Bernhardt and Biscontin 2016; Asadzadeh and Soroush 2017; Zhu et al. 2017). However, the number of particles in most DEM simulations is very limited and is thus far from the real physical model owing to considerations of computational efficiency; thus the extension of the DEM to problems at real-world scale is still questionable.

In fact, the phenomenological models have been widely adopted for engineering application (Zhang et al. 2013; Kouretzis et al. 2014; Jin et al. 2017). Yin et al (2013) presented a framework of critical-state based model, which was developed based on the Mohr-Coulomb model by implementing the critical state concept (Jin et al. 2016c; Yin et al. 2016) with non-linear elasticity, non-linear plastic hardening, and a simplified three-dimensional strength criterion. The state-dependent peak strength and stress-dilatancy (contraction or dilation) are well captured by the model (Jin et al. 2017). Despite this critical-state framework have been widely used, the inherent anisotropy and the cyclic effect still need to be further considered, especially under the prerequisites of without increasing the model parameters and ease to use.

1.5 Thesis organization

As it is evident from the foregoing discussion, although experimental investigations of the simple shear tests have been widely studied, some limitations remain. In this thesis, simple shear tests were performed on Fontainebleau sand, with the experimental results analysed within the critical state soil mechanics framework. This thesis comprises following chapters:

- 1) Presents the simple critical state-based model (SIMSAND) and its finite element implementation
- 2) Enhances the SIMSAND model by considering principal stress rotation and applying it to study stress inhomogeneity in the simple shear test
- 3) Estimates normal effective stress degradation in sand during undrained cyclic simple shear tests
- 4) Estimates volumetric strain accumulation in sand during drained cyclic simple shear tests
- 5) Suggests a cyclic SIMSAND model accounting for the experimental results obtained from Fontainebleau sand during cyclic triaxial to simple shear tests, and simulates pile penetration and cyclic tests using FE code in conjunction with the enhanced cyclic SIMSAND model.
- 6) Summarizes the main conclusions of the research study while proposing recommendations for further research.

Chapter 2 A straightforward procedure of determining parameters of SIMSAND model

2.1 Introduction

Mechanical behaviour of sand has been widely investigated by numerous researchers during the last decades, from which various constitutive models have been proposed. To unify the modelling of sand with different densities, the critical state concept is necessarily adopted, such as the classical elasto-plasticity (Duncan and Chang 1970; Jefferies 1993; Gajo and Muir Wood 1999; Taiebat and Dafalias 2008; Yin et al. 2013; Yin et al. 2016), hypoplastic models (Kolymbas 1991; Wu and Bauer 1993; Wu et al. 1996), micromechanical models (Chang et al. 2010; Yin et al. 2010a; Yin and Chang 2013; Yin et al. 2014). However, the incorporation of the critical state increases the number of model parameters with high relevance in terms of parameters sensitivity. Then, these parameters are difficult to be measured from laboratory tests in a direct way. Therefore, an efficient and effective way is recommended for applying these models to engineering practice.

In general, two main methods have been used for determining those directly immeasurable parameters: the trial and error method and the inverse analysis method. In the former method, numerous values of parameters need to be tried by conducting a lot of simulations, until obtaining the apparent best fit to experiment results. It's a time-consuming procedure and mainly depends on the knowledge of operators. In the latter one, the optimal parameters are usually inversely analysed through a larger number of simulations with computational demand.

Different from above methods, to reduce the computational demand a straightforward procedure for determining model parameters is proposed in this chapter. In the following sections, a simple critical-state based sand model with a nonlinear critical state line is introduced first. Then, a straightforward procedure for determining parameters is proposed based on the derivation of constitutive equations with the recommendation of some measurements to be adopted. Experimental tests on Toyoura sand are selected as an example for clarifying the use of the procedure and the validation. Furthermore, the model is implemented into a finite element code, and numerical modelling of a series of footing tests is performed using the straightforwardly determined parameters. The proposed procedure is validated as an efficient and reliable bridge from constitutive modelling to finite element analysis.

2.2 Simple critical-state based sand model

The simple critical-state based sand model (marked as SIMSAND) is proposed based on experimental observations and existing modelling methods. According to the elasto-plasticity theory, the total strain rate is conventionally composed of the elastic and plastic strain rates:

$$\dot{\varepsilon}_{ij} = \dot{\varepsilon}_{ij}^e + \dot{\varepsilon}_{ij}^p \quad (2-1)$$

where $\dot{\varepsilon}_{ij}$ denotes the (i,j) component of the total strain rate tensor, and the superscripts e and p stand, respectively, for the elastic and plastic components.

2.2.1 Elastic behaviour

For the elastic part of the model, the isotropic elasticity assumption is adopted, and the increments can be calculated by the following law:

$$\dot{\varepsilon}_v^e = \frac{\dot{p}'}{K}, \quad \dot{\varepsilon}_d^e = \frac{\dot{q}}{3G} \quad (2-2)$$

where K and G are the elastic bulk and shear moduli, adopting the same form proposed by (Richart et al. 1970) which implies a constant Poisson's ratio ν :

$$K = K_0 \cdot p_{at} \frac{(2.97 - e)^2}{(1 + e)} \left(\frac{p'}{p_{at}} \right)^\zeta, \quad G = G_0 \cdot p_{at} \frac{(2.97 - e)^2}{(1 + e)} \left(\frac{p'}{p_{at}} \right)^\zeta \quad (2-3)$$

where K_0 and G_0 are reference values of bulk modulus and shear modulus; ζ is a constant parameter controlling the nonlinearity of confining stress effect; e is void ratio; p' is the mean effective stress ($p' = \sigma'_{ii}/3$); p_{at} is the atmospheric pressure used as reference pressure ($p_{at} = 101.325$ kPa).

Since the isotropic compression test can be easily conducted and can also be an initial stage of shear test, it is recommended to use K_0 and ν as input parameters with $G_0 = 3K_0(1 - 2\nu)/2(1 + \nu)$.

2.2.2 Plastic behaviour

A shear sliding yield surface, as used in previous models (Vermeer, 1978; Pietruszczak and Mroz, 1980; Jefferies, 1993; Gajo and Muir Wood, 1999; Yin et al., 2013), is adopted, as shown in Figure 2.1:

$$f = \frac{q}{p'} - \frac{M_p \varepsilon_d^p}{k_p + \varepsilon_d^p} \quad (2-4)$$

where f is the yield function; q is the deviatoric stress ($q = \sqrt{3J_2} = \sqrt{3s_{ij}s_{ij}/2}$); k_p relates to the plastic shear modulus controlling the initial slope of the curve of $q/p' - \varepsilon_d^p$; M_p is the stress ratio corresponding to the peak strength in p' - q space with $M_p = 6\sin(\phi_p)/(3 - \sin(\phi_p))$ in compression; ε_d^p is the deviatoric plastic strain ($\varepsilon_d^p = \sqrt{2e_{ij}e_{ij}/3}$).

The plastic strain can be calculated by the flow rule:

$$\dot{\varepsilon}_{ij}^p = d\lambda \frac{\partial g}{\partial \sigma'_{ij}} \quad (2-5)$$

where g is the plastic potential function; $d\lambda$ is the plastic multiplier depending on the stress rate and the plastic hardening law.

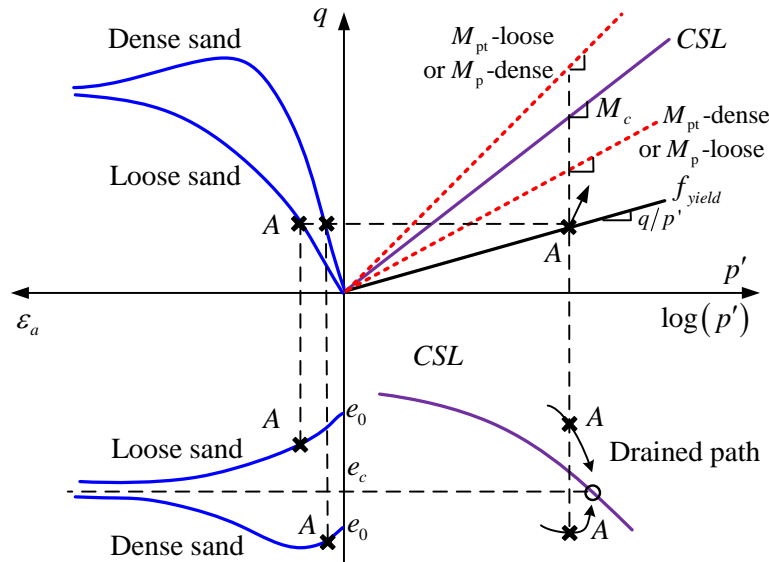


Figure 2.1 Principle of SIMSAND model

In order to take into account the dilation or contraction behaviour during shear sliding, a non-associated flow rule is introduced, which is expressed as follows:

$$\frac{\partial g}{\partial \sigma'_{ij}} = \frac{\partial g}{\partial p'} \frac{\partial p'}{\partial \sigma'_{ij}} + \frac{\partial g}{\partial q} \frac{\partial q}{\partial \sigma'_{ij}} \quad \text{with} \quad \frac{\partial g}{\partial p'} = A_d \left(M_{pt} - \frac{q}{p'} \right) \quad \text{and} \quad \frac{\partial g}{\partial q} = 1 \quad (2-6)$$

where M_{pt} is the stress ratio corresponding to the phase transformation line (PTL) in p' - q space with $M_{pt} = 6\sin(\phi_{pt})/(3 - \sin(\phi_{pt}))$ calculated from the phase transformation friction angle, ϕ_{pt} . Eq. (2-7) implies the following stress-dilatancy relationship:

$$\frac{\dot{\varepsilon}_v^p}{\dot{\varepsilon}_d^p} = A_d \left(M_{pt} - \frac{q}{p'} \right) \quad (2-7)$$

where A_d is the stress-dilatancy parameter controlling the evolution of volumetric strain ε_v with axial strain ε_a or deviatoric strain ε_d during shearing.

2.2.3 Critical state and interlocking effect

According to the critical state concept and experimental observations, a simple nonlinear critical state line proposed by Li and Wang (1998) to calculate the critical state void ratio e_c was adopted as follows:

$$e_c = e_{ref} - \lambda \left(\frac{p'}{p_{at}} \right)^\xi \quad (2-8)$$

where e_{ref} is a reference void ratio corresponding to the void ratio at $p'=0$ for simplicity, λ and ξ are constants controlling the nonlinear slope of the CSL. However, for high stress level this equation cannot guarantee the positiveness of the critical void ratio. A slight modification was thus made in this chapter using the logarithmic scale of void ratio instead of normal scale,

$$\log e_c = \log e_{ref} - \lambda \left(\frac{p'}{p_{at}} \right)^\xi \Rightarrow e_c = e_{ref} \exp \left[-\lambda \left(\frac{p'}{p_{at}} \right)^\xi \right] \quad (2-9)$$

The interlocking effect suggested by Been and Jefferies (1985) can be introduced as follows:

$$M_p = M \exp \left[-n_p (e - e_c) \right], \quad M_{pt} = M \exp \left[n_d (e - e_c) \right] \quad (2-10)$$

where n_p and n_d are model interlocking parameters, which controls the degree of interlocking by neighbouring particles according to (Yin et al. 2010a; Yin and Chang 2013); M is the slope of critical state line in p' - q space (with $M_c = 6 \sin \phi_c / (3 - \sin \phi_c)$ in triaxial compression).

As shown in Figure 2.1, Eq. (2-10) implies that in a loose structure with $e > e_c$, the phase transformation stress ratio M_{pt} is bigger than M , and the peak stress ratio M_p is smaller than M , which allows the loose structure to be contractive during deviatoric loading with a strain-hardening strength. In a dense structure with $e < e_c$, the phase transformation stress ratio M_{pt} is smaller than M , and the peak stress ratio M_p is bigger than M , which allows the dense structure to be first contractive and then dilative during deviatoric loading with a peak strength followed by a ductile stage. For both loose and dense structures, when the stress state reaches the critical state line, the void ratio e becomes equal to the critical void ratio e_c , then zero dilation or contraction takes place. Thus, the constitutive equations guarantee that stresses and void ratio reach simultaneously the critical state in the p' - q - e space.

In order to interpolate M_p and M_{pt} between their values for compression and those for extension by means of the Lode's angle θ (Sheng et al. 2000), the following expression for M is proposed

$$M = M_c \left[\frac{2c^4}{1 + c^4 + (1 - c^4) \sin 3\theta} \right]^{\frac{1}{4}} \quad (2-11)$$

where $c = (3 - \sin \phi_c) / (3 + \sin \phi_c)$, assuming the same critical state friction angle for different Lode's angles. The Lode's angle is expressed as $-\pi/6 \leq \theta = \sin^{-1}(-3\sqrt{3}J_3/2J_2^{3/2})/3 \leq \pi/6$. J_2 and J_3 are the second and third invariants of the deviatoric stress tensor, given by $J_2 = s_{ij}s_{ij}/2$, $J_3 = s_{ij}s_{jk}s_{ki}/3$. Eq. (2-10) combined with Eq. (2-11) leads to different values of M_p and M_{pt} for different values of Lode's angle assuming the same friction angle.

The plastic multiplier $d\lambda$ can be calculated in a conventional way according to plasticity:

$$d\lambda = \frac{\left[\frac{\partial f}{\partial \sigma_{ij}} \right]^T [D_{ijkl} \dot{\epsilon}_{kl}]}{\left[\frac{\partial f}{\partial \sigma_{ij}} \right]^T \left[D_{ijkl} \frac{\partial g}{\partial \sigma_{kl}} \right] - \frac{\partial f}{\partial \epsilon_d^p} \frac{\partial g}{\partial q}} \quad (2-12)$$

Combining Eq.s (2-1) to (2-12), the stress-strain relationship can be solved for test simulations.

Major assumptions inherent in the constitutive law are as follows: the total strain decomposed in elastic and plastic strains, hyperbolic hardening of stress ratio versus deviatoric plastic strain, only elastic behaviour in isotropic compression, non-associated flow rule and the concept of critical state. Note that the stress reversal technique for describing the cyclic behaviour of sand by Yin et al. (2013) was not included in this study, since the current emphasis focuses on the determination of parameters based on tests under monotonic loading.

2.2.4 Summary of model parameters

The nonlinear critical state line based SIMSAND model requires calibrating eleven parameters, which can be divided into three groups based on their physical meaning as follows: (1) elasticity related parameters: K_0 , ζ and ν ; (2) critical state related parameters: ϕ_c , e_{ref} , λ and ξ ; (3) plasticity and interlocking parameters: A_d , k_p , n_p and n_d .

Plasticity interlocking parameters were usually determined by curve fitting that requires a good understanding of constitutive modelling and trial-error procedure (Jefferies 1993; Manzari and Dafalias 1997; Gajo and Muir Wood 1999).

2.3 Procedure for determining parameters

For introducing the straightforward method to determine the parameters of SIMSAND model, a series of synthetic tests including isotropic compression test and drained triaxial tests were generated by the SIMSAND model using a set of given model parameters (see Table 2.1 and Figure 2.2). The main purpose of using the synthetic test data is to illustrate the proposed determination procedure. The ideal synthetic test data used in the proposed procedure can reduce the effect of test errors so that the reasonability and reliability of the proposed method can be theoretically demonstrated. Then the real test data will be used to further demonstrate the feasibility of the proposed procedure. Only one isotropic compression test and three drained triaxial tests with different confining stresses p'_0 and different initial void ratios e_0 are needed for the back calculation procedure.

Table 2.1 Values of model parameters for generating test data

Parameters	K_0	ζ	ν	ϕ_c	e_{ref}	λ	ξ	k_p	A_d	n_p	n_d
Example	100	0.6	0.25	30	0.875	0.085	0.229	0.0015	1.2	2	1.5

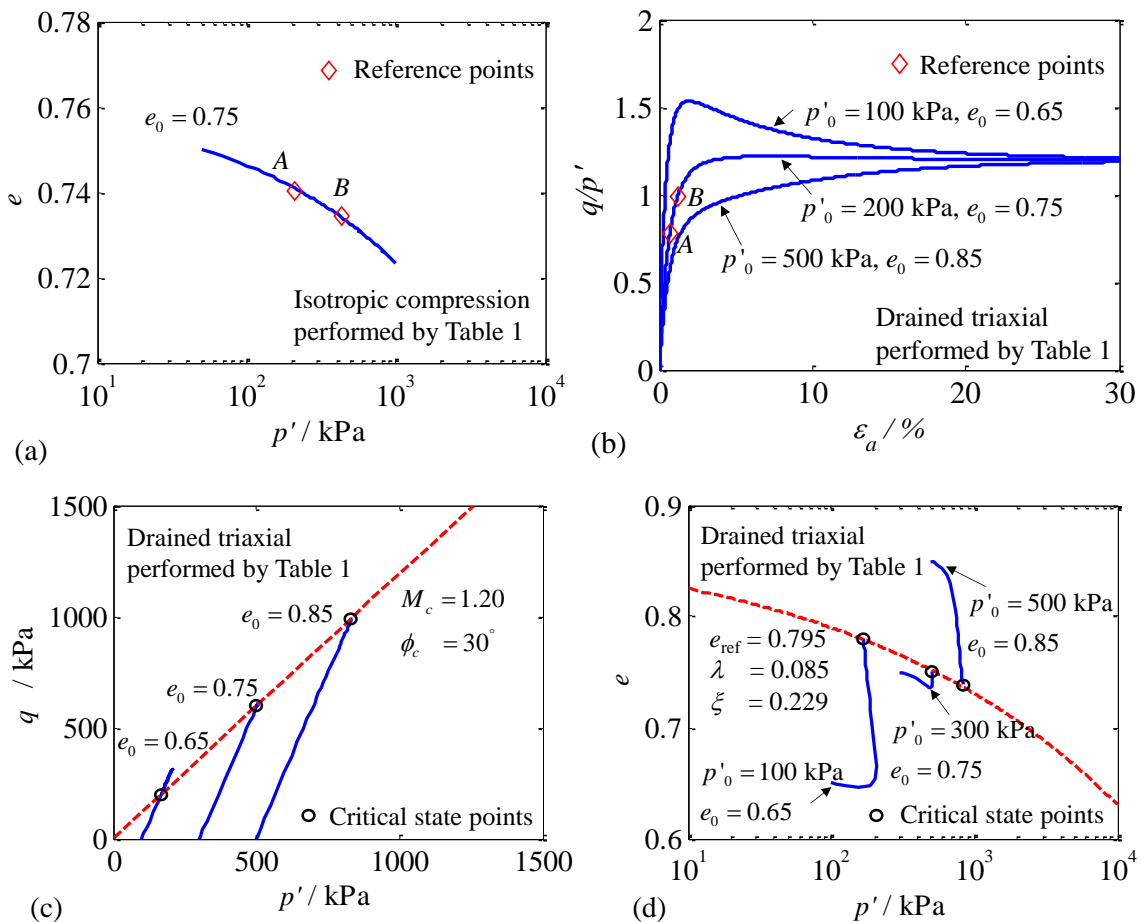


Figure 2.2 Synthetic data using a set of given model parameters for isotropic compression test and conventional drained triaxial tests: (a) void ratio versus mean effective stress, (b) stress

ratio versus axial strain, (c) mean effective stress and deviatoric stress and (d) void ratio versus mean effective stress

The proposed determination procedure is divided into three steps, as shown in the flow chart of Figure 2.3. First, the elasticity parameters are determined using the isotropic compression test data. Then, the critical state parameters can be determined based on at least three drained triaxial tests. Finally, the interlocking related parameters can be determined based on one drained triaxial test. The details of the procedure are presented in following sections.

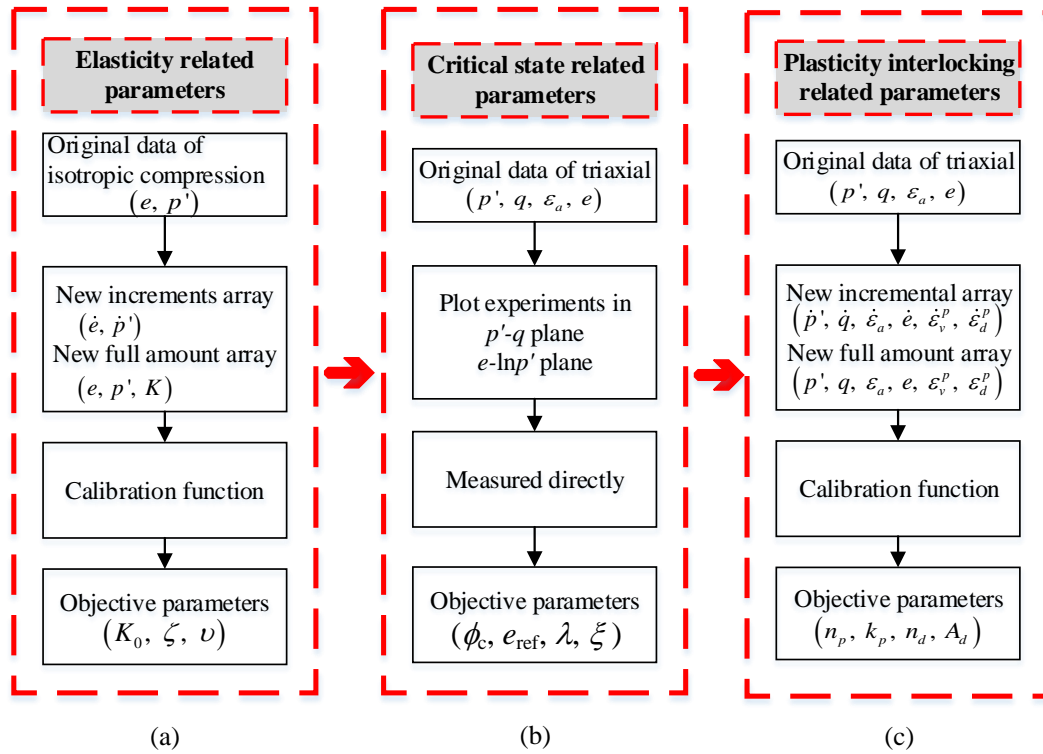


Figure 2.3 Procedure of proposed straightforward method from (a) elasticity related parameters, (b) critical state related parameters to (c) plasticity interlocking related parameters

2.3.1 Determination of the elasticity related parameters

According to Eq. (2-3), for any point on the isotropic compression curve, the relationship between K , p' and e is unique, where p' and e are measured in the experimental curves, and bulk modulus of each point are calibrated by the Eq. (2-13).

$$K = \frac{\dot{p}'}{\dot{\epsilon}_v^e} = \frac{\dot{p}'}{\dot{e}}(1 + e_0) \quad (2-13)$$

Since two parameters K_0 and ζ must be determined, two equations corresponding to different points on the isotropic compression curve are necessary to form an equation set. For this purpose, two points “A” (K_A, e_A, p'_A) and “B” (K_B, e_B, p'_B) were selected on the isotropic

compression curve, as shown in Figure 2.4. Then, the corresponding equation set are expressed in Eq. (2-14).

$$\begin{cases} K_A = K_0 p_{at} \frac{(2.97 - e_A)^2}{(1 + e_A)} \left(\frac{p'_A}{p_{at}} \right)^\zeta \\ K_B = K_0 p_{at} \frac{(2.97 - e_B)^2}{(1 + e_B)} \left(\frac{p'_B}{p_{at}} \right)^\zeta \end{cases} \Rightarrow \begin{cases} \zeta = \ln \left[\left(\frac{2.97 - e_B}{2.97 - e_A} \right)^2 \left(\frac{1 + e_A}{1 + e_B} \right) \frac{K_A}{K_B} \right] / \ln \left(\frac{p'_A}{p'_B} \right) \\ K_0 = \frac{K_A}{p_{at}} \frac{(1 + e_A)}{(2.97 - e_A)^2} \left(\frac{p_{at}}{p'_A} \right)^\zeta \end{cases} \quad (2-14)$$

Thus, the two elasticity parameters can be solved. Details can be found in MATLAB CODE-1 in Appendix A. In order to obtain a reliable set of parameters, multiple calculations with different combinations of two different points on the compression curve are needed to give an average result.

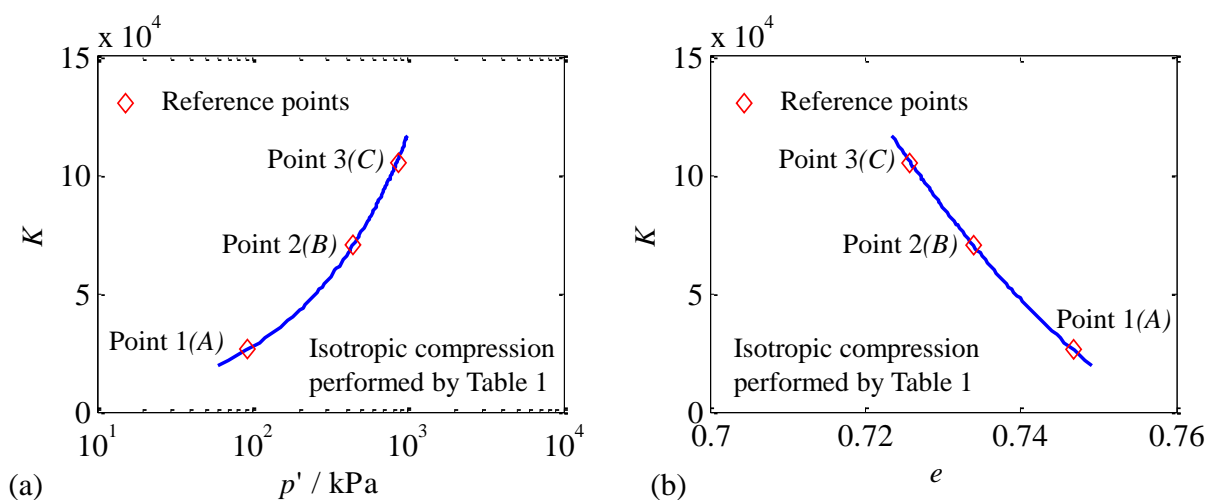


Figure 2.4 New interpreted curves from isotropic compression curve in (a) Elastic bulk moduli versus mean effective stress and (b) Elastic bulk moduli versus void ratio

Table 2.2 shows the results of multiple calculations corresponding to different combinations of selected points, based on which the average values of $K_0=97.5$ and $\zeta=0.6$ were obtained. Only a slight difference between determined values and objective values was found, which demonstrates that the proposed method to determine the elasticity parameters is feasible.

For G_0 , which can be calculated according to $G_0=3K_0(1-2\nu)/2(1+\nu)$, the Poisson's ratio can be assumed to a value close to 0.2 or can be calculated by the friction angle ϕ_c assuming a well accepted one-dimensional compression condition according to Jacky's formula ($K_0=1-\sin\phi_c$), expressed as follows,

$$\nu = \left(3 - 2 \frac{G}{K} \right) / 2 \left(3 + \frac{G}{K} \right) \quad (2-15)$$

where $G/K=1/(2\eta)$ with $\eta=3\sin(\phi_c)/(3-2\sin(\phi_c))$.

Note that in the proposed procedure $\nu=0.2$ was first set as default value, and was updated by the Eq. (2-15) when the friction angle was measured later on.

Table 2.2 Calibration of elasticity related parameters K_0 and ζ based on synthetic data

No	$p'_{(A)}$ /kPa	$e_{(A)}$	$p'_{(B)}$ /kPa	$e_{(B)}$	ζ	K_0
1	100	0.746	500	0.732	0.607	96.81
2	100	0.746	900	0.725	0.603	96.81
3	500	0.732	900	0.725	0.602	99.01
The average value					0.604	97.56

2.3.2 Determination of critical state related parameters

For determining the critical state parameters, the conventional approach was adopted. Based on the results of drained triaxial tests shown in Figure 2.2 (c), the slope of the critical state line $M_c = 1.20$ can be measured from the $p'-q$ space, and the friction angle $\phi_c=30^\circ$ was then obtained by Eq. (2-16). Once ϕ_c is obtained, the Poisson's ratio ν is updated using Eq.(2-15) Normally a 20% strain is considered as the test reached the critical state (Biarez & Hicher 1994). If the strain during the test ranges from 10% to 20%, it is suggested to extend the data to the 20% strain by the quadratic multinomial method. Note that, for dense sand, the deformation ceases to be homogeneous at a certain strain, and a localisation of large deformations occurs. Such tests will give a false value of the friction angle ϕ_c corresponding to perfect plasticity. Therefore, dense samples are strongly not recommended for the critical state related parameters determination.

$$\phi_c = \text{asin}\left(\frac{3M_c}{6 + M_c}\right) \quad (2-16)$$

For non-linear CSL, three critical state points are needed. The MATLAB data fitting function "lsqcurvefit" (to solve nonlinear curve-fitting or data-fitting problems based on least-squares) can be used to solve three critical state parameters. Details can be found in MATLAB CODE-2 in Appendix A. By this way, the parameters $e_{\text{ref}} = 0.875$, $\lambda = 0.085$ and $\xi = 0.229$ were obtained by fitting the results of triaxial tests at critical state in the $e-\ln p'$ space, as shown in Figure 2.2 (d). It can be seen all the obtained values of critical state parameters are similar to the objective values.

Note that for dense sand, shear bands were usually formed, which induces non-uniformity of the specimen, which also implies that the data can no longer be used for

constitutive interpretation. Tests on dense sand are not recommended to back-calculate the related mechanical parameters of soil due to the strain localization. For loose and medium dense materials, the influence of shear banding is considered to be slight up to 20% of axial strain, and the mechanical response of the sample can be widely accepted as the elementary behaviour of the soil (Biarez and Hicher 1994). As a result, triaxial tests on loose and medium dense samples are strongly recommended for parameters determination.

2.3.3 Determination of plasticity interlocking related parameters

This section presents the procedure to determine plasticity interlocking related parameters (see Figure 2.3 (c)). According to Eq. (2-4), a relationship between stress ratio (q/p') and deviatoric plastic strain ε_d^p is given.

For a given triaxial test result with $q/p'-\varepsilon_a$ and $\varepsilon_v-\varepsilon_a$, the ε_v^p and ε_d^p should be first calculated and accumulated by Eq. (2-17) as follows,

$$\dot{\varepsilon}_v^p = \dot{\varepsilon}_v - \dot{\varepsilon}_v^e = \dot{\varepsilon}_v - \frac{\dot{p}'}{K} \quad \text{and} \quad \dot{\varepsilon}_d^p = \dot{\varepsilon}_d - \dot{\varepsilon}_d^e = \dot{\varepsilon}_d - \frac{\dot{q}}{3G} \quad (2-17)$$

where K and G were obtained by Eq. (2-3) in the previous section. Details can be found in MATLAB CODE-3 in Appendix A.

Then, the curve $q/p'-\varepsilon_d^p$ can be obtained, as shown in Figure 2.5 (a). Because of two unknown parameters (k_p and n_p) involved in Eq. (2-4) with Eq. (2-10), a system of equations including at least two equations on different points from the $q/p'-\varepsilon_d^p$ curve (e.g. point A and point B) is necessary to solve the hyperbolic-type nonlinear equation,

$$\begin{cases} \left(\frac{q}{p'} \right)_A - \frac{M_c \exp[-n_p(e - e_c)]_A (\varepsilon_d^p)_A}{k_p + (\varepsilon_d^p)_A} = 0 \\ \left(\frac{q}{p'} \right)_B - \frac{M_c \exp[-n_p(e - e_c)]_B (\varepsilon_d^p)_B}{k_p + (\varepsilon_d^p)_B} = 0 \end{cases} \quad (2-18)$$

where e_c can be obtained based on Eq. (2-8) or (2-9) in the second step. Then, using MATLAB, the roots of (k_p and n_p) in Eq. (2-18) can be easily solved by the function “fzero” (to solve the root of nonlinear function). Details can be found in MATLAB CODE-4 in Appendix A.

Similarly, for the other two parameters A_d and n_d accounting for contractive or dilative behaviour, the relationship between $\dot{\varepsilon}_v^p/\dot{\varepsilon}_d^p$ and q/p' was obtained based on Eq. (2-7), as shown in Figure 2.5 (b). Then an equation set involving two stress-dilatancy related parameters can be formed as follows:

$$\begin{cases} \left(\frac{\dot{\varepsilon}_v^p}{\dot{\varepsilon}_d^p} \right)_A = A_d \left(M_c \exp[n_d (e - e_c)]_A - \left(\frac{q}{p'} \right)_A \right) \\ \left(\frac{\dot{\varepsilon}_v^p}{\dot{\varepsilon}_d^p} \right)_B = A_d \left(M_c \exp[n_d (e - e_c)]_B - \left(\frac{q}{p'} \right)_B \right) \end{cases} \quad (2-19)$$

Again, by the MATLAB function “fzero”, Eq. (2-19) can be also easily solved. Two parameters A_d and n_d were thus directly determined. Details can be found in MATLAB CODE-4 in Appendix A.

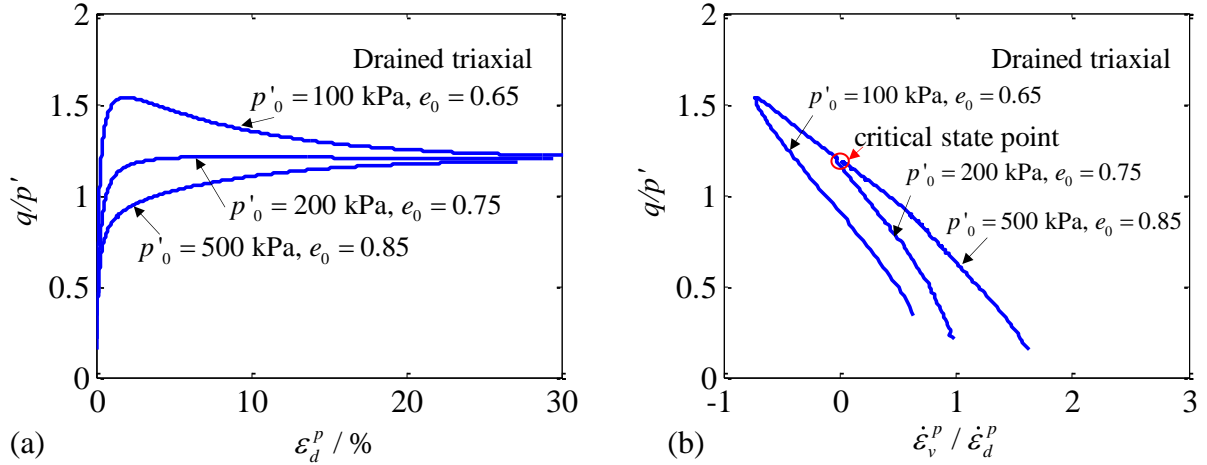


Figure 2.5 Increments of plastic strain of drained triaxial tests: (a) stress ratio versus deviatoric plastic strain; (b) stress ratio versus ratio of plastic strain increment

It should be pointed out that the key issue for the identification procedure is the position of selected points on the curves. When the selected point is close to the critical state, the ratio $e - e_c$ is close to 0 and the stress ratio q/p' is close to M_c . Then the value of $M_c \exp[n_d (e - e_c)] - (q/p')$ is close to zero, which would result in calculation error. Therefore, the value of A_d is sensitive to the position of selected points used in the calculation. For determining the parameters A_d and n_d , the selected points before reaching the critical state are suggested for obtaining reasonable and reliable parameters. Moreover, in the real testing on dense sand, the deformation ceases to be homogeneous at a certain strain (closed to 2% ~ 3% strain), and a localisation of large deformations occurs. Such tests will give false values of parameters corresponding to perfect plasticity. Therefore, the available data for dense sand is ranged in the 3% strain.

To obtain more accurate and reliable parameters, multiple calculations with different combinations of two selected points on the test curve are needed to give an average value of parameters. These points are suggested to be selected in the range of 3% strain, because of that over 3% strain will lead to inhomogeneity of the sample in the laboratory testing, especially for dense sand. Based on many simulations in this way, three combinations involving two points corresponding to different strain levels were estimated to be enough and

as simple as possible in the calculation for one test. Then the same calculations are suggested on the other two tests with different confining stresses and void ratios. Table 2.3 shows the calculated interlocking related parameters for each combined of selected points and each selected triaxial test. Figure 2.6 presents the comparisons between determined parameters and objective values, which demonstrates a good agreement. Using the average values of interlocking related parameters combined with the elasticity and critical state parameters determined previously, the tests for calibration were simulated, as shown in Figure 2.7, demonstrating the accuracy and reliability of the proposed determination procedure.

Note that, for experimental curves usually exhibiting scattering, a primary procedure to smooth these curves is necessary, for instance using MATLAB function “smooth” to polish the experimental data.

Table 2.3 Calibration of plasticity interlocking related parameters based on synthetic data

ε_a %		$p'_0=100$ kPa, $e_0=0.65$				$p'_0=300$ kPa, $e_0=0.75$				$p'_0=400$ kPa, $e_0=0.85$			
A	B	n_p	k_p	n_d	A_d	n_p	k_p	n_d	A_d	n_p	k_p	n_d	A_d
1	1.5	1.99	0.0015	1.67	1.09	2.07	0.0018	1.59	1.25	2.15	0.0013	1.27	1.29
1	2	1.99	0.0015	1.31	1.08	2.04	0.0018	1.59	1.25	2.11	0.0013	1.13	1.29
1.5	2	1.99	0.0015	1.16	1.05	2.38	0.0017	1.59	1.25	2.08	0.0013	1.58	1.28
average		1.99	0.0015	1.38	1.07	2.16	0.0018	1.59	1.25	2.11	0.0013	1.33	1.29

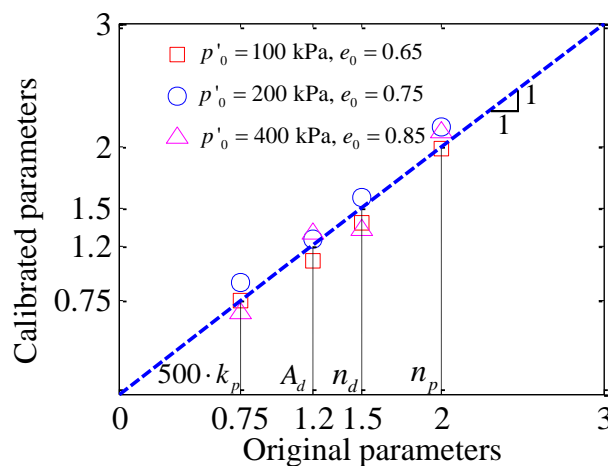


Figure 2.6 Comparison between original given and calibrated parameters

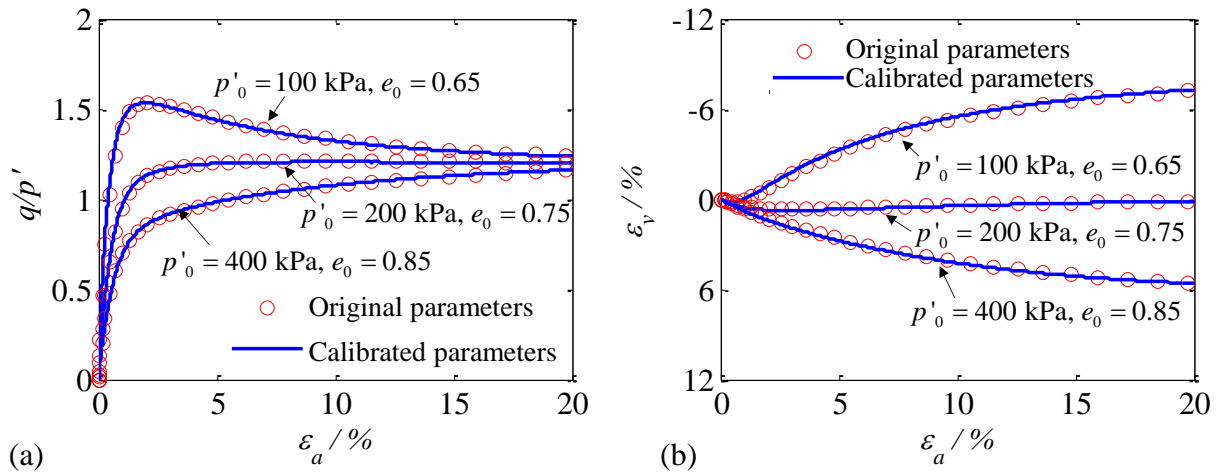
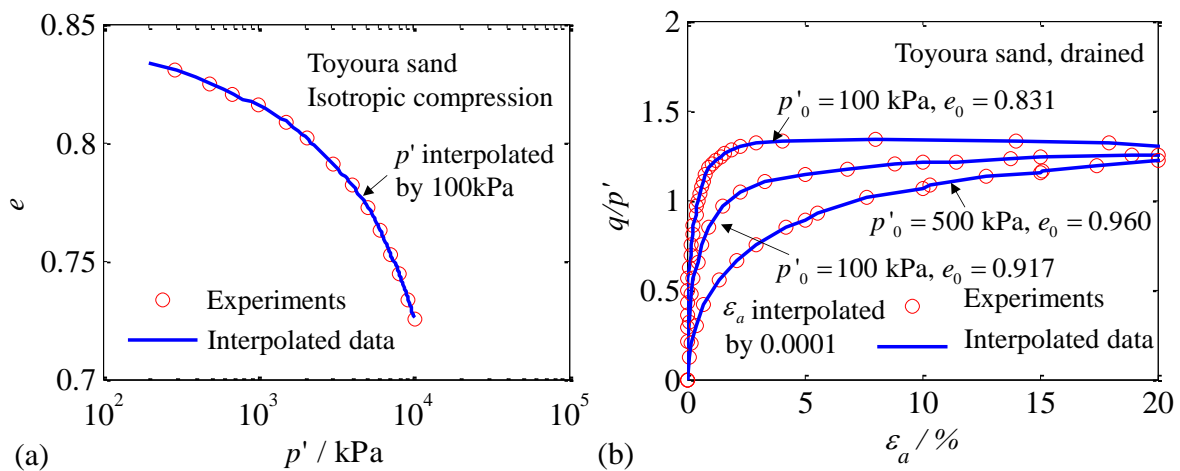


Figure 2.7 Comparison between synthetic results and simulated results by calibrated parameters: (a) stress ratio versus axial strain; (b) volumetric strain versus axial strain

2.4 Validation by real laboratory tests

For evaluating the proposed straightforward approach, a series of conventional test results including those from an isotropic compression test and drained triaxial tests performed on Toyoura sand by (Miura et al. 1984) were selected to conduct the parameter determination with the proposed method. Figure 2.8 shows the experimental results of selected isotropic compression test and drained triaxial tests.

First, based on the result of isotropic compression test, the change of bulk moduli was calculated by Eq. (2-13) using MATLAB CODE-1, as shown in Figure 2.9. Three calculations involving different points corresponding to different stress levels on isotropic compression curve were conducted. Table 2.4 presents the determined results with the average values of $K_0=130$ and $\zeta=0.52$. Note that if the experimental points are not dense enough to provide satisfying points in the calculation, the interpolation of experimental curve is necessary to re-generate an experimental curve with more points, as shown in Figure 2.9.



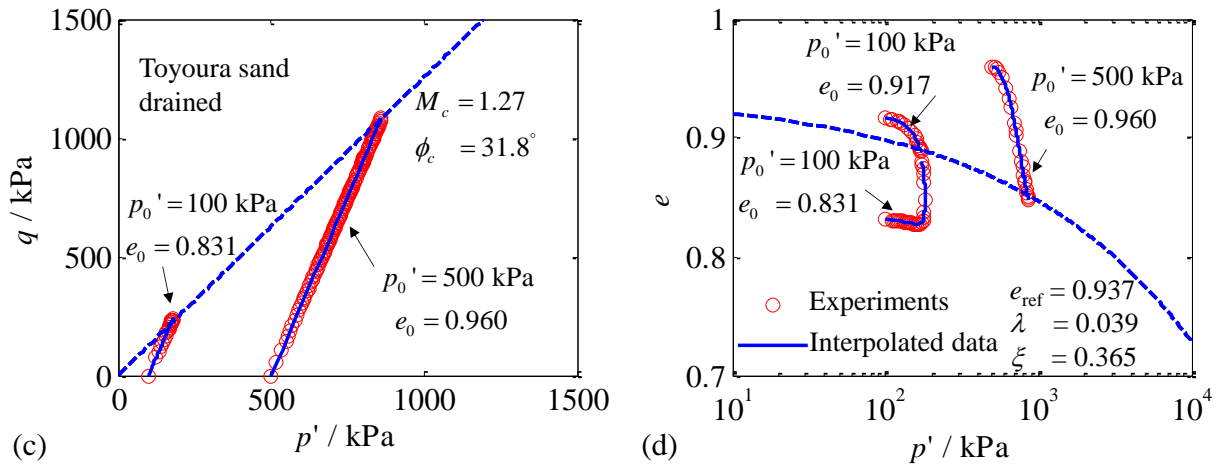


Figure 2.8 Experimental results of isotropic compression and conventional drained triaxial tests on Toyoura sand for calibrating parameters: (a) void ratio versus mean effective stress, (b) stress ratio versus axial strain, (c) mean effective stress and deviatoric stress and (d) void ratio versus mean effective stress

Table 2.4 Calibration of model parameters K_0 and ζ for Toyoura sand

No	$p'_{(A)}$ /kPa	$p'_{(B)}$ /kPa	ζ (average)	K_0 (average)
1	300	600	0.49	138
2	300	900	0.52	134
3	600	900	0.57	120
The average value			0.52	130

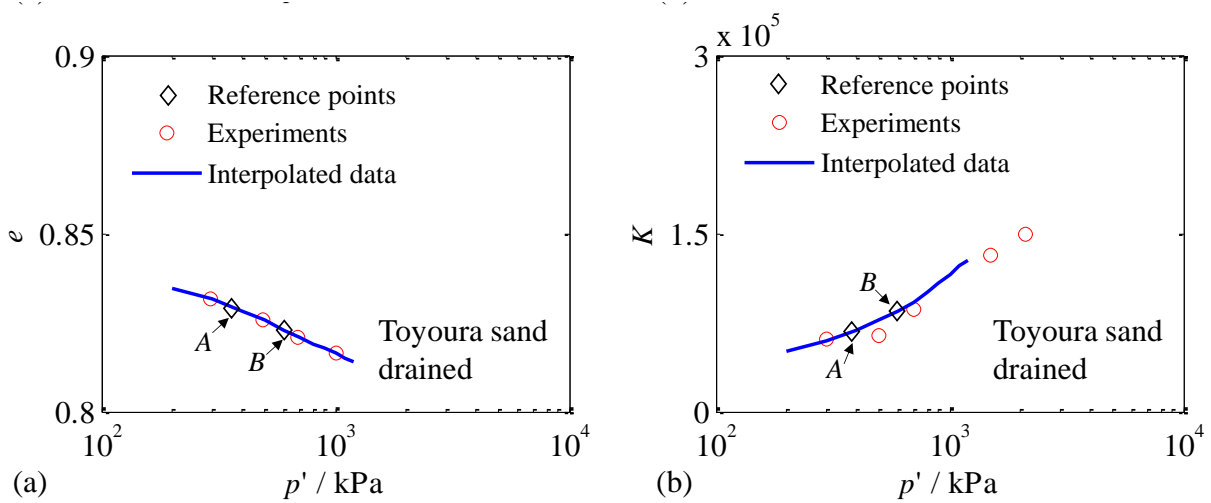


Figure 2.9 Interpreted results from isotropic compression curves of Toyoura sand for calibrating parameters: (a) void ratio versus mean effective stress and (b) Elastic bulk moduli versus mean effective stress

Based on experimental results of three drained triaxial tests, the slope of the critical state line $M_c=1.27$ and corresponding friction angle $\phi_c=31.8^\circ$ were directly measured from the p' - q space. The parameters $e_{ref}=0.937$, $\lambda=0.039$ and $\xi=0.365$ were obtained using MATLAB CODE-2 based on the e - $\ln p'$ space. Figure 2.8 (c and d) shows the results of the calibration for critical state line parameters on Toyoura sand.

Finally, according to the procedure for determining interlocking related parameters, the drained triaxial test ($p'_0=100$ kPa, $e_0=0.831$ shown in Figure. 2.10) was selected to perform the calibration using MATLAB CODE-3 and 4. Using Eq. (2-18), the parameters k_p and n_p were easily obtained by the code and are presented in Table 2.5. Similarly, based on Eq. (2-19), the dilatancy related parameters A_d and n_d were also determined by the code, presented in Table 2.5. The average value of four interlocking related parameters based on three drained tests ($p'_0=100$ kPa, $e_0=0.831$), ($p'_0=100$ kPa, $e_0=0.917$) and ($p'_0=500$ kPa, $e_0=0.960$) were finally determined.

All the determined parameters of the model by the proposed method are summarized in Table 2.6. Besides the test data for calibration, another three drained and six undrained triaxial tests performed on isotropically consolidated Toyoura sand were simulated by SIMSAND model using the determined parameters for the validation. Figures 2.11-2.13 present all the simulations generally in agreement with experimental data. All the comparisons demonstrate the determined parameters by the proposed approach are reasonable and reliable.

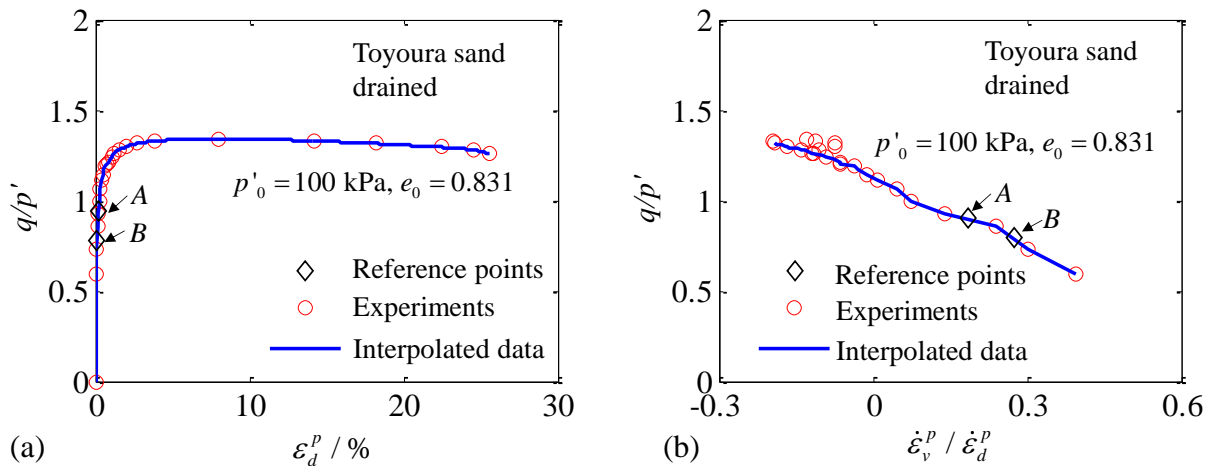


Figure 2.10 Increments of plastic strain of drained triaxial tests on Toyoura sand: (a) stress ratio versus deviatoric plastic strain; (b) stress ratio versus ratio of plastic strain increment

Table 2.5 Calibration of model parameter A_d , n_d , k_p and n_p for Toyoura sand

Tests	ε_a %(A)	ε_a %(B)	n_p	k_p	n_d	A_d
$p_0=100\text{kPa}$, $e_0=0.831$	1	2	1.35	0.0026	1.37	0.57
	1	3	1.38	0.0032	1.57	0.63
	2	3	1.43	0.0032	1.98	0.83
$p_0=100\text{kPa}$, $e_0=0.917$	1	2	5.56	0.0036	5.96	0.59
	1	3	5.67	0.0035	5.66	0.89
	2	3	5.83	0.0033	-	-
$p_0=500\text{kPa}$, $e_0=0.960$	1	2	3.99	0.0045	1.55	0.94
	1	3	3.44	0.0046	1.56	0.91
	2	3	2.78	0.0056	1.57	0.85
Average value of parameters			3.49	0.0038	2.65	0.78

Table 2.6 Summary of model parameters by back calculation procedure for Toyoura sand

Parameters	K_0	G_0	ζ	ϕ_c	e_{ref}	λ	ξ	k_p	A_d	n_p	n_d
Toyoura sand	130	78	0.52	31.8	0.937	0.039	0.365	0.0038	0.78	3.49	2.65

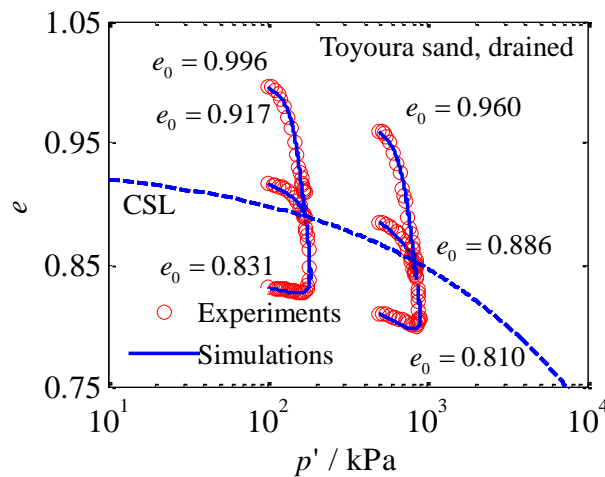


Figure 2.11 Comparison between experiments and simulations for six drained triaxial tests on Toyoura sand under confining stresses of 100 kPa and 500 kPa plotted in void ratio versus mean effective stress space

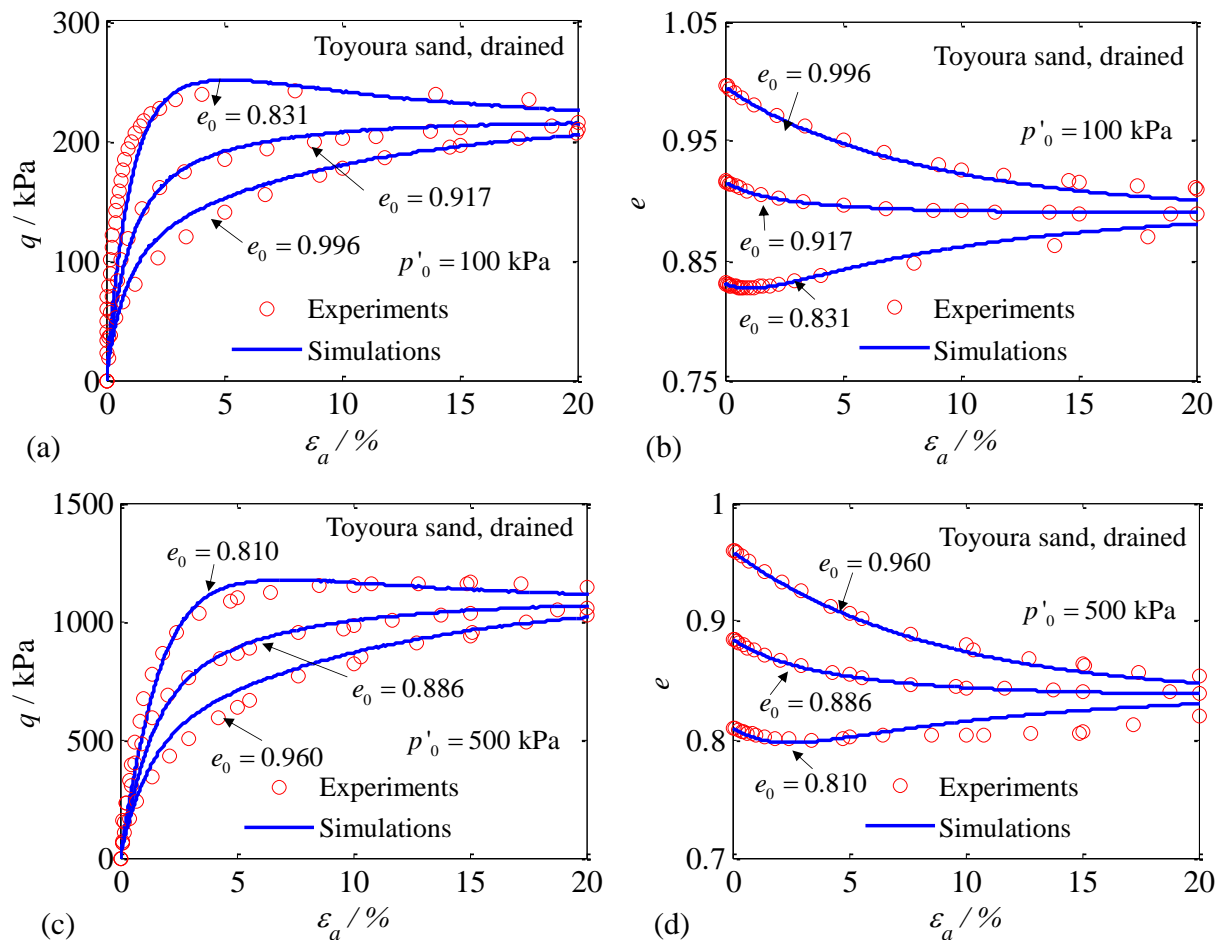
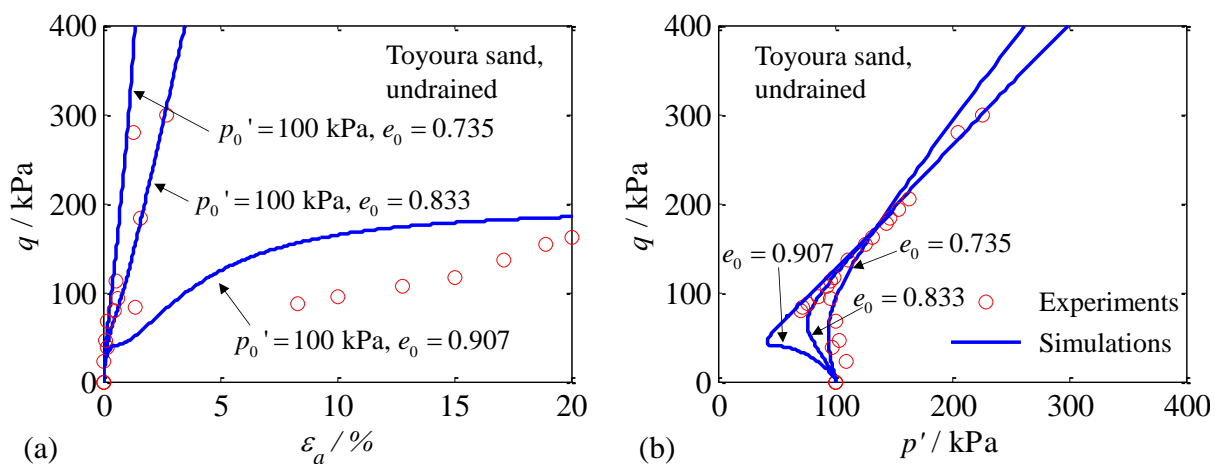


Figure 2.12 Comparison between experiments and simulations for six drained triaxial tests on Toyoura sand under confining stresses of 100 kPa and 500 kPa plotted in (a) and (c) deviatoric stress versus axial strain, (b) and (d) void ratio versus axial strain



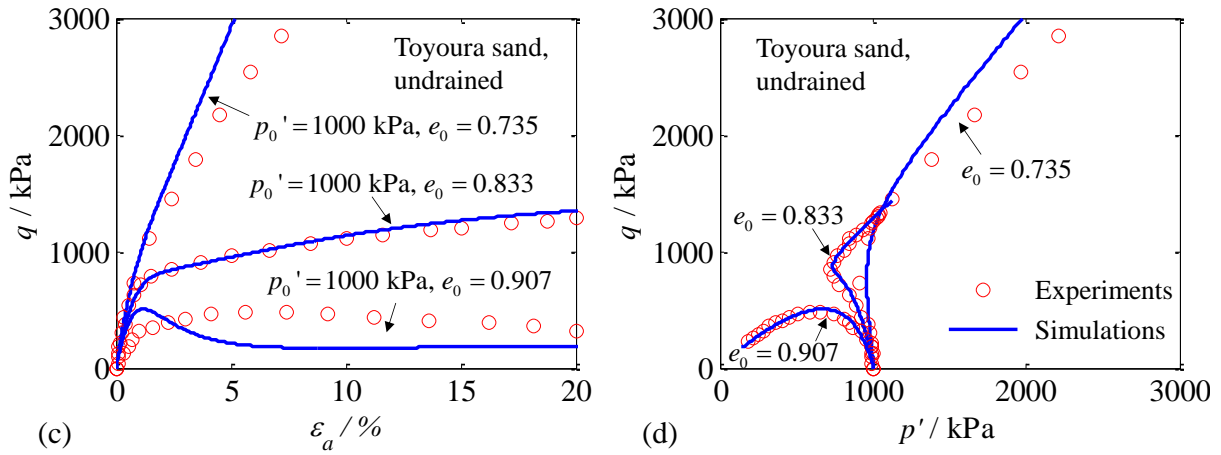


Figure 2.13 Comparison between experiments and simulations of undrained triaxial tests on Toyoura sand under confining stresses of 100 kPa and 1000 kPa plotted in (a) and (c) deviatoric stress versus axial strain, (b) and (d) stress path in mean effective stress and deviatoric stress

2.5 Implementation into a finite element code

2.5.1 Explicit finite element method

The explicit solution method in the commercial FE code ABAQUS can be used to overcome the mesh distortion problems inherent in large deformation analysis, such as the simulation of simple shearing or pile penetrating performed in this study. The explicit solution method, with the code ABAQUS, was thus adopted. The numerical scheme is presented in Figure 2.14 with a brief introduction, as follows:

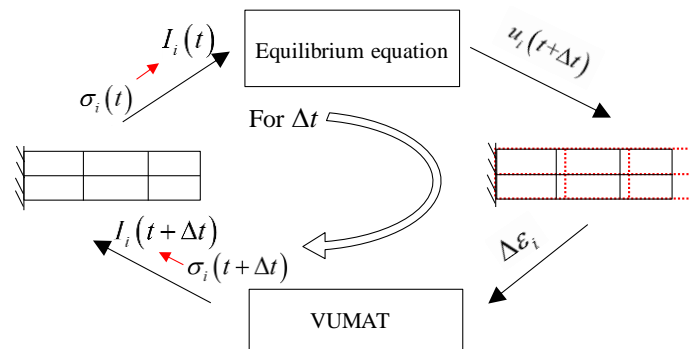


Figure 2.14 Flow chart of explicit finite element analysis based on ABAQUS/Explicit

First, the equilibrium condition is written with the balance of inertial and external force at time t :

$$M\ddot{u}_{(t)} = P_{(t)} - I_{(t)} \quad (2-20)$$

where M is the mass matrix, P is the applied external force vector and I is the internal force vector.

Accelerations and velocities at a particular point, caused by external loads, are assumed to be constant during a time increment. The equations of motion for the body are then integrated using the explicit time-central difference integration rule, which is expressed as follows:

$$\begin{cases} \dot{u}_{(t+\frac{\Delta t}{2})} = \dot{u}_{(t-\frac{\Delta t}{2})} + \frac{\Delta t_{(t+\Delta t)} + \Delta t_{(t)}}{2} \ddot{u}_{(t)} \\ u_{(t+\Delta t)} = u_{(t)} + \Delta t_{(t+\Delta t)} \dot{u}_{(t+\frac{\Delta t}{2})} \end{cases} \quad (2-21)$$

where u is the displacement and the subscript t refers to the time in an explicit dynamic step; \dot{u} is the velocity; and Δt is the increment of time. For the stability of calculation, the time increment Δt , which is smaller than a limited value, is recommended as $\Delta t \approx L_{\min}/c_d$, where L_{\min} is the smallest element dimension of the entire mesh; $c^d = \sqrt{(\lambda + 2\mu)/\rho}$ with Lamé elastic constants λ and μ ; and ρ is the material density.

Then, in our study, the incremental displacements ($\Delta u = \Delta t_{(t+\Delta t)} \dot{u}_{(t+\frac{\Delta t}{2})}$) were used to calculate the incremental strain through compatibility equations, which would be called on by the constitutive model to update stresses, and then inertial forces, up to a new equilibrium condition. More information about the solution can be found in the manual for ABAQUS/Explicit (Hibbitt et al. 2001).

The enhanced SIMSAND model was implemented into ABAQUS/Explicit as a user-defined material model via the user material subroutine VUMAT. The procedure for model implementation followed that of (Hibbitt et al. 2001). In ABAQUS/Explicit, combined with VUMAT, the strain increment on the element $\Delta \varepsilon$ at Δt was initially solved by ABAQUS using the presented explicit time-central-differential integration method. Then, the stress increment $\Delta \sigma$ was updated through VUMAT using the solved $\Delta \varepsilon$ (described as the stress integration in the following paragraphs).

For the stress integration, the cutting plane algorithm, proposed by Ortiz and Simo (1986), was adopted. According to the flow rule, the plastic multiplier $d\lambda$ is the key for obtaining the plastic strain. The direct method for calculating $d\lambda$ is explicit; however, the explicit solution needs a very small incremental step to ensure the accuracy of calculation. The algorithm presented here is semi-implicit, which can yield an accurate result with a bigger step size. Thus, by using this algorithm, the efficiency and effectiveness of the calculation can be improved.

According to (Ortiz and Simo 1986), $d\lambda$ can be expressed as follows:

$$d\lambda = \frac{-f(\sigma_n + d\sigma, \kappa^*)}{-\frac{\partial f}{\partial \sigma} D \frac{\partial g}{\partial \sigma} + \frac{\partial f}{\partial \kappa^*} \frac{\partial \kappa^*}{\partial \varepsilon^p} \frac{\partial g}{\partial \sigma^*}} \quad (2-22)$$

where f is the yield function; g is the potential plastic function; D is the elastic matrix; κ^* is the hardening variable; and ε^p is the plastic strain.

Figure 2.15 shows the schematic diagram of a general cutting plane algorithm. The task contains the calculation procedure of the stress increment, corresponding to a given strain increment. First, a strain increment $\Delta\varepsilon$ is assumed to be elastic and loaded based on the stress point σ_n . Then, the value of yield function f , corresponding to the trial stress point $\bar{\sigma}_{n+1}$, is calculated. If the value of f is smaller than zero, this indicates that the loading state is in the elastic domain. Therefore, the stress is updated according to the generalised Hooke's law. Otherwise, the loading state is transited from the elastic to the elastoplastic domain. The updated stress σ and the hardening parameter κ^* are then calculated using the following equations:

$$\begin{cases} \sigma = \sigma - D d\lambda \frac{\partial g}{\partial \sigma} \\ \kappa^* = \kappa^* + \frac{\partial \kappa^*}{\partial \varepsilon^p} d\lambda \frac{\partial g}{\partial \sigma^*} \end{cases} \quad (2-23)$$

where $d\lambda$ is calculated according to Eq. (2-22). The updated terms are then used to update f along the return path shown in Figure 2.15, until the loop converges when f is smaller than the tolerance error (which is 10^{-7} in this study). The final stress point, with the hardening parameter, is obtained as σ_{n+1} , which is the real stress point corresponding to the strain increment $\Delta\varepsilon$.

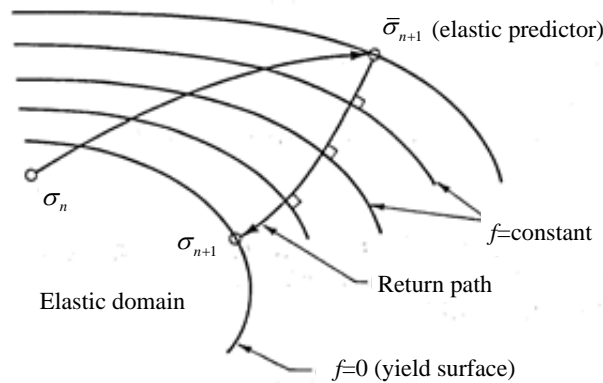


Figure 2.15 Schematic diagram of a general cutting plane algorithm

Using the implicit integration scheme mentioned above, the trial stress is modified under the consideration of plastic strains occurring, until the convergence is reached. The flow chart of the updating procedure is shown in Figure 2.16. Details of derivatives for the solutions described here are summarized in Appendix. Note that in the explicit scheme of ABAQUS, the strain increment is already small, because it skipped the over-relaxation of stress inside the yield surfaces.

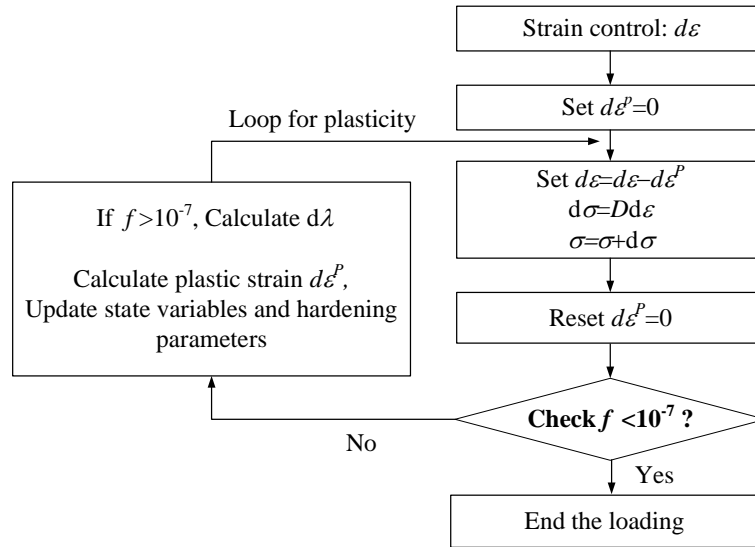


Figure 2.16 Flow chart of the cutting plane algorithm

The derivatives for the numerical integration described in the chapter are briefly presented for numerical analyses. The derivative of yield function on the increment of stress vector can be expressed as

$$\begin{aligned}
 \frac{\partial f}{\partial \sigma_{ij}} &= \frac{\partial f}{\partial p'} \frac{\partial p'}{\partial \sigma_{ij}} + \frac{\partial f}{\partial q} \frac{\partial q}{\partial \sigma_{ij}} \\
 \frac{\partial f}{\partial p'} &= -\frac{q}{p'^2} \\
 \frac{\partial f}{\partial q} &= \frac{1}{p'} \\
 \frac{\partial p'}{\partial \sigma_{ij}} &= \left[\frac{1}{3} \quad \frac{1}{3} \quad \frac{1}{3} \quad 0 \quad 0 \quad 0 \right]^T \\
 \frac{\partial q}{\partial \sigma_{ij}} &= \frac{3s_{ij}}{2q} = \frac{3}{2q} \left[\sigma_{11} - p' \quad \sigma_{22} - p' \quad \sigma_{33} - p' \quad \sigma_{12} \quad \sigma_{13} \quad \sigma_{23} \right]^T
 \end{aligned} \tag{2-24}$$

The derivative of yield function on the harden parameters can be expressed as

$$\frac{\partial f}{\partial \kappa^*} = \frac{\partial f}{\partial \varepsilon_d^p} = \frac{-k_p M_p}{(k_p + \varepsilon_d^p)^2} \quad (2-25)$$

The derivative of hardening parameters on plastic strain can be expressed as

$$\frac{\partial \kappa^*}{\partial \varepsilon^p} = \frac{\partial \varepsilon_d^p}{\partial \varepsilon_d^p} = 1 \quad (2-26)$$

The derivative of potential function on increment of stress vector can be expressed as

$$\begin{aligned} \frac{\partial g}{\partial \sigma_{ij}} &= \frac{\partial g}{\partial p'} \frac{\partial p'}{\partial \sigma_{ij}} + \frac{\partial g}{\partial q} \frac{\partial q}{\partial \sigma_{ij}} \\ \frac{\partial g}{\partial p'} &= A_d \left(M_{pt} - \frac{q}{p'} \right) \\ \frac{\partial g}{\partial q} &= 1 \end{aligned} \quad (2-27)$$

2.5.2 Evaluation by modelling of footings

A series of circular footing model tests on Toyoura sand were performed by Tomita et al. (2012). The footings have a same circular cross section with a diameter $B = 20$ mm and a height of 80 mm. Three footing tests were performed on Toyoura sand with three different relative densities ($e_0 = 0.67, 0.71$ and 0.85). Note that the model tests adopted herein are to highlight the reasonability of the parameters determined by the proposed procedure. In terms of extrapolating results from the model tests to the behaviour of prototype footings, the scale effects of the geometric and stress should be considered (Fellenius and Altaee, 1994). Furthermore, the effect of density (initial void ratio) should also be considered. The effects of density and stress-scale on extrapolating results from the model tests to the behaviour of prototype footings can be simulated through employing the presented SIMSAND model. The effect of the geometric scale can also be simulated by using the FEM method to simulate the real scale of prototype footing.

The axisymmetric finite-element model with 5628 elements for 20B large model was generated, as shown in Figure 2.17 with the same dimension as model tests. Each FE element has four nodes axisymmetric with one reduced integration point (named as CAX4R element in ABAQUS). The footing structure was modelled using rigid body since its deformation is negligible comparing to soil. According to Tomita et al. (2012), the initial stress condition before loading is K_0 condition, and the value of K_0 was set to be 0.48 according to Jaky's formula. The contact between footing structure and soil is of surface-to-surface type with its interface described by the classical Coulomb friction law (the friction coefficient $\mu = \tan(\phi_\mu/2) = 0.28$). The parameters of Toyoura sand determined previously were adopted here for all simulations.

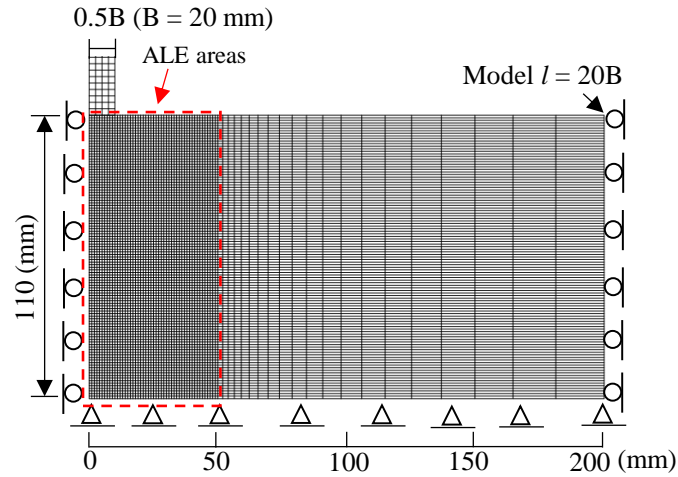


Figure 2.17 Finite element model for footing tests by ABAQUS

Figure 2.18 shows the comparisons of “ q_b - s ” curves between measurements and simulations for footing tests, where q_b represents the bearing load and s is the surface settlement. All the comparisons demonstrate that the predictions of bearing capacity by the model using determined parameters of Toyoura sand by the proposed method are in a good agreement with the measurements. Furthermore, the simulated distributions of mean effective stress by the nonlinear CSL based SIMSAND model for three tests with different initial void ratios are plotted in Figure 2.19. Similar distribution shape can be found in three simulations. But a general lower stress level was obtained for the test of bigger void ratio, which reveals the smaller bearing capacity achieved in Figure 2.18 since the strength of sand is pressure dependent.

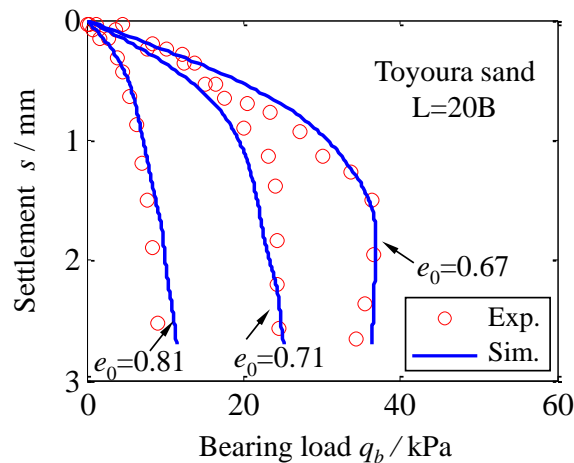


Figure 2.18 Comparison between measurements and predictions of bearing load versus settlement for three footing tests in sand with three different initial void ratios

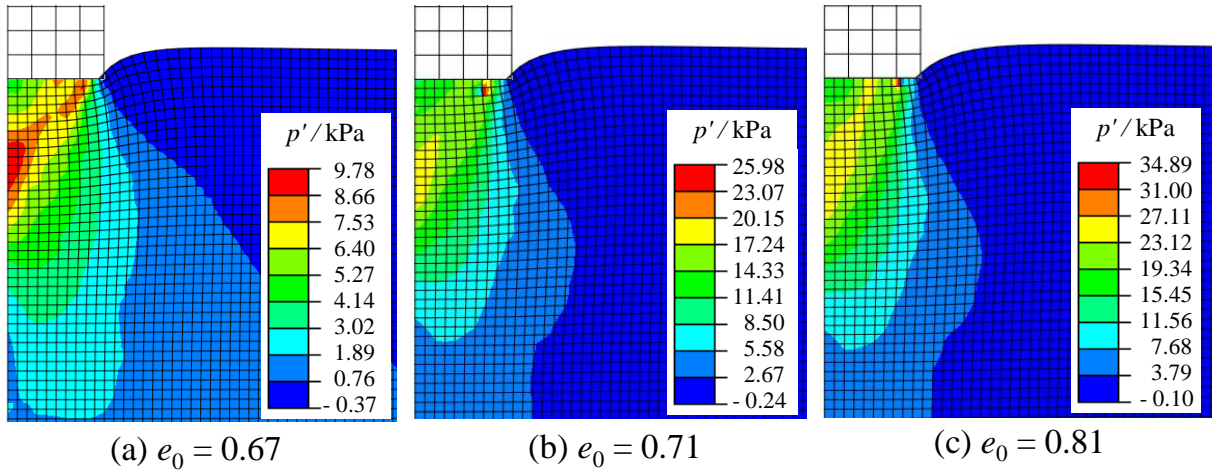


Figure 2.19 Simulated mean effective stress field of three footings at the settlement of 2.8 mm for the initial void ratio of: (a) $e_0=0.67$; (b) $e_0=0.71$; (c) $e_0=0.81$

2.6 Conclusion

A straightforward method for determining parameters was proposed in this chapter. The parameters were analysed based on a simple critical-state based sand model. The whole procedure of parameters determination can be divided into three steps. First, the elasticity related parameters K_0 , ζ and ν were determined by isotropic compression test. Then, the critical state line related parameters ϕ_c , e_{ref} and λ were directly measured based on triaxial tests. Finally, a series of equations for calculating the plasticity interlocking parameters A_d , n_d , k_p and n_p were developed. Based on these equations, the plasticity interlocking related parameters can be determined by using one triaxial test. The whole procedure was coded using MATLAB.

To evaluate the feasibility of the straightforward method, one isotropic compression test and three drained triaxial tests on Toyoura sand were selected for parameters determination. The determined parameters were verified by simulating other three drained and six undrained triaxial tests on the same material. All comparisons between experimental results and numerical simulations demonstrate that the proposed procedure is capable of calibrating the model parameters.

Furthermore, the nonlinear CSL based model is implemented into a finite element code, and numerical modelling of a series of footing tests were performed using the above determined parameters. Overall, the proposed back calculation procedure is validated as an efficient and reliable bridge from critical state based constitutive modelling to finite element analysis.

Chapter 3 Finite element analysis of simple shear test

3.1 Introduction

Simple shear tests have been widely used to assess the shearing strength of soil, as well as to simulate its response under field loading conditions (such as slope, pile driving, landslides and earthquakes). However, some features of these apparatuses remain unclear, which has limited related experimental investigations, as they cannot be directly measured. An assessment of the location of surface failure, the radial stress acting on the lateral boundary and the degree of principal stress/strain rotation are thus some issues related to the simple shear test (Vaid and Sivathayalan 1996; Wijewickreme et al. 2005; Dabeet 2014). Moreover, compared to the ideal simple shear condition, the absence of complementary shear stress on the lateral boundary leads to stress inhomogeneity for cylindrical specimens (Budhu 1984), which complicates laboratory investigations. Therefore, an efficient and effective method should be recommended for estimating the inhomogeneity of a specimen.

The finite element method (FEM) can be considered as an ideal analysis tool for investigating the distribution of stress and strain in soil specimens. Several two-dimensional (2D) simulations have been conducted to reproduce the stress inhomogeneity behaviour in simple shear tests (Budhu and Britto 1987; Dounias and Potts 1993; Wang et al. 2004; Grognet 2011). However, as a result of the 2D plane-strain assumption, which is only suitable for cubical specimens, only limited results and discussions regarding the boundary effects can be provided. Recently, a more advanced three-dimensional (3D) FE modelling was presented by Doherty and Fahey (2011), who used the Modified Cam-Clay model. Only the strength degradation, as caused by the stress inhomogeneity, was investigated using model parameters of Kaolin clay, without considering the anisotropic nature of soil.

In this chapter, a numerical approach for simulating the simple shear test is presented, based on FEM and advanced soil models. A critical-state-based sand model was first enhanced and implemented into the FE code, in which the effect of principal stress rotation during the simple shear process was considered. A series of GDS-type monotonic simple shear tests, on Fontainebleau sand cylindrical specimens, were carried out for the simulations. Then, a 3D FE analysis was conducted to accommodate the real size and boundaries of the GDS-type apparatus. Finally, complementary simple shear simulations were conducted to study the boundary effects on the inhomogeneity in the specimen, for different aspect ratios of a cylindrical specimen.

3.2 Enhanced constitutive model

3.2.1 Basic framework of SIMSAND model

The adopted SIMSAND model was developed based on the Mohr-Coulomb model by implementing the critical state concept with nonlinear elasticity, non-linear plastic hardening, and a simplified three-dimensional strength criterion (Yin et al. 2013; Jin et al. 2016a; Jin et al. 2016c; Wu et al. 2017). The basic constitutive equations are summarized in Table 3.1. The definitions of model parameters were also presented in Chapter 2.2.

Table 3.1 Basic constitutive equations of SIMSAND

Components	Constitutive equations	Parameters
Elasticity	$\delta \varepsilon_{ij}^e = \frac{1}{2G} \delta \sigma'_{ij} - \frac{\nu}{2G(1+\nu)} \delta \sigma'_{kk} \delta_{ij}$ $G = G_0 p_{at} \frac{(2.97 - e)^2}{(1 + e)} \left(\frac{p'}{p_{at}} \right)^\zeta$	K_0 ν ζ
Yield surface in shear	$f_s = \frac{q}{p'} - H$	-
Critical state line	$e_c = e_{ref} \exp \left[-\lambda \left(\frac{p'}{p_{at}} \right)^\xi \right]$	e_{ref} λ ξ
Hardening rule for shear	$H = \frac{M_p \varepsilon_d^p}{k_p + \varepsilon_d^p}$	k_p
Potential surface in shear	$\frac{\partial g_s}{\partial p'} = A_d \left(M_{pt} - \frac{q}{p'} \right); \quad \frac{\partial g_s}{\partial s_{ij}} = \{1 \ 1 \ 1 \ 1 \ 1 \ 1\}$	A_d
Inter-locking effect	$\tan \phi_p = \left(\frac{e_c}{e} \right)^{n_p} \tan \phi_c \quad \tan \phi_{pt} = \left(\frac{e_c}{e} \right)^{-n_d} \tan \phi_c$	ϕ_c n_p n_d
Three-dimensional strength criterion	$M_p = \frac{6 \sin \phi_p}{3 - \sin \phi_p} \left[\frac{2c_1^4}{1 + c_1^4 + (1 - c_1^4) \sin 3\theta} \right]^{\frac{1}{4}} \quad \text{with } c_1 = \frac{3 - \sin \phi_p}{3 + \sin \phi_p}$ $M_{pt} = \frac{6 \sin \phi_{pt}}{3 - \sin \phi_{pt}} \left[\frac{2c_2^4}{1 + c_2^4 + (1 - c_2^4) \sin 3\theta} \right]^{\frac{1}{4}} \quad \text{with } c_2 = \frac{3 - \sin \phi_{pt}}{3 + \sin \phi_{pt}}$	-

3.2.2 Consideration of soil anisotropy

Fabric anisotropy has been widely recognised as affecting the strength of granular material (Oda 1972; Miura et al. 1986; Oda and Nakayama 1989; Yao and Kong 2011; Gao and Zhao 2012, 2017). A simple methodology was adopted to enhance the model by incorporating a parameter of a cross-anisotropy joint invariant during the simple shear condition, to extend the original isotropic strength to an anisotropic strength in sand. In this

method, the fabric tensor F_{ij} , as proposed by (Oda and Nakayama 1989), is used to describe the degree of cross anisotropy:

$$F_{ij} = \begin{bmatrix} F_z & 0 & 0 \\ 0 & F_x & 0 \\ 0 & 0 & F_y \end{bmatrix} = \frac{1}{3+\Delta} \begin{bmatrix} 1-\Delta & 0 & 0 \\ 0 & 1+\Delta & 0 \\ 0 & 0 & 1+\Delta \end{bmatrix} = \frac{1}{3} \begin{bmatrix} 1 & 0 & 0 \\ 0 & 1 & 0 \\ 0 & 0 & 1 \end{bmatrix} + \frac{2\Delta}{9+3\Delta} \begin{bmatrix} -2 & 0 & 0 \\ 0 & 1 & 0 \\ 0 & 0 & 1 \end{bmatrix} \quad (3-1)$$

where Δ is a parameter to describe the fabric anisotropic distribution of granular material, with $0 < \Delta < 1$ being a typical range for sand.

The joint invariant A was adopted based on the theory of tensor (Wang 1970), which was formulated to relate the deviatoric part of the fabric tensor and deviatoric stress tensor:

$$A = \frac{s_{ij}d_{ij}}{\sqrt{s_{mn}s_{mn}}\sqrt{d_{mn}d_{mn}}} \quad (3-2)$$

where s_{ij} ($= \sigma_{ij} - p' \delta_{ij}$) is the deviatoric stress tensor, d_{ij} ($= F_{ij} - F_{kk} \delta_{ij} / 3$) is the deviatoric part of the fabric tensor and δ_{ij} is the Kronecker delta.

The incorporation of the anisotropic strength technique in this chapter is similar to that seen in (Li and Dafalias 2002; Gao and Zhao 2012), in which the effect of the anisotropy function was introduced into the strength criterion. The anisotropic interpolation function was formulated by the joint invariant A and cross anisotropy parameter Δ . The original isotropic peak strength M_p and phase transformation strength M_{pt} were modified by the anisotropic correction function, as follows:

$$M'_p = M_p \exp[g(A, \Delta)], \quad M'_{pt} = M_{pt} \exp[g(A, \Delta)] \quad (3-3)$$

where $g(A, \Delta)$ is an anisotropic interpolation function, which was employed in a similar form by Pietruszczak and Mroz (2000, 2001) as per Eq. (3-4):

$$g(A, \Delta) = -c_1 \cdot \Delta \cdot (1 + A) = -\tilde{c}_1 \cdot (1 + A) \quad (3-4)$$

where c_1 denotes a material parameter. For an isotropic sand sample, $\Delta = 0$, $g(A, \Delta) \equiv 0$. For a cross-anisotropic sand sample with $0 < \Delta < 1$, $g(A, \Delta)$ varies with the change of A and Δ . In most applications, the degree of fabric anisotropy Δ may not be conveniently measured. To address this difficulty, the combined term $c_1 \cdot \Delta$ was considered as a single material parameter as $\tilde{c}_1 = c_1 \cdot \Delta$, and thus only \tilde{c}_1 requires to be calibrated instead of determining the exact value of Δ .

In addition, experimental comparisons between triaxial and simple shear tests by Vaid and Sivathayalan (1996) showed that the shear stiffness of simple shear tests is smaller than

that observed in triaxial tests. The main reason for this degradation of shear stiffness is the anisotropy of stress during the principal stress rotation process because of a simple shearing stage. This degradation was modelled by Yang and Yu (2006a, b; 2010) by introducing a non-coaxial plastic strain. In our critical-state-based model, the shear stiffness depended on the parameter k_p controlling the slope of the hyperbolic curve $q/p - \varepsilon_d^p$ as seen in Table 3.1. Therefore, an anisotropic correction function was proposed to multiply parameter k_p , (Eq. (3-5)), to deduce the shear stiffness with the development of principal stress rotation:

$$k'_p = k_p \cdot \exp[\tilde{c}_2 \cdot (1 + A)] \quad (3-5)$$

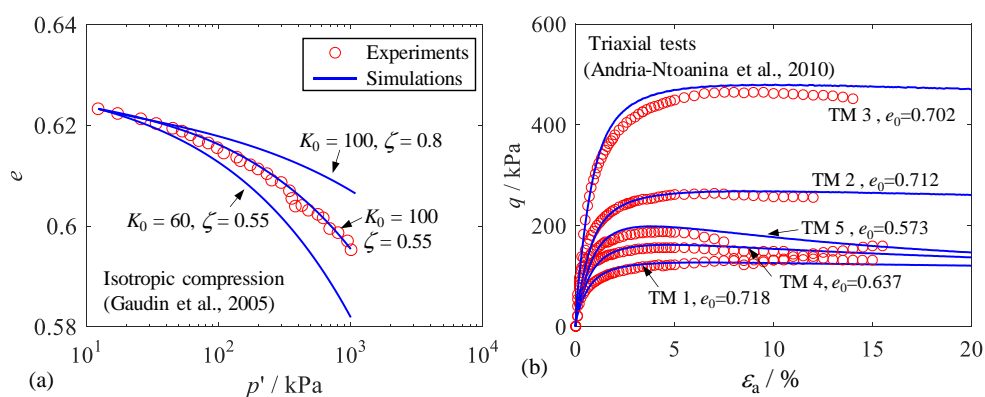
where \tilde{c}_2 is a material parameter.

Then, M_p , M_{pt} and k_p in the SIMSAND model were replaced by M'_p , M'_{pt} and k'_p to reflect the effects of principal stress rotation on the mechanical behaviour of sand.

3.2.3 Calibration of the model from triaxial tests on Fontainebleau sand

Because, in this study, NE34 Fontainebleau sand was used for simple shear tests, a series of conventional triaxial tests (Benahmed 2001; Andria-Ntoanina et al. 2010) and an isotropic compression test (Gaudin et al. 2005) were selected to assess the parameters determination, as shown in Figure 3.1. The determination is based on one isotropic compression test and five drained triaxial tests.

The parameters K_0 and ζ were determined by fitting the isotropic compression test conducted by Gaudin et al. (2005) with $K_0 = 100$ and $\zeta = 0.55$, as shown in Figure 3.1(a). $G_0 = 60$ was calculated based on $G_0 = 3K_0(1-2\nu)/2(1+\nu)$, taking a typical value of Poisson's ratio: $\nu = 0.25$.



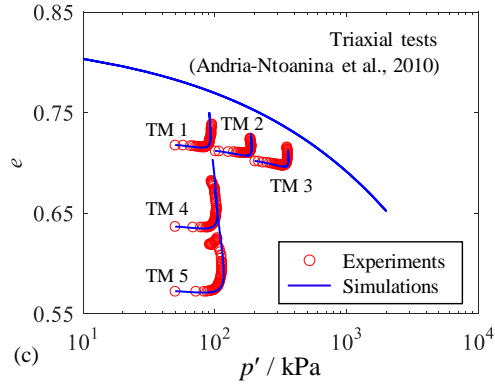


Figure 3.1 Parameters determination from isotropic compression and triaxial drained tests on Fontainebleau NE34 sand: (a) isotropic compression line, (b) deviatoric stress versus axial strain, and (c) void ratio versus mean effective stress

A series of drained triaxial tests, under low confining pressures up to 400 kPa (marked as TM1~TM11 in Table 3.2), were performed on NE34 Fontainebleau sand; by (Andria-Ntoanina et al. 2010) and are then selected. The friction angle $\phi = 33.2^\circ$ was measured from the p' - q plot, according to the experimental results. The parameters e_{ref} , λ and ξ , controlling the position of CSL, and k_p , A_d , n_p and n_d , accounting for the shear sliding, can be determined by try-error or a more straightforward means (Wu et al. 2017). Note that the test data only extend to an axial strain of 10%; because the shear bands in the samples prevent to reach critical states. Thus, an optimisation-based inverse analysis was adopted in this case to identify all these model parameters by selecting five objective tests “TM1~TM5”. Details of the optimisation procedure can be found in Jin et al. (2016a, b, c), in which studies it was successfully applied to different soils using the same kind of tests as objectives.

Table 3.2 Drained triaxial tests on Fontainebleau sand with different void ratios

Tests	TM1	TM2	TM3	TM4	TM5	TM6	TM7	TM8	TM9	TM10	TM11
e_0	0.718	0.712	0.702	0.637	0.573	0.637	0.638	0.636	0.584	0.573	0.571
σ_c / kPa	50	100	200	50	50	100	200	400	100	200	400

The values of parameters were summarized in Table 3.3 for later simulations of simple shear tests. Other drained triaxial tests, shown in Table 3.2, and undrained triaxial tests as performed by Benahmed (2001), were simulated using the identified parameters. Figure 3.2 shows the comparison between experimental and numerical results for drained triaxial tests on medium-density and high-density sand under confining stresses of 100kPa, 200kPa and 400kPa. Figure 3.3 shows the comparison for the undrained triaxial tests, under confining stresses of 100kPa (TMFO1), 200kPa (TMFO2) and 400kPa (TMFO3), on very loose Fontainebleau sand samples ($e_0 \cong 0.89$). All comparisons demonstrate a good performance of

the predictive ability of the model for sand with variable initial densities under different confining stresses.

Table 3.3 Summary of model parameters for Fontainebleau sand

Group	Elastic			CSL				Shearing-sliding			
Parameters	K_0 /kPa	ν	ζ	e_{ref}	λ	ξ	$\phi_c / ^\circ$	k_p	A_d	n_p	n_d
Values	100	0.25	0.51	0.811	0.055	0.46	33.2	0.0022	0.39	1.9	4

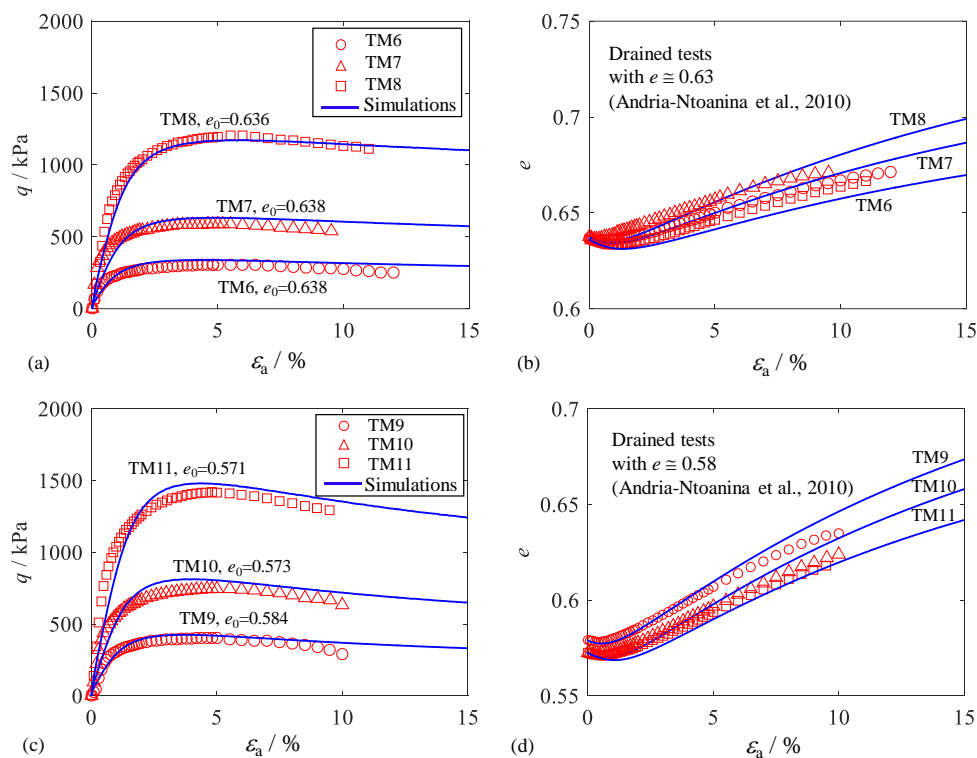


Figure 3.2 Simulation results of triaxial drained tests on medium dense and very dense Fontainebleau sand: (a, c) deviatoric stress versus axial strain; (b, d) deviatoric stress versus void ratio

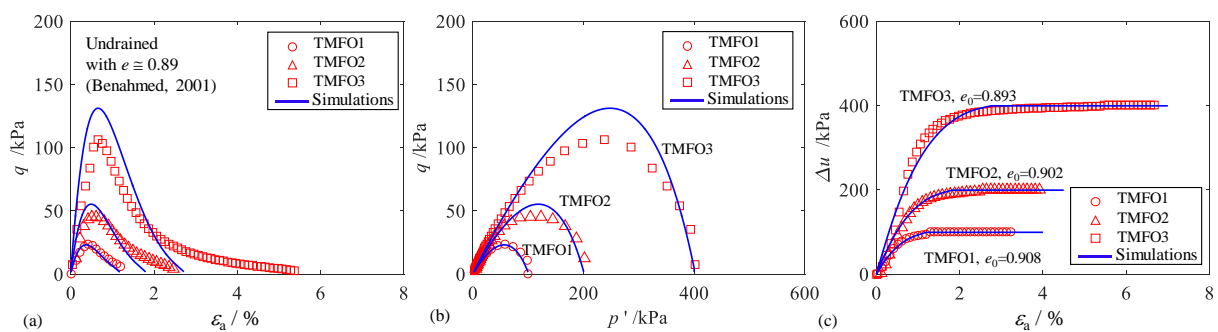


Figure 3.3 Simulation results of triaxial undrained tests on very loose Fontainebleau sand: (a) deviatoric stress versus axial strain; (b) deviatoric stress versus mean effective stress for undrained tests; (c) pore pressure versus axial strain for undrained

3.2.4 Sensitivity of anisotropic parameters at simple shear condition

The parametric analysis was conducted based on the ideal simple shear condition, in the interests of studying the sensitivity of the incorporated parameters (\tilde{c}_1 and \tilde{c}_2), which can be identified based on experimental results of the simple shear tests. Figure 3.4 shows the simulated results, considering the parameters of Fontainebleau sand NE34 in Table 3.3, with different values of parameters \tilde{c}_1 and \tilde{c}_2 . This shows that the parameter \tilde{c}_1 controls the degradation rate of shear strength, while \tilde{c}_2 controls the degradation rate of shear stiffness. Lower shear strength and dilatancy were obtained when increasing \tilde{c}_1 , as shown in Figure 3.4(a-c), while a lower shear stiffness and dilatancy were attained by increasing \tilde{c}_2 , as shown in Figure 3.4(d-f).

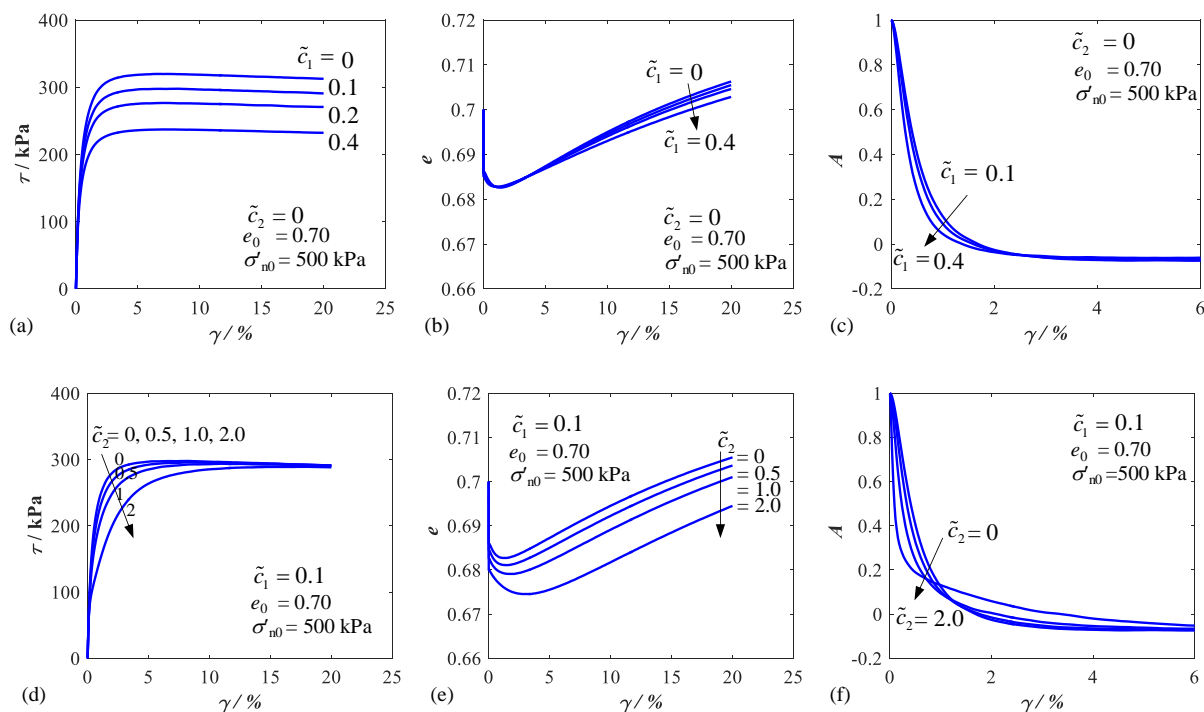


Figure 3.4 Model simulation for stress strain relation based on incorporation parameters, (a, b, c) constant a with different \tilde{c}_1 ; (d, e, f) constant \tilde{c}_1 with different a

3.3 Finite element analysis of simple shear tests

3.3.1 Laboratory simple shear tests

To validate the FE approach with the enhanced model, some simple shear tests were conducted using a commercial GDS Instruments simple shear apparatus, the design of which is close to that of its NGI counterpart (Bjerrum and Landva 1966; Hooker 2002). The tested material was Fontainebleau sand NE34, a fine siliceous sand with sub-rounded grains (Figure 3.5), which is a reference material in France for geotechnical applications, and the same as that used in triaxial tests by (Aghakouchak et al. 2015; Pra-ai and Boulon 2017). Its main

characteristics, summarized in Table 3.4, are a mean grain size of about 210 μm , a coefficient of uniformity of 1.53, minimum and maximum void ratios of 0.510 and 0.882, respectively, a specific weight of 26.00 kN/m^3 (Andria-Ntoanina et al. 2010; Pra-Ai 2013).

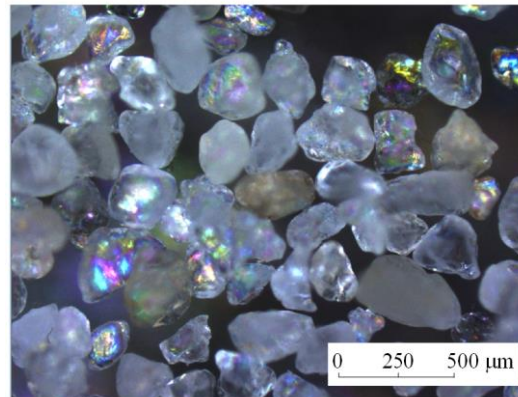


Figure 3.5 Particle shape of Fontainebleau sand

Table 3.4 Physical properties of standard Fontainebleau sand

Grain shape	S_iO_2 : %	D_{50} (mm)	$C_u(D_{60}/D_{10})$	G_s	e_{max}	e_{min}
Sphericity	99.70	0.21	1.53	2.65	0.882	0.510

The servo-controlled system is capable of conducting stress- or strain-controlled loading paths in both horizontal and vertical directions. The basic features of this apparatus are summarised in Figure 3.6: (i) the cylindrical specimens were reconstituted with a size of $D_0 = 70$ mm in diameter and $H_0 = 25$ mm in height (aspect ratio of $H_0/D_0 = 0.36$); (ii) the specimens were confined in a soft butyl membrane with a thickness of 0.2 mm, itself placed against stacks of rigid circular Teflon-coated thin rings (1 mm each) with 70 mm inner diameter, which maintained a constant cross-sectional area but allowed simple shear deformation; (iii) on both the top and bottom sides of the specimen, the sand was in contact with rough sintered stainless steel plates to prevent any sliding between the pedestals and the specimen.

A series of monotonic constant volume and constant normal stress simple shear tests were carried out, as shown in Table 3.5. The constant volume condition (“undrained condition”) was ensured by constraining the height of the specimen to a constant value after K_0 -consolidation. Note that all the tests were done in dry conditions. The constant normal stress condition (“drained condition”), meanwhile, was attained by constraining the normal stress on the top surface of the specimen following the K_0 -consolidation. All the experimental results were later used for FE analysis.

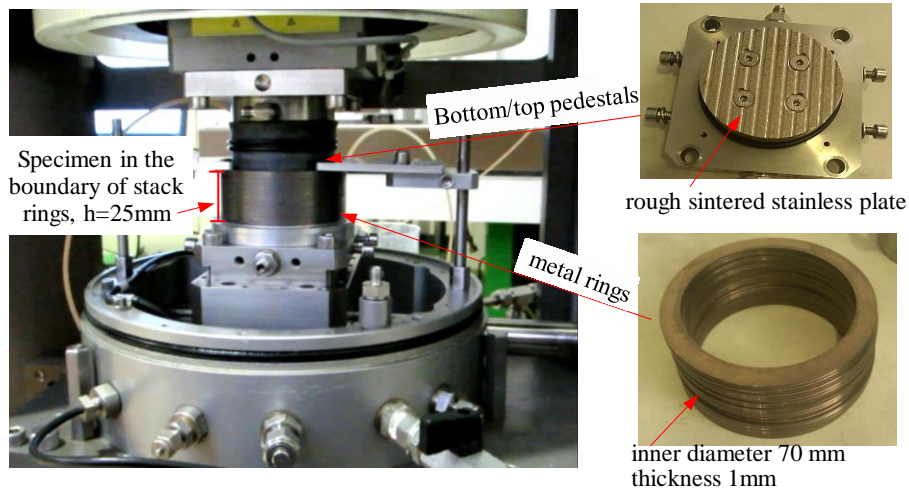


Figure 3.6 Details of cylindrical boundary for simple shear specimen

Table 3.5 Summary of monotonic simple shear tests on Fontainebleau sand

No.	Loading type	e_0 (initial)	e' (after K0)	σ'_{n0} (kPa)
S-1	Constant normal stress	0.70	0.691	104
S-2	Constant normal stress	0.70	0.688	208
S-3	Constant normal stress	0.70	0.678	416
S-4	Constant volume	0.68	0.666	208
S-5	Constant volume	0.68	0.654	416

3.3.2 Finite element modelling

The simple shear test was modelled in 3D, as shown in Figure 3.7. In other words, the model had the same size than the GDS simple shear apparatus presented in Figure 3.6. Owing to symmetry, only half of the cylinder specimen was modelled and a total of 11,000 elements were discretised for the cylinder specimen by the form of C3D8R elements in ABAQUS, as shown in Figure 3.7(c-d). The metal rings and top/bottom plates were considered as the boundaries of the column specimen and modelled as a rigid body. The metal rings had an inner diameter of 70 mm and a thickness of 1 mm, while the top and bottom plates were both 70 mm in diameter and 2.5 mm in thickness. A total of 29 rigid rings were stacked and used to restrain the lateral displacement of the specimen, and two rigid (top and bottom) plates were used to restrain its vertical displacement. The frictionless contact was applied between the cylinder specimen and rigid boundaries (rings and frictional pedestals). The top and bottom surfaces of the specimen were coupled respectively to the top and bottom rigid plates to prevent any sliding between them and the specimen.

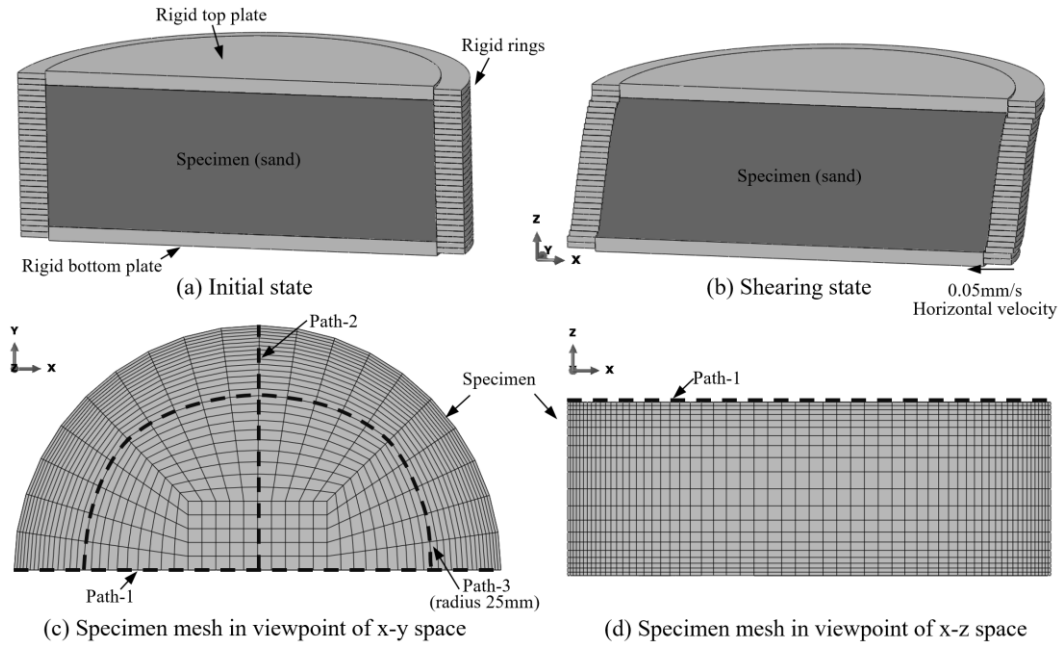


Figure 3.7 Three-dimensional FEM model for simple shear tests: (a) initial state, (b) shearing state, (c) mesh in viewpoint of x-y space, (d) mesh in viewpoint of x-y space.

Two steps, the K_0 consolidation and shearing processes respectively, were conducted to simulate the simple shear test. In the first step (K_0 consolidation), forces equal to 0.2kN, 0.4kN and 0.8kN were applied on the top plate respectively to generate the initial normal stress (σ'_{n0}) corresponding to 104kPa, 208kPa and 416kPa respectively. Then, for the shearing process, the simulation was conducted by moving the bottom plate at a rate of 0.05 mm/s, while the top plate was fixed to zero velocity rate in x and y directions. A total time of 100s was spent to produce a 20% shear strain. The boundary conditions of the simulation were considered similar to the physical laboratory-based GDS simple shear test. The constant normal stress simple shear tests were simulated by maintaining the constant normal force on the top plate; the constant volume simple shear tests were simulated by keeping the specimen at a constant height during the shearing process.

The measurement approach for the displacement and force was similar to that for the physical laboratory test. The effective normal stress σ'_n and shear stress τ were obtained by calibrating the vertical and horizontal force respectively, which are measured on the bottom plate. The shear strain γ was obtained as $\gamma = \Delta d / H_c$ (where H_c is the sample height at the start of the shearing and Δd is the horizontal displacement). The stress states, along with the x-axis (Path-1), y-axis (Path-2), and 25 mm radius circle (Path-3), were monitored respectively to assess the stress inhomogeneity during the shear process, as shown in Figures 3.7(c-d).

The simple shear test, conducted with the constant normal stress condition with an initial state ($\sigma'_{n0} = 104$ kPa, $e_0 = 0.7$ as S-1), was simulated based on the FE model to calibrate the incorporated parameters (\tilde{c}_1 and \tilde{c}_2) for Fontainebleau sand. In addition, similar simulation

without such incorporation (as $\tilde{c}_1 = 0$ and $\tilde{c}_2 = 0$) was also conducted to highlight the model's performance when incorporating parameters \tilde{c}_1 and \tilde{c}_2 . The simulations and experiments are compared in Figure 3.8, which shows that the simulated results with the incorporation of the parameters $\tilde{c}_1 = 0.18$ and $\tilde{c}_2 = 2.0$ were generally in agreement with the experimental results. Thus, the values of the calibrated incorporation parameter ($\tilde{c}_1 = 0.18$ and $\tilde{c}_2 = 2.0$) will be used for subsequent simulations of monotonic simple shear tests.

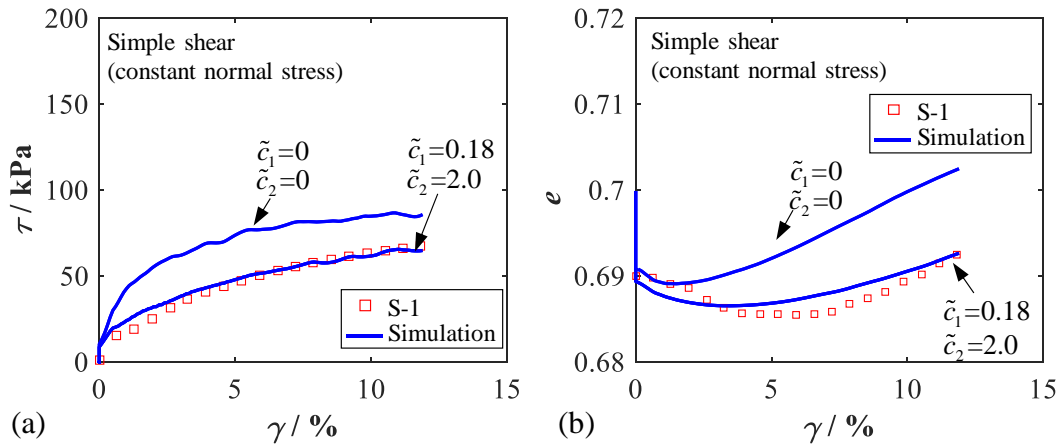


Figure 3.8 Calibration of anisotropic parameters: (a) shear strain versus shear stress (b) shear strain versus void ratio

3.3.3 Test validation

To validate the performance of the FE analysis with the enhanced model, four additional monotonic simple shear tests, presented in Table 3.5, were respectively simulated based on the 3D full simple shear model (Figure 3.7). Figure 3.9 presents the comparisons between simulations and experiments, including constant normal stress and constant volume conditions. The monotonic behaviour (contraction or dilation), for both constant normal stress and constant volume conditions, can generally be captured based on the 3D full size simple shear model. Therefore, the stress inhomogeneity for specimens can be analysed based on the FEM simulation results which are associated with difficulties to direct investigations in the laboratory (Budhu 1984).

3.3.4 Distribution of normal stress

Figure 3.10 presents the evolution of the vertical stress distribution along three paths on the top surface of the specimen for the constant normal stress simple shear test (test S-3). These three paths were described previously in Figure 3.7, which were used to assess the stress inhomogeneity along the x-axis (Path-1), the y-axis (Path-2) and the circle with 25 mm radius (Path-3). During the shearing process, the stress inhomogeneity increases with shear strain level, and the lowest and highest vertical stresses are located in the lateral (right and

left) boundaries. The results also indicate that the vertical stress can remain almost constant in the centre zone of the specimen.

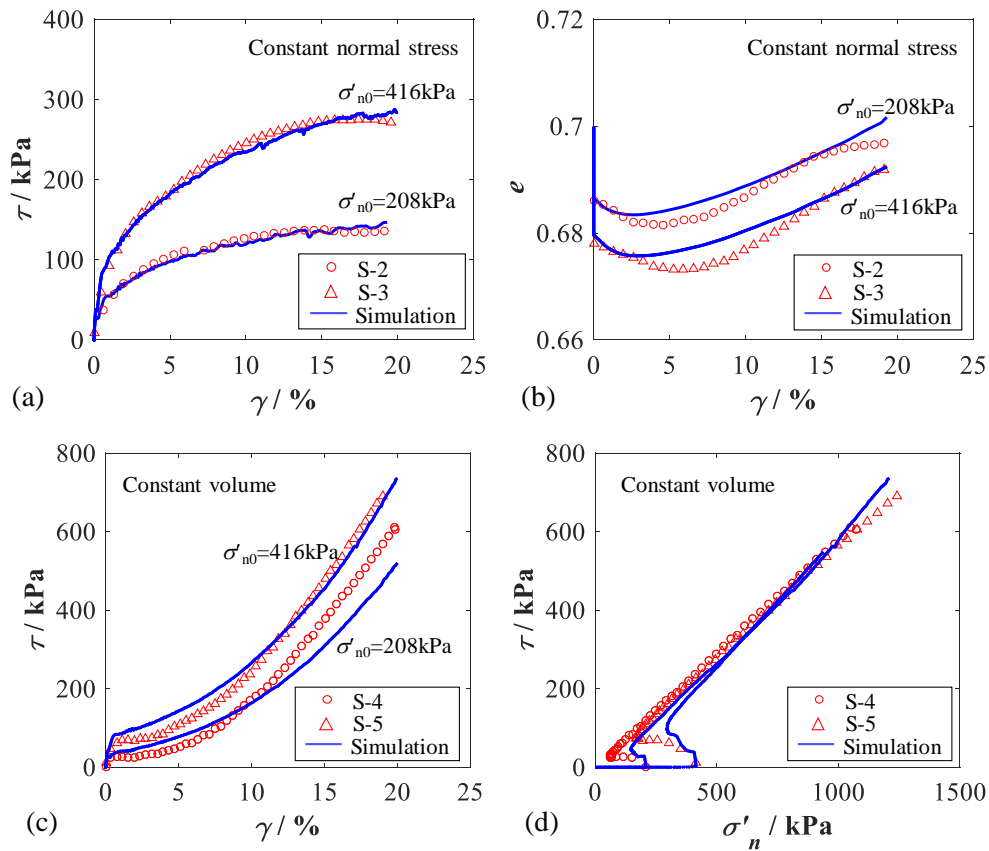


Figure 3.9 Simulation results by ideal and full three-dimensional simple shear tests (a) constant normal stress simple shear in γ - τ space; (b) constant normal simple shear in γ - e space; (c) constant volume simple shear in γ - τ space; (d) constant volume simple shear in σ'_n - τ space.

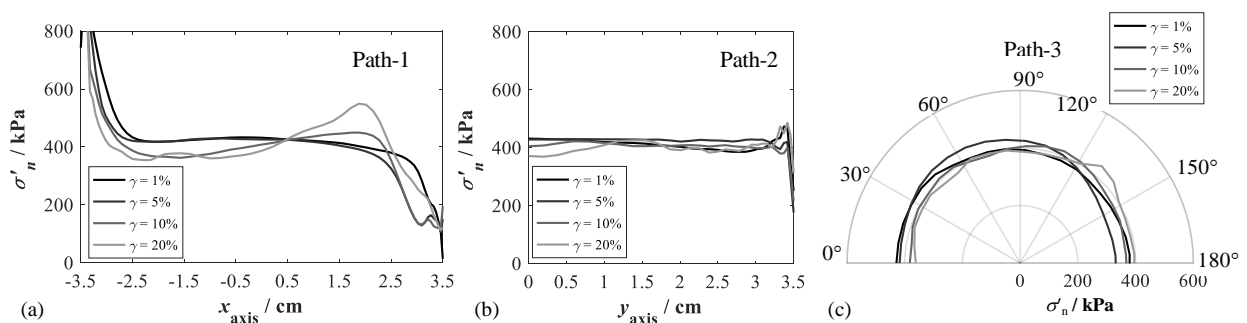


Figure 3.10 The distribution of vertical effective stress for constant normal stress test S-3 (a) along with path-1, (b) along with path-2 and (c) along with path-3

The distribution of vertical stress for constant volume tests (test: S-5) is also presented in Figure 3.11. Unlike the constant normal stress condition, as a result of the boundary condition of constant volume, the vertical stress will first decrease at a relatively low shear strain level (contraction) and then increase (dilation). Compared to the constant normal stress test, similar

behaviour of vertical distribution can be found in that the lowest and highest value are also located in the lateral boundaries and fairly uniformly located in the centre zone.

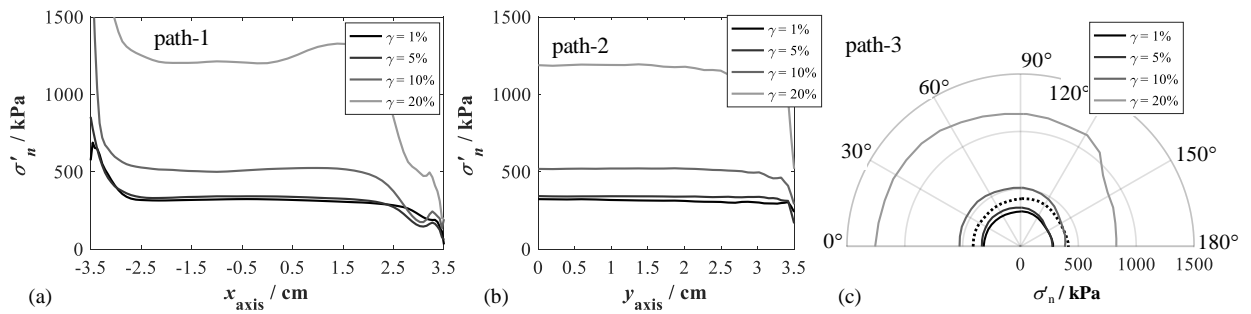


Figure 3.11 The distribution of vertical effective stress for constant volume test S-5 (a) along with path-1, (b) along with path-2 and (c) along with path-3

To study the stress inhomogeneity caused by the absence of complementary shear stress on the lateral boundary, a total of 11,000 Gauss points were summarised based on the total number of discretized elements of FEM modelling. Figure 3.12 illustrates the normal distributions (see Eq.(3-6)) of vertical stress σ'_z based on all Gauss points in the FEM during the shearing process for both constant normal stress and constant volume simple shear tests:

$$f(x | \mu, \sigma^2) = \frac{1}{\sqrt{2\pi\sigma^2}} \exp\left(-\frac{(x-\mu)^2}{2\sigma^2}\right) \quad (3-6)$$

where $f(x)$ is the probability density function, μ the mean of the distribution of sample x and σ the standard deviation, in which the sample x corresponds to the vertical stress σ'_z , shear stress τ , deviatoric plastic strain ε_d^p or the anisotropic variable A in probability analysis.

For the constant normal stress simple shear test, the mean value μ corresponds to the mean vertical stress σ'_z , which remains stable and close to the initial normal stress (as $\sigma'_n = 416\text{kPa}$). The deviation σ corresponds to the degree of stress inhomogeneity, which gradually increases with the increase of shear strain, as shown in Figure 3.12(a-d). In addition, a similar evolution of stress inhomogeneity (the standard deviation increases with the shear strain γ) can also be found based on the constant volume simple shear test, as demonstrated in Figure 3.12(e-h).

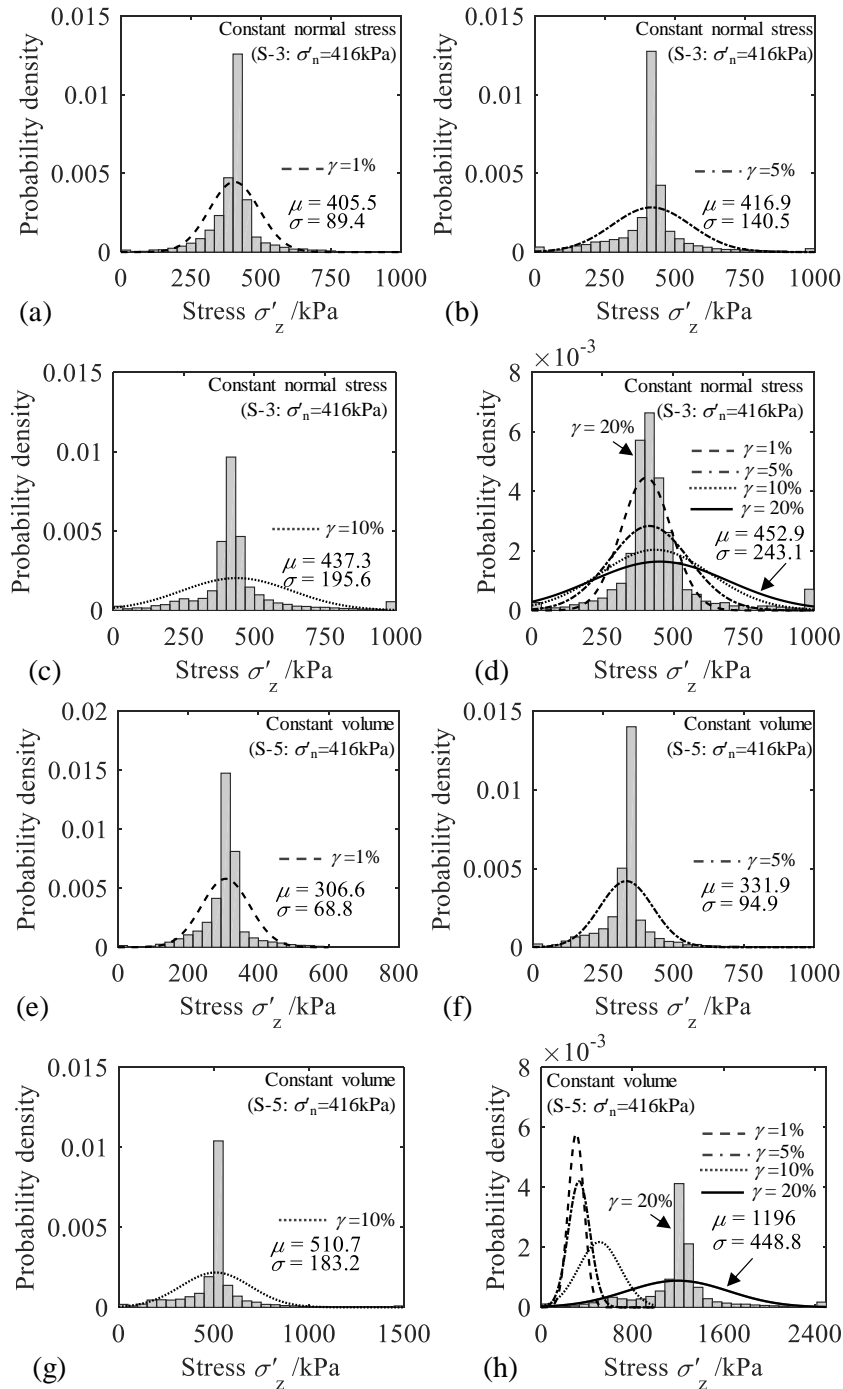


Figure 3.12 Normal distribution of vertical stress σ'_z with constant normal stress condition (a) $\gamma=1\%$, (b) $\gamma=5\%$, (c) $\gamma=10\%$ and (d) $\gamma=20\%$; and with constant volume condition (e) $\gamma=1\%$, (f) $\gamma=5\%$, (g) $\gamma=10\%$ and (h) $\gamma=20\%$.

3.3.5 Distribution of shear stress, deviatoric plastic strain and anisotropic variable

Based on the simulation results of the constant normal stress test (test: S-3), the evolutions of shear stress τ (corresponding to σ'_{xz} in FE simulation), deviatoric plastic strain ε_d^p and the anisotropic variable A are presented in Figure 3.13. For the early shearing stage (stress strain γ below or equal to 1%), the shear stress, deviatoric plastic strain and anisotropic variable A were fairly homogeneous into the specimen, especially in the central or middle

zones. For the shearing stage over 5% stress strain, the peak value of shear stress gradually spreads from the upper left and lower right corners to the central zone. A diagonal separation zone of deviatoric plastic strain ε_d^p can be found in the specimen. In addition, because of the absence of friction between the lateral boundaries and specimen, shear stress τ and deviatoric plastic strain ε_d^p at lateral boundaries are almost zero during shearing process, which could be the reason behind stress/strain inhomogeneity, leading to progressive failure. These simulated tendencies of diagonal accumulated zones of shear stress τ and deviatoric plastic strain ε_d^p are similar to those of the physical failure zone recorded by radiographs (Budhu 1984, 1988).

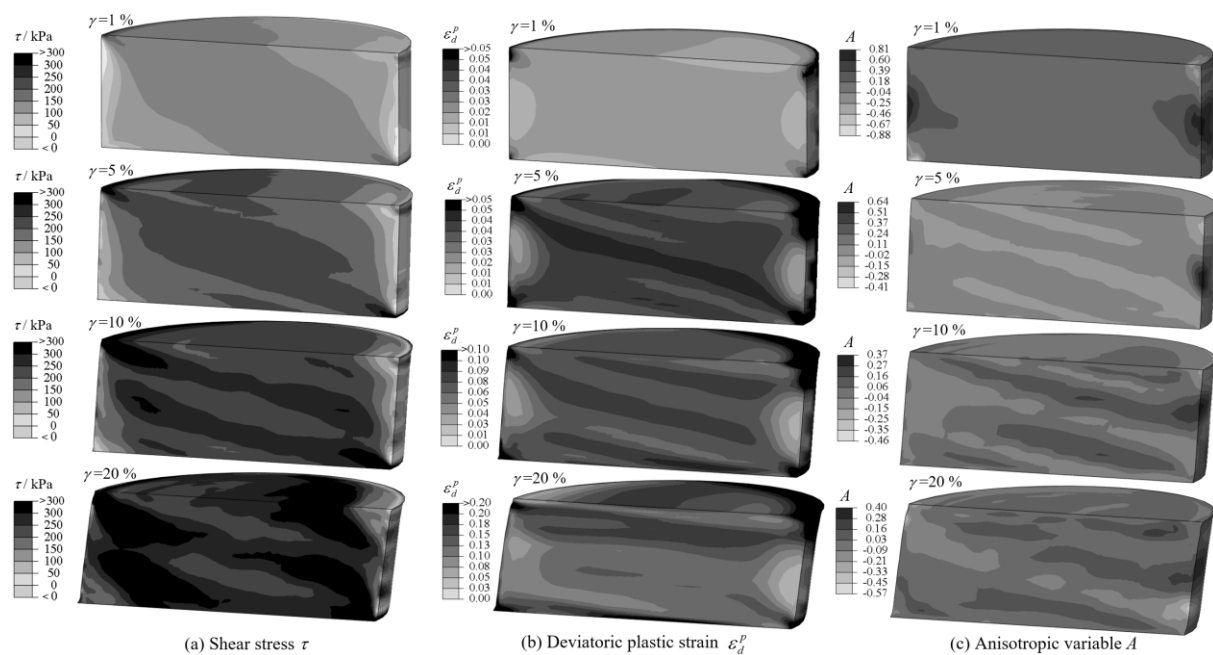


Figure 3.13 Profiles of successive simple shearing process for constant normal stress condition at $\sigma_n = 416\text{kPa}$: (a) contours of shear stress τ , (b) contours of deviatoric plastic strain ε_d^p ; (c) contours of anisotropic variable A .

Figure 3.14 presents the profiles of shear stress τ , deviatoric plastic strain ε_d^p and anisotropic variable A for the constant volume simple shear (test: S-5). Similarly to the profiles obtained by the constant normal stress tests (test: S-3), a diagonal zone of accumulated deviatoric plastic strain ε_d^p is formed from the upper left to lower right corners. Because of the boundary condition of constant height for the specimen, this accumulation of deviatoric plastic strain ε_d^p in the diagonal zone was more obvious than in the constant normal stress condition. The anisotropic variable A was also accumulated along the diagonal zone in the specimen, as shown in Figures 3.13(c) and 3.14(c).

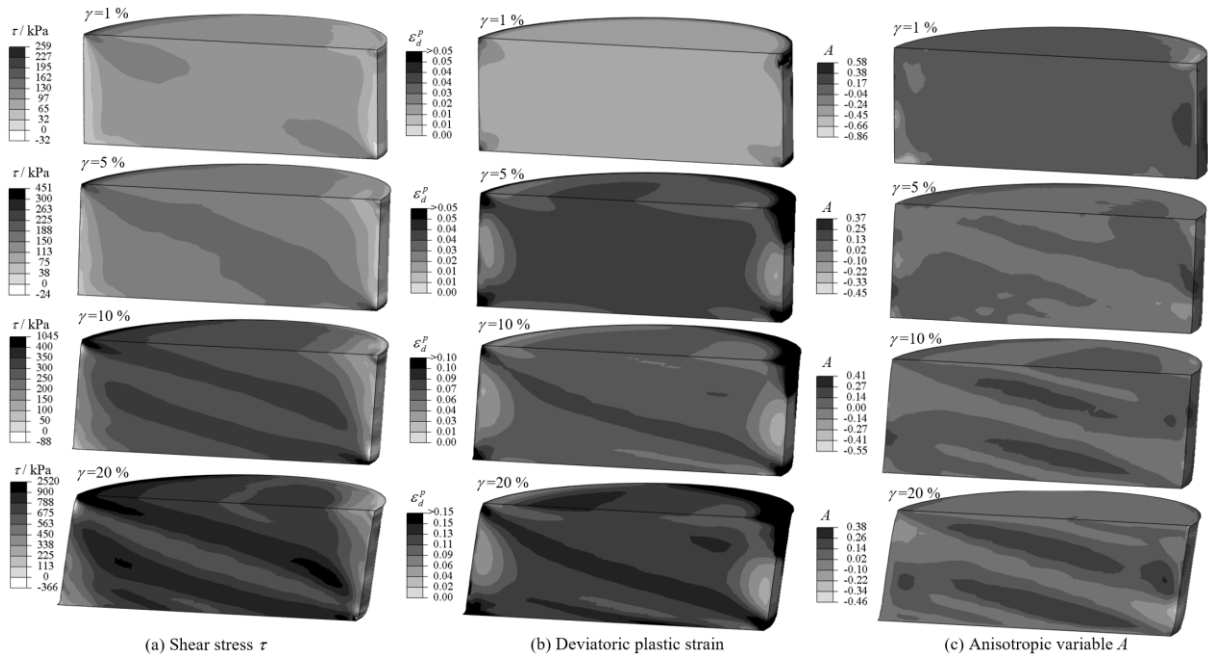
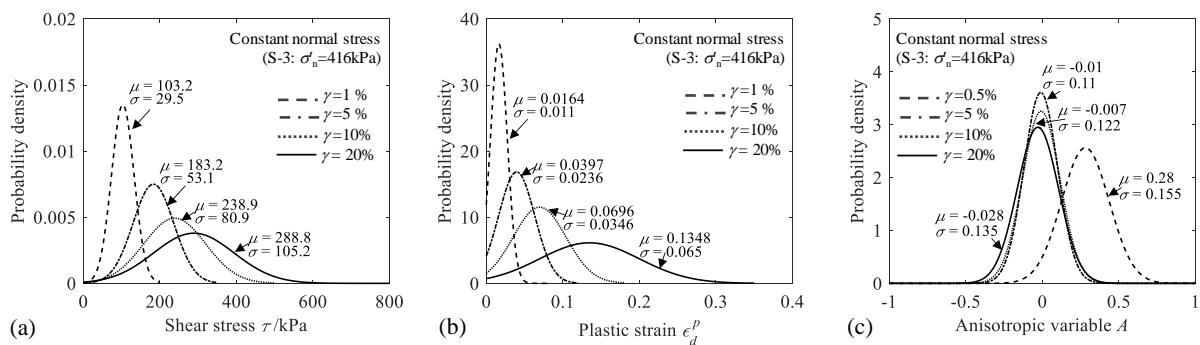


Figure 3.14 Profiles of successive simple shearing process for constant volume condition at $\sigma'_n = 416\text{kPa}$: (a) contours of shear stress τ , (b) contours of deviatoric plastic strain ϵ_d^p ; (c) contours of anisotropic variable A .

Figure 3.15 presents the probability analysis of inhomogeneity behaviour for three simulated state variables (τ , ϵ_d^p and A), based on all Gauss points in FE modelling. It may be observed that the evolution of normal distribution was similar for both the shear stress τ and deviatoric plastic strain ϵ_d^p , in that the deviations enlarged with the strain level, which corresponds to the inhomogeneity of shear stress or plastic strain when greatly increased. Moreover, for the anisotropic variable A as seen in Figure 3.15 (c, f), the deviation of the distribution was much changed at the low shear strain level as $\gamma = 0.5\%$ (also seen in Figure 3.4), meaning it would then not be sensitive to the increasing of shear strain (over 1%).



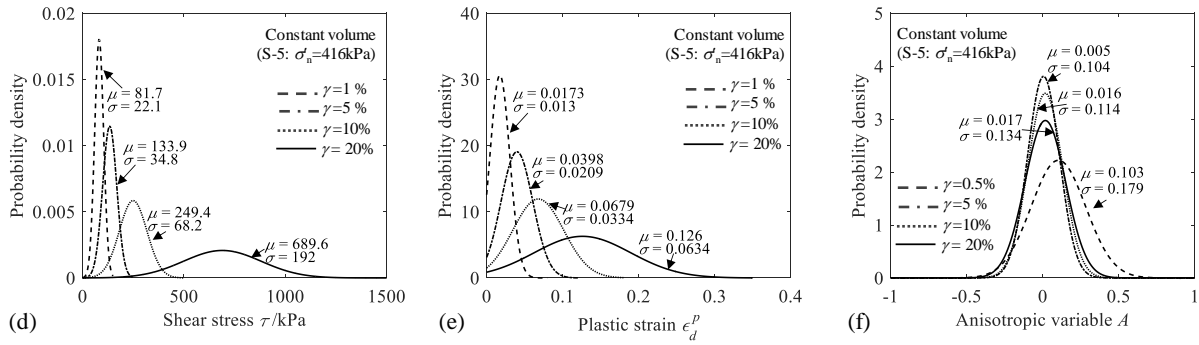


Figure 3.15 Probability distribution analysis with increasing of shear strain based on constant normal stress (a) shear stress, (b) plastic strain and (c) anisotropic variable, and constant volume (d) shear stress, (e) plastic strain and (f) anisotropic variable

3.4 Evaluation of aspect ratio of sample

3.4.1 Finite element modelling

The effect of the aspect ratio for a GDS-type cylindrical specimen was also investigated in this chapter. Three specimens of varying height ($H_0 = 15\text{ mm}$, 25 mm and 35 mm) were modelled, as shown in Figure 3.16. A total of 11,000, 11,000 and 13,750 elements were discretized respectively for the three aspect ratios ($H_0/D_0 = 0.21$, 0.36 and 0.5), in which same elements number 11000 for the cases of different heights $H_0 = 15\text{ mm}$ and 25 mm . The boundary condition of each aspect ratio is consistent with the GDS simple shear apparatus, which was introduced previously. Forces equal to 0.4 kN and 0.8 kN were applied on the top plate to generate initial normal stress ($\sigma'_{n0} = 208$ and 416 kPa , respectively). Then, to address the different aspect ratios, a 20% shear strain γ was applied by moving the bottom plate at the rate of 0.03 mm/s , 0.05 mm/s and 0.07 mm/s respectively, in 100s, for cases of height $H_0 = 15\text{ mm}$, 25 mm and 35 mm , which corresponds to same shear strain rate for each test, as 0.2% strain per second.

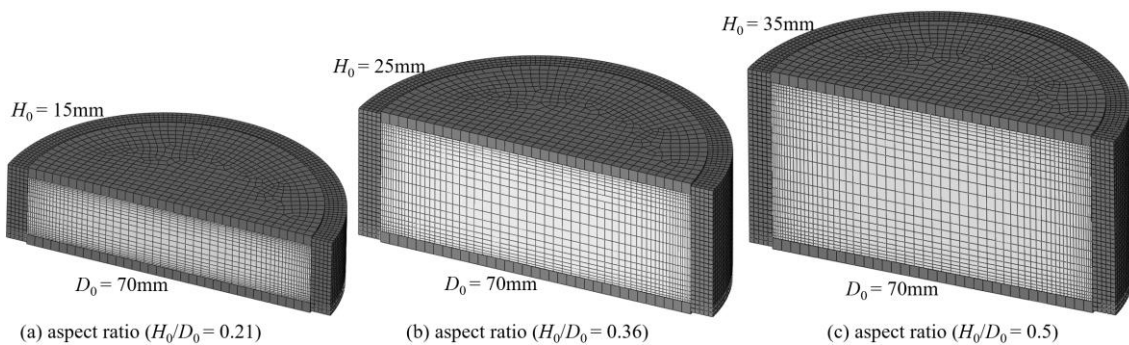


Figure 3.16 Finite element meshes for different aspect ratio of cylinder specimen: (a) $H_0 = 15\text{ mm}$; (a) $H_0 = 25\text{ mm}$; (c) $H_0 = 35\text{ mm}$

3.4.2 Simulation results for different aspect ratios

Numerical models with three initial height-to-diameter ratios ($H_0/D_0 = 0.21, 0.36$ and 0.5) were conducted with both constant normal stress and constant volume conditions to investigate the effect of aspect ratios. The stress-strain relationships simulated by the three aspect ratios are compared in Figure 3.17, which shows that the aspect ratio affects both the shear stiffness and shear strength. For the model with aspect ratio $H_0/D_0 = 0.5$, this corresponds to the smallest value of peak strength as well as strain dilatancy (or void ratio). Moreover, similar results regarding the peak shear stress and volumetric strain can be found between the aspect ratios $H_0/D_0 = 0.36$ and 0.21 . The influence of aspect ratios on shear modulus or strength tends to stabilise for a certain value, as close to 0.36 as possible for the GDS-type simple shear tests, which presents a similar size effect feature as seen in experimental studies (Amer et al. 1984; Amer et al. 1986; Reyno et al. 2005).

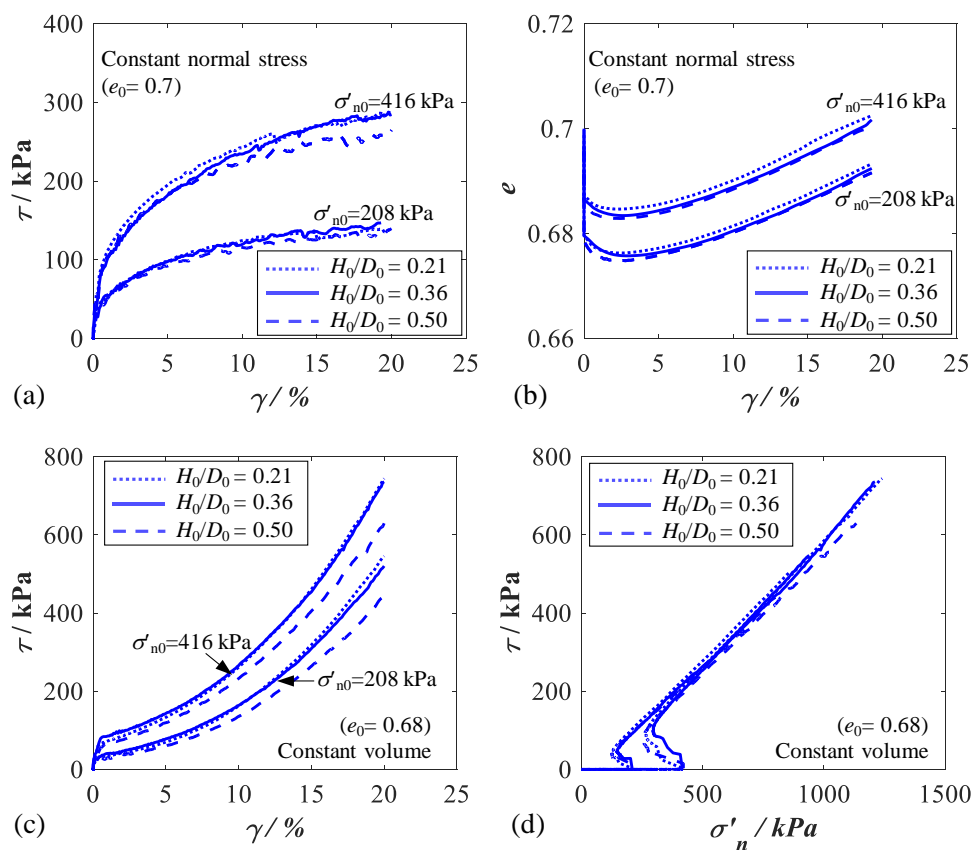


Figure 3.17 Comparison results between different aspect ratios of specimens: (a) constant normal stress simple shear in γ - τ space; (b) constant normal simple shear in γ - e space; (c) constant volume simple shear in γ - τ space; (d) constant volume simple shear in σ'_n - τ space.

3.4.3 Inhomogeneity analysis

Figure 3.18 presents the distribution of vertical stress and shear stress along Path-1 on the top surface of the specimen at shear strain $\gamma = 10\%$ for three aspect ratios. The stress inhomogeneous behaviour can be found according to the stress distribution along the

horizontal direction on the top surface of the specimen. However, the inhomogeneous level among three aspect ratios cannot be easily demarcated, as a result of its similar distribution curve.

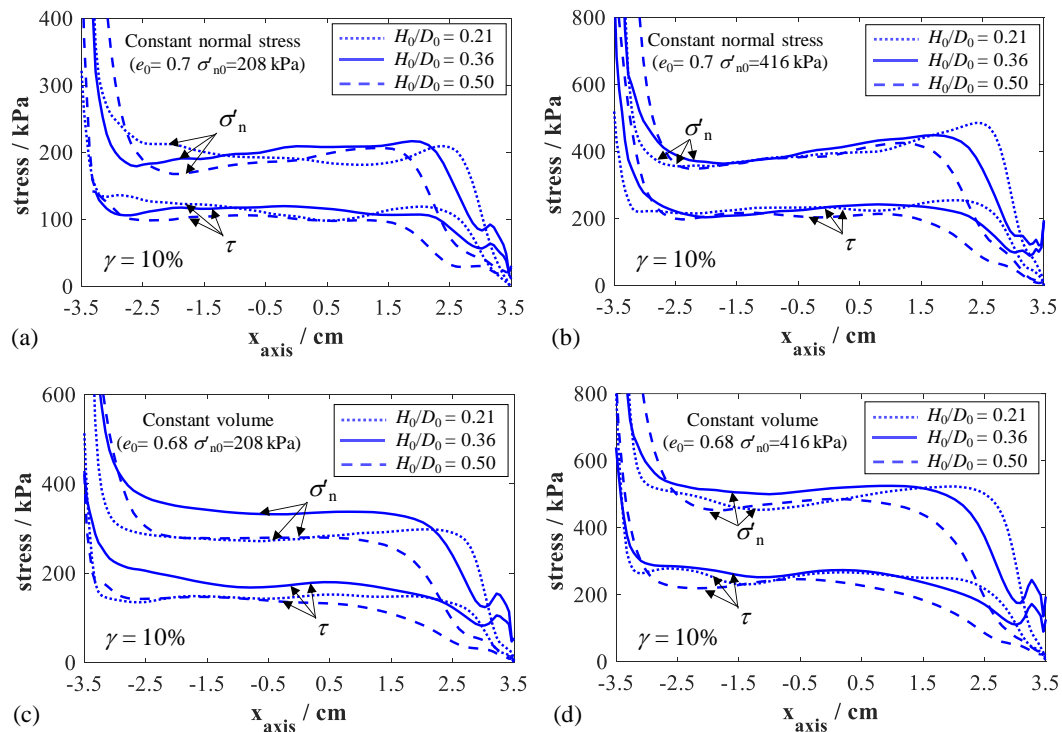


Figure 3.18 Results for different aspect ratios of specimens about distribution of normal stress and shear stress on the Path-1: (a) constant normal stress condition ($\sigma'_{n0} = 208\text{kPa}$); (b) constant normal stress condition ($\sigma'_{n0} = 416\text{kPa}$); (c) constant volume condition ($\sigma'_{n0} = 208\text{kPa}$); (d) constant volume condition ($\sigma'_{n0} = 416\text{kPa}$)

The contour of shear stress τ , deviatoric plastic strain ε_d^p and anisotropic variable A are presented in Figures 3.19–3.20 (cases of $H_0/D_0 = 0.21, 0.36$ and 0.5), to compare the inhomogeneous behaviour between different aspect ratios of the specimen. For the case of $H_0/D_0 = 0.5$, because of the higher-stacked rings (lateral boundary), the horizontal displacement of each ring could not follow a highly linear change from the bottom to top boundaries. A more non-uniform vertical boundary, along with the height of the specimen column, was formed, compared to the cases of $H_0/D_0 = 0.21$ and 0.36 . In addition, for the higher aspect ratios of the specimen, the preferential dilation zone (as the dark colour in the contours of shear stress τ and deviatoric plastic strain ε_d^p in Figures 3.19–3.20) could not easily diffuse from the upper left and lower right corners to the centre zone, and a larger magnitude of stress and strain accumulated in the centre zone of the specimen, as it was the case for $H_0/D_0 = 0.5$. Therefore, greater inhomogeneity will be developed for a higher aspect ratio specimen column, leading to a degradation of the strength and dilatancy behaviour of the specimen.

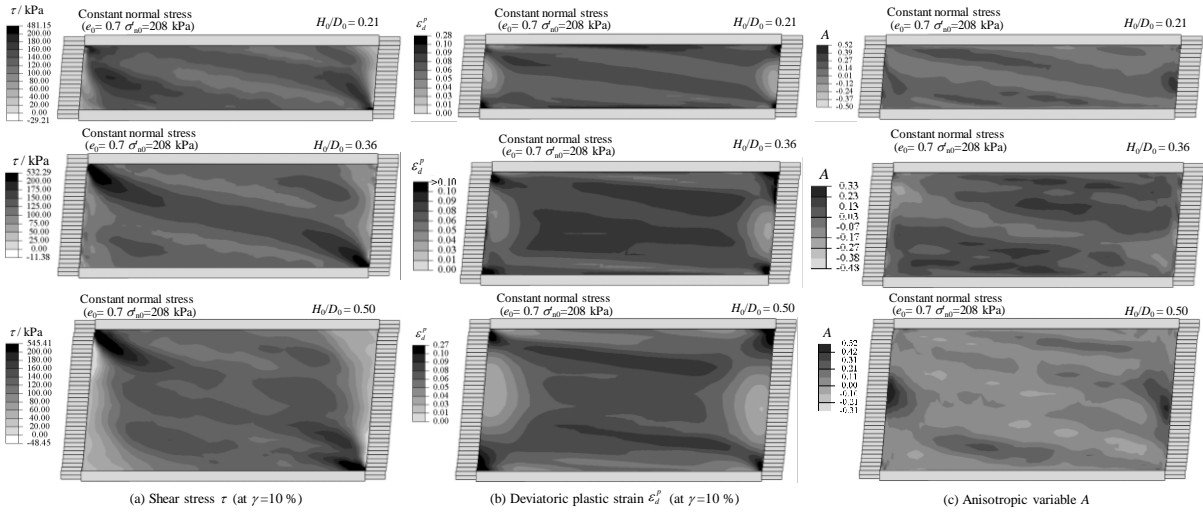


Figure 3.19 Comparisons of different aspect ratios of specimens for the constant normal stress condition (test S-2): (a) contour of shear stress at $\gamma = 10\%$, (b) contour of deviatoric plastic strain at $\gamma = 10\%$, (c) contour of Anisotropic variable A at $\gamma = 10\%$

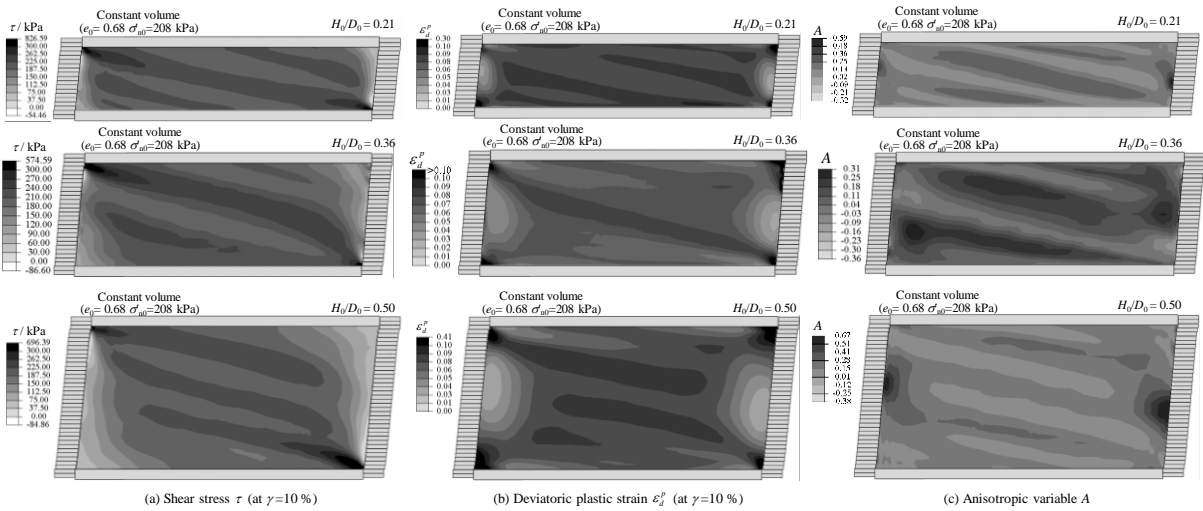


Figure 3.20 Comparisons of different aspect ratios of specimens for the constant volume condition (test S-4): (a) contour of shear stress at $\gamma = 10\%$, (b) contour of deviatoric plastic strain ε_d^p at $\gamma = 10\%$, (c) contour of Anisotropic variable A at $\gamma = 10\%$

Figure 3.21 presents the histogram of the variables (σ_z , τ and ε_d^p) for the aspect ratio $H_0/D_0 = 0.36$, based on the constant normal stress and constant volume simple shear conditions. By fitting simulated variables of all the Gauss points in the FE model based on the probability function (Eq. (3-6)), three normal distributions, corresponding to different aspect ratios, were obtained to study the effect of the aspect ratio on the inhomogeneity of specimens. It may be observed that the highest aspect ratio, $H_0/D_0 = 0.5$, corresponds to the greatest value of deviations σ , meaning that a higher aspect ratio will generate greater inhomogeneity (see Figure 3.21) as well as a lower stress level (see Figure 3.17).

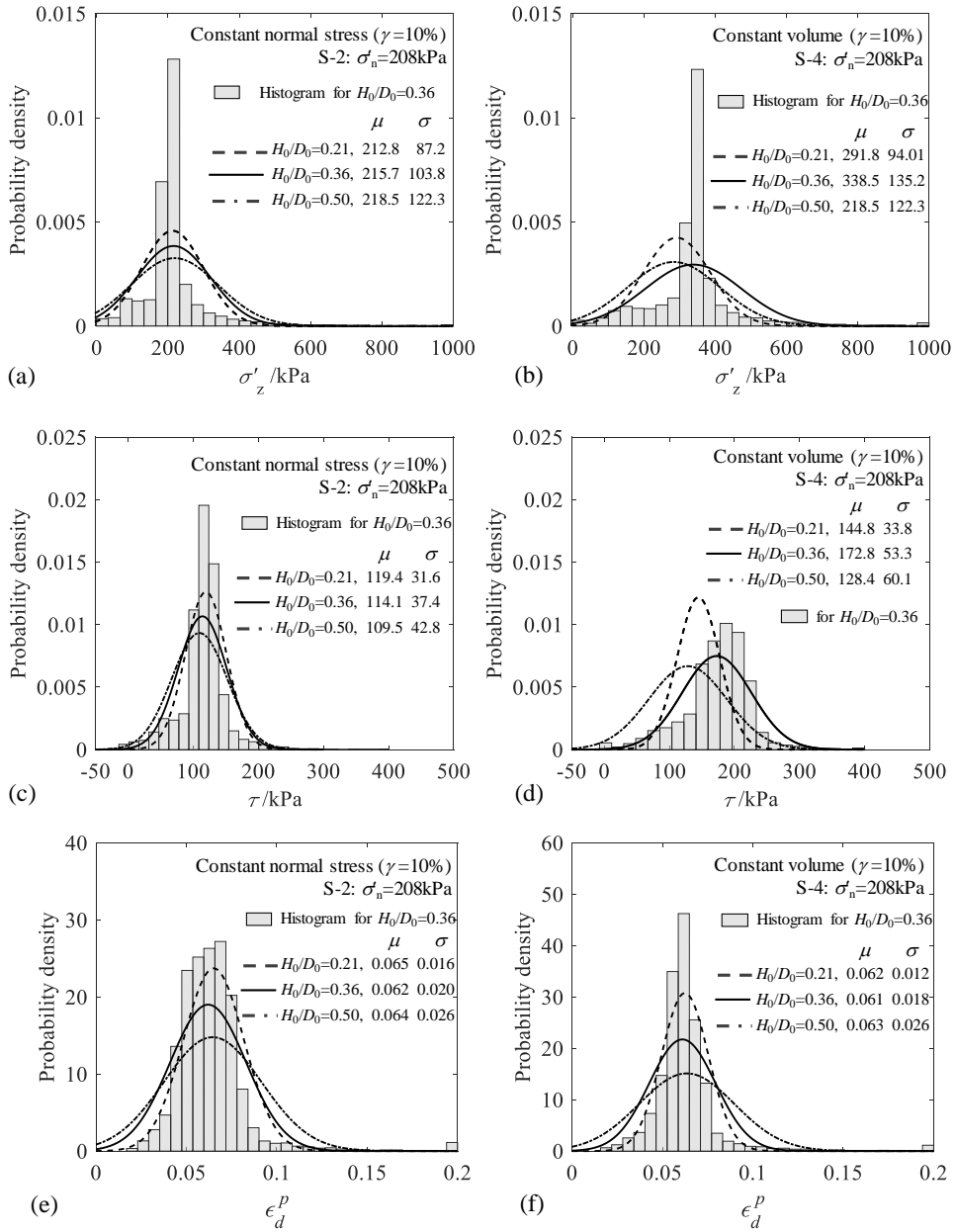


Figure 3.21 Probability distribution analysis with different aspect ratios at 10% shear strain: (a-b) for vertical stress σ'_z , (c-d) for shear stress τ and (e-f) for deviatoric plastic strain ϵ_d^p

3.5 Conclusion

A numerical approach to model simple shear tests, under the influence of sample size, was developed. The approach was based on a FE analysis, with implementation of the critical-state-based model. The adopted model was extended from the original isotropic strength to an anisotropic strength by incorporating a parameter of a cross-anisotropy joint invariant. The inherent anisotropy behaviour during the simple shear condition was thereby captured.

Then, a series of cylindrical specimen GDS-type monotonic simple shear tests on Fontainebleau sand were conducted under both constant normal stress and constant volume loading conditions. 3D FE simulations with the same size and boundaries of laboratory GDS-type apparatus were carried out to validate the performance of FE analysis with the enhanced model. Moreover, the inhomogeneity features for the physical specimen were also illustrated based on the FE simulation, which cannot be assessed using ideal single element simple shear condition.

Finally, some complementary simulations to study the sample size effect were conducted for different aspect ratios of the cylindrical specimen. Comparisons show that a higher aspect ratio specimen results in greater stress inhomogeneity in the specimen in terms of stress and strain distributions. This study can improve our understanding of the simple shear test condition and provide a computational tool for analysis of specimens' inhomogeneity behaviour.

Chapter 4 Normal effective stress degradation in sand under undrained simple shear condition

4.1 Introduction

Pile foundations are generally subjected to lateral and axial, monotonic and cyclic loads, as for example it is the case for wind turbines. Because the severity of the loads can induce a degradation of the shaft capacity (Jardine et al. 2005; Andersen 2009; Gavin et al. 2011; Bekki et al. 2016), in particular due to the axial cyclic components, it needs to be more deeply investigated. Indeed, the initial horizontal effective stress at the interface between the soil and the pile, governing the level of the local shear resistance and thus the global shaft capacity, could be gradually reduced due to the volumetric behaviour of the soil or the generation of excess pore pressure during cyclic loading. Therefore, it is highly valuable to develop analytical methods which address the changes of the soil properties so that the evolution of the shaft capacity of piles under cyclic loading can be more easily interpreted.

In order to investigate the soil response under cyclic loading, various cyclic tests such as triaxial tests, simple or direct shear tests, torsional shear tests (Hyodo et al. 1991; Yoshimine et al. 1998; Yoshimine et al. 1999; Vaid et al. 2001; Dupla and Canou 2003; Andersen 2009; Aghakouchak et al. 2015), have been conducted, usually by assuming uniform load-controlled cycles on the specimen in undrained conditions. Based on these soil element tests, various empirical equations have been proposed for predicting the soil response concerning the generation of pore pressure or the degradation of the effective normal stress.

Based on cyclic triaxial tests, (Seed and Idriss 1971b) have defined a uniformed ‘S’ shape for the generation of excess pore pressure which can be formulated by an arcsine function depending on a normalized number of cycles to liquefaction (Mitchell and Dubin 1986; Polito et al. 2008; Chang et al. 2014; Mohtar et al. 2014; Porcino et al. 2015). Ishibashi et al. (1977) have developed a model of incremental pore pressure depending on the shear stress amplitude and the number of cycles (Sherif et al. 1978; Ishibashi et al. 1982; Krishnaswamy and Thomas Isaac 1995; Georgiannou and Tsomokos 2008; Konstadinou and Georgiannou 2014). Nemat-Nasser and Shokooh (1979) have introduced an ‘energy-based’ method in which the generation of excess pore pressure is related to the amount of dissipated energy (shear work) during cyclic loading (Towhata and Ishihara 1985; Law et al. 1990; Green et al. 2000; Dief and Figueroa 2007).

Note that the influence of the initial average shear stress, which is however known as a key factor in the cyclic resistance of sand (Vaid and Chern 1983; Vaid et al. 2001; Yang and

Sze 2011; Yang and Pan 2017), has not been considered in these predictive models. Hence, a more efficient approach for describing more precisely the degradation of the effective normal stresses acting on a pile shaft must include the investigation of the influence of the initial average shear stress.

Until now, only laboratory experiments have been considered to quantify the degradation of the effective normal stress due to shearing. Most experimental studies have limited this scope on results from triaxial tests. In spite of their shortcomings (Andersen 2009), simple shear tests have been preferred to triaxial tests since the interface shearing is much better reproduced through this type of testing, even if direct shear testing could also be considered (Pra-ai 2013; Pra-ai and Boulon 2017). Similarly, even if it is now currently accepted that the shearing of a soil–pile interface occurs at a relatively constant normal stiffness (Fakharian and Evgin 1997), a conservative approach would be to perform constant volume simple shear tests, which maximize the degradation of the effective normal stress, as previously done in (Lambe and Whitman 1969; Dyvik et al. 1987; Andersen 2009) for instance. The stress state of a soil element around the pile foundation is shown in Figure 4.1. The soil element is subjected to cyclic loading with symmetrical loading ($\tau_{ave} = 0$) or non-symmetrical loading ($\tau_{ave} \neq 0$).

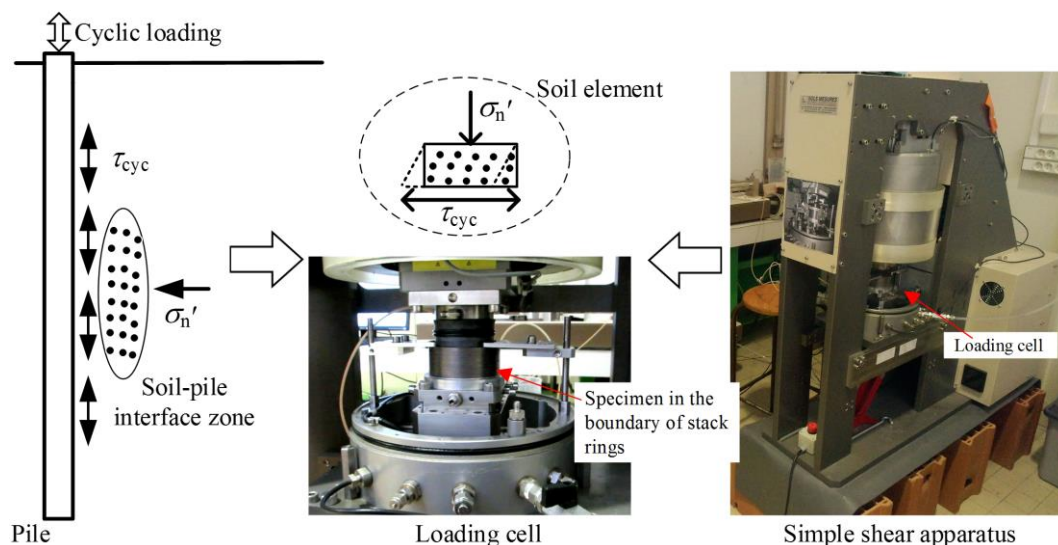


Figure 4.1 Analysis of soil element adjacent to pile based on simple shear apparatus

From the above literature review, the following points could be noted. Firstly, in the laboratory, soil element tests would greatly simplify the testing operation and reduce significantly the financial cost compared to full size or even model pile tests for studying the soil response during cyclic loading. Secondly, the effect of the initial average shear stress is rarely investigated. Thirdly, compared to triaxial tests, simple shear tests are acknowledged to provide more representative loading conditions for interface shearing.

This study, therefore, aims to provide a contribution to characterize the degradation of the effective normal stress based on undrained monotonic and cyclic simple shear tests on

Fontainebleau sand and to develop a procedure for calibrating this degradation. Following these objectives, the first task was to determine through undrained monotonic simple shear tests, the phase transformation line (PTL), since the position of the PTL governs the volumetric behavior and, therefore, the pore pressure evolution. Then, the number of cycles to the instability (liquefaction for tests with null average shear stress and cyclic mobility for tests with average shear stress) was investigated based on the results of cyclic simple shear tests under different loading conditions. Furthermore, an empirical formulation expressing the degradation of the effective normal stress during cyclic loading was developed. Then, experimental data on Fraser River sand and a carbonate sand from Quiou (France) obtained through simple shear tests on the one hand, and on Karlsruhe sand subjected to triaxial loading on the other hand, were selected from the literature review to verify the proposed calibration procedure. Finally, a series of additional tests were performed on Fontainebleau sand in order to verify the accuracy of the proposed empirical equation.

4.2 Material and testing program

The tested material is the Fontainebleau sand NE34. As a reference material in France for geotechnical applications, this sand has been used in many experimental studies. Its cyclic behavior has been relatively well documented at the scale of the representative elementary volume in laboratory tests as well as at the scale of soil–structure interactions (Dupla and Canou 1994; Gaudin et al. 2005; Andria-Ntoanina et al. 2010; Yang et al. 2010; Pra-Ai 2013; Sim et al. 2013c; Aghakouchak et al. 2015; Pra-ai and Boulon 2017), resulting in the establishment of Poulos’ cyclic stability diagram (Poulos 1988).

The constant volume condition is ensured by constraining the height of the sample to a constant value after the K_0 -consolidation. Compared to a truly undrained test where the evolution of excess pore pressure can be directly measured, the normal effective stress σ'_n on the horizontal plane continuously varies to fulfill the constant volume condition during simple shear testing. The assumption that the change in the applied normal effective stress is equal to the excess pore which would have developed in a truly undrained test has been validated by Dyvik et al. (1987), and has been applied in extensive laboratory testing during the last two decades.

The experimental campaign consisting of monotonic and cyclic simple shear tests is presented in Table 4.1. For the cyclic tests, sine cycles with a frequency of 0.05 Hz were applied. The dry specimens, prepared by air pluviation, were first consolidated under K_0 -condition up to a given initial effective normal stress σ'_{n0} . Three series of constant volume simple shear tests were carried out:

- 1) The first series consisted of monotonic simple shear tests, which were performed at different initial effective normal stresses ($104 \leq \sigma'_{n0} \leq 416$ kPa) and different void ratios after consolidation ($0.59 \leq e_0 \leq 0.74$). The objective of this part was to determine the

shear stress at phase transformation state τ_{pt} , for different void ratios after consolidation e_0 and different initial effective normal stresses σ'_{n0} .

- 2) The second series consisted of symmetrical cyclic simple shear tests (the average shear stress τ_{ave} was null). Several tests with different cyclic shear stress amplitudes ($5.2 \leq \tau_{cyc} \leq 62.4$ kPa) and initial normal stresses ($104 \leq \sigma'_{n0} \leq 416$ kPa) on medium dense specimens were performed. The objective of this part was to study the influence of the cyclic shear stress τ_{cyc} on the number of cycles to liquefaction N_L .
- 3) The third series consisted of non-symmetrical cyclic simple shear tests ($\tau_{ave} \neq 0$), with different cyclic shear stress amplitudes ($10.4 \leq \tau_{cyc} \leq 41.6$ kPa) and different average shear stresses ($5.2 \leq \tau_{ave} \leq 41.6$ kPa) on medium dense specimens under an effective normal stress $\sigma'_{n0} = 416$ kPa. Two sets of loading conditions, namely shear stress-reversal ($\tau_{cyc} > \tau_{ave}$) and no shear stress-reversal ($\tau_{cyc} \leq \tau_{ave}$), were applied. The objective in this part was to study the influence of the average shear stress τ_{ave} on the number of cycles to liquefaction N_L .

Table 4.1 Summary of experiments on tested Fontainebleau sand

Test No.	Loading type		e_0	D_{r0} %	σ'_{n0} (kPa)	τ_{pt} (kPa)	τ_{ave} (kPa)	τ_{cyc} (kPa)	τ_{ave}/σ'_{n0}	CSR	N_L
m1	Monotonic		0.744	37.1	104	6.6	-	-	-	-	-
m2	Monotonic		0.688	52.2	104	12.8	-	-	-	-	-
m3	Monotonic		0.631	67.5	104	16.1	-	-	-	-	-
m4	Monotonic		0.586	79.6	104	25	-	-	-	-	-
m5	Monotonic		0.644	64.0	208	28.1	-	-	-	-	-
m6	Monotonic		0.733	40.1	312	26	-	-	-	-	-
m7	Monotonic		0.730	40.9	312	25.5	-	-	-	-	-
m8	Monotonic		0.679	54.6	312	34	-	-	-	-	-
m9	Monotonic		0.627	68.5	312	44	-	-	-	-	-
m10	Monotonic		0.617	71.2	312	59	-	-	-	-	-
m11	Monotonic		0.615	71.8	312	60	-	-	-	-	-
m12	Monotonic		0.651	62.1	416	69	-	-	-	-	-
c13	Symmetrical loading		0.658	60.2	104	14	0	5.2	0	0.05	18
c14	Symmetrical loading		0.664	58.6	208	27	0	5.2	0	0.025	88
c15	Symmetrical loading		0.670	57.0	208	26	0	10.4	0	0.05	14
c16	Symmetrical loading		0.660	59.7	208	28	0	20.8	0	0.1	2
c17	Symmetrical loading		0.663	58.9	312	42	0	15.6	0	0.05	33
c18	Symmetrical loading		0.662	59.1	416	57	0	10.4	0	0.025	366
c19	Symmetrical loading		0.660	59.7	416	57	0	10.4	0	0.025	300
c20	Symmetrical loading		0.638	65.6	416	67	0	20.8	0	0.05	81
c21	Symmetrical loading		0.663	58.9	416	57	0	20.8	0	0.05	62
c22	Symmetrical loading		0.656	60.8	416	60	0	20.8	0	0.05	62
c23	Symmetrical loading		0.655	61.0	416	60	0	31.2	0	0.075	10
c24	Symmetrical loading		0.644	64.0	416	65	0	41.6	0	0.1	3
c25	Symmetrical loading		0.648	62.9	416	65	0	62.4	0	0.167	1
c26	Non-symm	Stress reversal	0.629	68.0	416	71	5.2	10.4	0.0125	0.025	600
c27	Non-symm	Stress reversal	0.654	61.3	416	60	5.2	20.8	0.0125	0.05	57
c28	Non-symm	Non-stress reversal	0.669	57.3	416	53	10.4	10.4	0.025	0.025	368
c29	Non-symm	Stress reversal	0.663	58.9	416	56	10.4	20.8	0.025	0.05	19
c30	Non-symm	Stress reversal	0.654	61.3	416	60	10.4	20.8	0.025	0.05	39
c31	Non-symm	Stress reversal	0.641	64.8	416	66	10.4	20.8	0.025	0.05	56
c32	Non-symm	Non-stress reversal	0.653	61.6	416	61	20.8	10.4	0.05	0.025	240
c33	Non-symm	Non-stress reversal	0.641	64.8	416	57	20.8	10.4	0.05	0.025	310
c34	Non-symm	Non-stress reversal	0.635	66.4	416	71	20.8	20.8	0.05	0.05	100
c35	Non-symm	Non-stress reversal	0.666	58.1	416	55	20.8	20.8	0.05	0.05	45
c36	Non-symm	Stress reversal	0.640	65.1	416	66	20.8	41.6	0.05	0.1	7
c37	Non-symm	Non-stress reversal	0.654	61.3	416	60	41.6	10.4	0.1	0.025	330
c38	Non-symm	Non-stress reversal	0.664	58.6	416	56	41.6	20.8	0.1	0.05	19

* Initial void ratio e_0 and relative densities D_{r0} were measured at the corresponding initial effective normal stress σ'_{n0} ; for monotonic loading, the shear stress at phase transformation state τ_{pt} was measured based on the experimental results, and for cyclic loading τ_{pt} was calculated based on the empirical equation Eq. (4-1); cyclic shear stress ratio CSR could be expressed by the cyclic shear stress τ_{cyc} over the initial effective normal stress σ'_{n0} ; N_L is the number of cycles to liquefaction.

4.3 Test results and interpretation

4.3.1 Monotonic stress-strain behavior

Figure 4.2 shows the stress-strain response of Fontainebleau sand samples during monotonic simple shear testing. The shear strain γ is defined as $\gamma = \Delta d / H_c$ (where H_c is the sample height at the start of the shearing, and Δd is the horizontal displacement). Under constant volume condition, the shearing induced, at first, a decrease of the effective normal stress before the phase transformation state was reached. The extreme points in the shear stress – effective normal stress diagram mark the change from contractancy to dilatancy and therefore the position of the phase transformation state. Beyond that state, the effective normal stress increased towards the failure line.

Figure 4.2(a, b) presents the influence of the void ratio after consolidation e_0 for a given effective normal stress of 312 kPa. The loosest specimen after consolidation exhibits the largest decrease of the effective normal stress. Figure 4.2(c, d) presents the influence of the initial effective normal stress level, from 104 kPa to 416 kPa, for a range of relative densities corresponding to a medium density. The friction angle at failure ϕ_f is equal to 30° . The phase transformation states are located on a unique straight line passing through the origin, whose slope corresponds to a friction angle of 24° . The phase transformation line (PTL) delineates two distinct volumetric behaviors (contractancy below PTL, dilatancy between PTL and failure line), which will subsequently govern the evolution of the samples during cyclic shearing.

In Figure 4.2(e,f), the effective normal stress (σ'_n) and the shear stress (τ) are normalized by the corresponding initial effective normal stress (σ'_{n0}) and the shear stress at phase transformation state (τ_{pt}), respectively. For the same initial effective normal stress, a smaller void ratio e_0 corresponds to a larger normalized effective normal stress ($\sigma'_{n-pt} / \sigma'_{n0}$) at the phase transformation state. For the same void ratio, the magnitude of the normalized stress at the phase transformation state ($\sigma'_{n-pt} / \sigma'_{n0}$, τ / τ_{pt}) is slightly affected by the value of the initial effective normal stress.

The values of the shear stress at phase transformation τ_{pt} are plotted in Figure 4.3a against the relative density after consolidation D_{r0} , defined in Eq. (4-1). It can be seen that the shear stress τ_{pt} depends on the void ratio e_0 and on the initial normal effective stress σ'_{n0} . In Figure 4.3b, the shear stress τ_{pt} is normalized by the initial effective normal stress σ'_{n0} and plotted as a function of D_{r0} . A non-linear relationship between the void ratio e_0 and the normalized shear stress τ_{pt} / σ'_{n0} is obtained and an empirical function can be deduced, which allows us to estimate the shear stress τ_{pt} , depending on the given parameters σ'_{n0} and e_0 , Eq.(4-1). The parameters M_1 and M_2 were calibrated by fitting the experimental data for Fontainebleau sand: $M_1 = 0.68$ and $M_2 = 1.76$.

$$\tau_{pt} = M_1 \cdot \sigma'_{n0} \cdot \tan \phi_{pt} \cdot D_{r0}^{M_2} \quad \text{with} \quad D_{r0} = \frac{e_{\max} - e_0}{e_{\max} - e_{\min}} \quad (4-1)$$

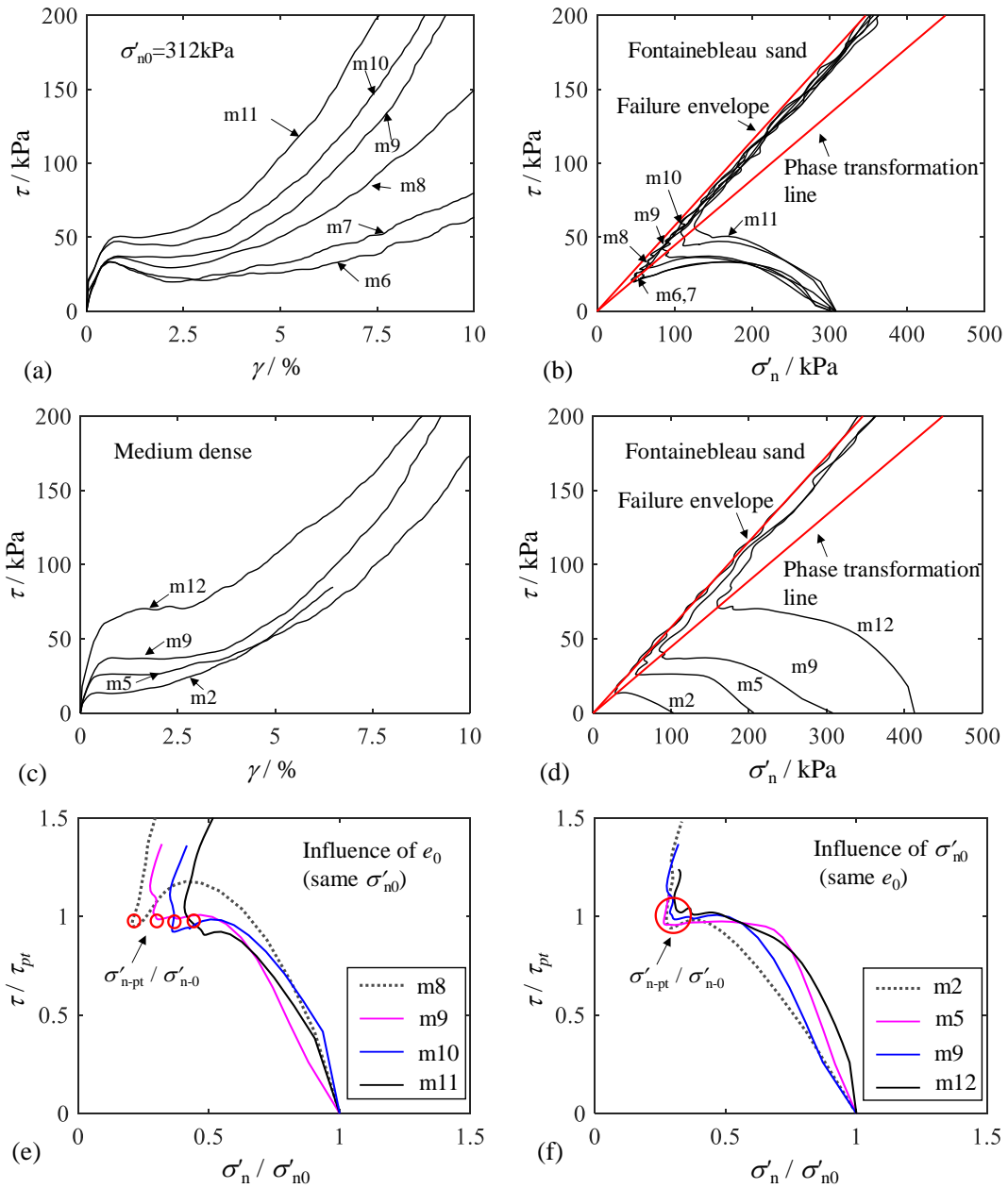


Figure 4.2 Undrained monotonic test results on Fontainebleau sand: (a-b) comparison results with different initial void ratios; (c-d) comparison results with different initial effective normal stresses; (e-f) normalized monotonic behaviour with different initial void ratios and effective normal stresses

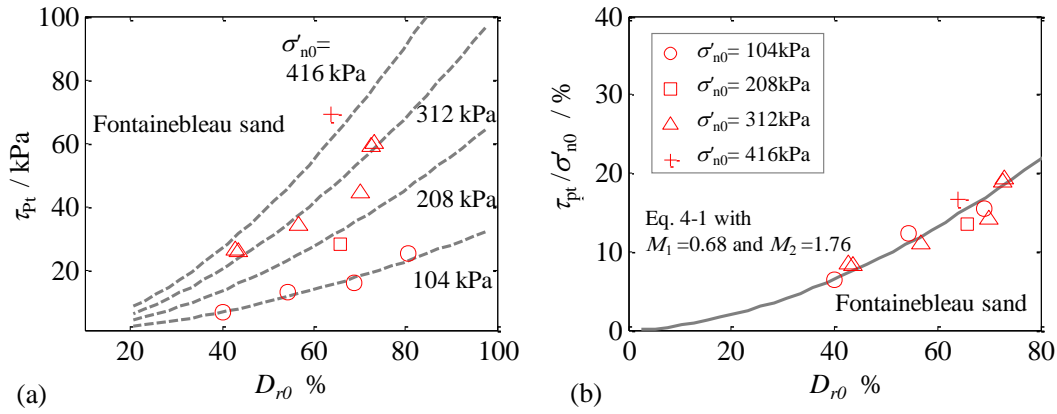


Figure 4.3 Shear stress at phase transformation as a function of experimental variables initial effective normal stress and relative density: (a) shear stress at phase transformation versus initial relative density; (b) normalized shear stress at phase transformation versus initial relative density

4.3.2 Symmetrical cyclic loading

13 constant volume symmetrical cyclic simple shear tests were performed on medium dense Fontainebleau sand specimens under various initial effective normal stresses ($\sigma'_{n0} = 104, 208, 312, 416$ kPa). A typical test result (Test c21: $\tau_{ave} = 0$ kPa, $\tau_{cyc} = 20.8$ kPa, $\sigma'_{n0} = 416$ kPa) is presented in Figure 4.4. Upon reaching the phase transformation line, the effective stress path started to follow a butterfly-shaped loop due to the continuous transition from contractancy to dilatancy. It also quickly approached the failure line, which resulted in a rapid generation of large shear strains (Figure 4.4a, b and c). The effective normal stress σ'_n decreased with the number of cycles, until reaching a minimum value ($\sigma'_n \approx 0$ kPa) when liquefaction occurred (Figure 4.4d). Under this condition, the specimen could no longer sustain any loading (loss of controllability of the test). In this example, the required number of cycles to trigger liquefaction N_L was equal to 62 ($N_L = 62$).

The degradation of the effective normal stress for all the symmetrical cyclic tests has been compiled in Figure 4.5, as a function of the initial normal effective stress σ'_{n0} and for different cyclic shear stresses τ_{cyc} . As expected, for a given effective initial normal stress, the number of cycles to liquefaction increased as the cyclic shear stress decreased. Likewise, a higher initial effective normal stress delayed the occurrence of liquefaction (greater N_L) since the distance between the initial stress state and the corresponding phase transformation state in the $(\sigma'_{n0} - \tau)$ stress plane was larger.

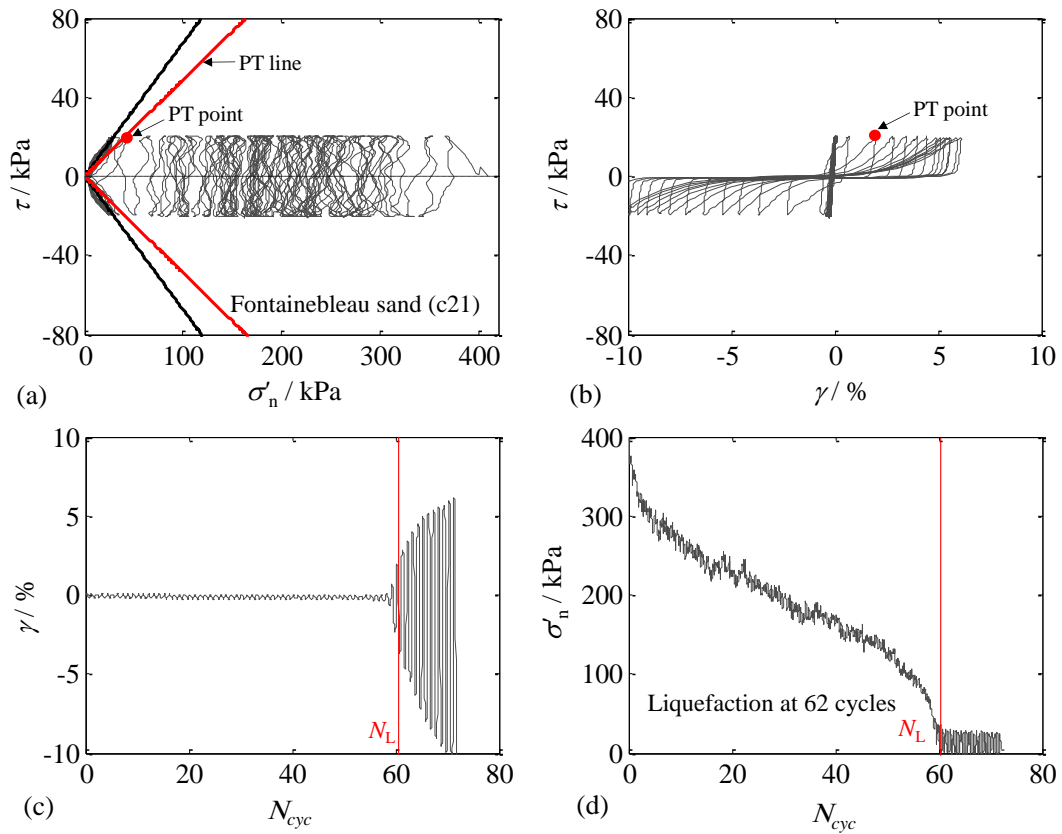


Figure 4.4 Symmetrical cyclic response of Fontainebleau sand: (a) shear stress versus effective normal stress; (b) shear stress versus shear strain, (c) shear strain versus number of cycles; (d) effective normal stress versus number of cycles

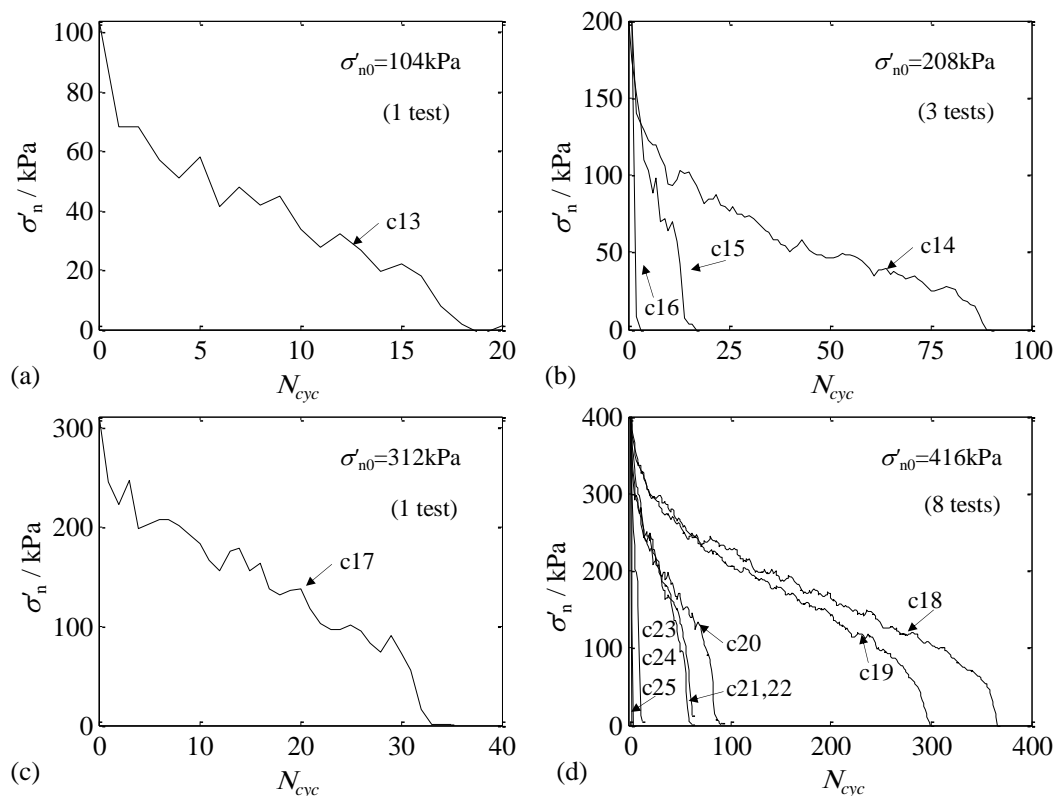


Figure 4.5 Degradation of effective normal stress under different initial effective normal stresses (a) 104 kPa, (b) 208 kPa, (c) 314 kPa and (d) 416 kPa

In order to establish a correlation between the cyclic shear stress and the number of cycles to liquefaction, the cyclic shear stress amplitude was normalized by the phase transformation shear stress τ_{pt} obtained through monotonic simple shear tests and calculated by Eq.(4-1). The results (points in Figure 4.6) are plotted versus the number of cycles to liquefaction N_L . The experimental data are then fitted assuming a power function between N_L and the normalized cyclic shear stress ratio τ_{cyc}/τ_{pt} , as indicated in Eq. (4-2). In the case of Fontainebleau sand, the power $\bar{\zeta}$ was found equal to 0.27.

$$\frac{\tau_{cyc}}{\tau_{pt}} = \frac{1}{N_L^{\bar{\zeta}}} \quad (4-2)$$

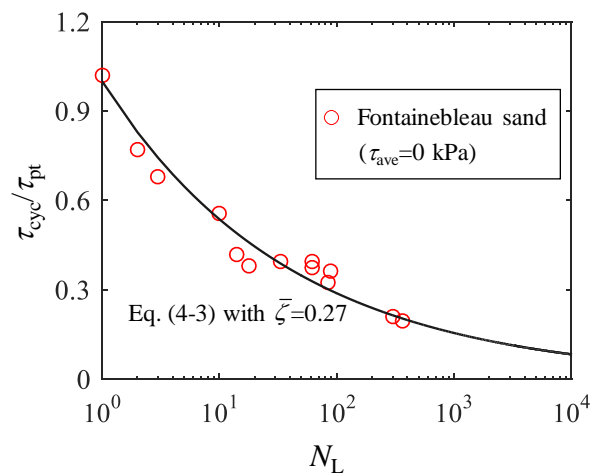


Figure 4.6 Normalized cyclic shear stress versus number of cycles to liquefaction

4.3.3 Non-symmetrical cyclic loading

14 constant volume non-symmetrical cyclic simple shear tests were performed on medium dense Fontainebleau sand samples with a given initial normal effective stress ($\sigma'_{n0} = 416$ kPa). Two loading conditions were imposed: stress reversal ($\tau_{cyc} > \tau_{ave}$) and no-stress reversal ($\tau_{cyc} < \tau_{ave}$) cyclic loading.

Figure 4.7 shows a typical test result (Test c30) for stress reversal cyclic loading ($\tau_{cyc} = 20.8$ kPa, $\tau_{ave} = 10.4$ kPa, $\sigma'_{n0} = 416$ kPa). The initial average shear stress was firstly reached in the undrained condition. The cyclic response was very similar to the one observed in the symmetrical case, except for a small evolution of the average shear strain. The comparison of Figures 4.4 and 4.7, for which the unique difference is the value of the average shear stress (0 kPa for Test c21 in Figure 4.4, 10.4 kPa for Test c30 in Figure 4.7), demonstrates that an increase of the average shear stress favours the degradation of the effective normal stress, since the number of cycles to liquefaction was reduced by a factor of about 1/3 (62 to 39 cycles).

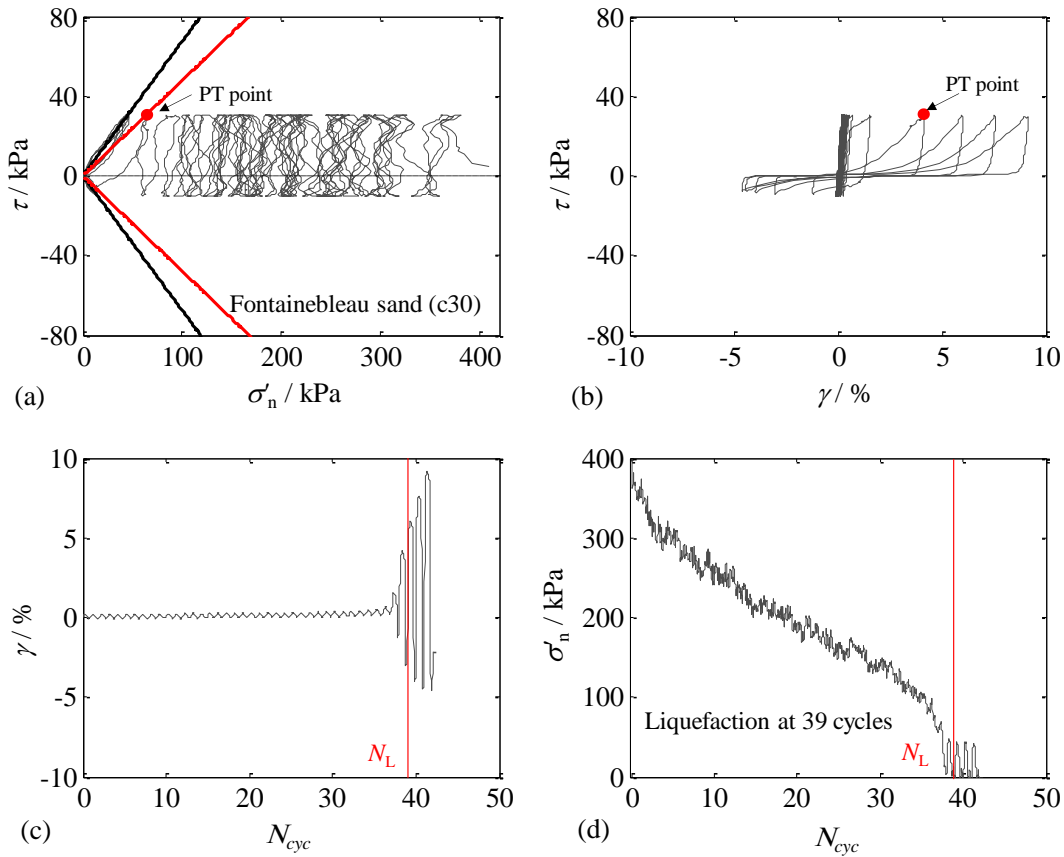


Figure 4.7 Non-symmetrical cyclic response of Fontainebleau sand with stress reversal loading: (a) shear stress versus effective normal stress; (b) shear stress versus shear strain, (c) shear strain versus number of cycles; (d) effective normal stress versus number of cycles

Similarly, a typical result of no-stress reversal cyclic loading (Test c38: $\tau_{cyc} = 20.8$ kPa, $\tau_{ave} = 41.6$ kPa, $\sigma'_{n0} = 416$ kPa) is reported in Figure 4.8. All the test loading conditions except the value of the average shear stress were the same, as in Tests c21 and c30 previously discussed. The instability, corresponding to a cyclic mobility mechanism, occurred at a smaller number of cycles (between 15 and 20 cycles), due to the proximity of the stress path to both the PT and failure lines. The effective normal stress reached a residual value (100 kPa in the case of Test c38). For this type of stress controlled simple shear test, the instability was determined by the condition of the effective normal stress reaching a residual value ($\sigma'_{n-residual} = 98$ kPa).

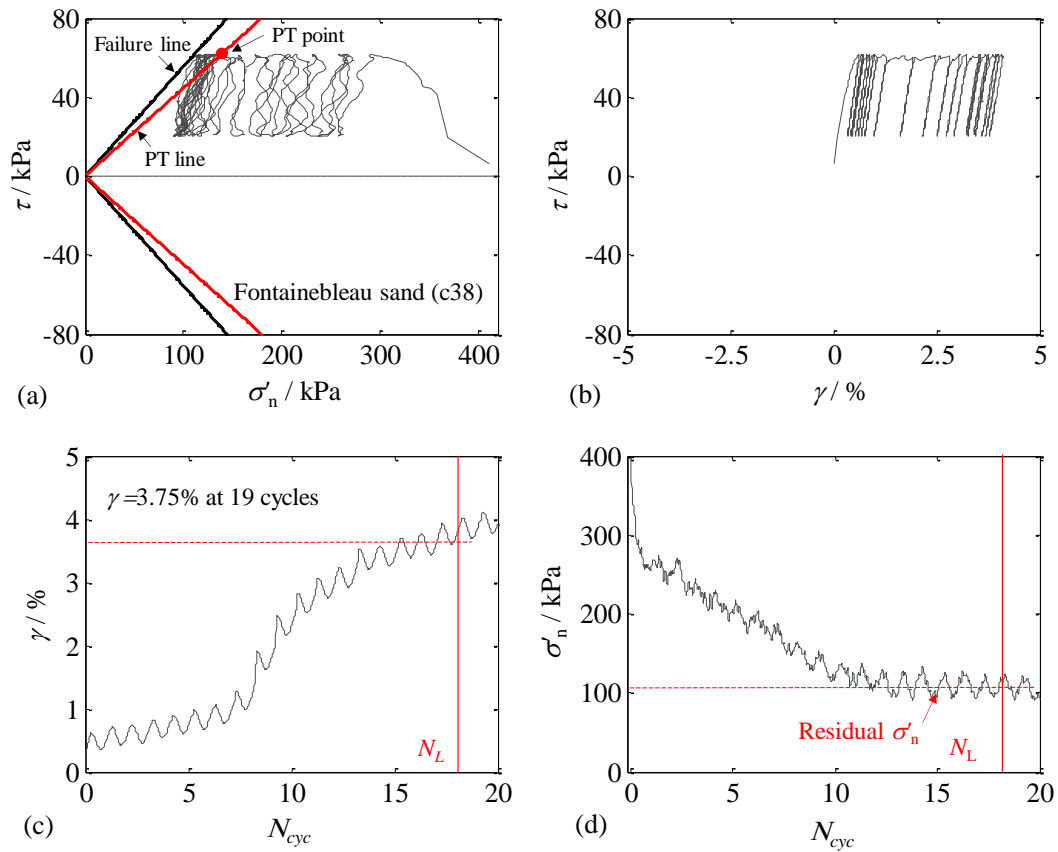


Figure 4.8 Non-symmetrical cyclic response of Fontainebleau sand with no-stress reversal loading: (a) shear stress versus effective normal stress; (b) shear stress versus shear strain, (c) shear strain versus number of cycles; (d) effective normal stress versus number of cycles

Figure 4.9 summarizes all the results relative to non-symmetrical cyclic tests under the same initial effective normal stress of 416 kPa with different average shear stresses. The results corresponding to the stress reversal condition for which the effective normal stresses decreased to zero, i.e. the liquefied state, were plotted in red. For the no-stress reversal condition, the effective normal stress decreased to a residual stress. For a better comparison of the results obtained under these two conditions, the number of cycles to instability (liquefaction or cyclic mobility) was defined by the effective normal stress reaching the limited final value. The degradation of the effective normal stress for all the non-symmetrical cyclic tests was plotted as a function of the cyclic shear stress τ_{cyc} and the average shear stress τ_{ave} in Figure 4.9. As expected, for a given average shear stress, the number of cycles to liquefaction increased with the decrease of the cyclic shear stress.

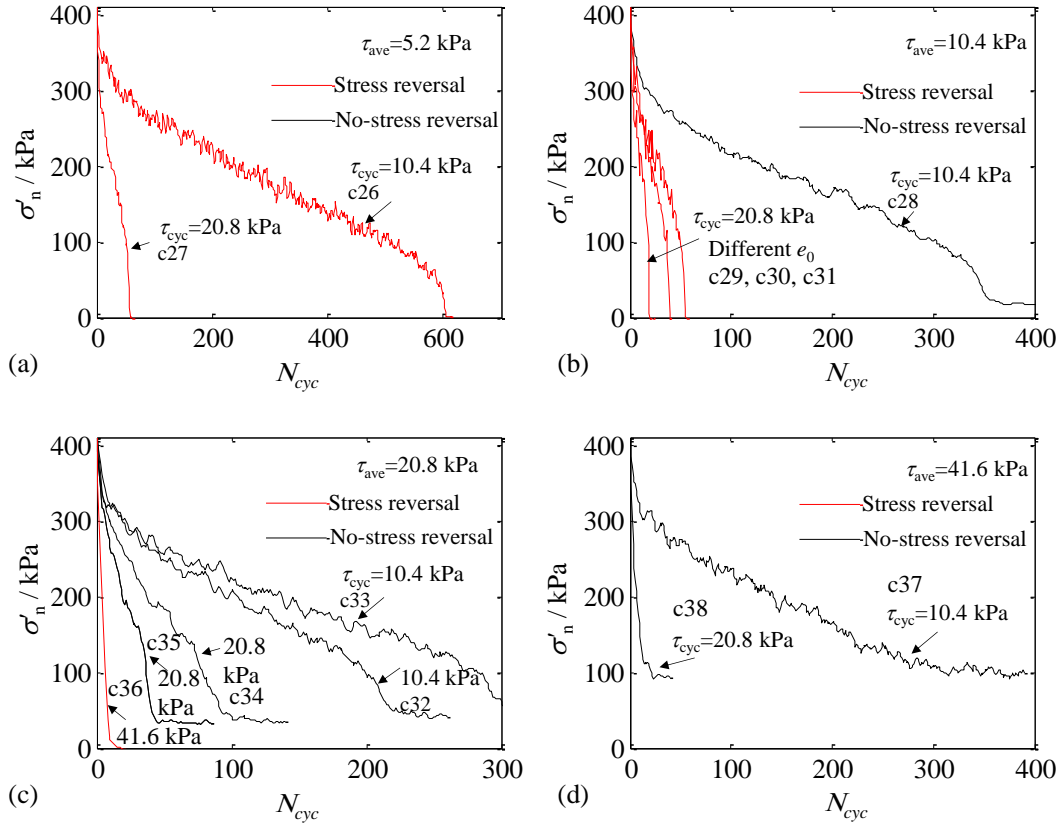


Figure 4.9 Degradation of effective normal stress under different average shear stresses: (a) 5.2 kPa; (b) 10.4 kPa; (c) 20.8 kPa; (d) 41.6 kPa

Figure 4.10(a) presents the hysteresis loops of non-stress reversal cyclic loading corresponding to the cyclic mobility final state which were used to calibrate the value of the residual effective normal stress ($\sigma'_{n\text{-residual}}$). The values of $\sigma'_{n\text{-residual}}$ corresponding to the maximum shear stress τ_{\max} which is equal to the average shear stress τ_{ave} plus the cyclic shear stress τ_{cyc} , are shown in Figure 4.10(b) for nine no-stress reversal cyclic tests. An empirical expression could be suggested to evaluate the residual effective normal stress, which is related to the Mohr-Coulomb failure line:

$$\sigma'_{n\text{-residual}} = \begin{cases} \chi \cdot \tau_{\max} \cdot \tan^{-1}(\phi_f) & ; (\tau_{\text{ave}} \geq \tau_{\text{cyc}}) \\ 0 & ; (\tau_{\text{ave}} < \tau_{\text{cyc}}) \end{cases} \quad (4-3)$$

where χ is a parameter obtained by fitting the data of non-stress reversal cyclic tests ($\chi = 0.77$ for Fontainebleau sand); τ_{\max} is the maximum shear stress equal to $\tau_{\text{ave}} + \tau_{\text{cyc}}$; ϕ_f is the friction angle at failure. A good agreement could be obtained between calculated results (dash blue line) and measurements (red symbols).

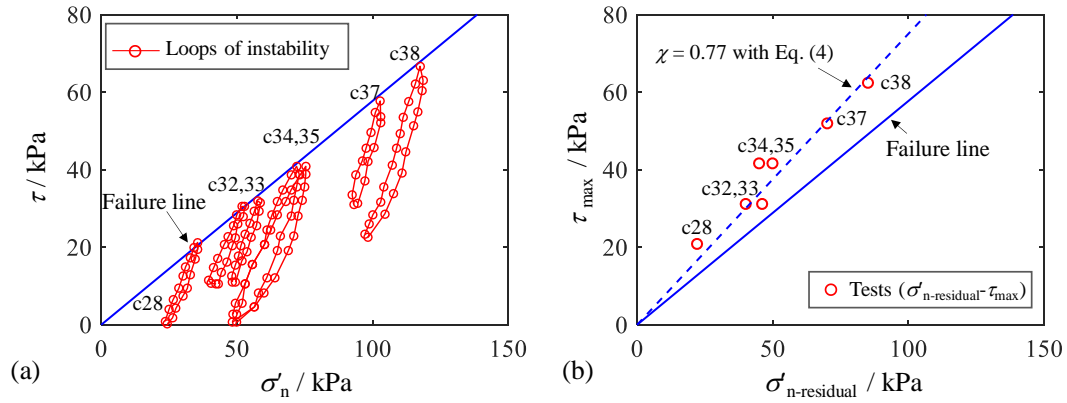


Figure 4.10 Evaluation of effective residual normal stress in no-stress reversal cyclic loading

4.4 Evaluation of the degradation of the effective normal stress

4.4.1 Number of cycles to liquefaction

The experimental data were mapped on a 3D plot, where two axes represent the stress ratios τ_{cyc}/τ_{pt} and τ_{ave}/τ_{pt} , and the third one, the number of cycles to instability (liquefaction or cyclic mobility) (Figure 4.11). This plot can be used to describe the cyclic resistance of Fontainebleau sand. For a constant level of normalized average shear stress (τ_{ave}/τ_{pt}), the number of cycles to instability decreases with the increase of the normalized cyclic shear stress (τ_{cyc}/τ_{pt}). Inversely, for a constant level of normalized cyclic shear stress (τ_{cyc}/τ_{pt}), the number of cycles to instability decreases with the increase of the normalized average shear stress (τ_{ave}/τ_{pt}).

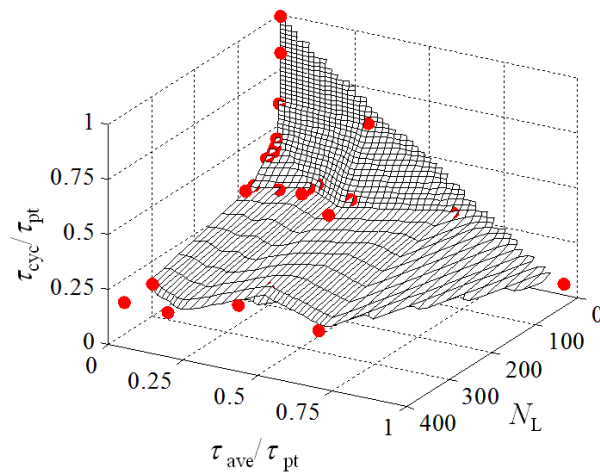


Figure 4.11 Cyclic resistance surface for cyclic simple shear tests on Fontainebleau sand

In order to formulate an expression for the number of cycles to instability, all the couples of normalized stresses (τ_{ave}/τ_{pt} , τ_{cyc}/τ_{pt}) were reported in a diagram of stability shown in Figure 4.12(a). The space is then delimited by the diagonal corresponding to a failure at the

first cycle. Instabilities reached at a higher number of cycles N_L fell on straight lines whose slope k decreased with N_L , as shown in Figure 4.12 (a). The slope k can be approximated by:

$$k = \frac{\tau_{cyc}/\tau_{pt}}{1 - \tau_{ave}/\tau_{pt}} = \frac{\tau_{cyc}}{\tau_{pt} - \tau_{ave}} \quad (4-4)$$

Figure 4.12 (b) correlates the calculated values of k and the corresponding values of N_L which can be expressed by:

$$N_L = \psi_1 \cdot \left(\frac{\tau_{cyc}}{\tau_{pt} - \tau_{ave}} \right)^{-\psi_2} \quad (4-5)$$

where ψ_1 and ψ_2 are parameters obtained by fitting the experimental results ($\psi_1 = 1.396$, $\psi_2 = 3.505$ for Fontainebleau sand).

The diagram in Figure 4.12(a) can be used to predict the number of cycles to instability (Jardine et al. 2005; Tsuha et al. 2012b). The influence of the average shear stress and of the cyclic shear stress has been taken into account in Eq. (4-4), whereas the link between cyclic and monotonic responses of sand is obtained by the variable τ_{pt} calibrated by Eq. (4-1), the function of the void ratio e and of the initial effective normal stress σ'_{n0} .

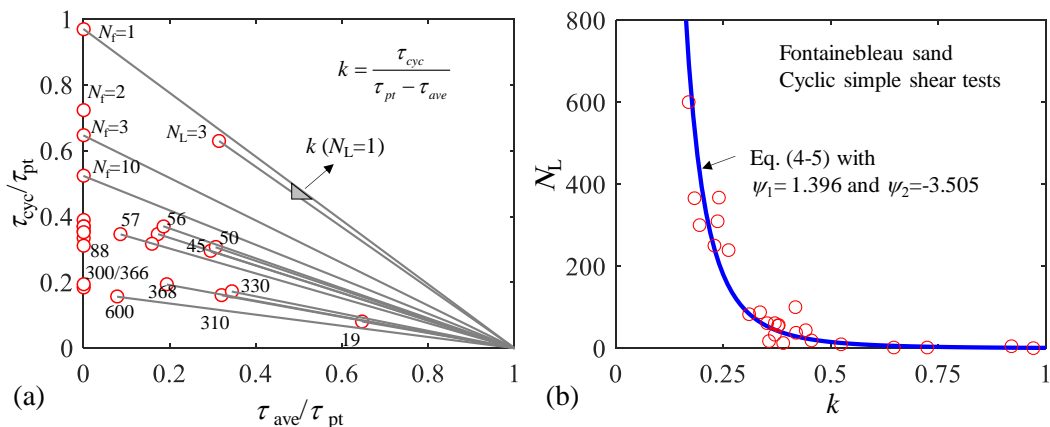


Figure 4.12 Cyclic resistance diagram for cyclic simple shear tests on Fontainebleau sand: (a) relationship between normalized cyclic shear stress and normalized average shear stress; (b) empirical curves for number of cyclic to liquefaction

4.4.2 Degradation of effective normal stress

During stress-controlled constant volume cyclic simple shear testing, the effective normal stress σ'_n decreases from its initial value either to zero or to a residual value. In agreement with the empirical expression of the pore pressure evolution suggested by Seed and Booker (Seed and Idriss 1971a), the degradation of the effective normal stress can be expressed by the following relation:

$$\frac{\sigma'_n - \sigma'_{n-residual}}{\sigma'_{n0} - \sigma'_{n-residual}} = \frac{2}{\pi} \arccos \left(\frac{N}{N_L} \right)^{\frac{1}{\bar{\theta}}} ; \left(\text{if } \tau_{ave} < \tau_{cyc}, \sigma'_{n-residual} = 0 \right) \quad (4-6)$$

where N is the current number of cycles and $\bar{\theta}$ is a material parameter.

To identify the material parameter $\bar{\theta}$, the effective normal stress σ'_n normalized by its initial value σ'_{n0} was represented as a function of the normalized number of cycles to instability (N/N_L), as shown in Figure 4.13. 6 experimental results (Tests c19, c20, c23, c26, c28 and c32) with different initial effective normal stresses, different cyclic shear stresses and different average shear stresses were selected to verify the empirical equation. The fitting of Eq. (4-6) with experimental data led to a value $\bar{\theta} = 3.4$ for Fontainebleau sand. By combining Eqs (4-5) and (4-6), the following relationship can be proposed:

$$\frac{\sigma'_n - \sigma'_{n-residual}}{\sigma'_{n0} - \sigma'_{n-residual}} = \frac{2}{\pi} \cdot \arccos \left(\frac{1}{\psi_1} \cdot N \cdot \left(\frac{\tau_{cyc}}{\tau_{pt} - \tau_{ave}} \right)^{\psi_2} \right)^{\frac{1}{\bar{\theta}}} \quad (4-7)$$

where $\sigma'_{n-residual} = 0$ kPa in the condition of cyclic stress reversal ($\tau_{cyc} > \tau_{ave}$) and $\sigma'_{n-residual}$ being calculated by using Eq. (4-3) in the condition of no-stress reversal ($\tau_{cyc} \leq \tau_{ave}$).

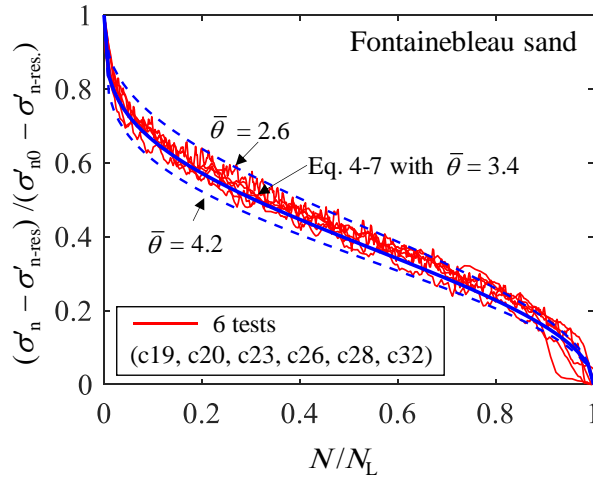


Figure 4.13 Normalized effective normal stress against normalized number of cycles to liquefaction

4.4.3 Calibration procedure

The calibration procedure for estimating the degradation of the normal effective stress is presented in Figure 4.14. Three successive steps are indicated in the calibration chart: (1) an expression of the shear stress at the phase transformation state needs to be obtained according to the results of monotonic testing as Eq.(4-1); (2) a cyclic resistance diagram (τ_{ave}/τ_{pt} , τ_{cyc}/τ_{pt} , N_L) for predicting the number of cycles to liquefaction is plotted based on the cyclic test results (with different cyclic shear stresses and average shear stresses) in order to calibrate the

parameters in Eq. (4-5); (3) the effective normal stress degradation is then calculated in order to calibrate Eqs. (4-6) and (4-7).

This analytical formulation can be easily used in practice to analyze the degradation of the shaft capacity for pile design. From this calibration procedure, a minimum of eight tests have to be considered for determining the material parameters, including at least 3 monotonic tests with different void ratios to determine the phase transformation state, 3 symmetrical cyclic loading tests with different cyclic stress amplitudes τ_{cyc} and 2 non-symmetrical cyclic loading tests with different average shear stresses τ_{ave} to study the degradation of the effective normal stress with the number of cycles.

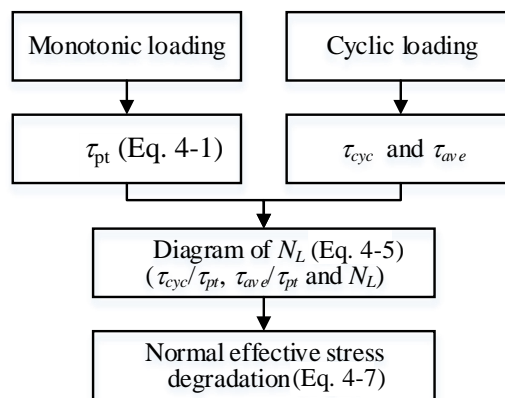


Figure 4.14 Calibration procedure for the degradation of the effective normal stress

In order to validate the whole procedure, simple shear tests on Fraser River sand (Sivathayalan 1994), Quiou carbonate sand (Porcino et al. 2008), and triaxial tests on Karlsruhe sand (Wichtmann and Triantafyllidis 2016a, 2016b) were selected. The physical properties of these three sands are presented in Table 4.2.

Table 4.2 Physical properties of three studied sands

Material	D_{50} (mm)	C_u	G_s	e_{max}	e_{min}
Fraser River sand	0.30	1.6	2.72	1.000	0.680
Quiou sand	0.65	2.8	2.70	1.169	0.763
Karlsruhe sand	0.14	1.5	2.70	1.054	0.677

The normalized shear stresses at PTL (τ_{pt}/σ'_{n0} for simple shear tests and $q_{pt}/2p'_0$ for triaxial tests) were plotted against the corresponding relative densities in Figure 4.15. The curves calculated from Eq.(4-1) as solid lines were fitted from the experimental data and the deduced parameters are given in Table 4.2. The cyclic stability diagram for calibrating the number of cycles to instability is shown in Figure 4.16. The parameters ψ_1 and ψ_2 could be obtained by fitting the experimental results as shown in Table 4.3. Therefore, the behavior of

different sands (quartz sand and carbonate sand) for different loading conditions (simple shear and triaxial loading) can be well expressed by Eq.s (4-1) and (4-5).

Table 4.3 Parameters of empirical model for number of cyclic to liquefaction

Material	M_1	M_2	ϕ_{pt} ($^\circ$)	ψ_1	ψ_2
Fontainebleau sand	0.68	1.76	24	1.396	3.505
Fraser River sand	1.233	1.478	30	3.183	2.787
Quiou sand	0.767	0.318	27	1.004	4.353
Karlsruhe sand	0.738	0.746	29.6	1.498	4.764

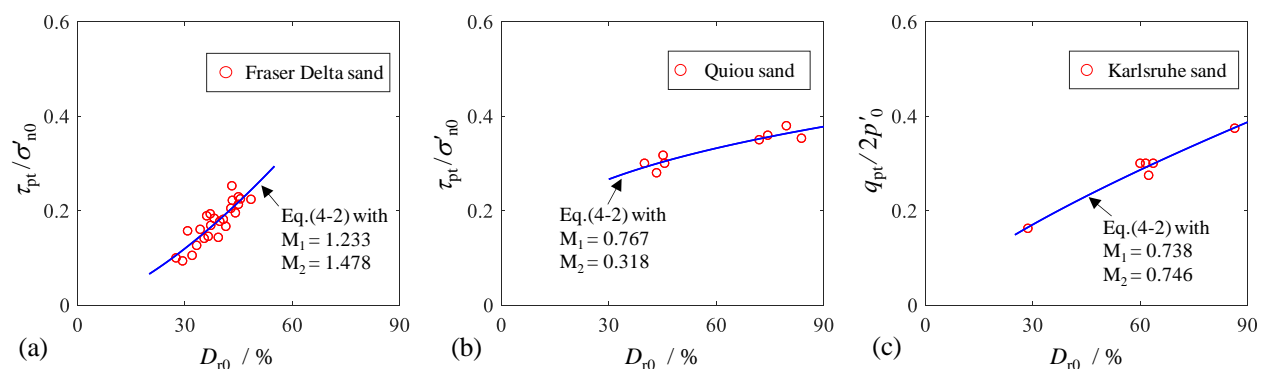


Figure 4.15 Calibration results of normalized shear stress at phase transformation state: (a) Fraser River sand; (2) Quiou sand; (3) Karlsruhe sand

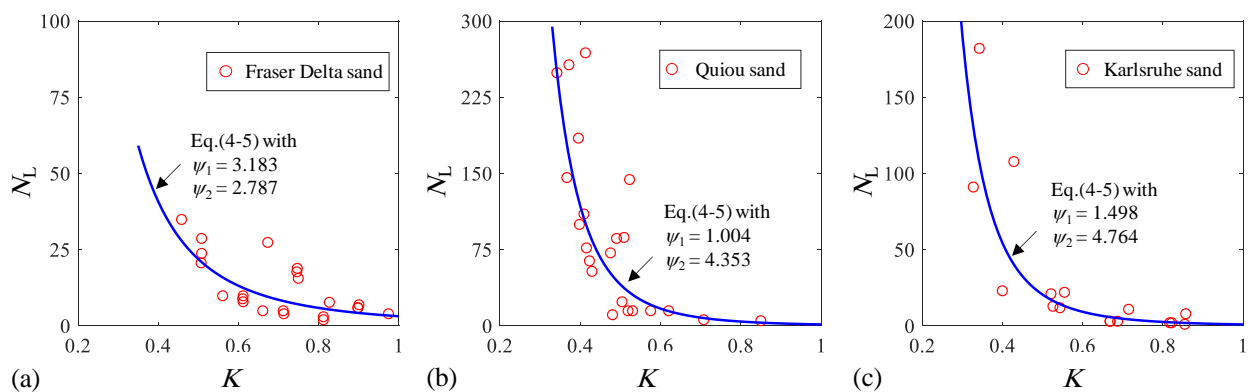


Figure 4.16 Calibration results of numbers of cycles to instability: (a) Fraser River sand; (2) Quiou sand; (3) Karlsruhe sand

4.4.4 Validation of the suggested relationship

The calibration procedure has provided the following parameters for Fontainebleau sand: $M_1 = 0.68$, $M_2 = 1.76$, $\psi_1 = 1.396$, $\psi_2 = 3.505$, $\theta_c = 3.4$. The tests presented in Table 4.1 can be considered as the training tests aimed to determine these parameters. 6 complementary tests with different loading conditions were selected and simulated to validate the performance of

Eq. (4-7). As shown in Figure 4.17(a), the results can be well predicted for different loading conditions including symmetrical cyclic loadings with different τ_{cyc} (Tests c19, c20 and c23) and non-symmetrical cyclic loadings with different τ_{ave} (Tests c26, c28 and c32).

To confirm the pertinence of this equation, a series of additional tests on Fontainebleau sand was performed at a consolidation stress level $\sigma'_{n0} = 500$ kPa with different loading paths including cyclic shear stresses from 12.5 kPa to 50 kPa and average shear stresses from 0 kPa to 50 kPa (Table 4.4). The results of these additional tests are presented in Figure 4.17(b), showing a behavior similar to the one obtained from the results of the training tests reported in Table 4.1. All additional tests were also simulated by Eq. (4-7) to verify the accuracy of the analytical method for predicting the mechanical behavior of a given sand. Figure 4.17(b) presents the comparison between the calculated effective normal stress (solid blue line) and the experimental data (red symbols). It demonstrates that Eq. (4-7) can successfully describe the evolution of the effective normal stress for a large range of average shear stresses and cyclic shear stresses.

Table 4.4 Summary of additional tests on Fontainebleau sand ($\sigma'_{n0} = 500$ kPa)

Test No.	e_0	τ_{ave} (kPa)	τ_{cyc} (kPa)	τ_{ave}/σ'_{n0}	CSR	τ_{pt} (kPa)	N_L
B1	0.619	0	12.5	0	0.025	85.5	1015
B2	0.626	0	25	0	0.05	81.6	74
B3	0.612	0	50	0	0.1	89.6	4
B4	0.613	12.5	25	0.025	0.05	89.0	64
B5	0.609	25	25	0.05	0.05	91.3	36
B6	0.619	50	25	0.1	0.05	85.5	1

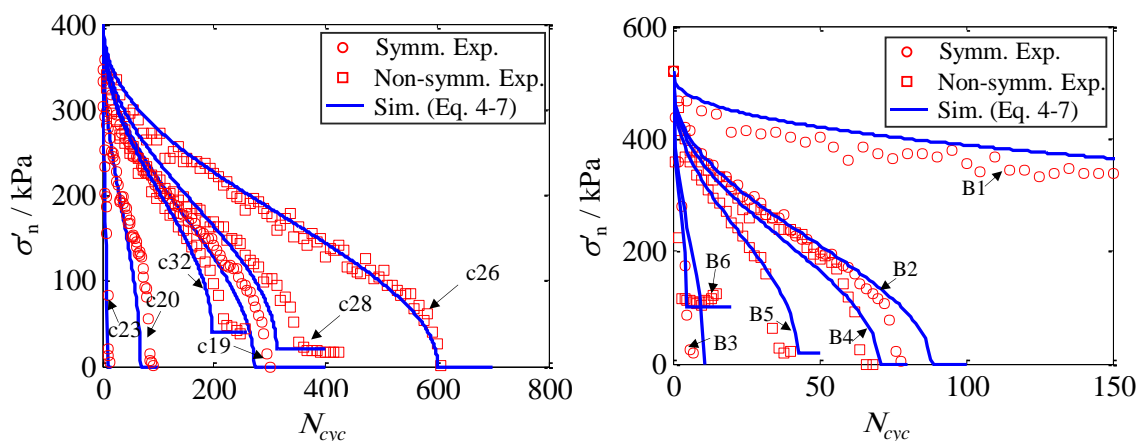


Figure 4.17 Comparisons between simulations and experiments on Fontainebleau sand: (a) training tests; (b) additional tests

4.5 Conclusions

The aim of the chapter has been to develop an analytical method for predicting the degradation of the effective normal stress of a soil element adjacent to a pile shaft under cyclic loading. The development of the analytical formulation was supported by a series of constant volume monotonic and cyclic simple shear tests performed on Fontainebleau sand specimens.

Monotonic simple shear tests on Fontainebleau sand with different void ratios and different initial normal effective stresses were firstly performed, allowing an empirical expression for calculating the shear stress at the phase transformation state to be suggested.

Then, cyclic simple shear tests were conducted under different initial effective normal stresses, cyclic shear stresses, and average shear stresses. Based on these experimental results, a cyclic resistance diagram was obtained, providing information concerning the number of cycles necessary to reach instability as a function of cyclic and average shear stress levels. The shear stress at the phase transformation state took into account the influence of void ratio and initial effective normal stress on the number of cycles to instability.

A calibration procedure for predicting the degradation of the effective normal stress was proposed. Following this procedure, an analytical expression to evaluate the normal effective stress degradation was developed with the following variables: void ratio, initial effective normal stress, cyclic shear stress, average shear stress and number of cycles. A series of additional tests including loading paths with different average shear stresses and cyclic shear stresses verified the proposed analytical expression. All comparisons between experimental results and simulations indicated that the proposed method is capable of predicting the degradation of the effective normal stress under constant volume cyclic shear loading.

Chapter 5 Cyclic volumetric strain accumulation of sand under drained simple shear condition

5.1 Introduction

During long-term cyclic loading, because of cyclic strain accumulation in the soils surrounding piles, the serviceability of a pile foundation will be adversely affected (Figure 4.1). According to the classical Mohr-Coulomb criterion, the mobilised shear stress acting on the pile shaft depends on the level of the radial effective stress applied to the soil-pile interface (Lehane et al. 1993; Jardine et al. 2005), meaning that any change in the radial effective stress or strain caused by cyclic loading will greatly affect the bearing capacity of the pile foundation. Hence, to explain the basic mechanisms of pile resistance under cyclic loading, a large number of field and/or laboratory-based model pile cyclic loading tests have been performed over the past few decades. For example, Jardine and Standing (2000, 2012) demonstrated that a high level of cyclic loading is highly detrimental to shaft capacity, based on their experimental results on an in-situ pile test being subjected to a large amount of axial cyclic loading. More recently, Yang et al. (2010), Tsuha et al. (2012a) and Rimoy (2013) presented a series of reduced-scale cyclic tests, using the mini-Imperial College pile (ICP), that demonstrated the cyclic degradation of radial stresses adjacent to the pile. All cyclic pile tests show that the shaft capacity depends on the mechanical response of a soil element (strain or excess pore pressure accumulation) adjacent to a pile under cyclic loading (Bekki et al. 2016; Le Kouby et al. 2016; Kerner et al. 2017). Thus, it is of great importance to study the cyclic behaviour of the soil element around the pile.

In a laboratory elementary test, to obtain high-quality and reliable data, in-situ conditions should be replicated as closely as possible. Three general types of laboratory equipment, with easily operable features, have been widely used to study the soil element's behaviour around the pile, including triaxial tests, direct interface shear tests and simple shear tests. Recently, the cyclic behaviour of soils has been widely studied via triaxial tests (Wichtmann et al. 2005; Coop and López-Querol 2012; Sim et al. 2013b; Mamou et al. 2017; Sun et al. 2017). However, without the principle stress rotation, the real shearing state of soils adjacent to the pile still cannot be adequately replicated, which utterly restricts its application to shaft degradation. Moreover, Boulon and Foray (1986) suggested that the constant normal stiffness condition can reproduce the interface pile-loading boundary conditions. Following this proposition, Pra-ai and Boulon (2017) performed a series of cyclic constant normal stiffness direct interface shear tests with a large number of cycles, to investigate the progressive degradation of normal effective stress. However, the value of normal stiffness depends on the

sample depth (through the pressuremeter modulus) and the pile radius, which also limits its general application.

Comparing it against triaxial tests and direct shear tests, Anderson (2009) pointed out that the simple shear test has been acknowledged to provide more representative loading conditions for shearing of soils adjacent to a pile, such as that the cyclic shear strain develops more symmetrically than triaxial tests and can also take into account the principle shear rotation during the shear process. That said, the simple shear test is unable to represent the relative displacement between the soil and the structure at the interface. A large number of undrained or constant volume cyclic simple shear tests have been conducted to investigate the cyclic responses of soils, including liquefaction, degradation of both shear stiffness and the damping ratio, and effective normal stress (Vaid et al. 2001; Matsuda et al. 2011; Da Fonseca et al. 2015; Porcino et al. 2015). However, the strain-related cyclic response has received less discussion, and the cyclic strain accumulation behaviour, under the drained or constant normal stress condition, remains unclear because of a lack of relevant tests, although it is considered an important impact factor for the analysis of shaft capacity (Wichtmann et al. 2005; Nikitas et al. 2017).

The aim of this chapter is to analyse the volumetric strain accumulation in sand specimens through cyclic simple shear tests under constant normal stress condition. A series of drained cyclic simple shear tests was first performed on Fontainebleau sand, which includes four initial states with different factors: (1) initial void ratios, (2) initial normal stresses, (3) cyclic shear stresses and (4) average shear stresses. Moreover, the experimental results were also interpreted to summarise the relationships between volumetric strain accumulation and each factor. Finally, the development of an analytical model, to predict the cyclic accumulation of volumetric strain, is expounded, taking into account the effect of the initial void ratio, initial normal stress, cyclic shear stress and average shear stresses.

5.2 Experimental investigation

5.2.1 Testing program

The drained simple shear testing was ensured by constraining a constant effective normal stress σ'_n on the dry specimen after K_0 -consolidation. The cyclic shear motion, inducing a cyclic shear stress τ_{cyc} , was generated by the displacement of the bottom pedestal, while the top one was horizontally fixed. For cyclic loading, sine cycles with a frequency of 0.2 Hz were applied. The volumetric strain $\varepsilon_v = \Delta H/H_c$ was measured by the change of the specimen height (ΔH) during the cyclic process over the height after consolidation (H_c).

To investigate the effects of different initial states and propose a general analytical model for calculating the volumetric strain accumulation, a total of 20 tests were conducted, as shown in Table 5.1 These tests can be divided into four groups as follows: (1) different initial

void ratio e_0 (No. 1–4); (2) different initial normal stress σ'_n (No. 2, 5–7); (3) different cyclic stress ratio $CSR = \tau_{cyc}/\sigma'_n$ (No. 8–12); and (4) different average stress ratio $\alpha = \tau_{ave}/\sigma'_n$ (No. 2, 13–15). In addition, other tests (No. 16–20), with initial states that differed from those of the first 15, were conducted to validate the analytical model.

Table 5.1 Experimental program of cyclic simple shear tests

No.	e_i	e_0	D_r /%	σ'_n /kPa	τ_{cyc} /kPa	τ_{ave} /kPa	α	CSR	N
1	0.697	0.668	57.6	416	41.6	0	0	0.1	5000
2	0.651	0.628	68.2	416	41.6	0	0	0.1	5000
3	0.592	0.568	84.3	416	41.6	0	0	0.1	5000
4	0.559	0.539	92.2	416	41.6	0	0	0.1	5000
5	0.646	0.623	69.7	52	5.2	0	0	0.1	5000
6	0.649	0.627	68.5	104	10.4	0	0	0.1	5000
7	0.650	0.619	70.5	208	20.8	0	0	0.1	5000
8	0.640	0.604	74.8	416	41.6	0	0	0.1	5000
9	0.635	0.606	74.3	416	50.0	0	0	0.12	5000
10	0.641	0.609	73.4	416	83.2	0	0	0.2	5000
11	0.635	0.601	75.4	416	104.0	0	0	0.25	5000
12	0.639	0.605	74.3	416	133.1	0	0	0.32	5000
13	0.650	0.628	68.2	416	41.6	20.8	0.05	0.1	5000
14	0.650	0.631	67.5	416	41.6	41.6	0.1	0.1	5000
15	0.650	0.629	67.8	416	41.6	83.2	0.2	0.1	5000
16	0.737	0.703	48.2	416	41.6	0	0	0.1	5000
17	0.552	0.536	93.4	416	41.6	0	0	0.1	5000
18	0.649	0.604	74.7	416	20.8	0	0	0.05	5000
19	0.639	0.606	74.2	416	166.4	0	0	0.4	5000
20	0.650	0.629	67.8	416	41.6	124.8	0.3	0.1	5000

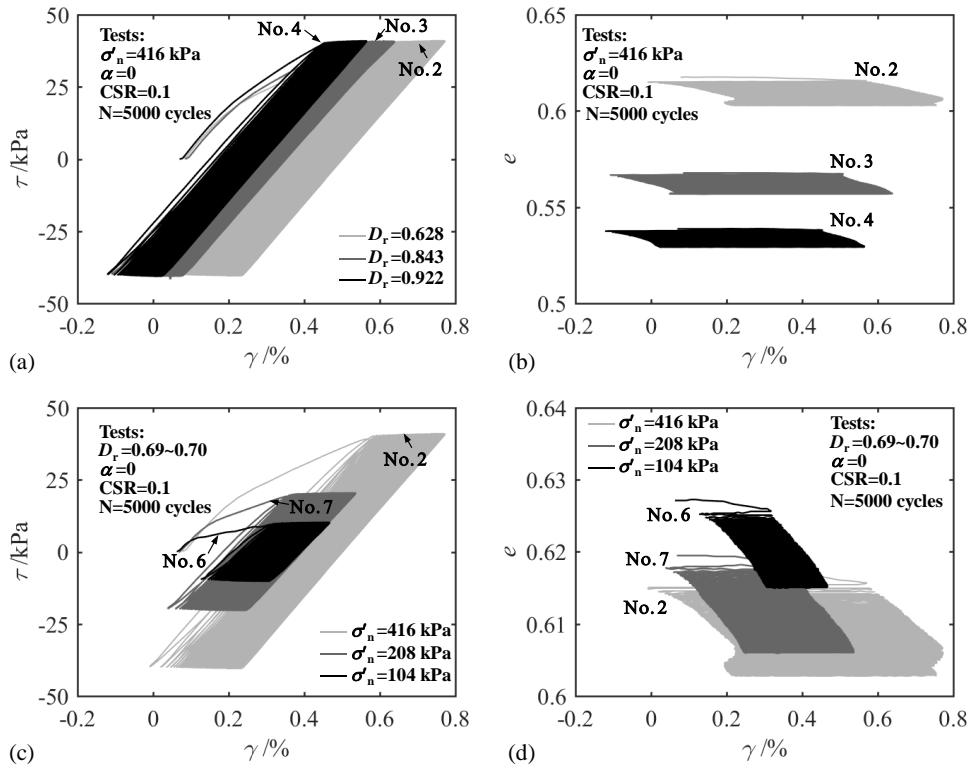
Noted: e_i is the initial void ratio; e_0 is void ratio after consolidation; D_r is relative density; σ'_n is normal effective stress; τ_{cyc} is cyclic shear stress; τ_{ave} is average shear stress and N is number of cycles. Furthermore, for the test considering the effect of average shear stress (as No.13, 14, 15 and 20), the initial average shear stress τ_{ave} is reached in drained condition, and its void ratio after initial average shearing respectively corresponds to 0.628(No.13), 0.628(No.14), 0.625(No.15) and 0.622(No.20).

5.2.2 Cyclic densification

Based on the experimental results, the cyclic responses of specimens were first studied by plotting the stress-strain paths, as seen in Figure 5.1. Four groups of experimental parametric analyses were carried out, as follows:

- 1) For different relative densities D_r (Figure 5.1 a-b), the stress-controlled cyclic shearing condition will lead to un-asymmetrical accumulation of shear strain γ , and the looser sand corresponds to a larger level of shear strain accumulation as well as of densification;
- 2) For different normal stress levels σ'_n (Figure 5.1 c-d), with the increase in the initial normal stress σ'_n , the magnitude of shear strain accumulation rises and also produces a larger level of densification for sand;
- 3) For different cyclic shear stress ratios (CSR) (Figure 5.1 e-f), it may be observed that the shear strain γ and void ratio e are highly sensitive to the amplitude of cyclic shear stress τ_{cyc} , in which a greater magnitude of CSR will lead to greater shear strain accumulation as well as a larger degree of densification, especially in the initial five cycles;
- 4) For different average shear stress ratios α (Figure 5.1 g-h), an increase in average shear stress will promote the accumulation of shear strain γ and restrain the magnitude of densification.

Overall, cyclic tests reveal that the volumetric strain is regularly accumulated during cyclic loading, and that it is possible to formulate the volumetric strain accumulation based on different effects (see details of the parametric study in section 5.3).



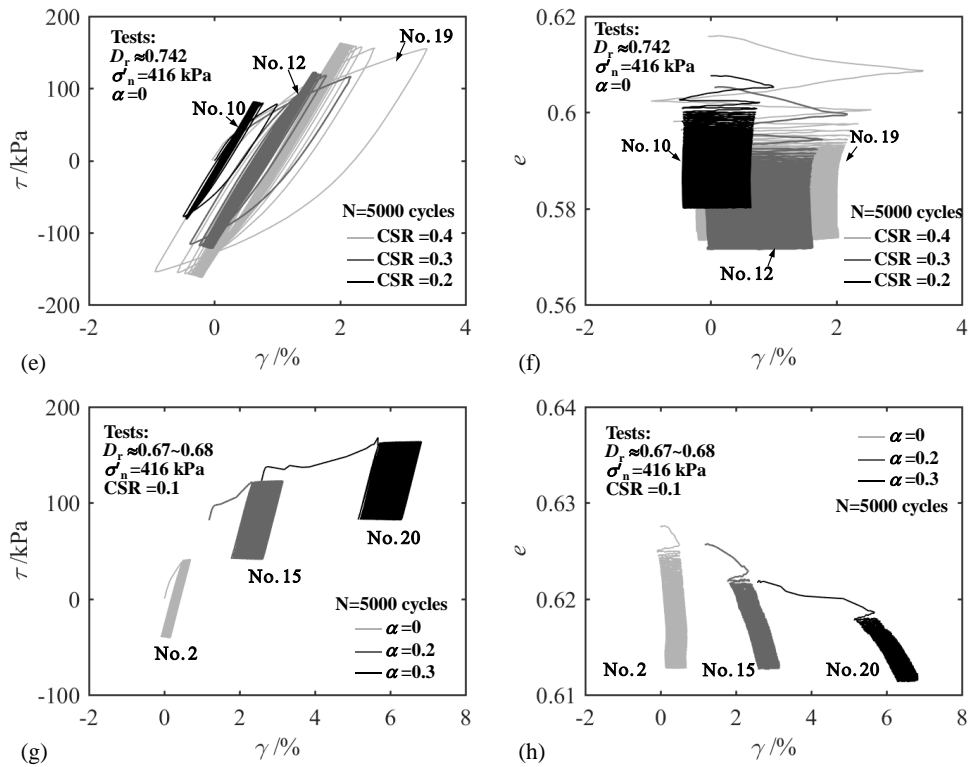


Figure 5.1 Summary of drained cyclic simple shear results: (a)-(b) comparisons by different initial relative densities; (c)-(d) comparisons by different effective normal stresses; (e)-(f) comparisons by different cyclic shear stress ratios and (g)-(h) comparisons by different average shear stress ratios.

5.2.3 Influence of strain accumulation to post-cyclic behaviour

A series of monotonic simple shear tests was also subsequently conducted after cyclic testing phases (see Table 5.1), to investigate the influence of strain accumulation to the peak shear strength ratio and phase transformation stress ratio.

Figure 5.2 presents the experimental results including the stress-strain paths (τ - γ - ϵ_v) and also the stress-dilatancy relation expressed by the stress ratio (τ/σ'_n) versus strain increment ratio ($d\epsilon_v/d\gamma$). According to these results, a unique critical state can be found for different initial conditions. Additionally, during long-term cyclic loading, volumetric strain gradually accumulates and the specimen becomes denser (see Figure 5.2(b, e, i and l)). Such cyclic densification enhanced the peak shear stress and also influenced the stress-dilatancy as shown in Figure 5.2(c, f, j and m) with the amount of dilation range greater than the contraction range. Moreover, Figure 5.2(j) shows that the larger cyclic shear stress ratio CSR corresponds to steeper slope of strain increment ratio. For instance, no strain contraction occurs for test No.8, which was conducted after the largest cyclic shear stress $\tau_{cyc}=160$ kPa.

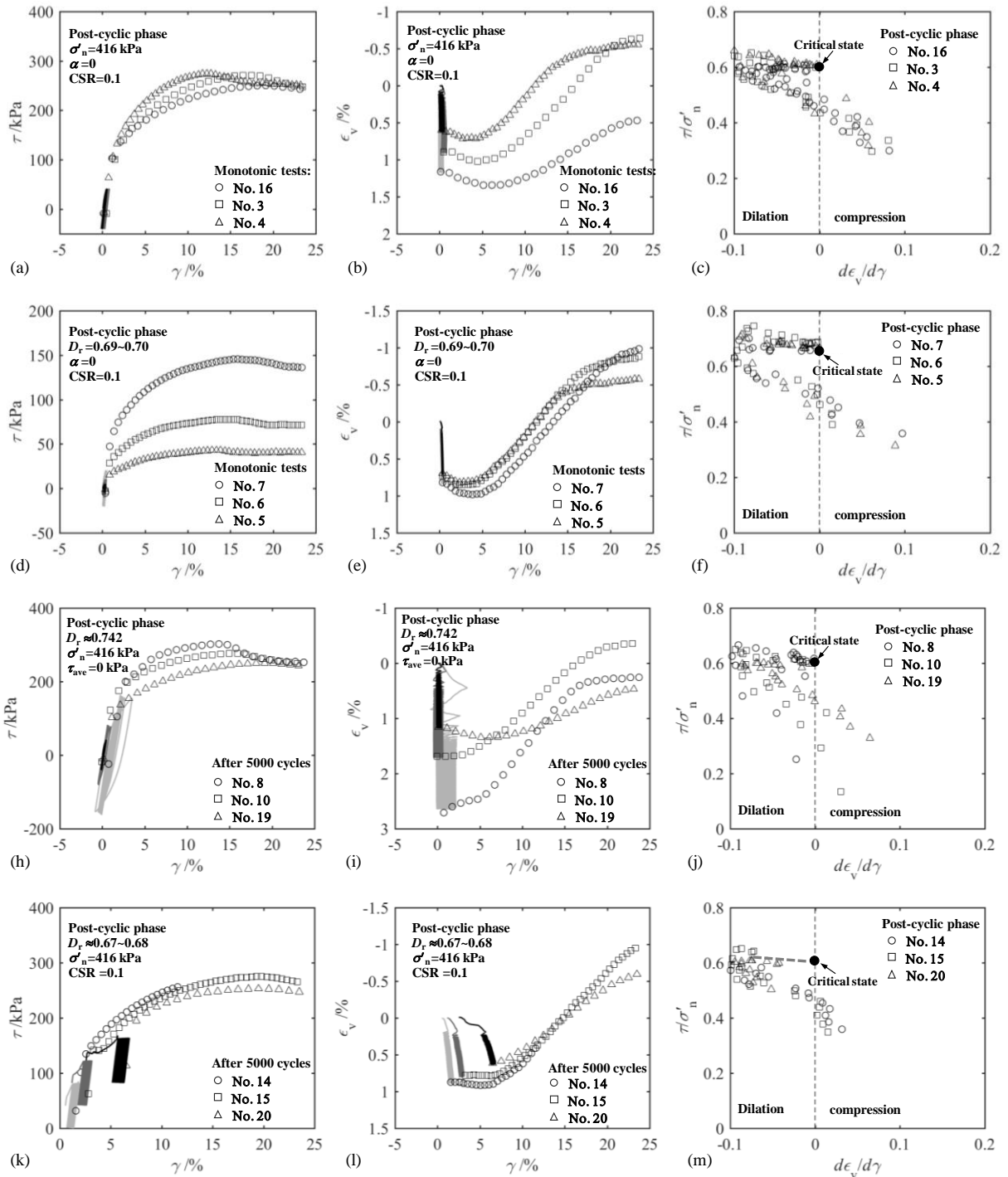


Figure 5.2 Summary of drained monotonic simple shear after 5000 cycles: (a)-(c) comparisons by different initial relative densities; (d)-(f) comparisons by different effective normal stresses; (h)-(j) comparisons by different cyclic shear stress ratios; (k)-(m) comparisons by different average shear stress ratios

5.3 Interpretation of experimental results

5.3.1 Effect of relative density

The effect of the relative density D_r , varying from 0.576 to 0.922 on strain accumulation ε_v , was studied, based on tests (No. 1–4) with constant cyclic shear stress and normal stress. Figure 5.3(a) demonstrates that sand with lower relative density has a higher strain accumulation, while Figure 5.3(b) presents the volumetric strains ε_v against the relative density D_r for selected numbers of cycles corresponding to $N = 3, 10, 100, 1000, 2000$ and 4000 respectively. Conventionally, the positive volumetric strain is for describing contractive behaviour and the negative volumetric strain is for describing dilative behaviour. This shows that the accumulated volumetric strain ε_v decreases linearly with the increase in relative density for each selected number, which can be expressed as:

$$\frac{\varepsilon_v}{\varepsilon_{v-D_r}^{ref}} = \left(\frac{D_r}{D_r^{ref}} \right)^{c_1} \quad (5-1)$$

where c_1 is the slope of the curve in the double-logarithmic plot; this can be considered as the same for different numbers of cycles. For convenience, the reference relative density is considered as $D_r^{ref} = 1$. Then six reference volumetric strains $\varepsilon_{v-D_r}^{ref}$ at $D_r^{ref} = 1$ in Figure 5.3(b) can be obtained for six selected numbers of cycles N , which is plotted in Figure 5.3(c). Based on this linear relationship, the reference volumetric strain can be expressed by:

$$\varepsilon_{v-D_r}^{ref} = n_1 \log(N + 1) \quad (5-2)$$

in which n_1 is the slope of the curve in the semi-logarithmic plot, with null volumetric strain at zero number of cycles.

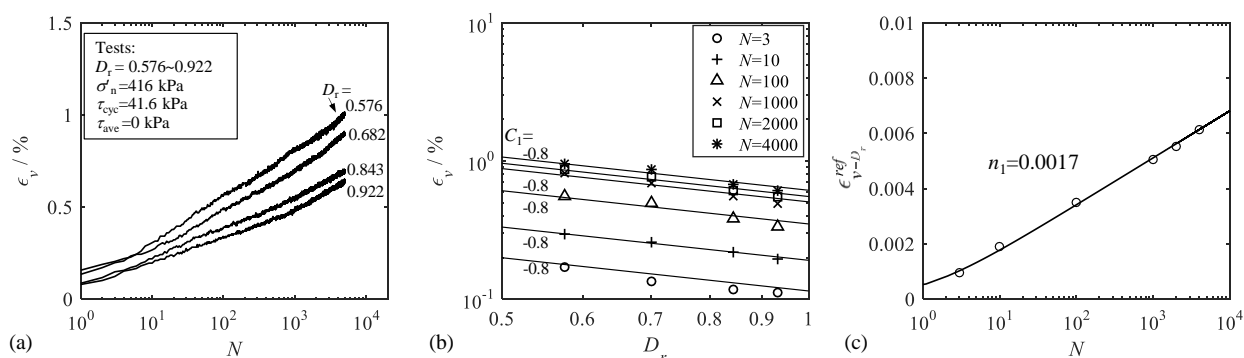


Figure 5.3 volumetric strain accumulation with different relative densities: (a) volumetric strain versus number of cycles; (b) volumetric strain versus relative density; (c) reference volumetric strain versus number of cycles

Substituting Eq.(5-2) in Eq.(5-1), the volumetric strain, evolving with the number of cycles and considering the effect of initial density, is finally expressed by:

$$\varepsilon_v = n_1 D_r^{C_1} \log(N+1) \quad (5-3)$$

5.3.2 Effect of normal stress level

The effect of the normal stress on strain accumulation, varying from 52 to 416kPa, was studied with a constant cyclic stress ratio (CSR = 0.1) and relative density ($D_r = 0.68 \sim 0.7$) based on tests (No. 2, 5–7). Figure 5.4(a) shows that sand with a higher normal stress corresponds to a higher volumetric strain accumulation; Figure 5.4(b) presents the volumetric strains ε_v versus the ratio of normalised normal stresses over atmospheric pressure ($p_{at} = 100\text{kPa}$) in each selected number of cycles, corresponding to $N = 2, 10, 100, 1000, 2000$ and 4000 respectively. This shows that the accumulated volumetric strain ε_v increases linearly with the increase in normal stress for each selected number, which can be expressed as:

$$\frac{\varepsilon_v}{\varepsilon_{v-\sigma'_n}^{ref}} = \left(\frac{\sigma'_n}{p_{at}} \right)^{C_2} \quad (5-4)$$

where C_2 is the slope of the curve in a double-logarithmic plot, which can be considered similar for different numbers of cycles. Six reference volumetric strains $\varepsilon_{v-\sigma'_n}^{ref}$ at $\sigma'_n = p_{at}$ in Figure 5.4 (b) can be obtained for six selected numbers of cycles N .

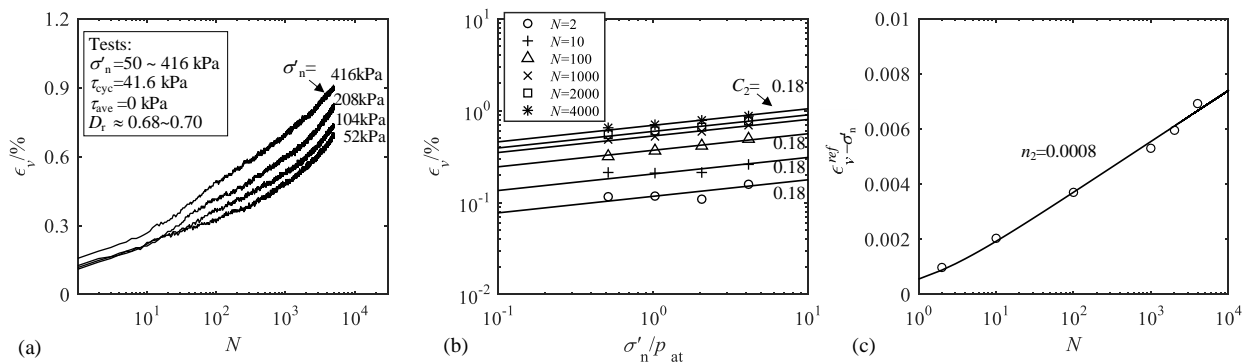


Figure 5.4 volumetric strain accumulation with different normal stress level: (a) volumetric strain versus number of cycles; (b) volumetric strain versus normal stress level; (c) reference volumetric strain versus number of cycles

Figure 5.4(c) presents the relationship between the reference volumetric strain and the cyclic number N in semi-logarithmic coordinates, which can be expressed by:

$$\varepsilon_{v-\sigma'_n}^{ref} = n_2 \log(N+1) \quad (5-5)$$

where n_2 is the slope of the curve in a semi-logarithmic plot with null volumetric strain at zero number of cycles. The evaluation of volumetric strain with number of cycles, considering the effect of normal stress, can ultimately be expressed as follows,

$$\varepsilon_v = n_2 \left(\frac{\sigma'_n}{p_{at}} \right)^{C_2} \log(N+1) \quad (5-6)$$

5.3.3 Effect of cyclic shear stress ratio

The effect of CSR ($= \tau_{cyc}/\sigma'_n$) on volumetric strain ε_v , varying from 0.1 to 0.32, was studied based on tests (No. 8–12) with constant normal stress ($\sigma'_n = 416\text{kPa}$), null average shear stress and constant relative density ($D_r = 0.73\sim 0.75$). Figure 5.5(a) shows that sand with a higher cyclic stress ratio corresponds to a higher rate of cyclic volumetric strain accumulation. To minimise the effects of normal stress and relative density, the volumetric strain ε_v was first normalised by the density-related function (Eq.(5-1)) and normal stress-related function (Eq.(5-4)), as shown in Eq.(5-7). Then, the normalized volumetric strain $\bar{\varepsilon}_v$ could be used to compare the cases between different CSRs.

$$\bar{\varepsilon}_v = \frac{\varepsilon_v}{D_r^{C_1} \cdot (\sigma'_n/p_{at})^{C_2}} \quad (5-7)$$

Figure 5.5(b) shows the normalised volumetric strains $\bar{\varepsilon}_v$ versus the CSR for selected numbers of cycles, corresponding to $N = 3, 10, 100, 1000, 2000$ and 4000 , respectively. This denotes that the relationship between normalised volumetric strains and CSRs for a selected cyclic number can be expressed as follows:

$$\bar{\varepsilon}_v = C_3 \cdot CSR^{\varepsilon_{v-CSR}^{ref}} \quad (5-8)$$

where C_3 is a constant corresponding to the value when the CSR equals one, and the slope corresponds to the reference volumetric strain $\varepsilon_{v-CSR}^{ref}$. Six reference volumetric strains $\varepsilon_{v-CSR}^{ref}$ were plotted against the selected numbers of cycles N in Figure 5.5 (c), which can be expressed by Eq.(5-9):

$$\varepsilon_{v-CSR}^{ref} = C_4 \cdot (N)^{C_5} \quad (5-9)$$

where C_4 and C_5 are CSR-related parameters obtained by fitting the curve.

The accumulated volumetric strain, taking into account the effect of CSR, can finally be derived by substituting Eq.(5-9) into Eq.(5-8), as follows:

$$\bar{\varepsilon}_v = C_3 \cdot CSR^{C_4 \cdot (N)^{C_5}} \quad (5-10)$$

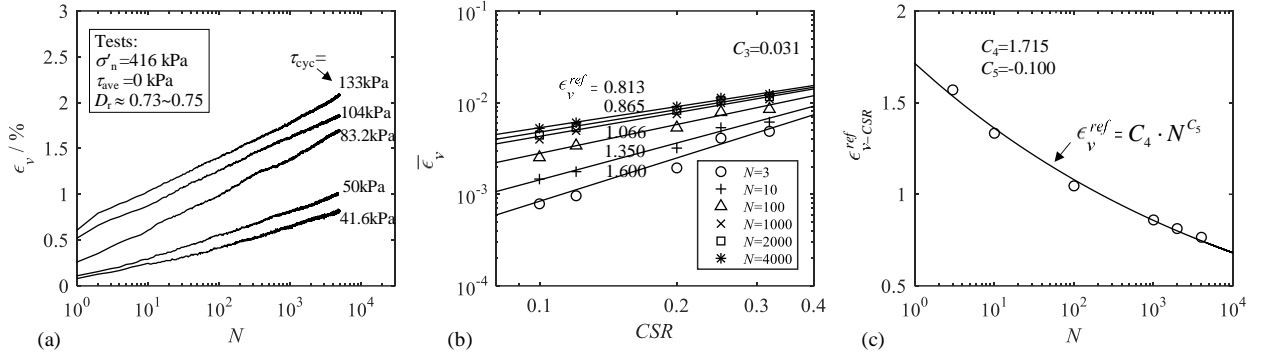


Figure 5.5 volumetric strain accumulation with different cyclic stress ratio: (a) volumetric strain versus number of cycles; (b) normalized volumetric strain versus cyclic shear stress ratio; (c) reference volumetric strain versus number of cycles

5.3.4 Effect of average shear stress ratio

The effect of the average shear stress ratio α ($= \tau_{ave}/\sigma'_n$) on volumetric strain ϵ_v , varying from 0 to 0.2, was studied based on tests (No. 2, 13–15) with constant normal stress and CSR. The initial average shear stress is reached in drained condition. Figure 5.6 (a) shows that sand with a higher average shear stress corresponds to a lower rate of volumetric accumulation. Figure 5.6 (b) presents the normalised volumetric strains $\bar{\epsilon}_v$ versus the average stress ratio, in the selected numbers of cycles corresponding to $N = 2, 10, 100, 1000, 2000$ and 4000. The accumulated, normalised volumetric strain $\bar{\epsilon}_v$ can be expressed by Eq.(5-11):

$$\bar{\epsilon}_v = (\bar{\epsilon}_v)_{\alpha=0} + \epsilon_{v-\alpha}^{ref} \cdot \alpha \quad (5-11)$$

where $(\bar{\epsilon}_v)_{\alpha=0}$ is the accumulated volumetric strain for the case with zero average shear stress. The reference volumetric strain $\epsilon_{v-\alpha}^{ref}$ corresponds to the slope of normalised volumetric strains versus average shear stress ratio for each selected number of cycles. This shows that the slope decreases from positive to negative with the increase in numbers of cycles.

Figure 5.6(c) presents the relationship between the six reference volumetric strains $\epsilon_{v-\alpha}^{ref}$ and the selected numbers of cycles N , which can be fitted by the linear expression in semi-logarithmic coordinates, per Eq.(5-12):

$$\epsilon_{v-\alpha}^{ref} = C_6 \log(N+1) + C_7 \quad (5-12)$$

where C_6 and C_7 are average shear stress ratio-related parameters. Substituting Eq.(5-12) into Eq.(5-11), the volumetric strain, evolving with the number of cycles and considering the effect of average shear stress, is finally expressed by Eq.(5-13):

$$\bar{\epsilon}_v = (\bar{\epsilon}_v)_{\alpha=0} + \alpha [C_6 \log(N+1) + C_7] \quad (5-13)$$

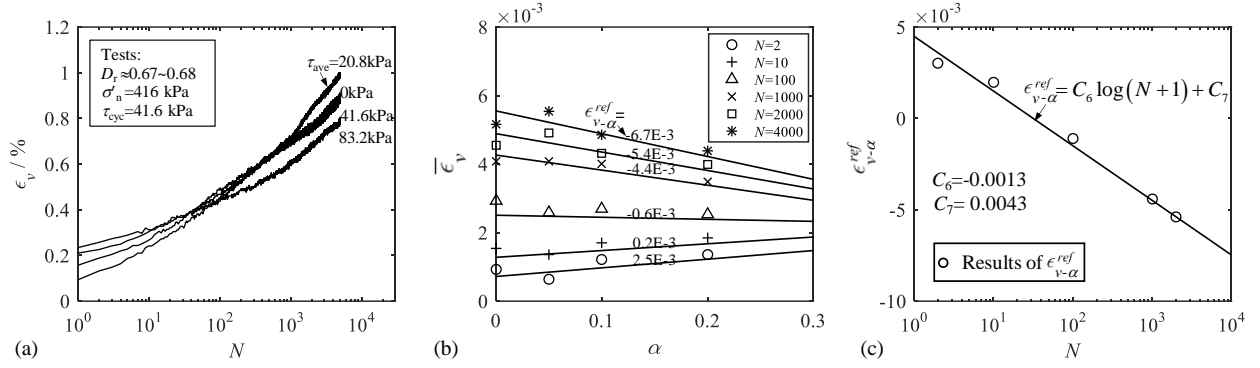


Figure 5.6 Volumetric strain accumulation with different average shear stress ratio: (a) volumetric strain versus number of cycles; (b) normalized volumetric strain versus average shear stress ratio; (c) reference volumetric strain versus number of cycles

5.4 Analytical model of volumetric strain accumulation

Based on the previous parametric study, we can conclude that the cyclic volumetric strain accumulation depends on four key factors: relative density, normal stress level, CSR and average shear stress ratio. Thus, a general analytical model can be derived by combining Eq.(5-7), (5-10) and (5-13) as follows:

$$\varepsilon_v = D_r^{C_1} \left(\frac{\sigma'_n}{p'_{at}} \right)^{C_2} \left[C_3 \cdot CSR^{C_4 \cdot N^{C_5}} + \alpha (C_6 \ln(N+1) + C_7) \right] \quad (5-14)$$

which has seven related parameters, as summarised in Table 5.2, that are calibrated by training tests, as shown in Figures 5.3-5.6.

Table 5.2 Summary of the empirical function with parameters of Fontainebleau sand

Function	Parameters	
D_r related function $f_{den} = (D_r / D_r^{ref})^{C_1}$	C_1	-0.8
σ'_n related function $f_{nor} = (\sigma'_n / p'_{at})^{C_2}$	C_2	0.18
CSR related function $f_{CSR} = C_3 \cdot CSR^{C_4 \cdot N^{C_5}}$	C_3	0.031
	C_4	1.715
	C_5	-0.100
α related function $f_\alpha = (C_6 \ln N + C_7) \cdot \alpha$	C_6	-0.0013
	C_7	0.0043

To validate the performance of the proposed analytical model, the previous training tests were selected to replicate the volumetric strain accumulation during cyclic loading, as shown

in Figure 5.7. Through comparison of the experimental results in Figures 5.3-5.6, it is shown that the calculated curves are in good agreement with the experimental results. Moreover, the basic characteristics of volumetric strain accumulation, considering the four effects, can be summarised as follows:

- 1) For different relative densities (D_r) with $CSR = 0.1$, the accumulation ratio gradually decreases with the increase in density (Figure 5.7(a)).
- 2) The effect of the initial normal stress σ'_n is similar to the effect of relative densities (D_r); that is, the accumulation ratio gradually rises with increasing normal stress (Figure 5.7(b)).
- 3) For CSRs, a greater value will produce a larger accumulation from the first cycle to the subsequent 5000 cycles, which means that the volumetric strain is highly sensitive to the CSR throughout the cyclic process (Figure 5.7(c)).

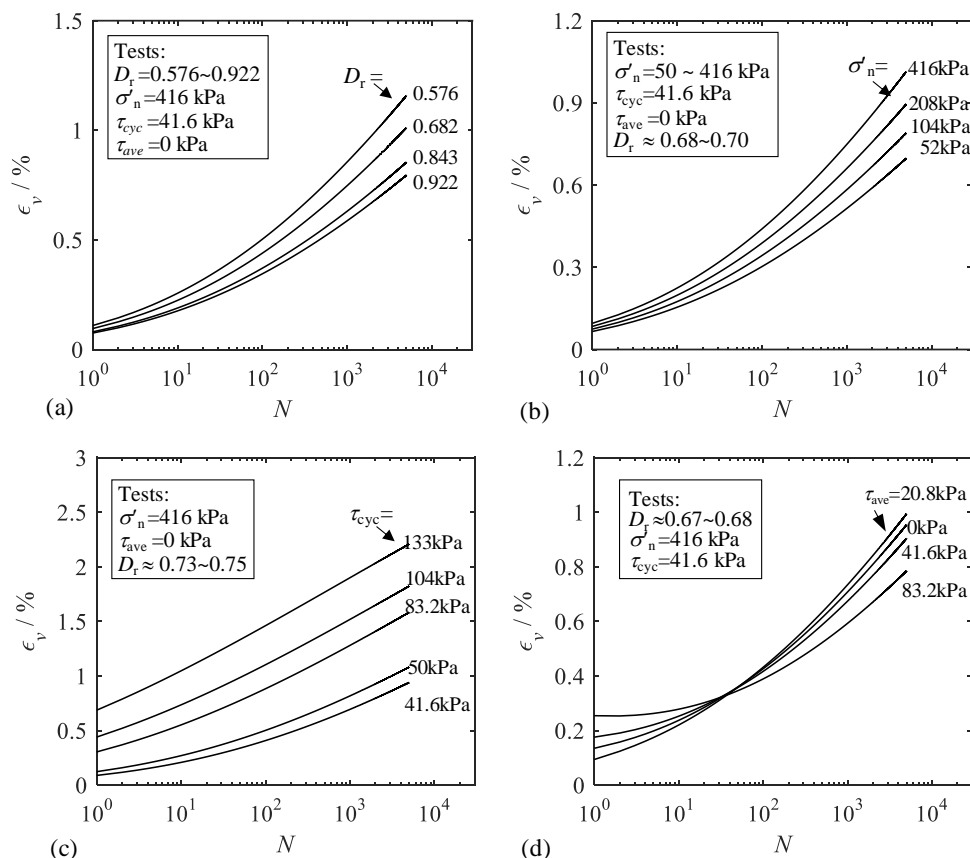


Figure 5.7 Performance of analytical model: (a) calibration with different relative densities; (b) calibration with different effective normal stresses; (c) calibration with different cyclic shear stress; (d) calibration with different average shear stress

5.5 Validation

Furthermore, five no-training tests (No. 16–20) were simulated, based on the calibrated parameters, to verify the accuracy of the analytical method. A good agreement between the predictions and experiments can be found in Figure 5.8, which indicates that the analytical model can successfully describe the cyclic responses in terms of volumetric strain.

Figure 5.9 presents the experimental results regarding evolution of the volumetric strain with cyclic loading from 10 to 4000 cycles, based on six groups including different combinations of the key factors D_r , σ'_n , CSR and α . The volumetric strain surfaces, as calculated by the analytical model, were first plotted in conjunction with the experimental results. A good agreement can be observed between the calculated surfaces and the results, which means that the latter can be extended into multi-dimensional space by the analytical model. Therefore, the model can be used to sensitively study the combined effects.

According to the six groups' results, we may see that, with increasing cyclic numbers, the calculated volumetric strain-related surface gradually enlarges along the axis of volumetric strain and gradually shrinks along the axis of the average shear stress ratio α . The most sensitive combined-effects group is a combination of D_r and CSR, as shown in Figure 5.9(b), in which the surface enlarges rapidly and forms a highly steep slope along both the D_r and CSR direction. In addition, the least sensitive combined-effects group is the combination of D_r and σ'_n , as seen in Figure 5.9(f) where the volumetric strain surface is enlarged almost in parallel with the cyclic number.

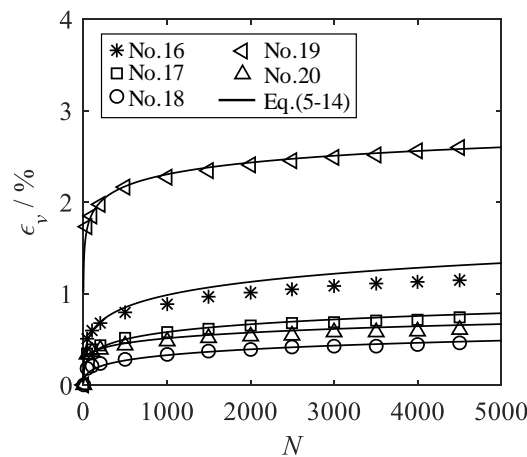


Figure 5.8 Validation of the analytical model by five additional tests No.16-20

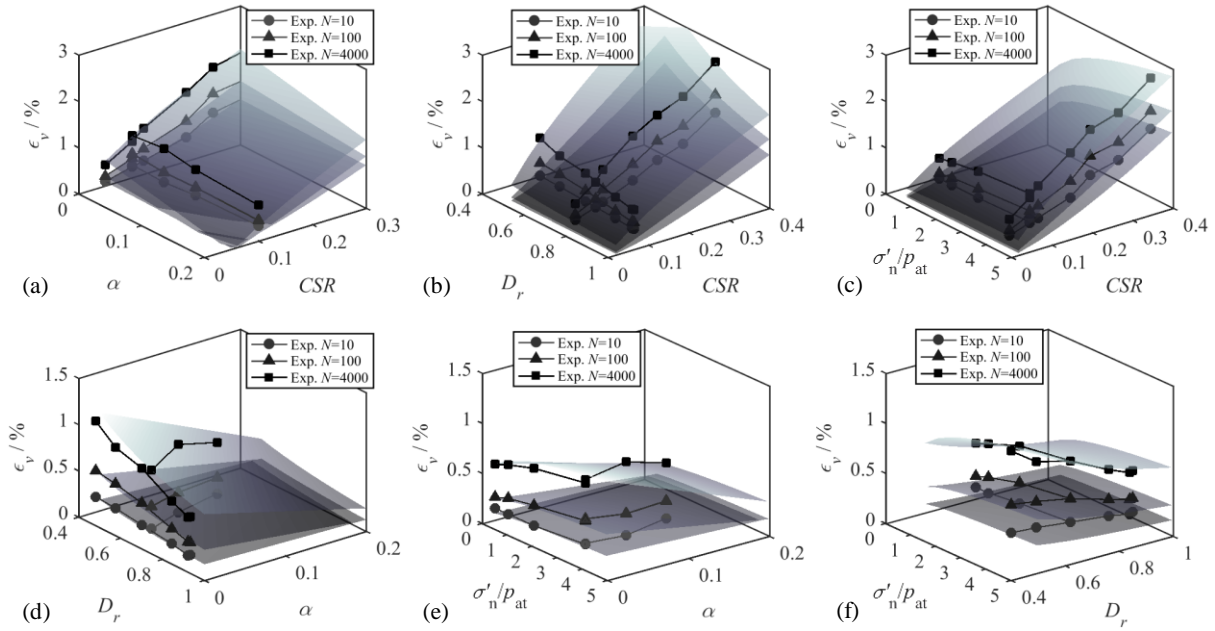


Figure 5.9 Volumetric strain accumulation evolution with 10, 100 and 4000 cycles for different effects of (a) α and CSR , (b) D_r and CSR , (c) σ'_n/p_{at} and CSR , (d) D_r and α , (e) σ'_n/p_{at} and α and (f) σ'_n/p_{at} and D_r

5.6 Conclusion

This work is focused on an investigation of the strain accumulation behaviour of a soil element subjected to a long-term cyclic loading, which can be used to interpret the cyclic strain accumulation of soil adjacent to the pile. To achieve this objective, certain key conclusions were drawn:

- 1) The constant normal stress cyclic simple shear tests can replicate the key response of cyclic strain accumulation considering different initial states, namely relative density, normal stress, cyclic shear stress and average shear stress.
- 2) The cyclic experimental results show that the volumetric strain regularly accumulates under different initial states, which indicates that it is possible to formulate the cyclic strain accumulation based on the four effects.
- 3) The interpretation of results indicates that the effect of the four key factors can be respectively formulated through a simple expression.
- 4) An analytical model of volumetric strain accumulation is developed, considering the abovementioned four effects. The parameters can be calibrated based on training tests. The applicability of the model is validated by predicting the remainder of the tests with the calibrated parameters.
- 5) The multi-dimensional sensitivity analysis can be performed based on the analytical

model. The accumulation of volumetric strain is greatly enhanced by CSR and resisted by average shear stress. The most sensitive effects-combined group is a combination of D_r and CSR ; the least sensitive effects-combined group is the combination of D_r and σ'_n .

Chapter 6 Modelling of cyclic behaviour of sand-pile foundation

6.1 Introduction

Nowadays, the finite element method (FEM) is considered as a useful tool in engineering design. The performance of finite element simulations depends chiefly on the constitutive models adopted. In past decades, pile tests have been simulated by employing different constitutive models, such as the Drucker–Prager (Susila and Hryciw 2003), Mohr–Coulomb (Susila and Hryciw 2003), critical-based (Kouretzis et al. 2014) and hyperplastic models (Qiu et al. 2011; Hamann et al. 2015). However, until now, the effect of the inherent anisotropy during principal stress rotation has not been considered in these simulations.

Accordingly, the previous enhanced SIMSAND model was adopted and modified with a view to incorporating a shear stress reversal technique so as to reproduce the cyclic effect. Undrained and drained cyclic triaxial tests under constant p' and under constant confining stress on Toyoura sand were first simulated to validate the performance of the model. The model was further evaluated by simulating cyclic triaxial and simple shear tests on Fontainebleau sand. After that, a series of model pile tests were simulated and the mechanical responses of sand surrounding the pile were also examined.

6.2 Incorporation of the shear stress reversal technique

The foregoing SIMSAND model was developed based on experimental sand behaviour, considering the sample under monotonic loading. When the direction of the shear stress changes during loading, the stress reversal effect on the stress–strain relationship needs to be incorporated.

The stress state and plastic strain at the moment of shear reversal can be determined as the reversal stress state (marked as σ_{ij}^R) and the reversal plastic strain state (marked as ε_{ij}^R). These two mechanical state variables can be updated when the shear reversal happens again which significantly influences subsequent shear behaviour (see Figure 6.1). As a consequence, the yield function has been revised to be

$$f = \sqrt{\frac{3}{2} (r_{ij} - r_{ij}^R)(r_{ij} - r_{ij}^R)} - H \quad (6-1)$$

where $r_{ij}=s_{ij}/p'$, with $s_{ij}=\sigma'_{ij}-p'\delta_{ij}$ as the mobilized stress ratio; $r_{ij}^R = s_{ij}^R/p'^R$ is the mobilized stress ratio at the moment of stress reversal and H is the hardening rule, which can be expressed as follows:

$$H = \frac{M_p^* \cdot \varepsilon_d^{p*}}{k_p + \varepsilon_d^{p*}} \quad (6-2)$$

The hardening rule given in Eq.(6-2) indicates the stress reversal method for the hardening rule used for both loading, unloading and reloading, with the peak stress ratio M_p^* and deviatoric plastic strain ε_d^{p*} at stress reversal able to be expressed by Eq.(6-3), in which $e_{ij}^{pR} = \varepsilon_{ij}^{pR} - \varepsilon_{kk}^{pR} \delta_{ij}/3$ is the plastic deviatoric strain tensor at the moment of stress reversal,

$$\begin{cases} M_{p(or pt)}^* = \sqrt{\frac{3}{2}} \left(M_{p(or pt)} \cdot n_{ij} - r_{ij}^R \right) \left(M_{p(or pt)} \cdot n_{ij} - r_{ij}^R \right) \\ \varepsilon_d^{p*} = \sqrt{\frac{2}{3}} \left(e_{ij}^p - e_{ij}^{pR} \right) \left(e_{ij}^p - e_{ij}^{pR} \right) \end{cases} \quad (6-3)$$

where the unit direction of the deviatoric stress increment n_{ij} can be calculated as follows:

$$n_{ij} = \frac{(r_{ij} - r_{ij}^R)}{\sqrt{(r_{ij} - r_{ij}^R)(r_{ij} - r_{ij}^R)}} \quad (6-4)$$

The revised expression of the flow rule (see Eq.(6-5)) implies that the amount of dilation is different upon shear reversal,

$$\frac{\partial g}{\partial p'} = A_d \left(M_{pt}^* - \sqrt{\frac{3}{2}} (r_{ij} - r_{ij}^R)(r_{ij} - r_{ij}^R) \right) \text{ and } \frac{\partial g}{\partial s_{ij}} = \sqrt{\frac{3}{2}} n_{ij} \quad (6-5)$$

where the stress ratio corresponding to the phase transformation line M_{pt}^* at the moment of stress reversal in the p' - q space can be calibrated by Eq.(6-3).

The estimation of Lode angle for calculating M_p and M_{pt} is thus modified to be $\theta = \frac{1}{3} \sin^{-1} \left(\frac{-3\sqrt{3}J_3'}{2J_2'^{3/2}} \right)$ with $J_2' = r'_{ij}r'_{ij}/2$, $J_3' = r'_{ij}r'_{jk}r'_{ki}/3$, where $r'_{ij} = r_{ij} - r_{ij}^R$.

Such a stress reversal technique is similar to that proposed by Gajo and Wood (1999), and also similar to that used in Masing's rule, in bounding surface plasticity (Taiebat and Dafalias 2008) and in subloading surface plasticity (Yamakawa et al. 2010).

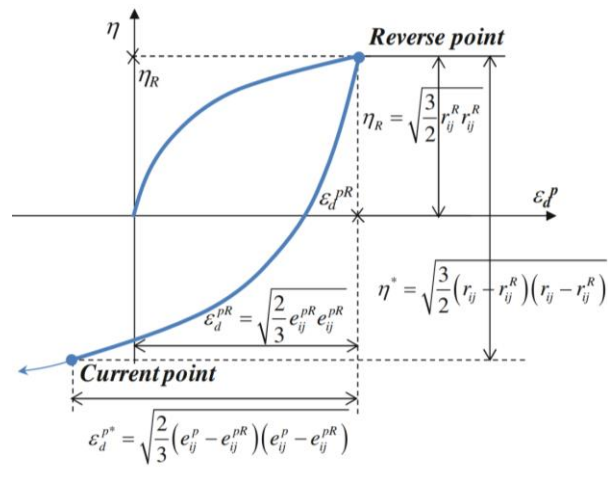


Figure 6.1 Principle of stress reversal in loading and unloading after (Yin et al. 2013)

6.3 Model validation on Toyoura sand

Different triaxial tests under cyclic loadings on Toyoura sand were selected for validation of the model. Toyoura sand is a uniform fine quartzic sand that consists of subrounded to subangular grains. It has been widely tested (Miura and Yamanouchi, 1975; Miura et al., 1984; Pradhan, 1989; Verdugo and Ishihara, 1996; Yoshimine et al., 1998; Uchida and Stedman, 2001). Toyoura sand has a maximum void ratio of 0.977, a minimum void ratio of 0.597 and a specific gravity of 2.65. The model parameters of Toyoura sand summarised in Table 2.6 (see Chapter 2).

6.3.1 Constant mean effective pressure cyclic triaxial tests

Paradhan (1990) conducted drained cyclic triaxial tests on Toyoura sand. However, the sand used by Paradhan (1990) came from a batch different from the one used by Verdugo and Ishihara (1996). Thus the index properties were slightly different. The same values of the parameters determined from the tests of Verdugo and Ishihara (1996) were used to simulate the drained cyclic test, except for the value of $\phi=32.3^\circ$ in compression according to the drained test with loading–unloading and reloading.

Figures 6.2(a)–(c) show the comparison between experiments and predictions for the cyclic triaxial test on loose Toyoura sand with an initial void ratio $e_0=0.845$ under constant $p'=98$ kPa. Figures 6.2(d)–(f) show the comparisons for a dense Toyoura sand with an initial void ratio $e_0=0.653$ under constant $p'=98$ kPa.

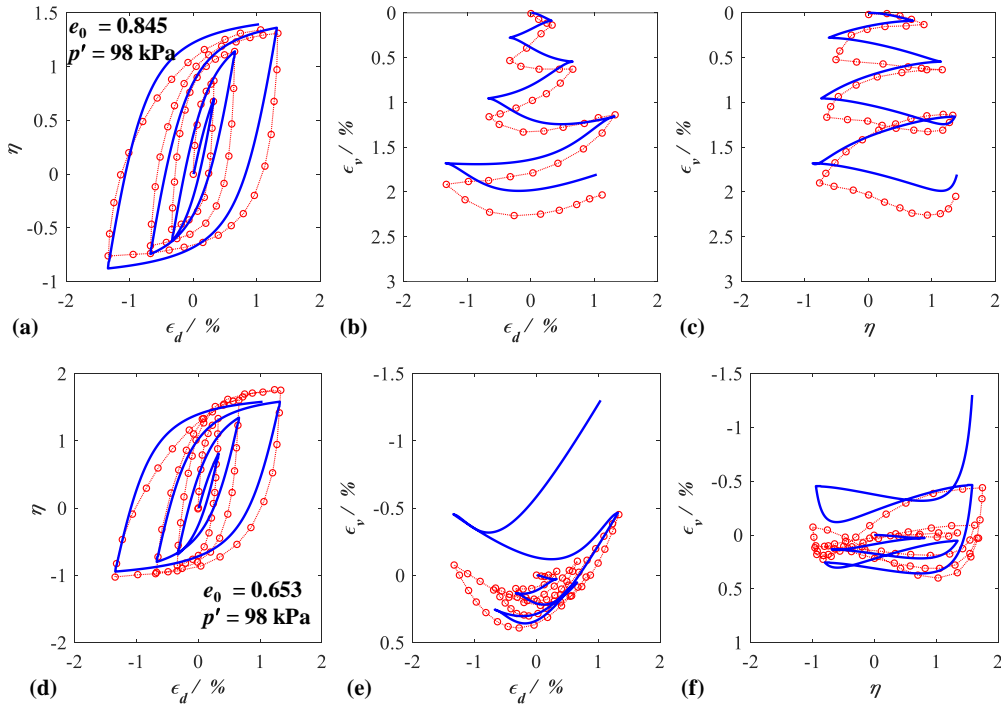


Figure 6.2 Comparison between experimental and numerical results of constant- p' drained cyclic tests on Toyoura sand: (a)-(c) loose specimen and (d)-(f) dense specimen

6.3.2 Drained cyclic triaxial tests

Figure 6.3 shows the comparisons between experiments and predictions for the drained cyclic triaxial test on loose Toyoura sand with an initial void ratio $e_0=0.863$ under constant confining stress $p'_0=98$ kPa. Good agreement was achieved between experimental data and numerical simulations. The slight difference in the volumetric strain might be the result of sample differences, because the values of the parameters used for predicting this test were determined by a different test. The enhanced model captured the overall trend: At small strain amplitudes, loose sand densifies and dense sand dilates.

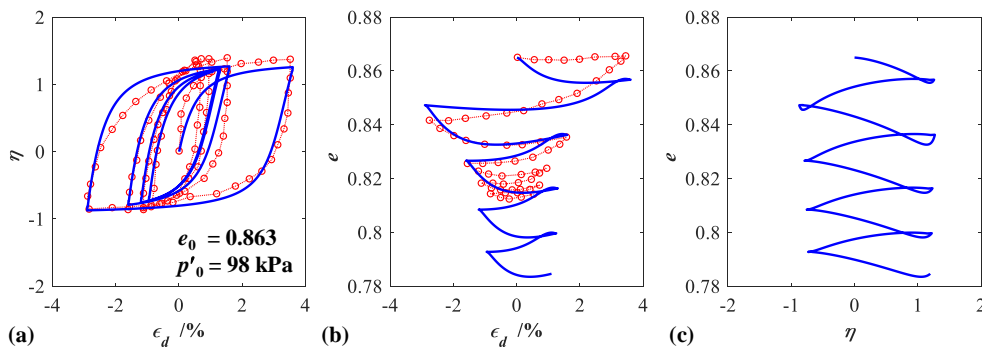


Figure 6.3 Comparison between experimental and numerical results for drained cyclic triaxial tests on Toyoura sand: in (a) stress ratio versus deviatoric strain, (b) void ratio versus deviatoric strain and (c) void ratio versus stress ratio

6.3.3 Undrained cyclic triaxial tests

Uchida and Stedman (2001) conducted undrained cyclic triaxial tests on Toyoura sand. In each test, an axial strain of 1% magnitude was applied in each cycle until liquefaction was obtained. The samples were prepared at relative densities of 30% and 50% and subjected to two initial confining pressures of 200 kPa and 400 kPa. The experimental and numerical results for the two samples are shown in Figure 6.4. The model parameters calibrated from the monotonic tests were used for the predictions of the cyclic tests. The model reproduces the general trend as depicted by the test. Despite the difference in the evolution of the mean effective stress between experiments and simulations, which may be attributed to the slight difference in properties (such as anisotropy) among sands from different batches, the fact that a looser Toyoura sand had a greater liquefaction potential under higher confining pressure was well determined by the model.

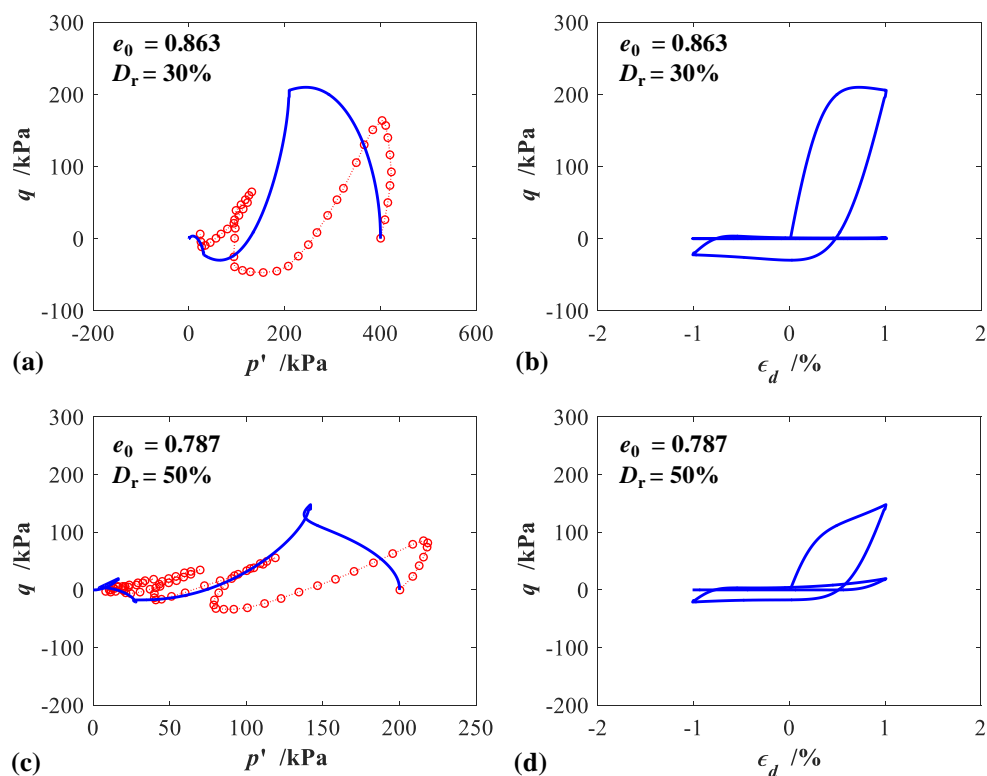


Figure 6.4 Comparison between the experimental and numerical results of undrained triaxial tests under cyclic loading on Toyoura sand with different initial void ratios: in (a) and (c) stress path in mean effective stress versus deviatoric stress; (b) and (d) deviatoric stress versus deviatoric strain

Simulations of undrained cyclic tests at constant stress amplitude with $q_{\max} = 55$ kPa and $q_{\min} = -55$ kPa (noted as $q_{\text{cyc}} = 55$ kPa for symmetric loading condition) were conducted on samples with different initial void ratios by using the foregoing values for the model parameters. As expected, the dense sample exhibited a cyclic mobility phenomenon (Figs. 6.5(a)–(b)), and the medium-dense sample exhibited also a cyclic mobility with higher

deformations and reached an almost liquefied state in fewer cycles than required for the dense sample (Figs. 6.5(c)–(d)). The loose sample reached complete liquefaction with large deformations in a few number of cycles (Figs. 6.5(e)–(f)). Thus the proposed model was able to predict the dependence of liquefaction potential on relative density of sand. Note that to allow more precise simulation of undrained cyclic tests, the model still needs further enhancement, such as the intergranular strain effect suggested by Niemunis and Herle (1997).

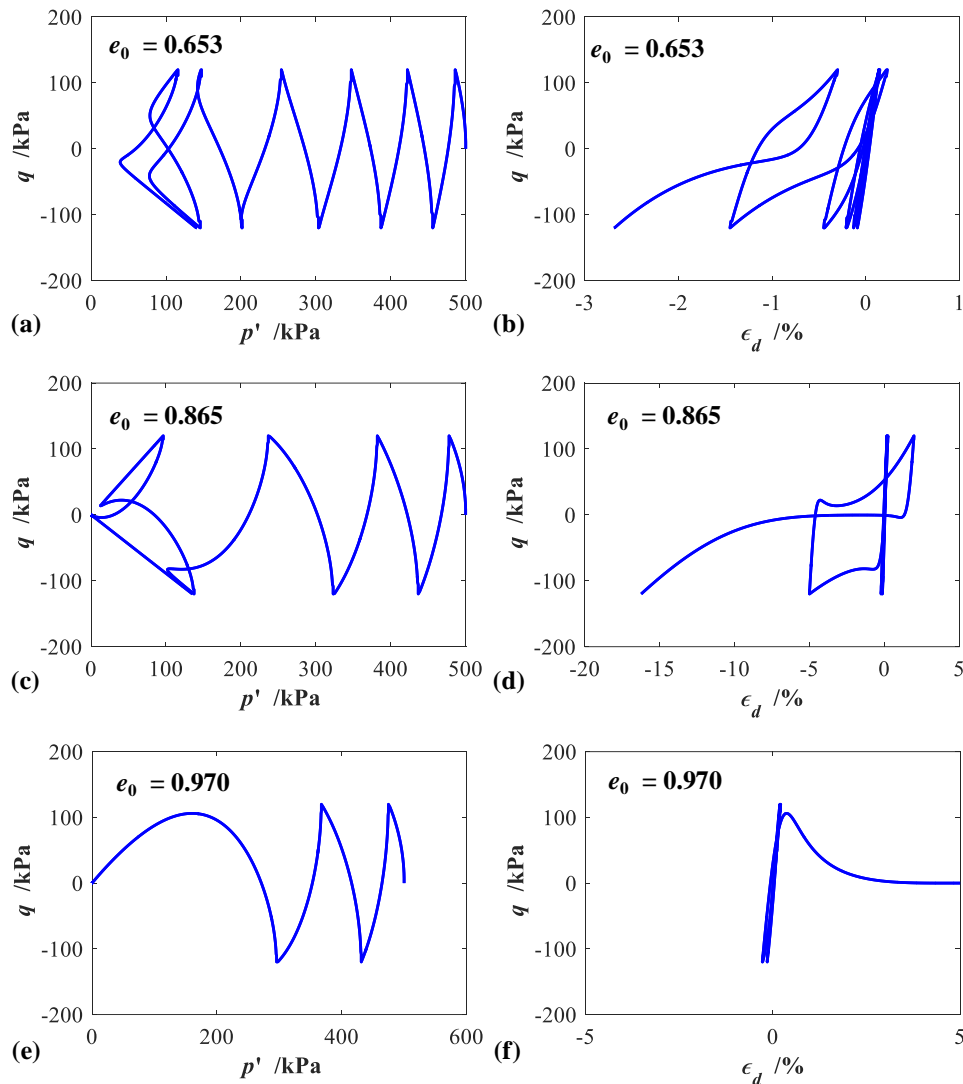


Figure 6.5 Comparison between the experimental and numerical results of undrained triaxial tests under cyclic loading on Toyoura sand with different initial void ratios: in (a), (c) and (e) stress path in mean effective stress versus deviatoric stress; (b), (d) and (f) deviatoric stress versus deviatoric strain

6.4 Model validation on Fontainebleau sand

6.4.1 Drained cyclic triaxial tests at constant- p'

Phong (1980) conducted drained cyclic triaxial tests at constant p' on Fontainebleau sand. Figure 6.6 shows the comparison between experiments and predictions for sand with an initial void ratio $e_0 = 0.72$ under constant $p' = 200$ kPa, (model parameters of Fontainebleau sand summarised in Table 3.2). A general agreement was achieved between experimental data and numerical simulations. The difference in the stress-strain might be due to sample differences since the values of the parameters used for predicting this test were determined by different laboratory, conducted by Andria-Ntoanina et al. (2010). Also, due to lack of considering the small strain effect after the stress reversal, the simulated initial stiffness is smaller than the experimental results, as dash line in Figure 6.6(a) (KOSEKI 1998). Therefore, to consider the effect of small strain stiffness during the stress reversal stage, the parameter k_p was modified by 0.5 times of the initial value, and parameters K_0 and G_0 were also modified by two times of the initial values. It shows a better result than the simulation without considering small strain stiffness.

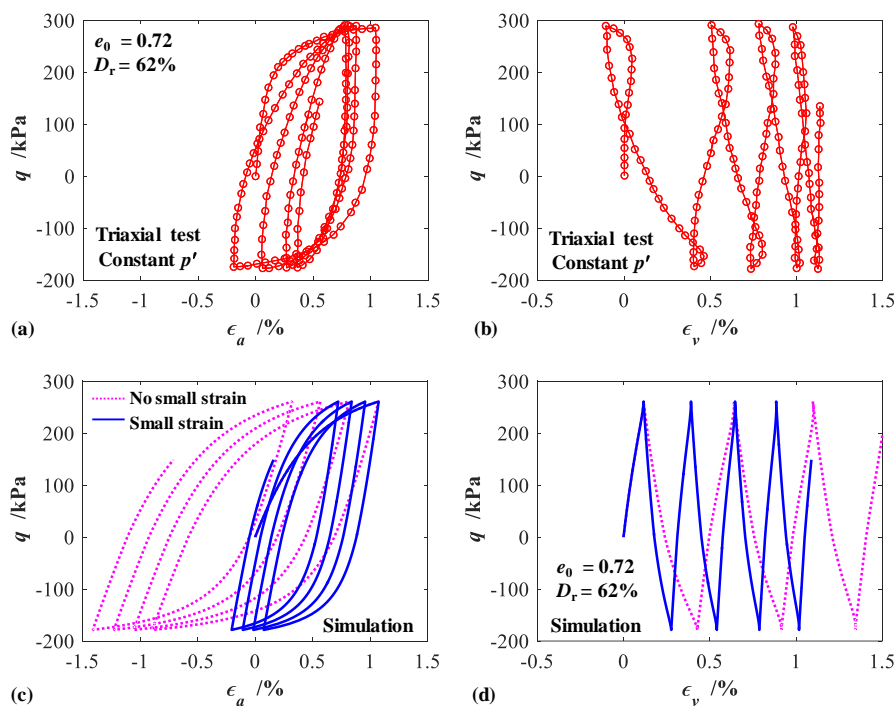


Figure 6.6 Comparison between experimental and numerical results of constant- p' drained cyclic tests on Fontainebleau sand: (a)-(b) experiment, and (c)-(d) simulation

6.4.2 Undrained cyclic triaxial tests

Andria-Ntoanina et al. (2010) conducted a series of undrained cyclic triaxial tests on Fontainebleau sand. In each test, the cyclic deviatoric stresses q_{cyc} ($=100, 55, 80$ and 48 kPa) were applied to the sample with 0.1 Hz frequency until liquefaction was obtained. The

samples were prepared at relative densities of 65% and 44% and subjected to two initial confining pressures of 200 kPa and 400 kPa. The experimental and numerical results for the two samples are shown in Figure 6.7 (for medium-dense sand) and Figure 6.8 (for loose sand). The model parameters calibrated from the monotonic tests were used for the predictions of cyclic tests (see Chapter 3). The model reproduces the general trend as depicted by the test. From comparison between tests and simulations, the difference in the evolution of the mean effective stress between experiments and simulations can be attributed to the slight difference in properties (such as anisotropy) among sands from different batches. In fact, the looser Fontainebleau sand has a greater liquefaction potential that can be well described by the model.

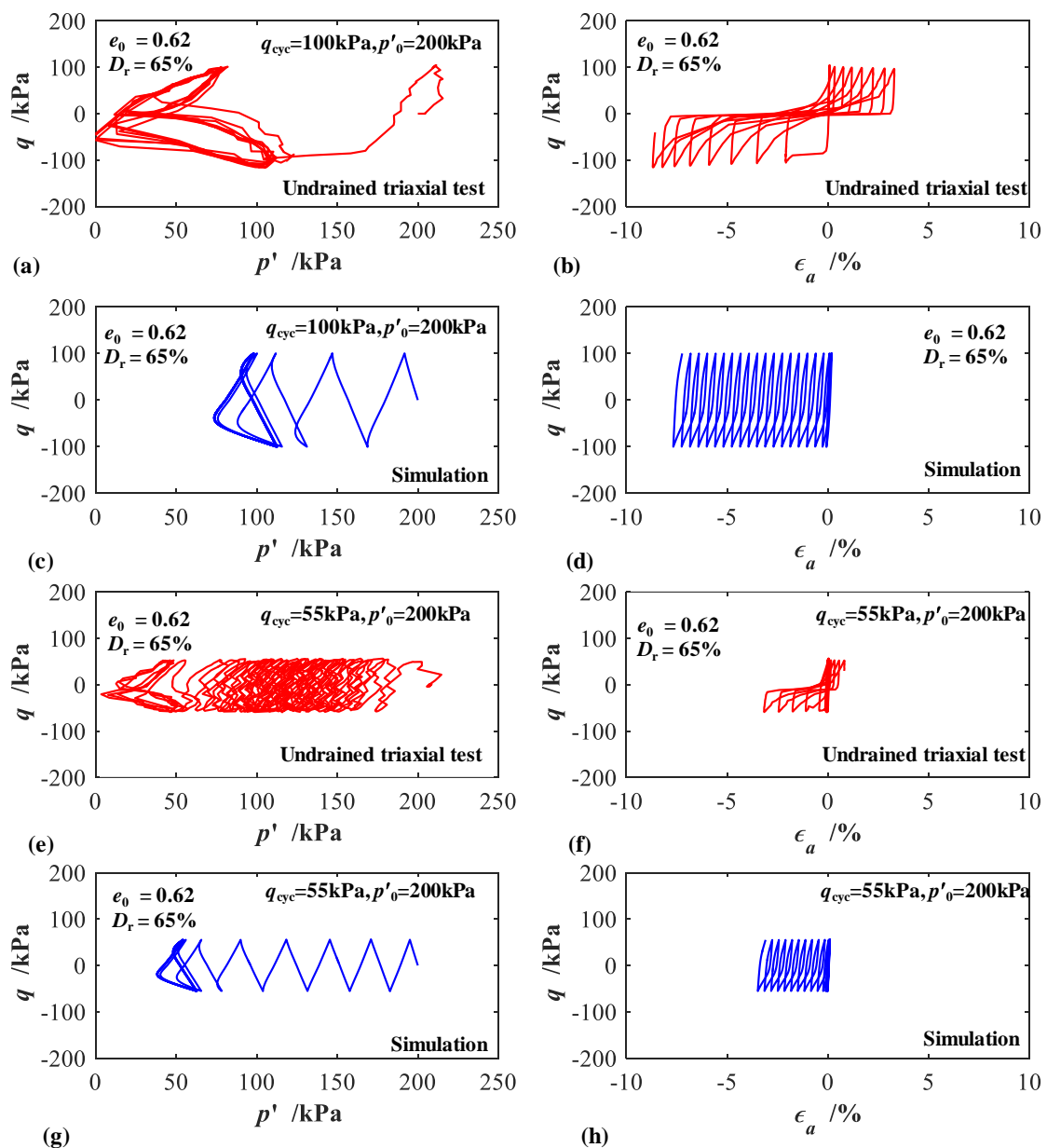


Figure 6.7 Comparison between experimental and numerical results of undrained cyclic tests on medium-dense Fontainebleau sand: (a)-(d) with $q_{cyc} = 100 \text{ kPa}$ and (e)-(h) with $q_{cyc} = 55 \text{ kPa}$

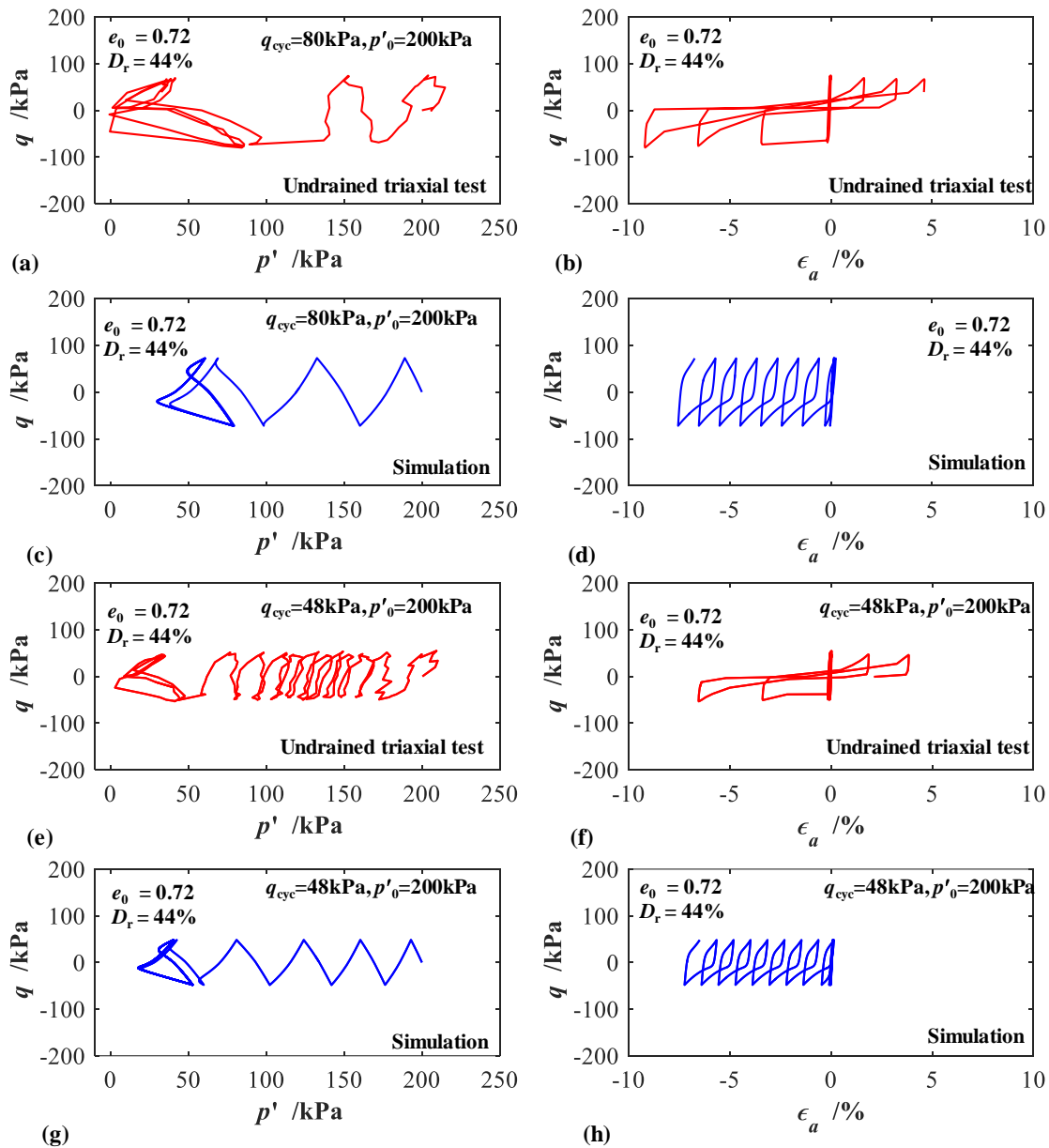
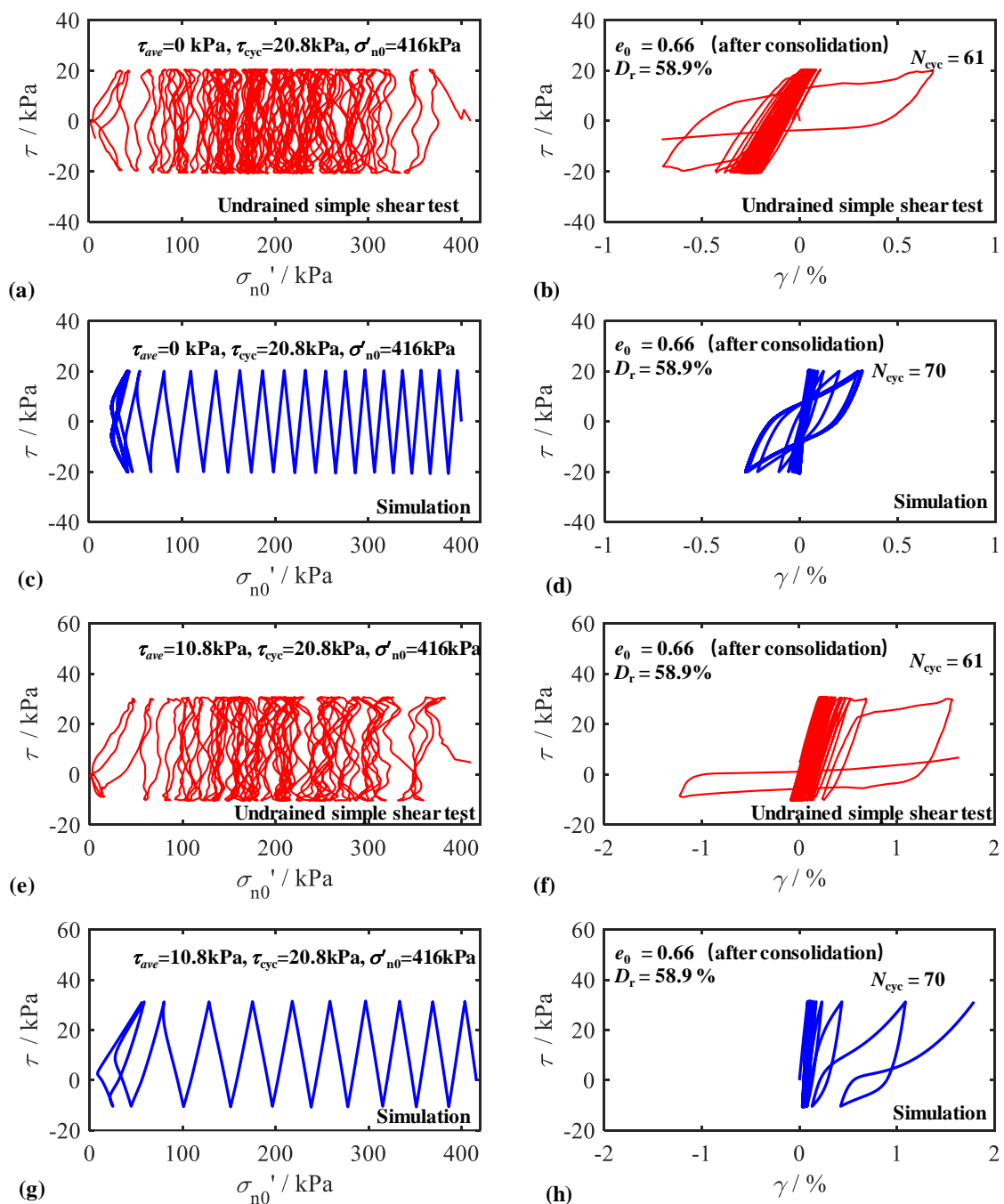


Figure 6.8 Comparison between experimental and numerical results of undrained cyclic tests on loose Fontainebleau sand: (a)-(b) experiment with $q_{cyc}=80\text{kPa}$, (c)-(d) simulation with $q_{cyc}=80\text{kPa}$ (e)-(f) experiment with $q_{cyc}=48\text{kPa}$ and (g)-(h) simulation with $q_{cyc}=48\text{kPa}$

6.4.3 Undrained cyclic simple shear tests

The undrained cyclic simple shear tests were simulated to validate the performance of the enhanced cyclic SIMSAND model. The principal stress rotation effect was also considered in the model by the jointed parameters \tilde{c}_1 and \tilde{c}_2 (see Chapter 3). The samples were prepared at relative densities of 59%, initial normal stress of 416 kPa and cyclic shear stress of 20.8 kPa and were subjected to three average shear stresses of 0 kPa, 20.8 kPa and 41.6 kPa. The experimental and numerical results for the three simple shear tests are shown in Figure 6.9.

For the simulation of symmetrical stress-controlled cyclic simple shear test as seen in Figure 6.9(a-d), the number of cycles to liquefaction in general agrees with the tests, but the shear strain after liquefaction is slightly underestimated. Additionally, for the non-symmetrical cyclic simple shear test with the stress reversal condition as seen in Figure 6.9(e-h), the liquefaction behaviour can also be well simulated, which is also combined with slight non-symmetrical cyclic shear strain accumulation. Furthermore, for the cyclic simple shear test with the non-stress reversal condition as Figure 6.9(i-l), the cyclic mobility behaviour (shear strain accumulation) can also be well simulated. Therefore, the cyclic behaviour of stress-controlled simple shear tests can be generally captured by the cyclic model.



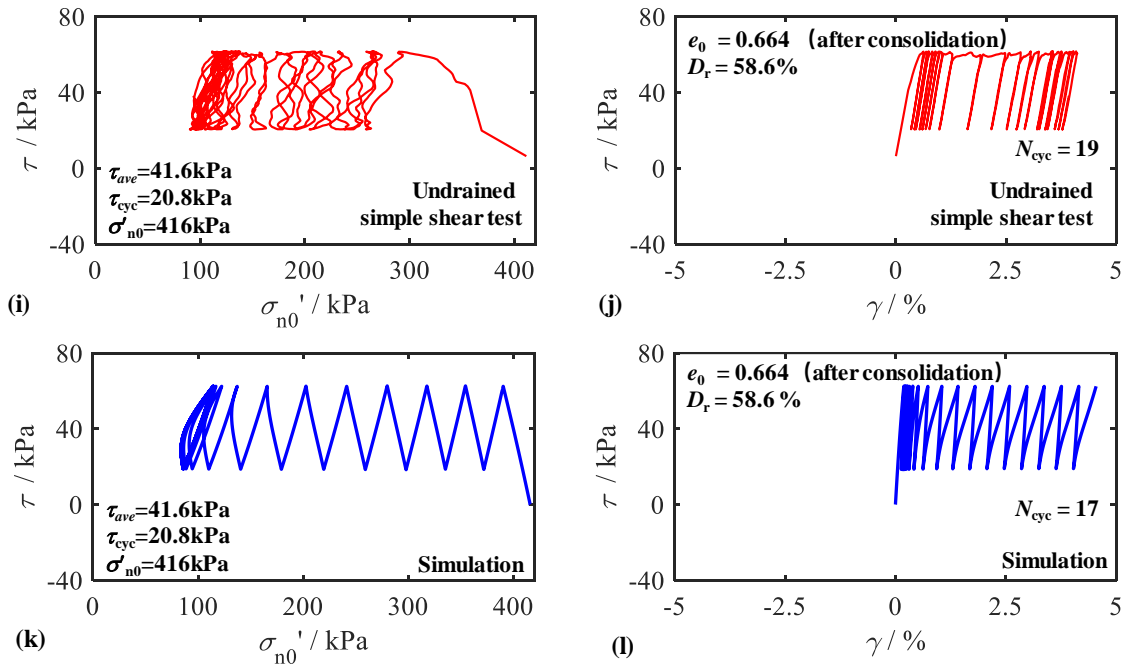


Figure 6.9 Experimental and numerical results of undrained cyclic tests on medium dense Fontainebleau sand on 416kPa initial normal stress: (a)-(d) comparison on condition ($\tau_{ave} = 0$ kPa, $\tau_{cyc} = 20.8$ kPa), (e)-(h) comparison on condition ($\tau_{ave} = 10.4$ kPa, $\tau_{cyc} = 20.8$ kPa) and (i)-(l) comparison on condition ($\tau_{ave} = 41.6$ kPa, $\tau_{cyc} = 20.8$ kPa)

6.4.4 Drained cyclic simple shear tests

The strain-controlled cyclic simple shear tests were also conducted on loose sand with initial void ratio of 0.70 and initial normal stress σ'_{n0} of 108 kPa so as to study the contractive and dilative behaviour of sand during the shearing condition, as shown in Figure 6.10(a)-(c). The tests were simulated by the cyclic enhanced SIMSAND model, as shown in Figure 6.10(d)-(f). General agreement was achieved between experiments and numerical simulations, demonstrating that the cyclic model can be used to describe the basic trend whereby loose sand densifies and dense dilates. Note that for tests the stiffness at small strains is over-predicted, which can be further improved by considering the feature of small strain stiffness.

Stress-controlled cyclic simple shear tests with initial conditions of $\tau_{ave} = 0$ kPa, $\tau_{cyc} = 41.6$ kPa, $\sigma'_{n0} = 416$ kPa and $e = 0.606$ (see Chapter 5) were also simulated by the cyclic model shown in Figure 6.11. Comparison of experimental and numerical results shows that the predicted results of volumetric strain slightly exceed the experimental results. The main reason for this difference between experiment and simulation should be relating to the over-predicted stiffness at small-strain level. Therefore the model needs further enhancement.

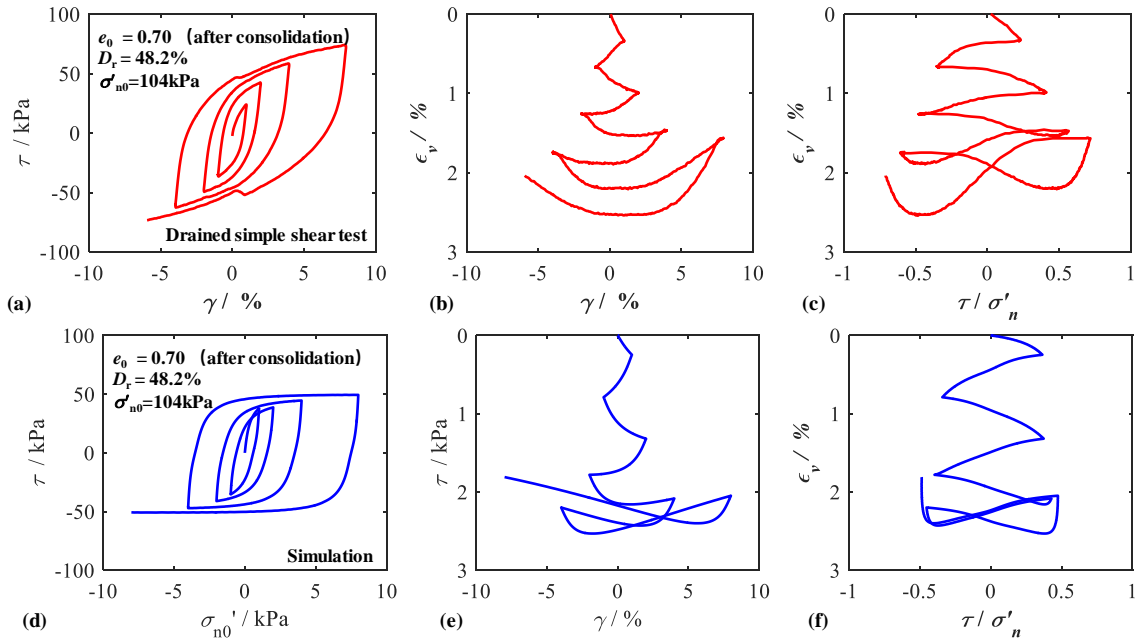


Figure 6.10 Comparison of experimental and numerical results of strain-controlled drained cyclic simple shear tests on loose Fontainebleau sand: (a-c) experiment and (e-g) simulation

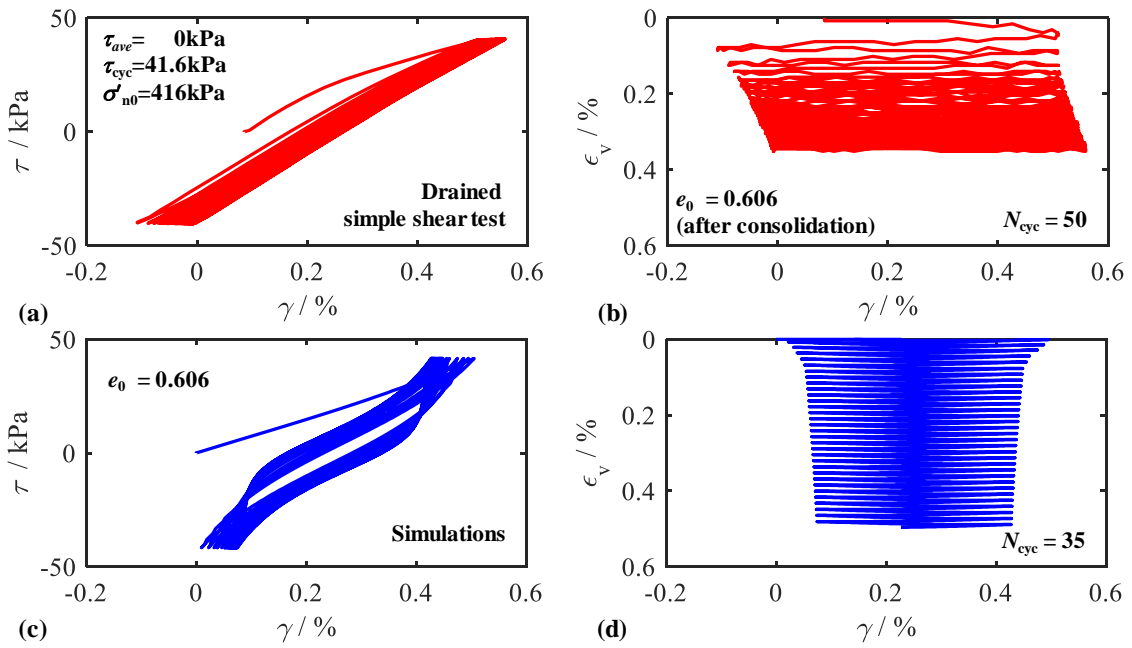


Figure 6.11 Comparison of experimental and numerical results of stress-controlled drained cyclic simple shear tests on medium dense Fontainebleau sand: (a-b) experiment and (c-d) simulation

6.5 Simulation of a mini-scale model pile penetration test

6.5.1 3SR mini-scale model pile and FE modelling

Mini-scale model pile penetration tests were conducted at 3SR Laboratory in Grenoble, using micro computed X-ray tomography (CT) for analysis of the displacement field around the mini-scale pile with a pseudotriaxial cell capable of applying lateral confinement pressure to the sand sample (Silva, 2014). A closed-ended conical model pile of apex angle 60° , 5 mm in diameter, was installed on the sand by monotonic loading under an isotropic confinement pressure, as seen in Figure 6.12.

According to the 3SR mini-scale model pile test, an axis-symmetric FE model with 3,500 elements was generated, as illustrated in Figure 6.13. The overall model size is 70 mm in diameter and 100 mm high (e.g. the same size than the tested sample). The bottom and top sides are fixed in both the vertical and the horizontal directions. The lateral side is free. The sand was discretised by four-node axisymmetric elements having one reduced integration point (CAX4R) in ABAQUS. Compared to sand, the deformation of the pile is negligible, so the pile was modelled as a rigid body having the same diameter and conical tip as the model pile in Figure 6.13. The ABAQUS/Explicit with Arbitrary Lagrangian-Eulerian (ALE) method was adopted for simulating the pile penetration tests and to deal with the mesh distortion problem with large deformation of at the edge of cone.

Pile-soil interaction was simulated as surface-to-surface contact using a classical Coulomb friction law. The friction coefficient was set to $\mu = \tan(\phi_\mu/2) = 0.3$. The total penetration displacement was 50 mm with a low penetration rate of 0.5 mm/s, in order to avoid numerical issues related to the sudden application of high strain rates and inertial effects. According to the experimental program, the initial stress (100 kPa and 200 kPa) was generated by applying lateral confinement pressure on Fontainebleau sand NE34 (relative density of approximately 70% corresponding to $e_0 = 0.62$), which is consistent with the mini-scale model pile tests. The pile penetrated into sand at a rate of 0.1 mm/s (Illanes 2014) up to 50 mm. The parameters of Fontainebleau NE34 sand in Table 3.2 were used for the simulation

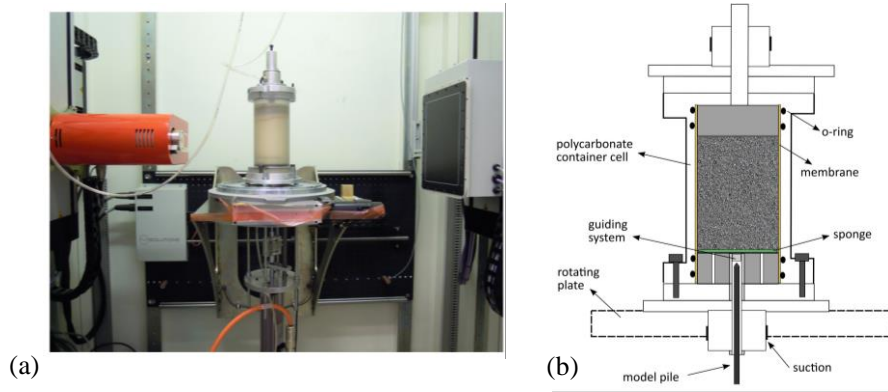


Figure 6.12 Details of 3SR mini-scale model pile tests (Silva 2014), (a) model pile with micro-CT scan apparatus and (b) geometry of model-pile penetration tests

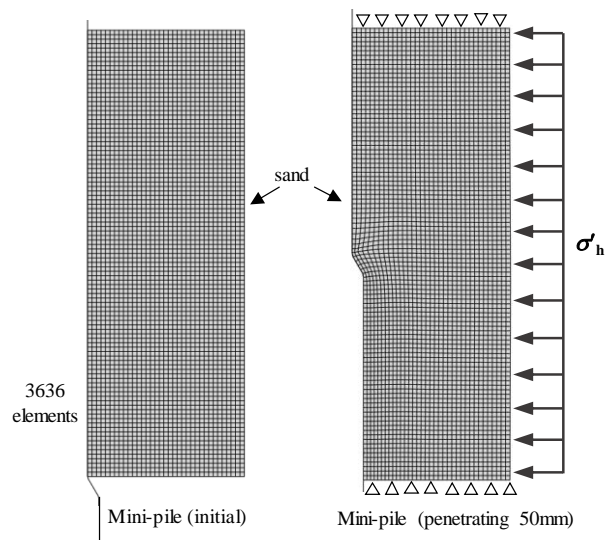


Figure 6.13 Finite element analysis of 3SR mini model pile

6.5.2 Simulation results

Figure 6.14 shows the simulated results of load-displacement curves during pile driving into sand, with total confining stresses σ_h of 100 kPa and 200 kPa. Similar simulations without incorporating parameters (as $\tilde{c}_1=0$ and $\tilde{c}_2=0$) were also conducted to highlight the model performance by incorporating the inherent anisotropy. The simulations and experiments were compared, revealing that the simulated results obtained using incorporating parameters $\tilde{c}_1=0.18$ and $\tilde{c}_2=2.0$ generally agree with the experimental results. It can be seen that the principal stress rotation of sand that occurred during the penetration would dramatically decrease pile resistance. The good agreement between the simulation and measurement was achieved using the proposed numerical platform in conjunction with the enhanced SIMSAND model. Moreover, the simulated result for the case of 200 kPa confining pressure shows a slight difference in the penetration load as seen in Figure 6.14(b), which may be attributed to the effect of the initial fabric anisotropy among sand from different batches.

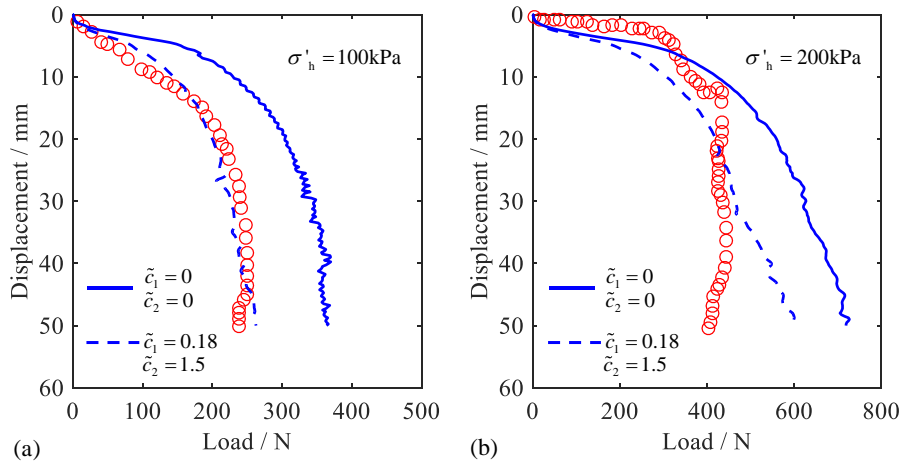


Figure 6.14 Comparison between experiment and simulation of 3SR mini model pile test with confining pressure of (a) 100kPa and (b) 200kPa

Figure 6.15 presents X-ray based measurements from a micro-CT scan apparatus, showing incremental vertical and horizontal strains in sand after a pile head displacement of 2 mm. The vertical and horizontal strain profiles of FE simulation results when the pile head penetrated 2 mm into sand were also plotted to compare with experimental results. The zones of vertical and horizontal strain distributions surrounding the cone agree well with the experimental results, showing that a high vertical contraction and horizontal dilation develop beneath the cone when the pile continuously penetrates into the sand.

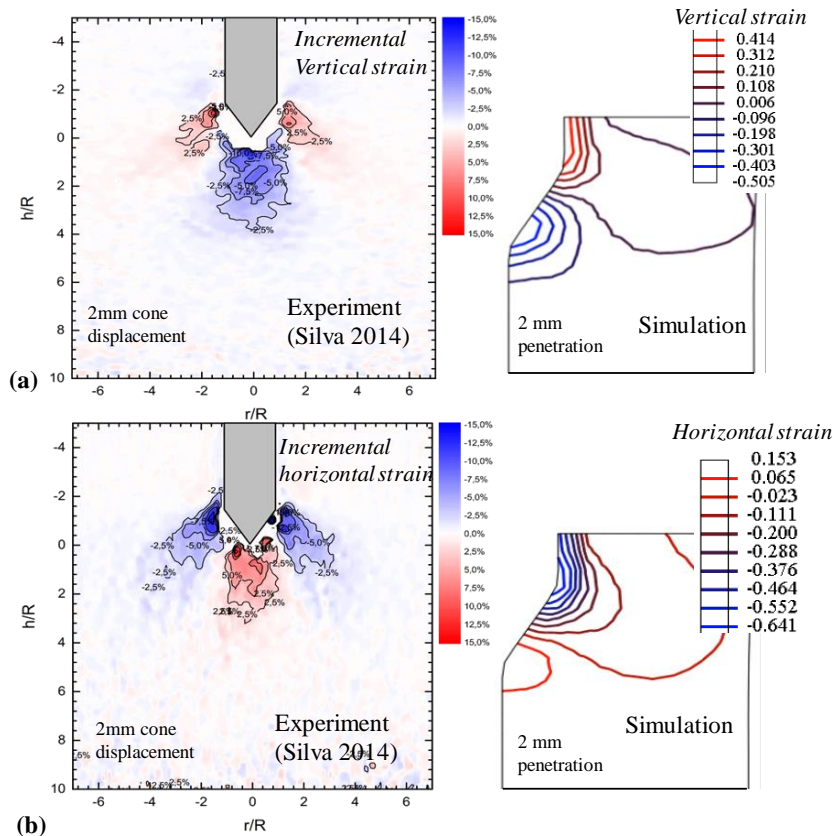


Figure 6.15 Comparison of strain profiles between experiment and simulation (a) vertical strain and (b) horizontal strain

6.5.3 Parametrical study

To investigate the influence of inherent anisotropy on pile resistance, a parametric analysis was further conducted based on a simulation of the mini-scale model pile test. A series of simulations were conducted by changing only the parameter \tilde{c}_1 ($=0, 0.1$ and 0.2 , which may correspond to different shearing strengths for the material). The simulated pile load against the penetration depth with different values of \tilde{c}_1 is shown in Figure 6.16(a). It can be seen that the cone resistance decreases with an increasing value of \tilde{c}_1 .

Similar simulations were also conducted by changing only the parameter \tilde{c}_2 ($=0.5, 1$ and 2). The simulated pile load against the penetration depth is shown in Figure 6.16(b) with different values of \tilde{c}_2 . It can be seen that the cone resistance decreases with an increasing value of \tilde{c}_2 (representing the great degradation of shearing stiffness).

Overall, the effect of inherent anisotropy during principal stress rotation by changing parameters \tilde{c}_1 and \tilde{c}_2 has a significant influence on the cone resistance. In summary, parameter \tilde{c}_1 controls the degradation rate of shear strength, and \tilde{c}_2 controls the degradation rate of shearing stiffness. These results reveal the simulation trend of simple shear tests.

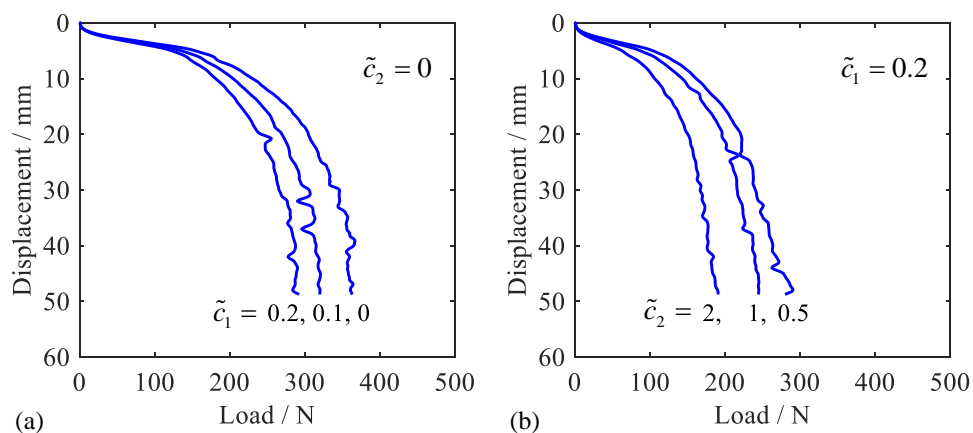


Figure 6.16 Influence of inherent anisotropy related parameters on pile resistance to investigate: (a) the effect of parameter \tilde{c}_1 , and (b) the effect of sensitivity of parameter \tilde{c}_2

6.6 Simulation of ICP model pile penetration test

6.6.1 ICP model pile and FE modelling

The model test of pile installation was conducted in the 3SR calibration chamber (Rimoy 2013). This test employed the Imperial College Pile (ICP): a pile scaled down to 36 mm outer diameter with a standard apex angle 60° closed-ended conical base, and 1.5 m long suitable for the laboratory calibration chamber testing (Jardine et al. 2009). The model experiment (ICP07) is illustrated in Figure 6.17. The soil used was Fontainebleau sand NE34.

An initial vertical stress of 150 kPa was applied on the top of sand by an upper membrane. The pile installation was displacement controlled at 2 mm/s. The pile resistance and the stress and strain profiles surrounding the driven pile were measured by transducers.

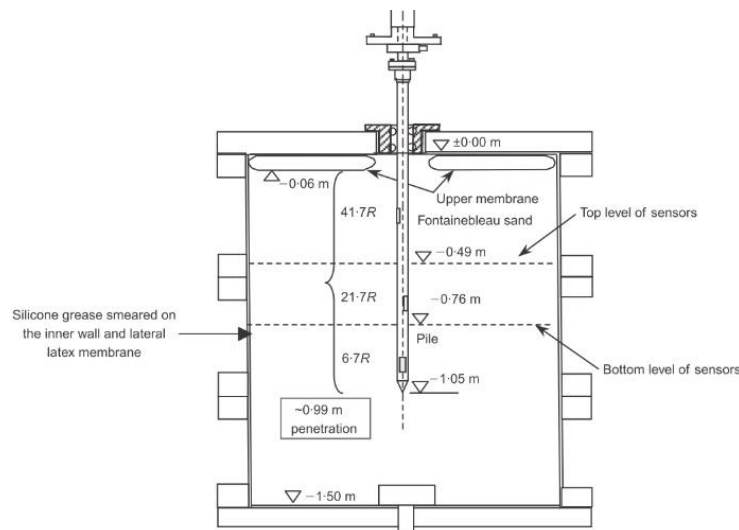


Figure 6.17 General arrangement for pile test (Rimoy 2013)

An axisymmetric finite element model with 5,700 elements was generated, as illustrated in Figure 6.18. The overall model size is 0.6 m width and 1.5 m height, large enough to avoid boundary constraints. The bottom side is fixed in both the vertical and the horizontal directions. The left and right sides are fixed only in the horizontal direction. The top side is free. The soil was modelled by four-node axisymmetric elements with one reduced integration point (CAX4R) in ABAQUS. Compared to that of soil, the deformation of the pile is negligible, so it was modelled as a rigid body having the same diameter and conical tip as the model pile. Four sensors were positioned surrounding the pile, with 2, 3, 5 and 8 pile radii (R).

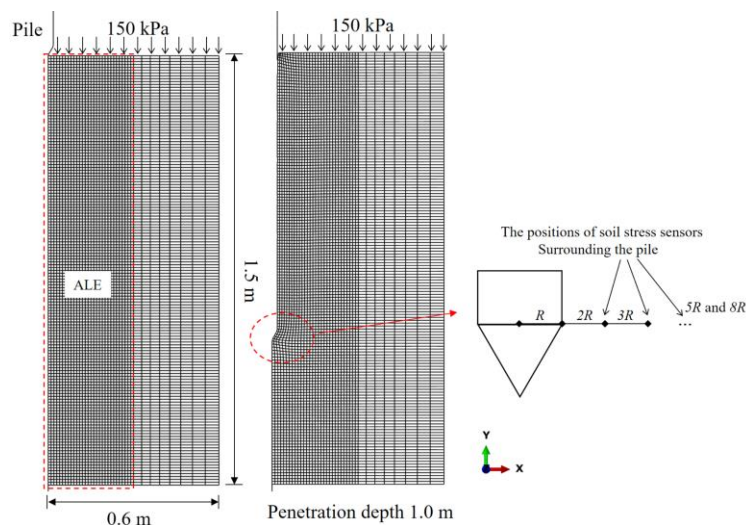


Figure 6.18 Modelling of ICP07 penetration tests

The initial stress was generated by self-weight with the unit weight of the soil $\gamma=16.3$ kN/m³ under $K_0=1-\sin\phi_\mu=0.48$, consistent with the model test (Yang et al. 2010). The pile–soil interaction was simulated by surface-to-surface contact with a classical Coulomb friction law. The friction coefficient was set to $\mu = \tan(\phi_\mu/2) = 0.3$. The total penetration displacement was 100 mm with a low penetration rate of 0.5 mm/s, thus to avoid numerical issues related to the sudden application of high strain rates, as well as inertial effects. This rate was about 4 times slower than the actual rate of the tests an acceptable figure, according to Kouretzis et al. (2014). The parameters of Fontainebleau NE34 sand in Table 3.2 were used for the simulation. The simulation of pile penetration was carried out in three steps: (1) generating the initial stress, (2) applying the vertical stress of 150 kPa to the top surface of sand and (3) penetrating the pile into the sand.

6.6.2 Simulation results

Figure 6.19 shows the simulated results of cone resistance q_c versus the depth of penetration Z for the pile penetration test ICP07, demonstrating that the prediction of cone resistance by the enhanced SIMSAND model using the parameters of Fontainebleau sand and anisotropic parameters generally agrees with the measurement.

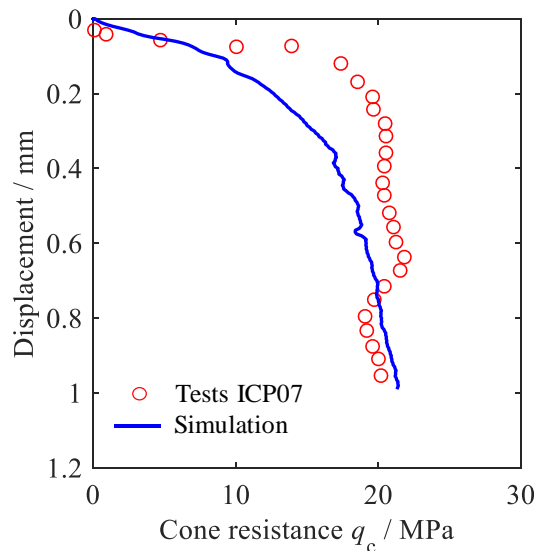


Figure 6.19 Comparison between experiment and simulation of model pile test in Fontainebleau sand for the pile resistance against the penetration depth

Based on the FE simulation, the radial stresses at three pile penetration depths (of $h=0.285$ m, 0.46 m and 0.74 m) and four radial levels (positioned $2R$, $3R$, $5R$ and $8R$ pile radii) were plotted against the experiments in Figure 6.20. It shows that the radial stress states surrounding the cone can be well predicted by considering different penetration depths and radial distances from the pile axis. The penetration depth effect is very clear for given radial distances ($3R$), and the radial stress tends to be less affected when the radial distances exceed 8 times pile radii during the pile penetration.

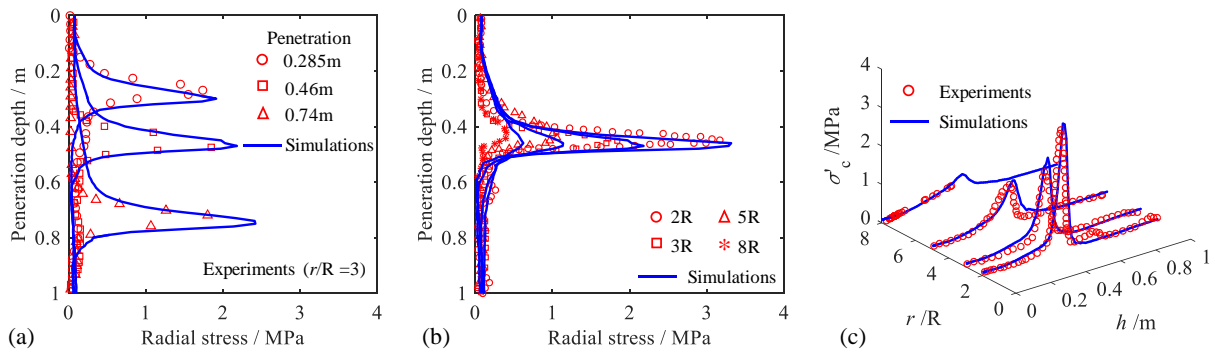


Figure 6.20 Comparison of radial stress between test and simulation considering (a) different penetration depth, (b) different radial distance, and (c) combined 3D plot

6.6.3 Monotonic response of sand surrounding the pile

The influence of the mean effective stress on pile resistance was selected to be plotted with three level of penetration depths (0.285, 0.46 and 0.76 m) in Figure 6.21. A high-stress level is reached around the pile tip. At 5 times the pile radii(R), a notable mean effective stress accumulation is still seen.

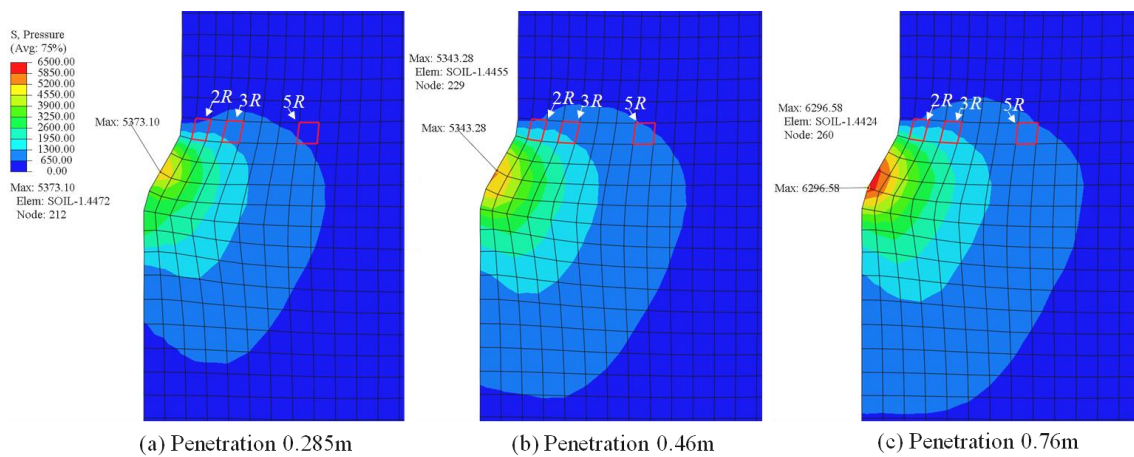


Figure 6.21 Simulation results of mean effective stress field around the cone of pile at the penetration depth of (a) 0.285m; (b) 0.46m and (c) 0.76m in Fontainebleau sand NE34

Figure 6.22 shows the displacement vectors when the pile penetration reached 0.46 m. During the pile penetrating process, the recirculation of sand particles occurred beneath the cone tip of the pile. Displacement vectors along cross sections of the pile, in the range of 4 times the radius of the pile ($4R$), are obviously changed in the direction of the sand particles' movement. Highly compacted sand particles from beneath the pile cone are pushed radially upward with the cone movement, then compressed against the pile surface by the surrounding soil.

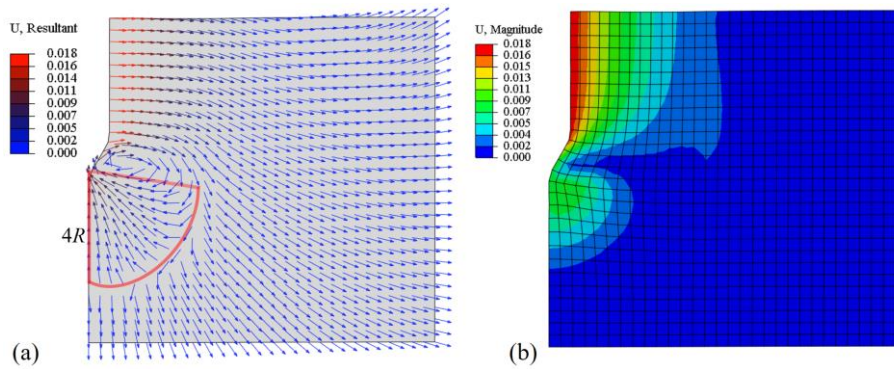


Figure 6.22 Displacement distribution surrounding the pile for penetration 0.46m (a) directions and (b) contours

Figure 7.23 presents the distributions of void ratio of sand surrounding the pile for different penetrating depths. It can be found that high-level densification occurs beneath the pile tip during the pile driving process. On the contrary, the density of sand along the shaft of pile becomes loose, due to the dilation induced by large deformation of surrounding sand.

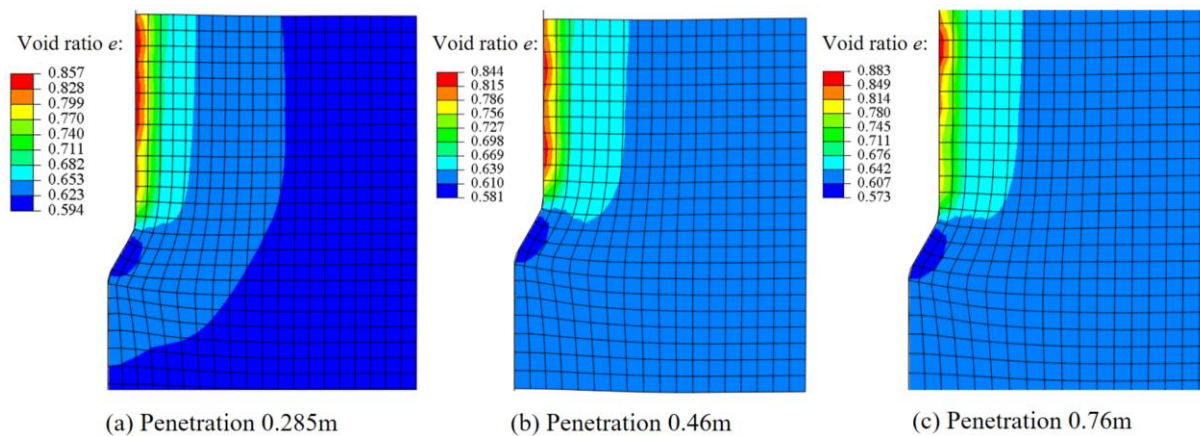


Figure 6.23 Simulated void ratio field of three penetration depths: (a) 0.285m, (b) 0.46m and (c) 0.76m

6.7 Simulation of cyclic model pile test

6.7.1 Modelling of cyclic pile test`

The cyclic model pile test on Fontainebleau sand NE34 was performed by Bekki et al. (2014, 2016) at École Nationale des Ponts et Chaussées (ENPC) in a calibration chamber system. As shown in Figure 6.24, the cylindrical calibration chamber had a diameter of 52.4 cm and a height of 70 cm. The sand sample was prepared by the air pluviation method (Dupla and Canou 1994; Andria-Ntoanina et al. 2010). The pile size of 36 mm outer diameter with a standard apex angle 60° closed-ended conical base was embedded in sand, 24 cm distant from the bottom of the chamber. The bottom and lateral sides were free and applied a horizontal pressure of 50 kPa and a vertical pressure of 125 kPa, respectively. For the cyclic test, sine

cycles of vertical displacement with a frequency of 1 Hz were applied in the vertical direction (alternating displacement of ± 0.5 mm).

According to the cyclic model pile test (Bekki et al. 2016), an axisymmetric finite element model with 1,220 elements was generated that had the same size as the test chamber, as illustrated in Figure. 6.24. The top surface was fixed in the y -direction, and the lateral and bottom boundaries were applied by the surface pressure (50 and 125 kPa, respectively). The embedded pile was modelled as a rigid body, and the sand was modelled by four-node axisymmetric elements with one reduced integration point (CAX4R) in ABAQUS. To avoid large element distortion during pile penetration, again the ALE technique was adopted around the cone, as seen in the dashed zone in Figure 6.24(c).

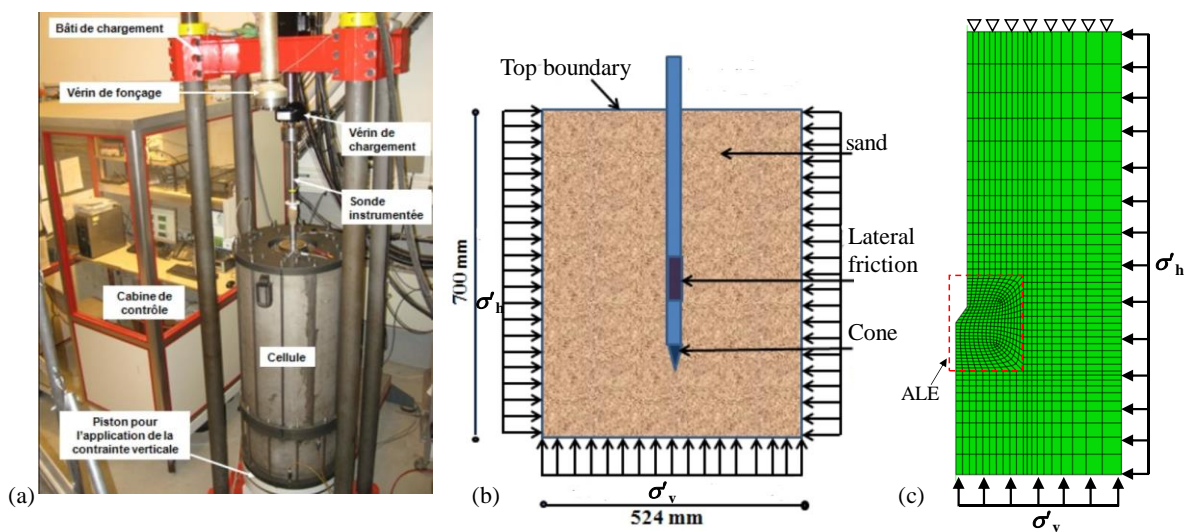


Figure 6.24 Geometry of cyclic model-pile penetration tests: (a) model-pile apparatus, (b) Geometry of centrifuge (Bekki et al. 2016) and (c) FEM modelling

Pile–soil interaction was simulated as surface-to-surface contact using a classical Coulomb friction law. The friction coefficient was set to $\mu = \tan(\phi_u/2) = 0.3$. According to the experimental program, the Fontainebleau sand NE34 (relative density of approximately 70% corresponding $e_0 = 0.62$) was first consolidated. The cyclic loading of the pile was conducted by applying alternating displacement according to the experiment.

6.7.2 Simulation results

Figure 6.25 shows the simulated results of cone resistance versus the vertical cyclic axial displacement. The prediction of cone resistance by the enhanced SIMSAND model using the parameters of Fontainebleau sand with anisotropy is in general agreement with the measurement for different number of cycles.

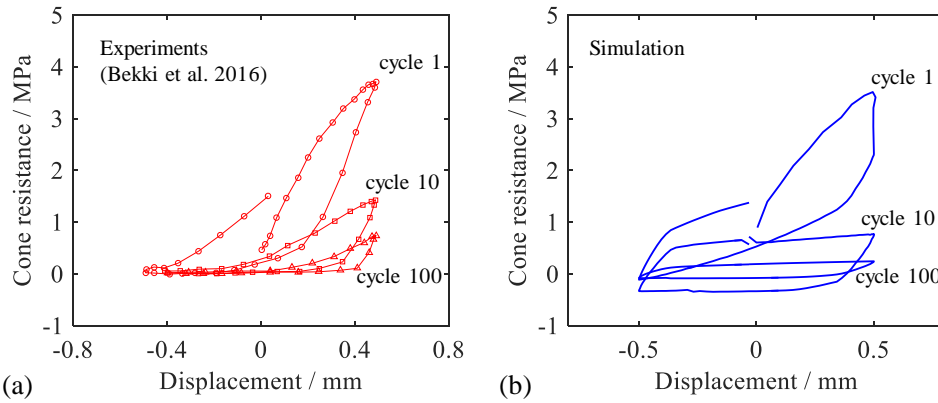


Figure 6.25 Cone resistance of cyclic model pile test (a) experiment and (b) simulation

6.7.3 Cyclic response of sand around pile

Figure 6.26 presents the void ratio of sand surrounding the pile for the different number of cycles. It can be found that a high-level densification zone accumulates around the cone at 100 cycles. Contrariwise, the density of sand particles adjacent to the cone becomes looser during the cyclic loading. Moreover, a large deformation can also be found surrounding the cone after 50 cycles.

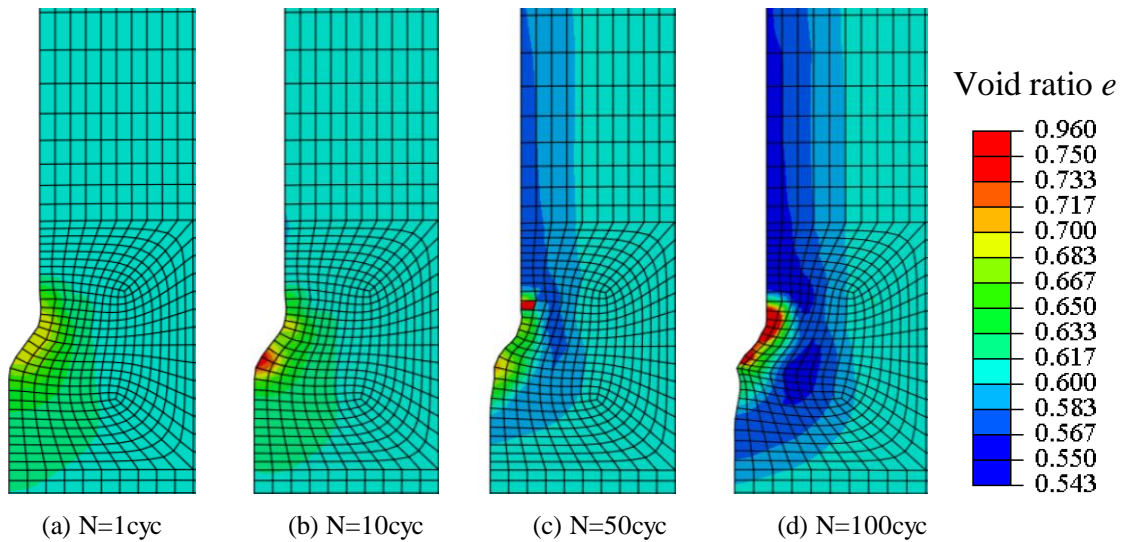


Figure 6.26 Cyclic densification behaviour surrounding the pile with different number of cycles (a) N=1 cycle, (b) N=10 cycles, (c) N=50 cycles and (c) N=100 cycles

6.8 Conclusion

The enhanced SIMSAND model with shear stress reversal technique was proposed to describe cyclic behaviours of sand. The results of undrained cyclic triaxial tests, drained cyclic triaxial tests under constant p' and under constant confining stress on Toyoura sand were well predicted by the cyclic model. Furthermore, the performance of the model was

validated by simulating the cyclic tests on Fontainebleau sand in both triaxial and simple shear loading conditions.

The capacity of the adopted FE platform with the enhanced cyclic SIMSAND model for large deformation analysis was further validated by simulating the model pile tests on Fontainebleau sand by different laboratories. Based on FE simulations, the basic features of sand surrounding the pile were presented: a high vertical contraction and horizontal dilation developed beneath the cone when the pile penetrates into the sand, with cyclic densification also occurring during the cyclic loading stage. Moreover, the extra features of the enhanced platform were also discussed based on the parametric study, which showed that effects of related inherent anisotropy parameters can amply control the shearing strength and stiffness during pile penetrating. All comparisons demonstrated that the enhanced FE platform is applicable to pile foundation design.

Chapter 7 General conclusions and perspectives

7.1 General conclusions

In this thesis, the simple shearing behaviour of Fontainebleau sand and its application to pile foundation were investigated. The main conclusions are presented as follows:

- 1) The soil elementary tests used to investigate soil mechanical behaviour surrounding the pile were first summarized while noting that the simple shear tests can amply reproduce the stress state of soil surrounding the pile. Then the latest experimental results for simple shear tests of sand were also reviewed with an eye to understanding the monotonic and cyclic simple shear behaviour of sand. Furthermore, current constitutive models, ranging from phenomenological and multiscale models to discrete element models, were outlined with the objective of selecting a robust model for use in finite element analysis for a pile foundation.
- 2) A recently developed critical state sand model (SIMSAND) was introduced along with a straightforward procedure for parameter determination. To evaluate the feasibility of this straightforward method, experimental results and numerical simulations for Toyoura sand were compared, demonstrating the proposed procedure's ability to calibrate the model parameters. The SIMSAND model was finally implemented into a finite element code, and numerical modelling was performed through a series of shallow foundation tests using the determined parameters. Overall, the proposed straightforward procedure was validated as an efficient and reliable bridge from critical state-based constitutive modelling to finite element analysis.
- 3) An enhanced SIMSAND model accounting for inherent anisotropy during the simple shear condition was developed, which was extended from the original isotropic strength to an anisotropic strength by incorporating parameters of cross anisotropy joint invariants. Based on finite element analysis, a series of three-dimensional FE simulations having the same size and boundaries as laboratory GDS-type apparatus was carried out. The performance of finite element analysis with the enhanced model was validated. In addition, the inhomogeneity features of the physical specimen were illustrated. Finally, some complementary simulations for studying sample size effect were conducted for different aspect ratios of the cylindrical specimen. This study can improve the understanding of the simple shear

test condition while providing a computational tool for analysis of inhomogeneous behaviour in the specimen.

- 4) A series of monotonic and cyclic undrained simple shear tests was performed on the Fontainebleau sand. Based on the monotonic results, an empirical expression for calculating shear stress at the phase transformation state was suggested that considered the effects of initial void ratios and initial normal effective stresses. Based on the cyclic results, a cyclic resistance diagram was obtained that provided information about the number of cycles necessary to reach instability as a function of cyclic and average shear stress levels. Furthermore, a calibration procedure for predicting the degradation of effective normal stress was proposed. Following this procedure, an analytical expression for evaluating normal effective stress degradation was developed with the following variables: initial void ratio, initial effective normal stress, cyclic shear stress, average shear stress, number of cycles. A series of additional tests including loading paths with different average shear stresses and cyclic shear stresses were used to verify the proposed analytical expression. All comparisons between experimental results and simulations indicated that the proposed method is capable of predicting degradation of effective normal stress under constant volume cyclic shear loading.
- 5) A series of monotonic and cyclic drained simple shear tests was performed on Fontainebleau sand considering different initial states-relative density, normal stress, cyclic shear stress and average shear stress. The interpretation of experimental results indicated that the effect of key factors (i.e., relative density, normal stress level, cyclic shear stress ratio and average shear stress ratio) can be respectively formulated using a simple expression. An analytical model of volumetric strain accumulation was developed considering the four aforementioned effects. The parameters were calibrated based on training tests. The applicability of the model was validated by predicting the rest of tests with the calibrated parameters.
- 6) An enhanced SIMSAND model featuring a shear stress reversal technique was introduced to describe cyclic behaviours of sand. The results of undrained cyclic triaxial tests and drained cyclic triaxial tests on Toyoura sand were well predicted. Moreover, the good performance was also validated by simulating the cyclic tests on Fontainebleau sand under both triaxial and simple shear conditions. Furthermore, simulations of the FE platform with an enhanced cyclic SIMSAND model for pile foundation were further validated through comparison of the results of model pile tests on Fontainebleau sand as performed by different laboratories. The basic features of sand adjacent to the pile were presented based on the FE simulations, including the development of high levels of vertical contraction and horizontal dilation beneath the cone when the pile penetrates into the sand, as well as

occurrence of cyclic densification during the cyclic loading stage. The extra features of the enhanced platform were also discussed based on the parametric study, which showed that effects of related inherent anisotropy parameters can amply control shearing strength and stiffness during pile penetrating. All comparisons demonstrated that the enhanced FE platform is applicable to the design of pile foundation.

7.2 Perspectives

Although the basic mechanical behaviours of soil have been investigated based on the GDS simple shear test as performed on Fontainebleau sand, inherent anisotropy during principal stress rotation, normal effective stress degradation and volumetric strain accumulation are described. What's more, the outstanding performance of the adopted SIMSAND model is also highlighted in simulation of soil elementary tests, as well as also for engineering pile penetration and cyclic loading tests. Some shortcomings remain, requiring further investigations:

- 1) More numerical studies need to be considered in relation to combined cyclic loading and application to pile foundation design in offshore engineering.
- 2) The mechanical response of soils surrounding the pile, together with the behaviour of pile foundation under complex loadings, calls for further study in hopes of gaining insights into the micromechanics and microstructure of soils.
- 3) The study could be further extended to a macro element-based design model.

References

- Aghakouchak, A., Sim, W. W., and Jardine, R. J. (2015). "Stress-path laboratory tests to characterise the cyclic behaviour of piles driven in sands." *Soils and Foundations*, 55(5), 917-928.
- Al-Douri, R. H., and Poulos, H. G. (1992). "Static and cyclic direct shear tests on carbonate sands."
- Amer, M., Aggour, M. S., and Kovacs, W. D. (1986). "Testing using a large-scale cyclic simple shear device."
- Amer, M. I. M., Aggour, M., and Kovacs, W. D. (1984). *Size Effect in Simple Shear Testing*, Department of Civil Engineering, The University of Maryland.
- Andersen, K. H. (2009). "Bearing capacity under cyclic loading-offshore, along the coast, and on land. The 21st Bjerrum Lecture presented in Oslo, 23 November 2007 " *Canadian Geotechnical Journal*, 46(5), 513-535.
- Anderson, K. (2009). "Bearing capacity under cyclic loading-offshore, along the coast, and on land." *Canadian Geotechnical Journal*, 46(5), 513-535.
- Andria-Ntoanina, I., Canou, J., and Dupla, J. (2010). "Caractérisation mécanique du sable de Fontainebleau NE34 à l'appareil triaxial sous cisaillement monotone." *Laboratoire Navier-Géotechnique. CERMES, ENPC/LCPC*.
- Asadzadeh, M., and Soroush, A. (2017). "Macro-and micromechanical evaluation of cyclic simple shear test by discrete element method." *Particuology*, 31, 129-139.
- Bekki, H., Tali, B., Canou, J., Dupla, J.-C., and Bouafia, A. (2014). "Behavior of Soil-structure interfaces under cyclic loading for large numbers of cycles: Application to piles." *Journal of Applied Engineering Science & Technology*, 1(1), 11-16.
- Bekki, H., Tali, B., Canou, J., Dupla, J.-C., and Bouafia, A. (2016). "Influence of the cyclic loading of very large number of cycles on the pile capacity." *Journal of Applied Engineering Science & Technology*, 2(2), 51-55.
- Benahmed, N. (2001). "Comportement mécanique d'un sable sous cisaillement monotone et cyclique: application aux phénomènes de liquéfaction et mobilité cyclique." *École Nationale des Ponts et Chaussées*.
- Bernhardt, M. L., and Biscontin, G. (2016). "Experimental validation study of 3D direct simple shear DEM simulations." *Soils and Foundations*, 56(3), 336-347.
- Bhattacharya, S., Lombardi, D., and Wood, D. M. (2011). "Similitude relationships for physical modelling of monopile-supported offshore wind turbines." *International Journal of Physical Modelling in Geotechnics*, 11, 58-68.
- Biarez, J., and Hicher, P.-Y. (1994). *Elementary mechanics of soil behaviour: saturated remoulded soils*, AA Balkema.
- Bjerrum, L., and Landva, A. (1966). "Direct simple-shear tests on a Norwegian quick clay." *Geotechnique*, 16(1), 1-20.

- Booker, J. (1976). "A computer program for the analysis of pore pressure generation and dissipation during cyclic or earthquake loading " *Earthquake engineering*.
- Boulon, M., and Foray, P. "Physical and numerical simulation of lateral shaft friction along offshore piles in sand." *Proc., Proceedings of the 3rd International Conference on Numerical methods in Offshore piling, Nantes, France*, 127-147.
- Budhu, M. (1984). "Nonuniformities imposed by simple shear apparatus." *Canadian Geotechnical Journal*, 21(1), 125-137.
- Budhu, M. (1988). "Failure state of a sand in simple shear." *Canadian Geotechnical Journal*, 25(2), 395-400.
- Budhu, M., and Britto, A. (1987). "Numerical analysis of soils in simple shear devices." *Soils and Foundations*, 27(2), 31-41.
- Chang, C., and Hicher, P.-Y. (2005). "An elasto-plastic model for granular materials with microstructural consideration." *International journal of solids and structures*, 42(14), 4258-4277.
- Chang, C., Yin, Z.-Y., and Hicher, P.-Y. (2010). "Micromechanical analysis for interparticle and assembly instability of sand." *Journal of Engineering Mechanics*.
- Chang, C. S., Chang, Y., and Kabir, M. G. (1992). "Micromechanics modeling for stress-strain behavior of granular soils. I: Theory." *Journal of geotechnical engineering*, 118(12), 1959-1974.
- Chang, C. S., and Misra, A. "Stress-strain behavior of sands-A microstructural approach." *Proc., Proceedings, Fourth International Symposium on Interaction of Non-Nuclear Ammunition with Structures, Panama City Beach, Florida*, 354-459.
- Chang, W.-J., Chang, C.-W., and Zeng, J.-K. (2014). "Liquefaction characteristics of gap-graded gravelly soils in K 0 condition." *Soil Dynamics and Earthquake Engineering*, 56, 74-85.
- Cole, E. (1969). "The behaviour of soils in the simple-shear apparatus." University of Cambridge.
- Coop, M., and López-Querol, S. (2012). "Drained cyclic behaviour of loose Dogs Bay sand." *Géotechnique*, 62(4), 281-289.
- Cuéllar, P., Georgi, S., Baeßler, M., and Rucker, W. (2012). "On the quasi-static granular convective flow and sand densification around pile foundations under cyclic lateral loading." *Granular Matter*, 14(1), 11-25.
- Cui, L., and Bhattacharya, S. (2016). "Soil-monopile interactions for offshore wind turbines." *Proceedings of the Institution of Civil Engineers-Engineering and Computational Mechanics*, 169(4), 171-182.
- Cundall, P. A., and Strack, O. D. (1979). "A discrete numerical model for granular assemblies." *geotechnique*, 29(1), 47-65.
- Da Fonseca, A. V., Soares, M., and Fourie, A. (2015). "Cyclic DSS tests for the evaluation of stress densification effects in liquefaction assessment." *Soil Dynamics and Earthquake Engineering*, 75, 98-111.

- Dabeet, A. (2014). "Discrete element modeling of direct simple shear response of granular soils and model validation using laboratory tests." University of British Columbia.
- Darve, F. (1990). "The expression of rheological laws in incremental form and the main classes of constitutive equations." *Geomaterials: Constitutive Equations and Modelling*, 123-148.
- Darve, F., and Labanieh, S. (1982). "Incremental constitutive law for sands and clays: simulations of monotonic and cyclic tests." *International Journal for Numerical and Analytical Methods in Geomechanics*, 6(2), 243-275.
- Dief, H. M., and Figueroa, J. L. (2007). "Liquefaction assessment by the unit energy concept through centrifuge and torsional shear tests." *Canadian Geotechnical Journal*, 44(11), 1286-1297.
- Doherty, J., and Fahey, M. (2011). "Three-dimensional finite element analysis of the direct simple shear test." *Computers and Geotechnics*, 38(7), 917-924.
- Dounias, G. T., and Potts, D. M. (1993). "Numerical analysis of drained direct and simple shear tests." *Journal of Geotechnical Engineering*, 119(12), 1870-1891.
- Duncan, J. M., and Chang, C.-Y. (1970). "Nonlinear analysis of stress and strain in soils." *Journal of Soil Mechanics & Foundations Div.*
- Dupla, J.-C., and Canou, J. (2003). "Cyclic pressuremeter loading and liquefaction properties of sands." *Soils and Foundations*, 43(2), 17-31.
- Dupla, J., and Canou, J. (1994). "Caractérisation mécanique du sable de Fontainebleau apartir d'essais triaxiaux de compression et d'extension." *Rapport Interne CLOUTERRE II, CERMES-ENPC*.
- Dyvik, R., Berre, T., Lacasse, S., and Raadim, B. (1987). "Comparison of truly undrained and constant volume direct simple shear tests." *Geotechnique*, 37(1), 3-10.
- Fakharian, K., and Evgin, E. (1997). "Cyclic simple-shear behavior of sand-steel interfaces under constant normal stiffness condition." *Journal of Geotechnical and Geoenvironmental Engineering*, 123(12), 1096-1105.
- Fu, P., and Dafalias, Y. F. (2011). "Fabric evolution within shear bands of granular materials and its relation to critical state theory." *International Journal for numerical and analytical methods in geomechanics*, 35(18), 1918-1948.
- Gajo, A., and Muir Wood, D. (1999). "A kinematic hardening constitutive model for sands: the multi-axial formulation." *International Journal for Numerical and Analytical Methods in Geomechanics*, 23(9), 925-965.
- Gajo, A., and Wood, M. (1999). "Severn-Trent sand: a kinematic-hardening constitutive model: the q-p formulation." *Géotechnique*, 49(5), 595-614.
- Gao, Z., and Zhao, J. (2012). "Efficient approach to characterize strength anisotropy in soils." *Journal of engineering mechanics*, 138(12), 1447-1456.
- Gao, Z., and Zhao, J. (2017). "A non-coaxial critical-state model for sand accounting for fabric anisotropy and fabric evolution." *International Journal of Solids and Structures*, 106, 200-212.

- Gaudin, C., Schnaid, F., and Garnier, J. (2005). "Sand characterization by combined centrifuge and laboratory tests." *International Journal of Physical Modelling in Geotechnics*, 5(1), 42-56.
- Gavin, K., Igoe, D., and Doherty, P. (2011). "Piles for offshore wind turbines: a state of the art review."
- Georgiannou, V., and Tsomokos, A. (2008). "Comparison of two fine sands under torsional loading." *Canadian Geotechnical Journal*, 45(12), 1659-1672.
- Green, R., Mitchell, J., and Polito, C. "An energy-based excess pore pressure generation model for cohesionless soils." *Proc., John Booker memorial symposium*, 16-17.
- Grognet, M. (2011). "The boundary conditions in direct simple shear tests: Developments for peat testing at low normal stress."
- Hamann, T., Qiu, G., and Grabe, J. (2015). "Application of a Coupled Eulerian–Lagrangian approach on pile installation problems under partially drained conditions." *Computers and Geotechnics*, 63, 279-290.
- Hibbitt, Karlsson, and Sorensen (2001). *ABAQUS/Explicit: User's Manual*, Hibbitt, Karlsson and Sorenson Incorporated.
- Hooker, P. "The development of automated testing in geotechnical engineering." *Proc., Proceeding of the Indian Geotechnical Conference*, 96-102.
- Hyodo, M., Murata, H., Yasufuku, N., and Fujii, T. (1991). "Undrained cyclic shear strength and residual shear strain of saturated sand by cyclic triaxial tests." *Soils and Foundations*, 31(3), 60-76.
- Illanes, M. F. S. (2014). "Experimental study of ageing and axial cyclic loading effect on shaft friction along driven piles in sands." Université Grenoble Alpes.
- Ishibashi, I., Sherif, M., and Tsuchiya, C. (1977). "Pore-pressure rise mechanism and soil liquefaction." *Soils and Foundations*, 17(2), 17-27.
- Ishibashi, I., Sherif, M. A., and Cheng, W.-L. (1982). "The effects of soil parameters on pore-pressure-rise and liquefaction prediction." *Soils and Foundations*, 22(1), 39-48.
- Ishihara, K., and Yamazaki, F. (1980). "Cyclic simple shear tests on saturated sand in multi-directional loading." *Soils and Foundations*, 20(1), 45-59.
- Iwashita, K., and Oda, M. (1998). "Rolling resistance at contacts in simulation of shear band development by DEM." *Journal of engineering mechanics*, 124(3), 285-292.
- Jardine, R., Chow, F., Overy, R., and Standing, J. (2005). *ICP design methods for driven piles in sands and clays*, Thomas Telford London.
- Jardine, R., and Standing, J. (2000). *Pile load testing performed for HSE cyclic loading study at Dunkirk, France*, Great Britain, Health and Safety Executive.
- Jardine, R., and Standing, J. (2012). "Field axial cyclic loading experiments on piles driven in sand." *Soils and foundations*, 52(4), 723-736.
- Jardine, R., Standing, J., Health, and Safety Executive, L. (2000). "Pile Load Testing Performed for HSE Cyclic Loading Study at Dunkirk, France Volume 1." *OFFSHORE TECHNOLOGY REPORT-HEALTH AND SAFETY EXECUTIVE OTO*.

- Jardine, R. J., Zhu, B., Foray, P., and Dalton, C. P. (2009). "Experimental arrangements for investigation of soil stresses developed around a displacement pile." *Soils and Foundations*, 49(5), 661-673.
- Jefferies, M. (1993). "Nor-Sand: a simple critical state model for sand." *Geotechnique*, 43(1), 91-103.
- Jin, Y.-F., Wu, Z.-X., Yin, Z.-Y., and Shen, J. S. (2017). "Estimation of critical state-related formula in advanced constitutive modeling of granular material." *Acta Geotechnica*, 1-23.
- Jin, Y.-F., Yin, Z.-Y., Shen, S.-L., and Hicher, P.-Y. (2016a). "Investigation into MOGA for identifying parameters of a critical-state-based sand model and parameters correlation by factor analysis." *Acta Geotechnica*, 11(5), 1131-1145.
- Jin, Y.-F., Yin, Z.-Y., Shen, S.-L., and Zhang, D.-M. (2016b). "A new hybrid real-coded genetic algorithm and its application to parameters identification of soils." *Inverse Problems in Science and Engineering*, 1-24.
- Jin, Y. F., Yin, Z. Y., Shen, S. L., and Hicher, P. Y. (2016c). "Selection of sand models and identification of parameters using an enhanced genetic algorithm." *International Journal for Numerical and Analytical Methods in Geomechanics*, 40(8), 1219-1240.
- Kerner, L., Dupla, J.-C., Cumunel, G., Argoul, P., Canou, J., and Pereira, J.-M. (2017). "Experimental Study on a Scaled Model of Offshore Wind Turbine on Monopile Foundation." *Models, Simulation, and Experimental Issues in Structural Mechanics*, Springer, 249-267.
- Kjellman, W. (1951). "Testing the shear strength of clay in Sweden." *Geotechnique*, 2(3), 225-232.
- Kolymbas, D. (1991). "An outline of hypoplasticity." *Archive of applied mechanics*, 61(3), 143-151.
- Konstadinou, M., and Georgiannou, V. (2014). "Prediction of pore water pressure generation leading to liquefaction under torsional cyclic loading." *Soils and Foundations*, 54(5), 993-1005.
- KOSEKI, J. (1998). "Inherent and stress-state-induced anisotropy in very small strain stiffness of a sandy gravel." *Pre-failure deformation behaviour of geomaterials*, 123.
- Kouretzis, G. P., Sheng, D., and Wang, D. (2014). "Numerical simulation of cone penetration testing using a new critical state constitutive model for sand." *Computers and Geotechnics*, 56, 50-60.
- Krishnaswamy, N., and Thomas Isaac, N. (1995). "Liquefaction analysis of saturated reinforced granular soils." *Journal of geotechnical engineering*, 121(9), 645-651.
- Lambe, T. W., and Whitman, R. V. (1969). "Soil mechanics, series in soil engineering." *John Wiley & Sons*.
- Law, K. T., Cao, Y., and He, G. (1990). "An energy approach for assessing seismic liquefaction potential." *Canadian Geotechnical Journal*, 27(3), 320-329.

- Le Kouby, A., Dupla, J. C., Canou, J., and Francis, R. (2016). "The effects of installation order on the response of a pile group in silica sand." *Soils and Foundations*, 56(2), 174-188.
- Lee, K. L., and Albaisa, A. "Earthquake induced settlements in saturated sands: 9F, 2T, 29R. J. GEOTECH. ENGG. DIV. V100, N. GT4, APR. 1974, P387-406." *Proc., International Journal of Rock Mechanics and Mining Sciences & Geomechanics Abstracts*, Pergamon, A164.
- Lehane, B., Jardine, R., Bond, A. J., and Frank, R. (1993). "Mechanisms of shaft friction in sand from instrumented pile tests." *Journal of Geotechnical Engineering*, 119(1), 19-35.
- Li, G., Liu, Y.-J., Dano, C., and Hicher, P.-Y. (2014). "Grading-dependent behavior of granular materials: from discrete to continuous modeling." *Journal of Engineering Mechanics*, 141(6), 04014172.
- Li, X. S., and Dafalias, Y. F. (2002). "Constitutive modeling of inherently anisotropic sand behavior." *Journal of Geotechnical and Geoenvironmental Engineering*, 128(10), 868-880.
- Liu, Y.-J., Li, G., Yin, Z.-Y., Dano, C., Hicher, P.-Y., Xia, X.-H., and Wang, J.-H. (2014). "Influence of grading on the undrained behavior of granular materials." *Comptes Rendus Mécanique*, 342(2), 85-95.
- Mamou, A., Powrie, W., Priest, J., and Clayton, C. (2017). "The effects of drainage on the behaviour of railway track foundation materials during cyclic loading." *Géotechnique*, 1-10.
- Manzari, M. T., and Dafalias, Y. F. (1997). "A critical state two-surface plasticity model for sands." *Geotechnique*, 47(2), 255-272.
- Mao, X., and Fahey, M. (2003). "Behaviour of calcareous soils in undrained cyclic simple shear." *Geotechnique*, 53(8), 715-727.
- Martin, G. R., Finn, W. L., and Seed, H. B. (1975). "Fundamentals of liquefaction under cyclic loading." *Journal of Geotechnical and Geoenvironmental Engineering*, 101.
- Mašín, D., and Khalili, N. (2012). "A thermo-mechanical model for variably saturated soils based on hypoplasticity." *International journal for numerical and analytical methods in geomechanics*, 36(12), 1461-1485.
- Matsuda, H., Hendrawan, A. P., Ishikura, R., and Kawahara, S. (2011). "Effective stress change and post-earthquake settlement properties of granular materials subjected to multi-directional cyclic simple shear." *Soils and Foundations*, 51(5), 873-884.
- Mitchell, R. J., and Dubin, B. I. (1986). "Pore pressure generation and dissipation in dense sands under cyclic loading." *Canadian Geotechnical Journal*, 23(3), 393-398.
- Miura, K., Toki, S., and Miura, S. (1986). "Deformation prediction for anisotropic sand during the rotation of principal stress axes." *Soils and Foundations*, 26(3), 42-56.
- Miura, N., Murata, H., and Yasufuku, N. (1984). "Stress-strain characteristics of sand in a particle-crushing region." *Soils and Foundations*, 24(1), 77-89.

- Mohtar, C. E., Bobet, A., Drnevich, V., Johnston, C., and Santagata, M. (2014). "Pore pressure generation in sand with bentonite: from small strains to liquefaction." *Géotechnique*, 64(2), 108.
- Mortara, G., Mangiola, A., and Ghionna, V. N. (2007). "Cyclic shear stress degradation and post-cyclic behaviour from sand–steel interface direct shear tests." *Canadian Geotechnical Journal*, 44(7), 739-752.
- Nemat-Nasser, S., and Shokooch, A. (1979). "A unified approach to densification and liquefaction of cohesionless sand in cyclic shearing." *Canadian Geotechnical Journal*, 16(4), 659-678.
- Niemunis, A., and Herle, I. (1997). "Hypoplastic model for cohesionless soils with elastic strain range." *Mechanics of Cohesive-frictional Materials*, 2(4), 279-299.
- Nikitas, G., Arany, L., Aingaran, S., Vimalan, J., and Bhattacharya, S. (2017). "Predicting long term performance of offshore wind turbines using cyclic simple shear apparatus." *Soil Dynamics and Earthquake Engineering*, 92, 678-683.
- Oda, M. (1972). "The mechanism of fabric changes during compressional deformation of sand." *Soils and foundations*, 12(2), 1-18.
- Oda, M., and Nakayama, H. (1989). "Yield function for soil with anisotropic fabric." *Journal of Engineering Mechanics*, 115(1), 89-104.
- Ortiz, M., and Simo, J. (1986). "An analysis of a new class of integration algorithms for elastoplastic constitutive relations." *International Journal for Numerical Methods in Engineering*, 23(3), 353-366.
- Oumarou, T. A., and Evgin, E. (2005). "Cyclic behaviour of a sand steel plate interface." *Canadian geotechnical journal*, 42(6), 1695-1704.
- Paradhan, T. B. S. (1990). "The behavior of sand subjected to monotonic and cyclic loadings." Japan: Kyoto University.
- Peacock, W. H. (1968). "Sand liquefaction under cyclic loading simple shear conditions." *Journal of Soil Mechanics & Foundations Div.*
- Phong, M. (1980). *Phénomènes cycliques dans les sols pulvérulents*.
- Pietruszczak, S., and Mroz, Z. (2000). "Formulation of anisotropic failure criteria incorporating a microstructure tensor." *Computers and Geotechnics*, 26(2), 105-112.
- Pietruszczak, S., and Mroz, Z. (2001). "On failure criteria for anisotropic cohesive-frictional materials." *International journal for numerical and analytical methods in geomechanics*, 25(5), 509-524.
- Polito, C. P., Green, R. A., and Lee, J. (2008). "Pore pressure generation models for sands and silty soils subjected to cyclic loading." *Journal of Geotechnical and Geoenvironmental Engineering*, 134(10), 1490-1500.
- Porcino, D., Caridi, G., and Ghionna, V. N. (2008). "Undrained monotonic and cyclic simple shear behaviour of carbonate sand." *Seed*, 15(1), 29-44.
- Porcino, D., Marcianò, V., and Granata, R. (2015). "Cyclic liquefaction behaviour of a moderately cemented grouted sand under repeated loading." *Soil Dynamics and Earthquake Engineering*, 79, 36-46.

- Poulos, H. G. (1988). "Cyclic stability diagram for axially loaded piles." *Journal of geotechnical engineering*, 114(8), 877-895.
- Pra-Ai, S. (2013). "Essais et modélisation du cisaillement cyclique sol-structure à grand nombre de cycles. Application aux pieux." Université Grenoble Alpes.
- Pra-ai, S., and Boulon, M. (2017). "Soil–structure cyclic direct shear tests: a new interpretation of the direct shear experiment and its application to a series of cyclic tests." *Acta Geotechnica*, 12(1), 107-127.
- Qiu, G., Henke, S., and Grabe, J. (2011). "Application of a Coupled Eulerian–Lagrangian approach on geomechanical problems involving large deformations." *Computers and Geotechnics*, 38(1), 30-39.
- Randolph, M. F., and Wroth, C. (1981). "Application of the failure state in undrained simple shear to the shaft capacity of driven piles." *Geotechnique*, 31(1), 143-157.
- Reyno, A., Airey, D., and Taiebat, H. "Influence of height and boundary conditions in simple shear tests." *Proc., International Symposium on Frontiers in Offshore Geotechnics*, Taylor & Francis/Balkema.
- Richart, F. E., Hall, J. R., and Woods, R. D. (1970). "Vibrations of soils and foundations."
- Rimoy, S. P. (2013). "Ageing and axial cyclic loading studies of displacement piles in sands."
- Roscoe, K. (1953). "An apparatus for the application to simple shear to soil samples." *Proc., 2nd ICSMFE, Zurich, 1953*, 1, 186-191.
- Roscoe, K. H. (1970). "The influence of strains in soil mechanics." *Geotechnique*, 20(2), 129-170.
- Seed, H. B., and Idriss, I. M. (1971a). "Simplified procedure for evaluating soil liquefaction potential." *Journal of Soil Mechanics & Foundations Div*, 91(9), 1249-1274.
- Seed, H. B., and Idriss, I. M. (1971b). "Simplified procedure for evaluating soil liquefaction potential." *Journal of Soil Mechanics & Foundations Div*.
- Seed, H. B., Martin, P. P., and Lysmer, J. (1975). *The generation and dissipation of pore water pressures during soil liquefaction*, College of Engineering, University of California.
- Sheng, D., Sloan, S., and Yu, H. (2000). "Aspects of finite element implementation of critical state models." *Computational mechanics*, 26(2), 185-196.
- Sherif, M. A., Ishibashi, I., and TSUCHIYA, C. (1978). "Pore-pressure prediction during earthquake loadings." *Soils and Foundations*, 18(4), 19-30.
- Sim, W. W., Aghakouchak, A., and Jardine, R. J. (2013a). "Cyclic triaxial tests to aid offshore pile analysis and design." 111-121.
- Sim, W. W., Aghakouchak, A., and Jardine, R. J. (2013b). "Cyclic triaxial tests to aid offshore pile analysis and design."
- Sim, W. W., Aghakouchak, A., and Jardine, R. J. (2013c). "Cyclic triaxial tests to aid offshore pile analysis and design." *Proceedings of the Institution of Civil Engineers-Geotechnical Engineering*, 166(2), 111-121.
- Sivathayalan, S. (1994). "Static, cyclic and post liquefaction simple shear response of sands." University of British Columbia.

- Sriskandakumar, S. (2004). "Cyclic loading response of Fraser River sand for validation of numerical models simulating centrifuge tests." University of British Columbia.
- Sun, Q., Cai, Y., Chu, J., Dong, Q., and Wang, J. (2017). "Effect of variable confining pressure on cyclic behaviour of granular soil under triaxial tests." *Canadian Geotechnical Journal*, 54(6), 768-777.
- Susila, E., and Hryciw, R. D. (2003). "Large displacement FEM modelling of the cone penetration test (CPT) in normally consolidated sand."
- Taiebat, M., and Dafalias, Y. F. (2008). "SANISAND: simple anisotropic sand plasticity model." *International Journal for Numerical and Analytical Methods in Geomechanics*, 32(8), 915-948.
- Tomita, Y., Nishigata, T., Masui, T., and Yao, S. (2012). "Load settlement relationships of circular footings considering dilatancy characteristics of sand." *International journal of GEOMATE: geotechnique, construction materials and environment*, 2(1), 148-153.
- Towhata, I., and Ishihara, K. (1985). "Shear work and pore water pressure in undrained shear." *Soils and Foundations*, 25(3), 73-84.
- Tsuha, C. d. H. C., Foray, P., Jardine, R., Yang, Z., Silva, M., and Rimoy, S. (2012a). "Behaviour of displacement piles in sand under cyclic axial loading." *Soils and Foundations*, 52(3), 393-410.
- Tsuha, C. H. C., Foray, P., Jardine, R., Yang, Z., Silva, M., and Rimoy, S. (2012b). "Behaviour of displacement piles in sand under cyclic axial loading." *Soils and foundations*, 52(3), 393-410.
- Uchida, K., and Stedman, J. "Liquefaction behavior of Toyoura sand under cyclic strain controlled triaxial loading." *Proc., Proceedings of the Eleventh International Offshore and Polar Engineering Conference, Stavanger, Norway*, 17-22.
- Vaid, Y., and Sivathayalan, S. (1996). "Static and cyclic liquefaction potential of Fraser Delta sand in simple shear and triaxial tests." *Canadian Geotechnical Journal*, 33(2), 281-289.
- Vaid, Y., Stedman, J., and Sivathayalan, S. (2001). "Confining stress and static shear effects in cyclic liquefaction." *Canadian Geotechnical Journal*, 38(3), 580-591.
- Vaid, Y. P., Byrne, P., and Hughes, J. (1981). "Dilation angle and liquefaction potential."
- Vaid, Y. P., and Chern, J.-C. (1983). "Effect of static shear on resistance to liquefaction." *Soils and Foundations*, 23(1), 47-60.
- Verdugo, R., and Ishihara, K. (1996). "The steady state of sandy soils." *Soils and foundations*, 36(2), 81-91.
- Wang, B., Popescu, R., and Prevost, J. H. (2004). "Effects of boundary conditions and partial drainage on cyclic simple shear test results—a numerical study." *International journal for numerical and analytical methods in geomechanics*, 28(10), 1057-1082.
- Wang, C.-C. (1970). "A new representation theorem for isotropic functions: An answer to Professor GF Smith's criticism of my papers on representations for isotropic functions." *Archive for Rational Mechanics and Analysis*, 36(3), 166-197.

- Wichtmann, T., Niemunis, A., and Triantafyllidis, T. (2005). "Strain accumulation in sand due to cyclic loading: drained triaxial tests." *Soil Dynamics and Earthquake Engineering*, 25(12), 967-979.
- Wichtmann, T., and Triantafyllidis, T. (2016a). "An experimental data base for the development, calibration and verification of constitutive models for sand with focus to cyclic loading: part I—tests with monotonic loading and stress cycles." *Acta Geotechnica*, 11(4), 739-761.
- Wichtmann, T., and Triantafyllidis, T. (2016b). "An experimental data base for the development, calibration and verification of constitutive models for sand with focus to cyclic loading: part II —tests with strain cycles and combined loading." *Acta Geotechnica*, 11(4), 763-774.
- Wijewickreme, D., Sriskandakumar, S., and Byrne, P. (2005). "Cyclic loading response of loose air-pluviated Fraser River sand for validation of numerical models simulating centrifuge tests." *Canadian Geotechnical Journal*, 42(2), 550-561.
- Wood, D., and Budhu, M. (2014). "The behaviour of Leighton Buzzard sand in cyclic simple shear tests."
- Wood, D., Drescher, A., and Budhu, M. (1979). "On the determination of stress state in the simple shear apparatus."
- Wu, W., and Bauer, E. (1993). "A hypoplastic model for barotropy and pyknotropy of granular soils." *Modern approaches to plasticity*, 383.
- Wu, W., Bauer, E., and Kolymbas, D. (1996). "Hypoplastic constitutive model with critical state for granular materials." *Mechanics of materials*, 23(1), 45-69.
- Wu, Z.-X., Yin, Z.-Y., Jin, Y.-F., and Geng, X.-Y. (2017). "A straightforward procedure of parameters determination for sand: a bridge from critical state based constitutive modelling to finite element analysis." *European Journal of Environmental and Civil Engineering*, 1-23.
- Yamakawa, Y., Hashiguchi, K., and Ikeda, K. (2010). "Implicit stress-update algorithm for isotropic Cam-clay model based on the subloading surface concept at finite strains." *International Journal of Plasticity*, 26(5), 634-658.
- Yang, J., and Sze, H. (2011). "Cyclic behaviour and resistance of saturated sand under non-symmetrical loading conditions." *Géotechnique*.
- Yang, Y., and Yu, H.-S. (2010). "Numerical aspects of non-coaxial model implementations." *Computers and Geotechnics*, 37(1), 93-102.
- Yang, Y., and Yu, H. (2006a). "A non-coaxial critical state soil model and its application to simple shear simulations." *International journal for numerical and analytical methods in geomechanics*, 30(13), 1369-1390.
- Yang, Y., and Yu, H. (2006b). "Numerical simulations of simple shear with non-coaxial soil models." *International journal for numerical and analytical methods in geomechanics*, 30(1), 1-19.

- Yang, Z., Jardine, R., Zhu, B., Foray, P., and Tsuha, C. (2010). "Sand grain crushing and interface shearing during displacement pile installation in sand." *Géotechnique*, 60(6), 469-482.
- Yang, Z., and Pan, K. (2017). "Flow deformation and cyclic resistance of saturated loose sand considering initial static shear effect." *Soil Dynamics and Earthquake Engineering*, 92, 68-78.
- Yao, Y.-P., and Kong, Y.-X. (2011). "Extended UH model: Three-dimensional unified hardening model for anisotropic clays." *Journal of engineering mechanics*, 138(7), 853-866.
- Yao, Y., Sun, D., and Matsuoka, H. (2008). "A unified constitutive model for both clay and sand with hardening parameter independent on stress path." *Computers and Geotechnics*, 35(2), 210-222.
- Yimsiri, S., and Soga, K. (2010). "DEM analysis of soil fabric effects on behaviour of sand." *Géotechnique*, 60(6), 483-495.
- Yin, Z.-Y., Chang, C. S., and Hicher, P.-Y. (2010a). "Micromechanical modelling for effect of inherent anisotropy on cyclic behaviour of sand." *International Journal of Solids and Structures*, 47(14), 1933-1951.
- Yin, Z.-Y., Chang, C. S., Hicher, P.-Y., and Karstunen, M. (2009). "Micromechanical analysis of kinematic hardening in natural clay." *International Journal of Plasticity*, 25(8), 1413-1435.
- Yin, Z.-Y., Chang, C. S., Karstunen, M., and Hicher, P.-Y. (2010b). "An anisotropic elastic–viscoplastic model for soft clays." *International Journal of Solids and Structures*, 47(5), 665-677.
- Yin, Z.-Y., Hicher, P.-Y., Dano, C., and Jin, Y.-F. (2016). "Modeling mechanical behavior of very coarse granular materials." *Journal of Engineering Mechanics*, 143(1), C4016006.
- Yin, Z.-Y., Xu, Q., and Hicher, P.-Y. (2013). "A simple critical-state-based double-yield-surface model for clay behavior under complex loading." *Acta Geotechnica*, 8(5), 509-523.
- Yin, Z.-Y., Zhao, J., and Hicher, P.-Y. (2014). "A micromechanics-based model for sand-silt mixtures." *International journal of solids and structures*, 51(6), 1350-1363.
- Yin, Z. Y., and Chang, C. S. (2013). "Stress–dilatancy behavior for sand under loading and unloading conditions." *International Journal for Numerical and Analytical Methods in Geomechanics*, 37(8), 855-870.
- Yoshimine, M., Ishihara, K., and Vargas, W. (1998). "Effects of principal stress direction and intermediate principal stress on undrained shear behavior of sand." *Soils and Foundations*, 38(3), 179-188.
- Yoshimine, M., Robertson, P., and Wride, C. (1999). "Undrained shear strength of clean sands to trigger flow liquefaction." *Canadian Geotechnical Journal*, 36(5), 891-906.
- Yu, H. (1998). "CASM: A unified state parameter model for clay and sand." *International Journal for Numerical and Analytical Methods in Geomechanics*, 22(8), 621-653.

- Zhang, C., Nguyen, G., and Einav, I. (2013). "The end-bearing capacity of piles penetrating into crushable soils." *Géotechnique*, 63(5), 341.
- Zhao, X., and Evans, T. M. (2009). "Discrete simulations of laboratory loading conditions." *International journal of geomechanics*, 9(4), 169-178.
- Zhu, H., Zhou, W.-H., and Yin, Z.-Y. (2017). "Deformation mechanism of strain localization in 2D numerical interface tests." *Acta Geotechnica*, 1-17.

Appendix A Matlab code for parameters of SIMSAND

A.1 MATLAB CODE-1 for elasticity parameters of sand

```
deps_v=-de/(1+e (1));
kk =dp./deps_v;
k_smooth=smooth(kk,1);
k_c= k_smooth;
%-----
ka=k_c(a);
kb=k_c(b);
ea=e(a);
eb=e(b);
pa=p(a);
pb=p(b);
zeta=(log(ka./kb*(1+ea)/(1+eb)*(2.97-eb)^2/(2.97-ea)^2))/(log(pa/pb));
k0a=ka/pat*(1+ea)/(2.97-ea)^2*(pat/pa)^zeta;
k0b=kb/pat*(1+eb)/(2.97-eb)^2*(pat/pb)^zeta;
k0=( k0a+ k0b)/2.;
```

A.2 MATLAB CODE-2 for parameters of critical state line

```
%----set function in p-q space
fun_m = @(M, p_m)M*p_m;
%----define CSL_M in p-q space
M0=1;
[M,resnorm,residual]=lsqcurvefit(fun_m,M0,p_m,q_m);
fi=180/pi*asin(3*M/(6+M));
%---set function in e-logp space
fun_ep = @(para_e, p_m) para_e(1)-para_e(2)*(p_m/101.325).^para_e(3);
%define CSL_e in e-lnp space
para_e0=[1 1 1];
[para_e,resnorm,residual]=lsqcurvefit(fun_ep,para_e0,p_m,e_m);
%---print parameters
eref=para_e(1)
lambda=para_e(2)
xi=para_e(3)
%-----
```

A.3 MATLAB CODE-3 for data re-interpretations:

```

%Calibrating the data matrix of parameters ec, epsdp, depsv_p, depsd_p.

%---step1. Interpolated each data by 0.0001 epsa
temp_ref=max(exp_epsa);
eps_temp=0:1/1000:temp_ref;
exp_q_cs=csaps(exp_epsa,exp_q,1,eps_temp);
exp_p_cs=csaps(exp_epsa,exp_p,1,eps_temp);
exp_e_cs=csaps(exp_epsa,exp_e,1,eps_temp);
exp_epsa_cs=eps_temp;
epsa=exp_epsa_cs;
q=exp_q_cs;
p=exp_p_cs;
e=exp_e_cs;
eta=q./p;
%
eref=0.875;           % reference section 3.3
lambda=0.085;        % reference section 3.3
xi=0.229;            % reference section 3.3
pat=101.325
ec=eref-lambda*(p/pat).^xi; % reference the Eq.(8)-a
%
%--- step2. Calibrating the array for dp ,dq depsv and depsd-----
dp=[0; p(2:length(p))-p(1:(length(p)-1))];
dq=[0; q(2:length(q))-q(1:(length(q)-1))];
e0=e(1);
epsv=-(e-e0)/(1+e0);
epsv=smooth(epsv,1);
depsv=[0; epsv(2:length(epsv))-epsv(1:(length(epsv)-1))];
epsd=epsa-epsv/3;
depsd=[0; epsd(2:length(epsd))-epsd(1:(length(epsd)-1))];
%
%-----step3. Calibrating the array of depsv_e, depsd_e, epsv_e and epsd_e
pat=101.325;
nu=0.25 ;           % reference the Eq.13
K0=97.56;           % reference the Table 2
n=0.604;           % reference the Table 2
K=K0*pat*((2.97-e).^2/(1+e))*(p/pat).^n;
G0=3*K0*(1-2*nu)/(2*(1+nu));
G=G0*pat*((2.97-e).^2/(1+e))*(p/pat).^n;
depsv_e=dp./K;
depsv_e=smooth(depsv_e, 1);
depsd_e=dq./(3*G);
depsd_e=smooth(depsd_e,1);
%-----
for i=1:length(depsv_e);
    if i==1
        epsv_e(i)=depsv_e(i);
    end
end

```

```

else
    epsv_e(i)=epsv_e(i-1)+depsv_e(i);
end
end
epsv_e=epsv_e';
%-----
for i=1:length(depsd_e);
    if i==1
        epsd_e(i)=depsd_e(i);
    else
        epsd_e(i)=epsd_e(i-1)+depsd_e(i);
    end
end
epsd_e=epsd_e';

%----- step4. Calibrating the array of depsv_p, depsd_p, epsv_p and epsd_p
depsv_p=depsv-depsv_e;
depsv_p=smooth(depsv_p,1);
%-----
depsd_p=depsd-depsd_e;
depsd_p=smooth(depsd_p,1);
%-----
for i=1:length(depsv_p);
    if i==1
        epsv_p(i)=depsv_p(i);
    else
        epsv_p(i)=epsv_p(i-1)+depsv_p(i);
    end
end
epsv_p=epsv_p';
%-----
for i=1:length(depsd_p);
    if i==1
        epsd_p(i)=depsd_p(i);
    else
        epsd_p(i)=epsd_p(i-1)+depsd_p(i);
    end
end
epsd_p=epsd_p';
%-----

```

A.4 MATLAB CODE-4 for interlocking parameters np, kp, nd and ad:

```

%---Solveing the Eq.(2-17,2-18) to get the objective parameters np, kp, nd, ad-----
%---step 1. get the col of the corresponding strain a and b.
% choosing the strain of points A and B
a=0.01 % point A
b=0.02 % point B
[row,col_a]=min(abs(exp_epsa_cs-a));
p1=col_a;
[row,col_b]=min(abs(exp_epsa_cs-a));
p2=col_b;
%---step 2. get the known parameters for the Eq.(17,18)
exp_epsa_a=exp_epsa_cs(p1);
exp_epsa_b=exp_epsa_cs(p2);
%-----
ece=e-ec;
ece_a=ece(p1);
ece_b=ece(p2);
%-----
epsdp_a=epsdp_p(p1);
epsdp_b=epsdp_p(p2);
%-----
qp=exp_q_cs./exp_p_cs;
qp_a=qp(p1);
qp_b=qp(p2);
%-----
depsvdp=depsv_p./depsd_p;
depsvdp_a=depsvdp(p1);
depsvdp_b=depsvdp(p2);
%----step 3. solve the Eq.(2-17,2-18) to get the roots (np, kp, nd, ad)
fnp=@(np)(epsdp_a*qp_b*M*exp(ece_a*(-np))...
-epsdp_b*qp_a*M*exp(ece_b*(-np))...
-qp_a*qp_b*(epsdp_a-epsdp_b)); np0=1;
np=fzero(fnp,np0);
%-----
mp_a=M*exp(ece_a*(-np));
kp_a=mp_a*epsdp_a/qp_a-epsdp_a;
%
mp_b=M*exp(ece_b*(-np));
kp_b=mp_b*epsdp_b/qp_b-epsdp_b;
%-----
fnd=@(nd)(...
depsvdp_a./(M*exp(ece_a*(nd))-qp_a)...
-depsvdp_b./(M*exp(ece_b*(nd))-qp_b));
nd0=1;
nd=fzero(fnd,nd0);
%-----
mpt_a=M*exp(ece_a*(nd));
ad_a=depsvdp_a/(mpt_a-qp_a);

```

```
%  
mpt_b=M*exp(ece_b*(nd));  
ad_b=depsvdp_b/(mpt_b-qp_b);  
%-----
```

List of Publications

- 1) **Wu Z-X**, Yin Z-Y, Jin Y-F, Geng X-Y. A straightforward procedure of parameters determination for sand: a bridge from critical state based constitutive modelling to finite element analysis. *European Journal of environmental and civil engineering*, 2017. <https://doi.org/10.1080/19648189.2017.1353442>
- 2) Yin Z-Y, **Wu Z-X**, Hicher P-Y. Modeling the monotonic and cyclic behavior of granular materials by an exponential constitutive function. *Journal of Engineering Mechanics ASCE*, 2018. DOI: 10.1061/(ASCE)EM.1943-7889.0001437.
- 3) **Wu Z-X**, Dano C, Hicher P-Y, Yin Z-Y. Estimating normal effective stress degradation in sand under undrained simple shear condition. *European Journal of environmental and civil engineering*, 2018. <https://doi.org/10.1080/19648189.2018.1521750>
- 4) **Wu Z-X**, Yin Z-Y, Dano C, Hicher P-Y. Finite element analysis of simple shear test using an enhanced critical state soil model considering inherent anisotropy (manuscript).
- 5) **Wu Z-X**, Yin Z-Y, Dano C, Hicher P-Y. Cyclic volumetric strain accumulation behaviour of sand under drained simple shear condition (manuscript).